

Titre: Development of High Barrier Nylon Based Multilayer Films
Title:

Auteur: Maryam Fereydoon
Author:

Date: 2014

Type: Mémoire ou thèse / Dissertation or Thesis

Référence: Fereydoon, M. (2014). Development of High Barrier Nylon Based Multilayer Films [Thèse de doctorat, École Polytechnique de Montréal]. PolyPublie.
Citation: <https://publications.polymtl.ca/1362/>

 **Document en libre accès dans PolyPublie**
Open Access document in PolyPublie

URL de PolyPublie: <https://publications.polymtl.ca/1362/>
PolyPublie URL:

**Directeurs de
recherche:** Abdellah Aji, & Hesam Tabatabaei
Advisors:

Programme: Génie chimique
Program:

UNIVERSITÉ DE MONTRÉAL

DEVELOPMENT OF HIGH BARRIER NYLON BASED
MULTILAYER FILMS

MARYAM FERAYDOON

DÉPARTEMENT DE GÉNIE CHIMIQUE
ÉCOLE POLYTECHNIQUE DE MONTRÉAL

THÈSE PRÉSENTÉE EN VUE DE L'OBTENTION
DU DIPLÔME DE PHILOSOPHIAE DOCTOR
(GÉNIE CHIMIQUE)
MARS 2014

UNIVERSITÉ DE MONTRÉAL

ÉCOLE POLYTECHNIQUE DE MONTRÉAL

Cette thèse intitulée:

DEVELOPMENT OF HIGH BARRIER NYLON BASED
MULTILAYER FILMS

présentée par: FEREYDOON Maryam

en vue de l'obtention de diplôme de: Philosophiae Doctor

a été dûment acceptée par le jury d'examen constitué de:

M. LAFLEUR Pierre, Ph.D., président

M. AJJI Abdellah, Ph.D., membre et directeur de recherche

M. TABATABAEI Hesam, Ph.D., membre et codirecteur de recherche

M. VIRGILIO Nick, Ph.D., membre

M. ELKOUN Said, Ph.D., membre

ACKNOWLEDGEMENTS

First of all, I would like to offer my deep and sincere gratitude to my supervisor, Prof. Abdellah Ajji. It was a great privilege to work with this wise and understanding professor and I do not forget all his supports and the trust he placed in me throughout the period of this project.

Professor Seyed Hesamoddin Tabatabaei, who co-supervised my thesis since 2012, has helped me a lot. His talent and his logical way of thinking as well as his patience, encouragements, advices, and guidance have been great value for me. I also acknowledge all the efforts he made for the improvement of the quality of the articles and eventually this thesis.

I would like to deeply thank Dr. Farhad Sadeghi for his great assistance, help and trainings at the beginning months of this research.

Special thanks to the technical staff of the chemical engineering department, especially Ms. Claire Cerclé, Ms. Melina Hamdine, Ms. Weawkamol Leelapornpisit, and Mr. Guillaume Lessard, for their help during this study. I am also thankful to Mr. Pierre-Marc Simard for his technical help at POLYNOV.

I would like to offer my deepest thanks to Ms. Claire Cerclé for her warm and quick response to my request for translating parts of this thesis to French and for her technical assistance during this project.

Financial support from NSERC (Natural Science and Engineering Research Council of Canada) and the industrial partners of 3SPack Chair Saputo and Prolamina is appreciable.

I also thank all my friends and colleagues for their unforgettable help during my PhD.

Finally, with all my heart, I would like to thank my beloved parents and husband, who have been always there for me in every situation. There will never be a right word to express my feeling of appreciation for their unconditional love.

RÉSUMÉ

Les films multicouches sont composés d'une couche de cœur possédant de bonnes propriétés barrières et mécaniques, prise en sandwich entre deux couches de polyoléfines. Cette composition est couramment utilisée dans l'industrie des emballages alimentaires afin d'améliorer les propriétés mécaniques et barrières à l'oxygène et à l'humidité des films. Au cours de cette étude, des films multicouches à base de nylon aromatique (MXD6), aliphatique (PA6) et leurs nanocomposites, à hautes propriétés barrières ont été développés. Les performances thermiques, barrières (oxygène et vapeur d'eau) et mécaniques des films multicouches ont été comparées entre elles, en faisant varier la couche de cœur (PA6, MXD6 ou leurs nanocomposites).

Dans la première partie de ce travail, des films de nylon aliphatique (PA6), de nylon aromatique (MXD6) ainsi que leurs nanocomposites, préparé par polymérisation in-situ avec 4wt% d'argile, ont été extrudés par calandrage à l'aide d'une extrudeuse de laboratoire et refroidis rapidement à l'aide de couteaux d'air. Les propriétés rhéologiques, cristallines, thermiques, barrières et mécaniques des résines pures et des films monocouches extrudés ont été étudiées et comparées.

Dans la seconde partie de ce travail, les films monocouches produits ont été étirés uniaxialement à 110 °C avec un rapport d'étirage variant de 1.5 à 5. L'alignement de l'argile généré par l'étirement des films de nanocomposites ont été mesurés à l'aide de trois techniques différentes : déconvolution des pics en FTIR, soustraction spectrale interactives en FTIR, et diffraction aux Rayons X. Il a été déterminé que les particules d'argile sont principalement orientées dans la direction machine (MD) et que leur orientation est améliorée sous l'effet de l'étirement uniaxial. L'effet des changements d'orientation des cristaux pour toutes les phases

cristallines et amorphes a été examiné à l'aide de la diffraction aux rayons X et de l'analyse trichroïque des spectres FTIR. Basé sur les modèles WAXD et les résultats en FTIR, il a été possible de proposer un model schématique afin de décrire le mécanisme de cristallisation du nylon en présence d'argile.

Dans la troisième partie de cette étude, l'effet de l'étirement uniaxial sur la structure cristalline, les propriétés thermiques, mécaniques et barrières à l'oxygène des nylons aromatiques et aliphatiques ainsi que de leur nanocomposites ont été étudiés et comparés.

Finalement, les films multicouches contenant en couche de cœur, le PA6, ou le MXD6, ou leur nanocomposites ont été produits en utilisant une unité de coextrusion calandrage de laboratoire. Les couches sandwich de peau sont en LLDPE, et agissent comme des couches barrières à l'humidité. Des films multicouches à 5 couches (une couche supplémentaire a été ajouté de chaque côté entre la couche de cœur et de peau afin d'en améliorer la compatibilité) ont également été produits. Durant le procédé, les paramètres de production ont été optimisés afin d'éliminer les instabilités interfaciales et d'améliorer l'uniformité des films multicouches. Les films produits ont été caractérisés et comparés.

ABSTRACT

Insufficient barrier properties of commercial thermoplastics to the permeation of atmospheric gases such as oxygen and water vapor are a major problem in the packaging industry. In particular, a high oxygen permeation rate reduces the shelf life of packaged food products, which results in higher costs for food processors and retail customers. Multilayer films having a core layer with good barrier and mechanical properties coextruded between two polyolefin layers have been used in food packaging industry to improve the mechanical performance and the barrier properties. Nylon is an engineering thermoplastic used in flexible packaging due to its high stiffness, toughness, tensile strength, flex crack and puncture resistance as well as low oxygen transmission rate. The objective of this research was fundamental understanding on the differences between properties of monolayer and multilayer aromatic and aliphatic nylon films and their nanocomposites.

In the selection of the aromatic and aliphatic nylons, particular attention paid to the oxygen barrier properties of the films as the targeted application is for food packaging and this property plays a critical role in determining shelf life of packed product. Resin characteristics particularly the rheological and thermal properties, morphology, molecular orientation, ability to crystallize (i.e. fast or slow crystallization rate), type of crystalline structure are the key factors for the production of the precursor films with appropriate crystallinity and orientation, which in turn control the final film properties. The extent of nanoclay intercalation and exfoliation, crystal structure, crystallinity, thermal, rheological, barrier and mechanical properties of polyamide 6 (PA6), poly (m-xylene adipamide) (MXD6) and their in-situ polymerized nanocomposites with 4 wt% clay were studied and compared. Dynamic rheological measurements confirmed a strong interfacial interaction between the silicate platelets and the MXD6 chains. A longer relaxation

time for the MXD6, which was related to its higher intermolecular interactions compared to the PA6, resulted in a slower rate of crystallization and lower crystallinity in the former. It was found that due to the stronger polymer chain interaction of the MXD6, there was a lower free volume and gas diffusion path for the MXD6 nanocomposite film compared to the PA6 nanocomposite.

In the second part of this project, the precursor monolayer films were uniaxially stretched at 110 °C with draw ratios varying from 1.5 to 5. The clay alignment was measured with three different techniques: FTIR peak deconvolution, FTIR interactive spectral subtraction and X-ray diffraction. It was found that the clay platelets are mainly oriented in the machine direction (MD) and their orientation improved upon uniaxial stretching. The changes in orientation of crystal axes of all the crystalline phases and amorphous region of the aromatic and the aliphatic nylons and their nanocomposites were examined using X-ray diffraction and Trichroic Infrared analyses. Based on the WAXD patterns and FTIR results, schematic models were proposed to describe the crystallization mechanism of the nylon in the presence of the clay platelets.

The crystalline and amorphous orientations as well as the clay alignment significantly affect the performance of the stretched films. In the third step of this study, the structural development of the aliphatic and aromatic nylons and their nanocomposite films during uniaxial stretching was investigated. The effect of uniaxial drawing on the morphology, crystallinity, thermal, mechanical and oxygen barrier properties of the polyamide 6 and the MXD6 as well as their in-situ polymerized nanocomposites were studied. A significant enhancement in the Young's modulus and tensile strength of the uniaxially stretched aliphatic and aromatic nylons was observed. The oxygen permeability and oxygen diffusion through the nylon nanocomposite films

were predicted with theoretical models and with incorporating structural parameters such as the crystalline phase orientation, clay aspect ratio and clay orientation.

In the last phase, coextruded multilayer films with the PA6 and MXD6 nylons as well as their in-situ polymerized nanocomposites, as an oxygen barrier layer (core), and a linear low-density polyethylene (LLDPE) as the moisture barrier layers (skin) with the adjacent tie were produced and characterized. The effect of core layer material on the thermal, optical, barrier and mechanical properties of the coextruded multilayer films has been investigated.

CONDENSÉ EN FRANÇAIS

Les propriétés barrières insuffisantes des thermoplastiques aux gaz atmosphériques tels que l'oxygène ou la vapeur d'eau sont un problème majeur dans l'industrie de l'emballage. En particulier, un taux de perméation à l'oxygène élevé réduit la durée de vie de l'aliment contenu dans l'emballage ce qui augmente les coûts pour les producteurs et les détaillants. Les films multicouches constitués d'une couche de cœur ayant de bonnes propriétés barrières et mécaniques prise en sandwich entre deux couches de polyoléfines est une solution couramment utilisée dans l'industrie de l'emballage alimentaire afin d'améliorer les performances mécaniques et barrières à l'oxygène des films. Au cours de ce travail, des films multicouches hautement barrières à l'oxygène ont été développés. Ces films ont été fabriqués à partir de Nylon aromatique (MXD6), aliphatique (PA6) et leurs nanocomposites. Les propriétés optiques, mécaniques et barrières à l'oxygène et à la vapeur d'eau de ces films ont été étudiées et comparées entre elles.

Au cours de la première partie de ce travail, des films monocouches d'épaisseurs comprises entre 30 et 70 μm de polyamide 6 (PA6), de poly (m-xylène adipamide) (MXD6) et leur nanocomposites polymérisés in-situ, ont été produits par extrusion calandrage. La structure de ces films ainsi que son influence sur leurs propriétés finales ont été étudiées en détails. La structure cristalline, les propriétés barrières, rhéologiques et mécaniques du PA6, du MXD6 et de leur nanocomposites ont été étudiées et comparées grâce à des techniques telles que la rhéologie ARES, la XRD (diffraction aux Rayon X), la DSC (Calorimétrie Différentielle), la TGA (analyse thermique gravimétrique), la perméabilité à l'oxygène et la traction. L'étude comparative des caractéristiques dynamiques ainsi que les spectres de relaxation des nanocomposites à base de nylon aliphatique et aromatique ainsi que des résines pures a permis de montrer, tel que décrit au Chapitre 5, une plus grande interaction intermoléculaire et un enchevêtrement des chaînes plus

important pour le nylon aromatique. Les résultats montrent que la cristallinité des films à base de MXD6 était plus basse que celle des films en PA6: cependant, la perméabilité à l'oxygène a été déterminée comme 5 fois meilleure avec ce dernier. L'incorporation d'argile dans la matrice de PA6 et de MXD6 a permis d'améliorer les propriétés barrière à l'oxygène de 40 et 45% respectivement. Le recuit permet également d'augmenter les propriétés barrières à l'oxygène et la cristallinité des films de PA6 et de MXD6 ainsi que de leurs nanocomposites. Cet effet est même plus prononcé pour ces derniers. La phase cristalline γ est prédominante pour les films PA6/clay (argile) alors que la forme cristalline des films PA6 se transforme en une phase α plus stable sous l'effet du recuit. De plus, le recuit cause la formation de cristaux γ et α dans les films de MXD6 et ses nanocomposites. MXD6 montre un module d'Young et une contrainte de traction plus importante comparé au PA6. L'élongation à la rupture et la dureté sont plus importantes pour le PA6 que pour le MXD6 due à la plus grande flexibilité du PA6. Pour les deux nylons (aromatique et aliphatique), le module et la contrainte au seuil de plasticité sont légèrement plus importants dans la direction machine MD que transverse TD. Ceci est attribué à l'orientation des chaînes dans la direction machine au cours du procédé d'extrusion calandrage. L'ajout d'argile au nylon améliore les performances mécaniques sans sacrifier la résistance au déchirement ou à la perforation.

Dans la seconde partie de ce travail, les films précurseurs monocouches ont été étirés uniaxialement à 110 °C avec des rapports d'étirage variant de 1.5 à 5. L'alignement des particules d'argile a été mesuré à l'aide de trois méthodes : déconvolution des pics en FTIR, soustraction spectrale interactive en FTIR et diffraction aux rayons X (XRD). Les résultats, présentés dans le Chapitre 6, ont montré que les palettes d'argile sont principalement orientées dans la direction MD et que leur orientation s'améliore sous l'action de l'étirement. Les effets

des changements d'orientation des axes des cristaux sur toutes les phases cristallines et la région amorphe ont été examinés grâce à la XRD et aux analyses trichroïques des spectres FTIR. Basé sur les modèles WAXD et les résultats en FTIR, des modèles schématiques sont proposés pour décrire le mécanisme de cristallisation du nylon en présence d'argile. Cette étude a montré que les palettes d'argile sont principalement orientées dans la direction MD et s'orientent plus encore au cours de l'étirement. Les résultats WAXD et FTIR montrent que les cristaux γ (200), appelés γ_1 sont principalement formés pendant le procédé d'extrusion avec refroidissement rapide. Seuls les films PA6/clay ont montré des structures cristallines γ (020), appelés γ_2 , supplémentaires. L'axe c des cristaux γ_1 est orientés selon les directions normales et transversales (ND-TD), alors que celui des cristaux γ_2 est orientés selon ND (direction normale). Ceci permet de conclure que les cristaux γ_2 sont formés perpendiculairement au plan (001) de la palette d'argile. L'orientation des deux formes de cristaux γ_1 et γ_2 augmente avec l'étirement uniaxial. De plus, les films nanocomposites à base de nylon aromatique ont montré une petite quantité de phase cristalline induite par la présence d'argile. Finalement, une orientation plus faible de la zone amorphe a été constatée pour les films de nanocomposite, ce qui peut s'expliquer par la gêne spatiale causée par la présence de l'argile.

Le Chapitre 7 présente les effets de l'étirement uniaxial sur les propriétés thermiques, barrières à l'oxygène et mécaniques des films précurseurs monocouches de PA6, de MXD6 et de leurs nanocomposites produits par extrusion calandrage. Les résultats ont montré que la perméabilité à l'oxygène des films étirés augmente jusqu'à l'atteinte d'une valeur d'un rapport d'étirage (DR) critique pour chaque échantillon. Passée cette valeur, plus d'étirage résulte en une baisse des performances de perméabilité à l'oxygène. La température de cristallisation froide (T_{cc}) des films étirés MXD6 et MXD6/clay est diminuée de façon drastique. La T_{cc} diminue

d'abord avec le DR jusqu'à atteindre un DR de 3 et par la suite augmente sous l'action d'un étirage plus important. Ce comportement est attribué à l'existence de molécules d'eau au cours de l'étirement ce qui cause une réduction de l'enthalpie de cristallisation à froid supplémentaire. Néanmoins, le niveau de cristallinité des films orientés augmente. Le module d'Young et la contrainte de traction des nylons aromatiques et aliphatiques augmentent avec la déformation uniaxiale, alors que la flexibilité et l'élongation à la rupture diminuent avec l'augmentation du DR. La flexibilité du MXD6 étiré est, au contraire, améliorée de façon remarquable en comparaison avec les films non étirés. L'élongation à la rupture des films de PA6 et de PA6/clay diminue avec DR alors qu'avec même une petite déformation uniaxiale, la flexibilité du MXD6 étiré est 25 fois meilleure que celle du film non étiré. Ce comportement est relié aux changements de mobilité des chaînes et à l'orientation du nylon aromatique sous l'effet de l'étirement uniaxial. Le modèle de Bharadwaj, basé sur l'orientation parfaite de la phase imperméable, est le plus approprié pour calculer la perméabilité à l'oxygène relative des films monocouches précurseurs. En considérant l'orientation expérimentale des argiles comme un paramètre clé, le modèle prédit avec succès les propriétés barrières à l'oxygène des films nanocomposites orientés. Cependant, l'aspect ratio effectif théorique calculé par ce modèle ne correspond pas aux valeurs moyennes expérimentales déterminé par l'analyse de la morphologie; généralement, le modèle surestime la valeur théorique de l'aspect ratio de l'argile.

Finalement, des films multicouches contenant comme couche de cœur, barrière à l'oxygène, du PA6 et du MXD6, ainsi que leur nanocomposites, ont été produits et caractérisés. Les couches de peau résistantes à l'humidité sont du LLDPE. Des films de cinq couches ont été produits (une couche de compatibilisant entre le LLDPE et le nylon est ajoutée de chaque côté afin d'améliorer la compatibilité des couches de peau et de coeur) à l'aide d'un système de co-extrusion

calandrage de laboratoire et rapidement refroidis avec des couteaux d'air. Dans le Chapitre 8, l'étude comparative des performances finales des différents films multicouches a été réalisée. Au cours du procédé d'extrusion, les paramètres d'extrusion ont été optimisés afin d'éliminer les instabilités interfaciales des fondus et d'améliorer l'uniformité des films multicouches. Les analyses rhéologiques dynamiques montrent que les matériaux sélectionnés peuvent être co-extrudés avec un minimum d'instabilités interfaciales entre les fondus dans le bloc d'alimentation. La cristallinité et les transitions thermiques des couches des films ont été étudiées à l'aide de la DSC et de la DSC modulée (MDSC). Une étude comparative a également été menée sur les propriétés mécaniques, optiques, barrières à l'oxygène et à la vapeur d'eau des différents films multicouches. Les films multicouches basés sur le MXD6 montrent des propriétés barrières à l'oxygène et à la vapeur d'eau supérieure à ceux basés sur du PA6. Cependant, ce sont les films multicouches basés sur le PA6 qui montrent la meilleure ténacité et résistance à la déchirure. Il a également été déterminé que les films multicouches basés sur le MXD6 pur montrent de meilleures propriétés de transparence, comparativement aux films de PA6 en raison de sa faible cristallinité.

TABLE OF CONTENT

ACKNOWLEDGEMENTS.....	III
RÉSUMÉ	IV
ABSTRACT.....	VI
CONDENSÉ EN FRANÇAIS	IX
TABLE OF CONTENT	XIV
LIST OF TABLES	XIX
LIST OF FIGURES	XXI
CHAPTER 1 : INTRODUCTION	1
CHAPTER 2 : LITERATURE REVIEW	5
2.1 Function of a package	5
2.2 High barrier polymers	8
2.3 Methods used to improve barrier properties	15
2.4 Nanocomposites for high barrier packaging	17
2.5 Stretching of polymer films	22
2.6 Multilayer packaging technologies	26
2.7 The measurement of the permeability of nanocomposites by models	28
2.8 Originality	37
2.9 Objectives	39
CHAPTER 3 : METHODOLOGY	40

3.1	Materials	42
3.2	Film preparation.....	43
3.3	Characterizations.....	46
3.3.1	Rheological properties.....	46
3.3.2	Thermal analysis	47
3.3.3	X-ray diffraction.....	48
3.3.4	Morphology.....	49
3.3.5	Barrier property.....	49
3.3.6	Mechanical properties	50
3.3.7	Optical property.....	51
3.3.8	Orientation.....	51
CHAPTER 4 : ORGANIZATION OF ARTICLES.....		54
CHAPTER 5 : ARTICLE 1 : RHEOLOGICAL, CRYSTAL STRUCTURE, BARRIER AND MECHANICAL PROPERTIES OF PA6 AND MXD6 NANOCOMPOSITE FILMS		57
5.1	Introduction.....	58
5.2	Experimental.....	61
5.2.1	Materials.....	61
5.2.2	Film Processing.....	62
5.3	Resin and film characterizations.....	63
5.4	Results and discussion	66
5.4.1	Rheological characterization.....	66
5.4.2	Dispersion state by XRD and TEM.....	73

5.4.3	Crystal structure	75	
5.4.4	Non-Isothermal crystallization	85	
5.4.5	Thermal degradation	88	
5.4.6	Oxygen permeability	91	
5.4.7	Mechanical properties	94	
5.5	Conclusions	98	
5.6	Acknowledgment	99	
5.7	References	100	
CHAPTER 6 : ARTICLE 2 : X-RAY AND TRICHOIC INFRARED ORIENTATION ANALYSES OF UNIAXIALLY STRETCHED PA6 AND MXD6 NANOCCLAY COMPOSITE FILMS			105
6.1	Introduction	106	
6.2	Experimental	109	
6.2.1	Materials	109	
6.2.2	Film preparation	110	
6.3	Characterization	111	
6.4	Results and Discussion	113	
6.4.1	Effect of Stretching on Orientation of Clay	115	
6.4.2	Effect of Stretching on Orientation of Nylons Crystalline Phase	124	
6.4.3	Effect of Stretching on Orientation of Amorphous Phase	140	
6.5	Conclusions	141	
6.6	Acknowledgments	142	

6.7	References.....	143	
CHAPTER 7 : ARTICLE 3: EFFECT OF UNIAXIAL DEFORMATION ON THERMAL, OXYGEN BARRIER AND MECHANICAL PROPERTIES OF PA6 AND MXD6 NANOCOMPOSITE FILMS			148
7.1	Introduction.....	149	
7.2	Experimental.....	152	
7.2.1	Materials.....	152	
7.2.2	Film preparation	153	
7.3	Characterization	154	
7.4	Results and Discussion	157	
7.4.1	Nanoclay dispersion	157	
7.4.2	Crystallinity.....	158	
7.4.3	Oxygen Permeation.....	165	
7.4.4	Mechanical Properties.....	174	
7.5	Conclusions.....	179	
7.6	Acknowledgment.....	180	
7.7	References.....	181	
CHAPTER 8 : ARTICLE 4: PROPERTIES OF CO-EXTRUDED NANOCLAY-FILLED ALIPHATIC NYLON (PA6)/LINEAR LOW-DENSITY POLYETHYLENE AND AROMATIC NYLON (MXD6)/LINEAR LOW-DENSITY POLYETHYLENE MULTILAYER FILMS.....			187
8.1	Introduction.....	188	

8.2	Experimental.....	191
8.2.1	Materials.....	191
8.2.2	Film preparation.....	193
8.3	Characterizations.....	194
8.4	Results and Discussion.....	198
8.4.1	Rheological properties of the polymer melts.....	198
8.4.2	Morphology of cross-section.....	201
8.4.3	Thermal properties.....	204
8.4.4	Barrier properties.....	209
8.4.5	Mechanical properties.....	214
8.4.6	Optical properties.....	220
8.5	Conclusions.....	221
8.6	Acknowledgment.....	222
8.7	References.....	223
CHAPTER 9 : GENERAL DISCUSSION.....		232
CHAPTER 10: CONCLUSIONS AND RECOMMENDATIONS.....		239
10.1	Conclusions.....	239
10.2	Recommendations.....	244
REFERENCES.....		246

LIST OF TABLES

Table 2.1 Cheese Packaging films [1]	8
Table 2.2 High barrier polymers and their specific barrier functions [1]	9
Table 2.3 High oxygen barrier polymers [1].	10
Table 3.1 List of materials used in this study and their main characteristics (reported by suppliers).....	43
Table 5.1 List of materials used in this study and their main characteristics (reported by suppliers).....	62
Table 5.2 Power-law frequency dependency of G' and G'' in the terminal zone.....	72
Table 5.3 Thermal properties of PA6, MXD6, and PA6/clay and MXD6/clay resins and films.	80
Table 5.4 Enthalpy of fusion, ΔH , total crystallinity, X_{tot} , onset crystallization temperature, T_o , and half time of crystallization, $t_{1/2}$, for the PA6, PA6/clay, MXD6 and MXD6/clay.	86
Table 5.5 Temperatures at different percentage of weight loss for PA6, MXD6, and nanocomposites.....	90
Table 5.6 Young's modulus, yield stress and elongation at break for the 30 μm films in MD and TD.	95
Table 6.1 Main characteristics of materials used in this study.	110
Table 7.1 Main characteristics of materials used in this study (reported by suppliers).....	153
Table 7.2 Predicted relative permeability (K) obtained from different models for PA6/clay and MXD6/clay.	167
Table 7.3 Predicted relative permeability (K) values from the Bharadwaj model for PA6/clay and MXD6/clay.	171

Table 8.1 Materials used in this study and their main characteristics (reported by the suppliers).	192
Table 8.2 Thermal properties of coextruded PA6/LLDPE, nano-clay filled PA6/LLDPE, MXD6/LLDPE and nano-clay filled MXD6/LLDPE multilayer films.	208
Table 8.3 Measured and calculated oxygen barrier properties of coextruded multilayer films.	212
Table 8.4 Mechanical properties (stiffness, tensile strength, elongation at break and toughness) of coextruded PA6/LLDPE, nano-clay filled PA6/LLDPE, MXD6/LLDPE and nano-clay filled MXD6/LLDPE multilayer films in MD and TD.	215

LIST OF FIGURES

Figure 2-1 Chemical structure of nylon 6 [1].	11
Figure 2-2 Schematic of the α and γ crystalline forms of PA6 [25].	12
Figure 2-3 Schematic of hydrogen bonding within the α and γ crystalline forms of nylon 6 as seen from end and side-view of each crystal [24].	13
Figure 2-4 Condense polymerization and chemical structure of MXD6 [29].	13
Figure 2-5 Crystal structure of poly (m-xylene adipamide) (MXD6) shown by projection on various planes: (a) the (100) plane; (b) the (120) plane; (c) the plane perpendicular to the c -axis [30].	14
Figure 2-6 Tortuous pathway of gas permeant through nanocomposite [49].	17
Figure 2-7 Dispersion state of nanoclays in a polymer matrix.	18
Figure 2-8 Schematic of clay orientation in cast nanocomposite films.	19
Figure 2-9 Nylon 6 nanocomposite formed through <i>in-situ</i> polymerization with modified montmorillonite [49].	20
Figure 2-10 Schematic of tortuous diffusion path through precursor and uniaxially stretched of PA6/clay film.	23
Figure 2-11 (a) SEM micrograph of the fracture surface of an extruded sample of a PET/PEN blend (70/30). (b) SEM micrograph of the tearing fracture surface of a biaxially oriented film of a PET/PEN blend (70/30) [87].	24
Figure 2-12 Structure evolution as a function of draw ratio for PA6 upon uniaxial stretching (a) at 120 °C and (b) at 180 °C [93].	26
Figure 2-13 Permeation of a substance through a plastic packaging material [107].	29
Figure 2-14 Direction of preferred orientation and normal vector of mineral sheets [110].	33

Figure 3-1 Experimental strategy.....	41
Figure 3-2 Stress-Strain curves for (a) PA6, (b) PA6/clay and (c) MXD6/clay films stretched at 110 °C.	45
Figure 5-1 Storage modulus (G') vs. time for (a) PA6 and PA6/clay at 220 and 240 °C and (b) MXD6 and MXD6/clay at 270 and 280 °C; $\omega = 6.28$ rad/s.....	67
Figure 5-2 Complex viscosity (η^*) vs. frequency for (a) PA6 and PA6/clay at 220 and 240 °C and (b) MXD6 and MXD6/clay at 270 and 280 °C.	69
Figure 5-3 Storage modulus (G') and Loss modulus (G'') vs. frequency for (a) PA6 and PA6/clay at 220 °C and (b) MXD6 and MXD6/clay at 270 °C. (c) Weighted relaxation spectra for the neat PA6 and neat MXD6 obtained from dynamic frequency data.....	71
Figure 5-4 X-ray diffraction patterns for neat nylons and nanocomposites.	74
Figure 5-5 TEM micrographs for (a, b, c) PA6/clay nanocomposite films and (d, e, f) MXD6/clay nanocomposite films.	75
Figure 5-6 XRD patterns for (a) compressed molded neat PA6 and PA6/clay nanocomposites, (b) neat PA6 and PA6/clay nanocomposite films, (c) compressed molded neat MXD6 and MXD6/clay nanocomposites and (d) neat MXD6 and MXD6/clay nanocomposite films.	76
Figure 5-7 DSC thermograms for PA6, PA6/clay, MXD6 and MXD6/clay films; (a) first heating ramp, (b) cooling (crystallization) ramp and (c) second heating ramp.	78
Figure 5-8 XRD patterns for (a) annealed neat PA6 and PA6/clay nanocomposite films and (b) annealed neat MXD6 and MXD6/clay nanocomposite films; annealing at 150 °C for 30 min....	82
Figure 5-9 First DSC heating thermograms for (a) PA6 and PA6/clay films and (b) MXD6 and MXD6/clay films before and after annealing at 150 °C for 30 min.....	84

Figure 5-10 Relative crystallinity vs. time at different cooling times for (a) PA6 and PA6/clay and (b) MXD6 and MXD6/clay.....	87
Figure 5-11 Thermal gravimetric curves for PA6, PA6/clay, MXD6, and MXD6/clay.....	89
Figure 5-12 Oxygen permeation through neat PA6 and MXD6 as well as their nanocomposites films (30 μm) before and after annealing.	91
Figure 5-13 Crystallinity of neat PA6 and MXD6 as well as their nanocomposites films (30 μm) before and after annealing.....	92
Figure 5-14 Measuring the aspect ratio of the clay layers for PA6/clay by image analysis. Silicate layers are laid in machine direction (MD).	94
Figure 5-15 Tear resistance for PA6, PA6/clay, MXD6 and MXD6/clay films (30 μm) in MD and TD.	96
Figure 5-16 Puncture resistance for PA6, PA6/clay, MXD6 and MXD6/clay films (30 μm).....	97
Figure 6-1 Surface (MD-TD plane) and cross-section (MD-ND plane) 2D WAXD patterns for precursor and stretched (DR=4) PA6 and PA6/clay films.....	114
Figure 6-2 Diffraction intensity profiles for PA6/clay and MXD6/clay films in the MD-ND plane.....	116
Figure 6-3 Herman orientation function (f_{001}) and pole figure of the (001) plane of clay along MD, TD, and ND for precursor and stretched (DR=4) PA6/clay and MXD6/clay films.....	118
Figure 6-4 (a) Trichroic FTIR spectra along MD, TD and calculated ND in the Si-O stretching region for precursor and stretched (DR=4) PA6 and PA6/clay. (b) The four peaks for the Si-O stretching bonds of silicate layers in MD, TD and ND spectra in oriented PA6/clay film.	120
Figure 6-5 Trichroic FTIR spectra along MD, TD, calculated ND and structural factor spectrum (S0) for MXD6 film, MXD6/clay film and nanoclay spectrum obtained by subtraction.....	121

Figure 6-6 (a) Peak fitting for the FTIR structural spectrum (SF) of clay. (b) Herman orientation function of clay obtained with peak fitting method for precursor and stretched (DR=4) PA6/clay and MXD6/clay nanocomposite films.	122
Figure 6-7 (a) and (b) Illustration of subtraction procedure for PA6/clay and MXD6/clay films. (c) and (d) Herman orientation function of clay versus draw ratio obtained by subtraction method for precursor and stretched PA6/clay and MXD6/clay.....	123
Figure 6-8 Diffraction intensity profiles along MD-TD plane (a) and (c), and MD-ND plane (b) and (d) for precursor and stretched (DR=4) PA6, PA6/clay, MXD6 and MXD6/clay films.	124
Figure 6-9 Pole figure and Herman orientation function (f_{200}) of the (200) plane of γ_1 crystal population along MD, TD, and ND for precursor and stretched (DR=4) PA6 and PA6/clay films.	127
Figure 6-10 FTIR spectra of α and γ phases along MD, TD, calculated ND and structural factor spectrum (S0) for precursor and stretched (DR=4) PA6 and PA6/clay films.	128
Figure 6-11 Orientation functions of γ_1 crystal population (a) b -axis, (b) a -axis, and (c) c -axis for precursor and stretched PA6 and PA6/clay films.	132
Figure 6-12 Trichroic FTIR spectra for precursor and stretched (DR=4) MXD6 and MXD6/clay films along MD, TD and ND.	133
Figure 6-13 Orientation function of amorphous phase from the Trichroism of the peaks at 1083 cm^{-1} for precursor and stretched MXD6/clay films.	135
Figure 6-14 Herman orientation function (f_{020}) of the 020 plane of γ_2 crystal population along MD, TD and ND for precursor and stretched (DR=4) PA6/clay films.....	136
Figure 6-15 (Top) Schematic of γ_2 (020) texturing parallel to the clay platelet. The monomer unit of the PA6 chain has been inspired from Ref. ⁵⁸ . (Bottom) Orientation function of γ_2 crystal	

population from the Trichroism of the peaks at 975 cm^{-1} for precursor and stretched PA6 and PA6/clay films.	138
Figure 6-16 (Top) Models for crystalline unit cell orientation of precursor and stretched PA6 and PA6/clay films. (Bottom) Schematics of clay, γ_1 and γ_2 crystal alignments in PA6/clay film. ...	139
Figure 6-17 Orientation function of amorphous phase from the Trichroism of the peaks at 1120 cm^{-1} for precursor and stretched PA6 and PA6/clay films.	140
Figure 7-1 (a) TEM micrographs and cross-section diffraction intensity profiles for precursor stretched (DR=4) PA6/clay and MXD6/clay in MD-ND plane. (b) 2D WAXD patterns and azimuthal intensity profiles at 2θ of the 001 clay reflection plane for precursor and stretched (DR=4) PA6/clay and MXD6/clay.	157
Figure 7-2 XRD patterns for precursor and stretched (DR=4) (a) PA6 and PA6/clay, and (b) MXD6 and MXD6/clay films.	159
Figure 7-3 First heating ramp of DSC thermograms for precursor and stretched (a) PA6, and (b) PA6/clay films.	160
Figure 7-4 First heating ramp of DSC thermograms for precursor and stretched (a) MXD6, and (b) MXD6/clay films.	162
Figure 7-5 Crystallinity of precursor and stretched (DR=4) PA6 and MXD6 and their nanocomposites films.	164
Figure 7-6 Histogram of calculated aspect ratio for (a) PA6/clay and (b) MXD6/clay films. ...	169
Figure 7-7 Oxygen permeation versus draw ratio for (a) PA6 and PA6/clay (b) MXD6 and MXD6/clay films.	169
Figure 7-8 Predictions of the Bharadwaj's model for relative oxygen permeability (K) as a function of clay orientation parameter (κ) and clay aspect ratio (ϕ) with considering the	

experimental clay volume fractions (\emptyset). Square and triangle symbols are experimental values for relative oxygen permeability for precursor (DR=1) and stretched (DR=5) PA6/clay and MXD6/clay films, respectively.	172
Figure 7-9 Oxygen transmission rate as a function of thickness for (a) MXD6 film, (b) stretched PA6, and (c) stretched MXD6 films.	174
Figure 7-10 Young's modulus as a function of draw ratio for (a) PA6, (b) PA6/clay, (c) MXD6, and (d) MXD6/clay film.	175
Figure 7-11 Tensile strength as a function of draw ratio for (a) PA6, (b) PA6/clay, (c) MXD6, and (d) MXD6/clay film.	177
Figure 7-12 Tensile strain at break as a function of draw ratio for (a) PA6, (b) PA6/clay, (c) MXD6, and (d) MXD6/clay film.	178
Figure 8-1 (a) Storage modulus (G') versus time for PA6, PA6/clay and LLDPE at 240 °C, and for MXD6 and MXD6/clay at 270 °C; $\omega = 6.28$ rad/s. (b) Complex viscosity (η^*) versus frequency for PA6, PA6/clay and LLDPE at 240 °C, and for MXD6 and MXD6/clay at 270 °C.	198
Figure 8-2 Photograph showing unstable (left-sides) and stable (right-sides) interfaces of five-layer coextruded multilayer (a) and (b) PA6/LLDPE films and (c) and (d) MXD6/LLDPE films.	200
Figure 8-3 FTIR micrograph of cross-section for coextruded PA6/LLDPE multilayer film.	202
Figure 8-4 Scanning electron micrographs of cross-section for (a) PA6/LLDPE and (b) MXD6/LLDPE coextruded multilayer films.	202
Figure 8-5 X-ray diffraction patterns for PA6/clay and MXD6/clay nanocomposites.	203

Figure 8-6 DSC thermograms for coextruded PA6/LLDPE, nano-clay filled PA6/LLDPE, MXD6/LLDPE and nano-clay filled MXD6/LLDPE multilayer films; (a) first heating ramp, (b) cooling (crystallization) ramp.	204
Figure 8-7 MDSC cold crystallization thermograms of coextruded MXD6/LLDPE and nano-clay filled MXD6/LLDPE multilayer films.....	207
Figure 8-8 Oxygen permeability for coextruded PA6/LLDPE, nano-clay filled PA6/LLDPE, MXD6/LLDPE and nano-clay filled MXD6/LLDPE multilayer films.	209
Figure 8-9 Oxygen permeability for monolayer film (a) LLDPE and LLDPE-g-MA. (b) PA6 and MXD6.	211
Figure 8-10 Water vapor transmission rate for coextruded PA6/LLDPE, nano-clay filled PA6/LLDPE, MXD6/LLDPE and nano-clay filled MXD6/LLDPE multilayer films.	213
Figure 8-11 Tear resistance for coextruded PA6/LLDPE, nano-clay filled PA6/LLDPE, MXD6/LLDPE and nano-clay filled MXD6/LLDPE multilayer films.	217
Figure 8-12 Puncture resistance for coextruded PA6/LLDPE, nano-clay filled PA6/LLDPE, MXD6/LLDPE and nano-clay filled MXD6/LLDPE multilayer films.	218
Figure 8-13 Flex crack resistance for coextruded PA6/LLDPE, nano-clay filled PA6/LLDPE, MXD6/LLDPE and nano-clay filled MXD6/LLDPE multilayer films.	219
Figure 8-14 Haze of coextruded PA6/LLDPE, nano-clay filled PA6/LLDPE, MXD6/LLDPE and nano-clay filled MXD6/LLDPE multilayer films.....	221

CHAPTER 1

INTRODUCTION

Packaging industry in the area of flexible films is growing rapidly. An important role of a package is to create an acceptable barrier between food and external environment, particularly water vapor, atmospheric gases such as O₂ and CO₂, and organic liquids. Shelf life, the time period that product remains in an acceptable conditions for use, strongly depends on the barrier properties of a package. The permeability of polymers depends on various factors such as chemical structure of the polymer, intermolecular bonding, free volume, crystallinity, functional additives, density, and thickness. Generally, monolayer films are permeable to a variety of gases and are not able to provide all the properties required to preserve food. Combination of different polymers in order to design multilayer structure with superior gas barrier (usually water vapor and oxygen), high mechanical and optical properties with the cost consideration is a challenge in food packaging industry. Multilayer films having a core layer with good barrier and mechanical properties coextruded between two polyolefin layers as the skin layers have attracted a lot of attentions for food packing applications.

Aliphatic nylons such as polyamide 6 (PA6) have been widely used in flexible packaging due to its remarkable barrier and mechanical properties. Its high melting point makes PA6 as a good candidate for the manufacturing of retorted bags in the packaging industry. However, its oxygen barrier is highly affected in the presence of high relative humidity. In the past two decades, a great interest has arisen in silicate clay polyamide 6 nanocomposites due to the good processability, high mechanical properties and high chemical resistance as well as low oxygen permeation.

The main application for nylon 6 in the flexible packaging is in the high gas barrier multilayer films, specifically to meet the necessary barrier properties (OTR of 9.3–15.5 cc/m².day.atm and WVTR of 15.5 g/m².day [1]) needed for the long shelf life in the cheese packaging.

Poly (m-xylene adipamide) (MXD6) is a semi-crystalline aromatic nylon with better mechanical performance, higher temperature resistance, greater barrier to oxygen and less moisture sensitivity in comparison with PA6 [2] and can be considered as a potential candidate to replace PA6 for some packaging applications. MXD6 keeps its excellent gas barrier properties even at high humidity conditions [3, 4]. Its other properties such as thermal stability, high bending strength and ease of stretching and/or thermoforming make MXD6 a potential candidate in flexible packaging. The remarkable ability of MXD6 to withstand the retort conditions without significant loss in barrier properties makes it a high potential candidate for replacing PA6 in retort applications [5]. Recently, the incorporation of nano-clay in MXD6 nylon has received some attention for further improvement in the gas barrier properties [6, 7]. A fundamental understanding on the differences in the properties of aromatic and aliphatic nylon films and their nanocomposites would be very important for packaging industry.

The main objective of this project is to fundamentally investigate the differences between properties of monolayer and multilayer aromatic and aliphatic nylon films and their nanocomposites. Resin characteristics particularly the rheological and thermal properties, morphology, the extent of clay intercalation and exfoliation, orientation (clay, amorphous and crystalline phases), crystallization rate, crystal structure and crystallinity on the final film properties are investigated.

To achieve this goal, first, monolayer cast films (30-70 μm) of polyamide 6 (PA6), poly (m-xylene adipamide) (MXD6) and their in-situ polymerized nanocomposites were produced to

investigate their structures in details and in relation to the final properties. The crystal structure, rheological, mechanical and barrier properties of the PA6, MXD6 and their nanocomposite films were studied and compared. The changes in orientation of clay and crystal axes of all the crystalline phases and amorphous region were examined using X-ray diffraction and Trichroic Infrared analyses. A detailed investigation of the structure evolution with stretching has been carried out. The effect of uniaxial stretching on orientation, morphology, crystallinity, oxygen barrier and mechanical properties of the neat PA6 and MXD6 and their nanocomposite films was also investigated. The oxygen permeability and oxygen diffusion through the aromatic and aliphatic nylon nanocomposite films have been predicted using theoretical models and with the incorporating structural parameters such as the crystalline phase orientation, the clay aspect ratio and the clay orientation. In the final step of this study, coextruded PA6/LLDPE and MXD6/LLDPPE multilayer films as well as their in-situ polymerized nanocomposites were produced and characterized. Five-layer films were prepared by cast coextrusion and their morphology, crystallinity, optical, tensile, oxygen and water vapor barrier properties as well as puncture, tear and flex crack resistances were analyzed.

Chapter 2 provides a literature review covering the following subjects: high barrier polymers; methods used to improve barrier properties of a polymer including incorporation of nanoclay; uniaxial stretching of polymer films and its influence on orientation, crystallinity, barrier and mechanical properties, and multilayer packaging technologies. The selected materials and the chosen methodology to achieve the objectives of this study are presented in Chapter 3. Chapter 4 briefly explains the organization of the papers reported in the thesis. In Chapter 5, the rheological, crystal structure, barrier and mechanical properties of the PA6 and MXD6 nanocomposite monolayer films were studied and compared. Chapter 6 discusses the effect of

drawing on the orientation of clay, crystal axes of all the crystalline phases and amorphous region of the uniaxially stretched neat and nanocomposite films of PA6 and MXD6 using X-ray and Trichroic Infrared orientation analyses. In Chapter 7, a detailed investigation was conducted on the uniaxial stretching role on thermal, oxygen barrier and mechanical properties of the PA6 and MXD6 nanocomposite films. Chapter 8 presents the results on the development of high barrier PA6/LLDPE and MXD6/LLDPE multilayer films. In Chapter 9 (general discussion) a full review regarding the most important factors affecting the barrier properties of monolayer and multilayer films is presented. Finally, Chapter 10 summarizes the most important conclusions of this thesis and outlines some recommendations for the future works in this area.

CHAPTER 2

LITERATURE REVIEW

2.1 Function of a package

Insufficient barrier properties of commercial thermoplastics to the permeation of atmospheric gases are a major problem in the packaging industry. In particular, a high oxygen permeation rate reduces the shelf life of packaged products, which results in higher costs for food processors and retail customers. In food packaging, especially for the dairy products such as cheese, the packaging material should provide excellent oxygen, moisture, odor and gas barrier protection to prevent spoilage and to extend the shelf life. The packaging films also require having good mechanical properties to protect food, and also to prevent the controlled atmosphere inside the package from being lost. Finally, a good package needs to have an acceptable optical property to preserve the general appearance expected by consumers. Based on the function of a package including its barrier, strength, ability to withstand abuse during filling and shipping, sealability, optical and clarity properties, the packaging materials could be classified into the three categories: flexible, semi-rigid and rigid.

Most food packages are composed of a multilayer film structure to achieve the desired requirements depending on the application. The multilayer films consisting of a core layer having good barrier and mechanical properties sandwiched between two polyolefin layers is commonly used in the food packaging industry. The resin selection and processing conditions are the important factors for the production of the multilayer films with desired properties.

Polymers for the multilayer film are selected for the specific properties and performance that they can provide in the final package structure to meet all the requirements for the specific

application in which they are being used. The selection of material can be conducted based on considerations such as availability from multiple suppliers or ability to provide specific performances over competitive packaging. Polymers are chosen for individual layers to achieve particular properties. Some of the key property requirements for high performance flexible packaging include the following [1]:

- *Barrier properties:* to prevent oxygen, moisture, light, odor, or atmosphere gases such as nitrogen and carbon dioxide from entering to the package. In some cases barrier to moisture, flavor or grease for leaving from the package might be required. In the cheese packaging, relative humidity inside the package has a direct impact on the weight loss and texture of cheese. At equilibrium condition, the relative humidity of the surrounding environment inside the package is equal to the cheese water activity, which influences its microbiological evolution over time. Barrier properties of a package are mostly characterized by measuring the oxygen and water vapor transition through the package.
- *Selective permeability:* in some packaging applications it is required to allow oxygen and carbon dioxide to permeate through the package at the specific calculated rate to extend the shelf life of fresh products. O₂, CO₂ and H₂O permeability are frequently measured and specified.
- *Abuse resistance;* to prevent damage to the package during transportation and in storage conditions. Abuse resistance may include tear strength, impact strength, puncture resistance, flex crack resistance, and modulus. Some packages require high toughness at low temperatures such as inside the refrigerated or freezer storage.
- *Sealability:* to allow packages to process at high speeds. Heat sealing of a thermoplastic material refers to a process by which sufficient heating under specific temperature and

pressure results in interdiffusion of polymer chain segments across the interface and causes the molecular entanglements, which are followed by cooling and crystallization. Sealability is characterized by heat-seal and hot tack strength, heat-seal and hot tack initiation temperatures, seal contamination performance, caulkability, and seal integrity. Heat strength or heat quality of a package is defined as the force per unit width of the seal required to separate the seal parts under specific test conditions. The seal ability of a package is depends on sealing pressure, sealing temperature, and dwell time (i.e. the spent time in the seal cycle when two polymer films are held together by the seal jaw). It is critically important for packages where the product drops into the package while the seal is still partly molten. Insufficient sealability of a package may result in a partial leakage.

- *Clarity*: package appearance is an important factor to attract consumers. The printability and package gloss are important factors impact consumer appeal.
- *Mechanical strength*: mechanical properties of a package mostly govern by high tensile strength and modulus as well as high toughness which are key factors to protect food from physical damage can be caused to the product, including shocks from drops, falls, and bumps; damage from vibrations arising from transportation modes, including road, rail, sea, and air; and compression and crushing damage arising from stacking during transportation or storage in warehouses, retail outlets, and the home environment.

Coextruded films containing three, five or seven layers are available in the market for cheese packaging, where three-layer coextruded film has the largest share (See table 2.1) [1].

Table 2.1 Cheese Packaging films [1]

Structure	Layers (%)		Gauge (μm)
Natural chuck cheese pouches			
LLDPE/Tie/EVOH//o-PET	75	10 15	40–60
LLDPE//PVDC//o-PP	75	10 15	50–60
LLDPE//PVDC//o-PET	75	10 15	45–50
EVA//PVDC	95	5	50–60
LLDPE//PVDC//o-PA	75	10 15	45–50
Vacuum bags for aging			
EVA//PVDC//o-PA	85	5 10	40–100
LLDPE/Tie/PA	80	10 10	40–100
EVA/Tie/PA	80	10 10	40–100
Shredded cheese			
PVDC//PA//LDPE	5 20	75	80–100
PVDC//PET//LDPE	5 20	75	80–100
PA/EVOH/Tie/LDPE	10 10 10	70	80–100
Processed cheese slices			
o-PP//EVA	50	50	20
PP/EVA	20	80	35–40

Effective packaging increases shelf life of product and reduces product waste, and in doing so protects or conserves much of the energy expended during the production and processing of the product [8].

2.2 High barrier polymers

The barrier characteristics of polymeric packaging materials are determined by the capacity of a polymer matrix to sorb the penetrant molecules, and the ability of the penetrant to diffuse through the polymeric materials. A polymer needs the following attributes in order to be used in barrier applications: polarity, high chain stiffness, high chain packing, intermolecular bonding, high glass transition temperature, and crystallinity or orientation [8]. At steady state times, the permeation of material through a polymer is a function of diffusivity and solubility in the polymer. The adsorption mechanisms of a permeant to the polymer and diffusion rate through it

can significantly influence the permeation rates [4]. Thus, the lower glass transition temperature, hence the lower solubility coefficient contributed to the lower permeability of the polymer [4]. The largest effect comes from the diffusion coefficient, hence the activation energy for permeation is a function of the segmental motions, polymer chain entanglements (dynamic free volume), and the polymer chain relaxation time [4].

Table 2.2 summarizes the main polymers used extensively for the barrier purpose in the multilayer film packaging.

Table 2.2 High barrier polymers and their specific barrier functions [1]

Barrier Material	Specific Barrier Function
Ethylene vinyl alcohol copolymer (EVOH)	Oxygen barrier, flavor/aroma barrier
Poly vinylidene chloride (PVDC)	Moisture, oxygen, flavor, aroma and some chemicals
Polyethylene terephthalate (PET)	Moisture barrier, some flavor/aroma barriers and some chemical barrier
Polyethylene naphthalate (PEN)	Oxygen barrier
Polyamide (PA6)	Oxygen barrier, aroma barrier and some oil barrier
Semi-crystalline polyamides (nylon MXD6)	Gas (O ₂ , CO ₂) barrier, aroma barrier
Liquid crystal polymer (LCP)	Oxygen barrier
High density polyethylene (HDPE)	Moisture barrier
Polypropylene (PP)	Moisture barrier
Ionomer	Oil barrier and chemical barrier for some agents

Ethylene vinyl alcohol copolymer (EVOH) has high barrier against aroma and oxygen. However, the moisture sensitivity of EVOH, especially at the high relative humidity (RH), lowers the mechanical performance and barrier properties of EVOH films [9]. Also, the exposure of EVOH films to high temperatures, such as in the retort processing, leads to a sharp decrease in the oxygen barrier properties at a given relative humidity [10]. In addition, due to the fast crystallization kinetics and high rigidity, EVOH cannot be used for thermoforming application

[10]. Poly (vinylidene chloride) (PVDC) is also used as an oxygen barrier material [11], however, it is not environmental friendly due to the generating toxic gases during incineration [12]. Poly (ethylene terephthalate) (PET) is used in packaging applications due to its advantages of high chain stiffness, high glass transition and melting temperatures and crystallinity. However, high oxygen and carbon dioxide permeability is a challenge for using PET for beverage packaging. Some effort has been done to enhance the gas barrier properties of PET by incorporating layered silicate nanoclay via melt compounding [13] or in-situ polymerization [14]. However, at high processing temperatures required for melt compounding of PET, the organo modifier of nanoclay undergoes thermal degradation resulting in a little effect of nanoparticles on the barrier properties of PET [15, 16]. Other studies also reported a reduction in the gas permeability of polyolefin nanoclay composite films, but oxygen permeation is still higher than the values of interest in some food packaging applications [17, 18]. Table 2.3 shows the oxygen transmission rate of a number of the high barrier plastic films that are well known in the market. The data indicate orders of magnitude differences among the oxygen barrier properties of different plastic films at dry and humid conditions.

Table 2.3 High oxygen barrier polymers [1].

Material	Oxygen permeability (cc.mm/m ² day.atm) at 0% relative humidity	Oxygen permeability (cc.mm/m ² day.atm) at 100 % relative humidity
LCP	0.003	0.003
PVDC	0.004	0.004
EVOH	0.003	0.25
MXD6	0.09	0.1
PA6	0.5	1.3
PET	1.5	1.5
PEN	0.3	0.3

Liquid crystalline polymers (LCP) can be used to produce thin film with high gas barrier ability [19-21] or can be used in blending with other polymers such as PET to improve their

barrier properties [22]. Liquid crystalline polymers have high modulus and excellent thermal and mechanical properties and low oxygen permeability, but they are so expensive and to date there is no report on using LCP in packaging applications [22].

Polyamide 6 (PA6) (Figure 2.1) is an aliphatic engineering thermoplastic that is extensively used in the food packaging due to its high stiffness, toughness, tensile strength, flex crack and puncture resistance as well as low oxygen transmission rate. However, the oxygen permeation of nylon films is affected by relative humidity. There are several studies that confirmed dramatic changes in the barrier property of nylon films in the presence of moisture [4, 23].

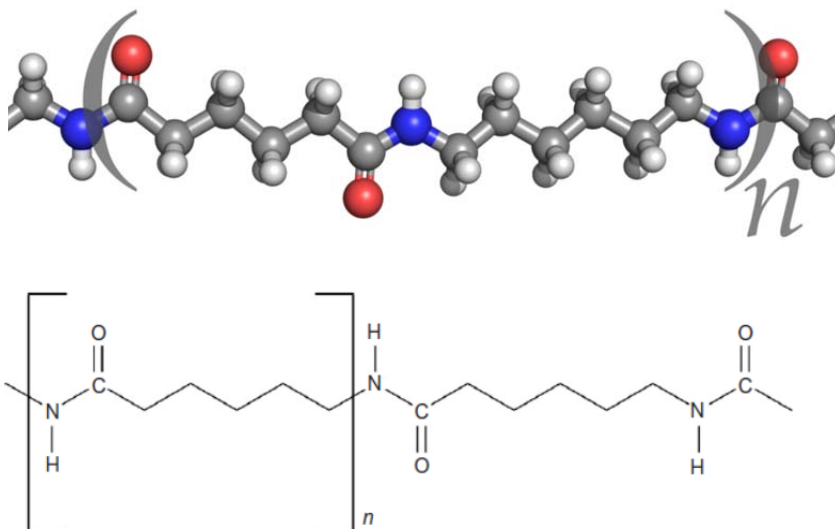


Figure 2-1 Chemical structure of nylon 6 [1].

From literature [24], PA6 could have two major crystalline phases: α and γ (Figure 2.2). The α phase has monoclinic unit cells with the dimensions of $a = 0.956$, $b = 1.724$, $c = 0.801$ nm and $\beta = 67.5^\circ$, where the γ phase has a pseudo hexagonal structure with the dimensions of $a = 0.472$, $c = 1.688$ nm and $\gamma = 120^\circ$ [24, 25]. The monoclinic α form with the H-bonds lying between the antiparallel chains (Figure 2.3), within (002) planes having a planar zigzag conformation, is promoted by slow cooling from the melt state [26, 27]. The α form is thermally the most stable crystal phase in nylons [26, 27] whereas the pseudo-hexagonal γ phase with the H-bonds linking

parallel chains (Figure 2.3), within (200) planes having a twisted chain conformation, can be developed under rapid cooling [28].

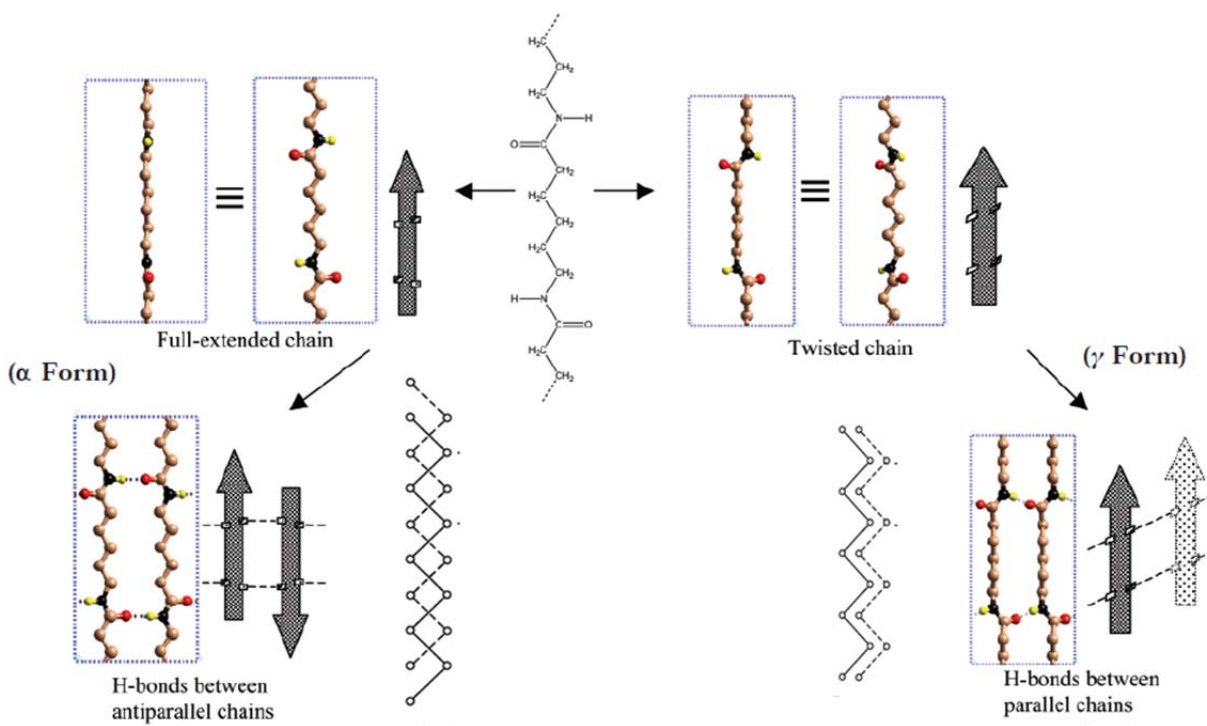


Figure 2-2 Schematic of the α and γ crystalline forms of PA6 [25].

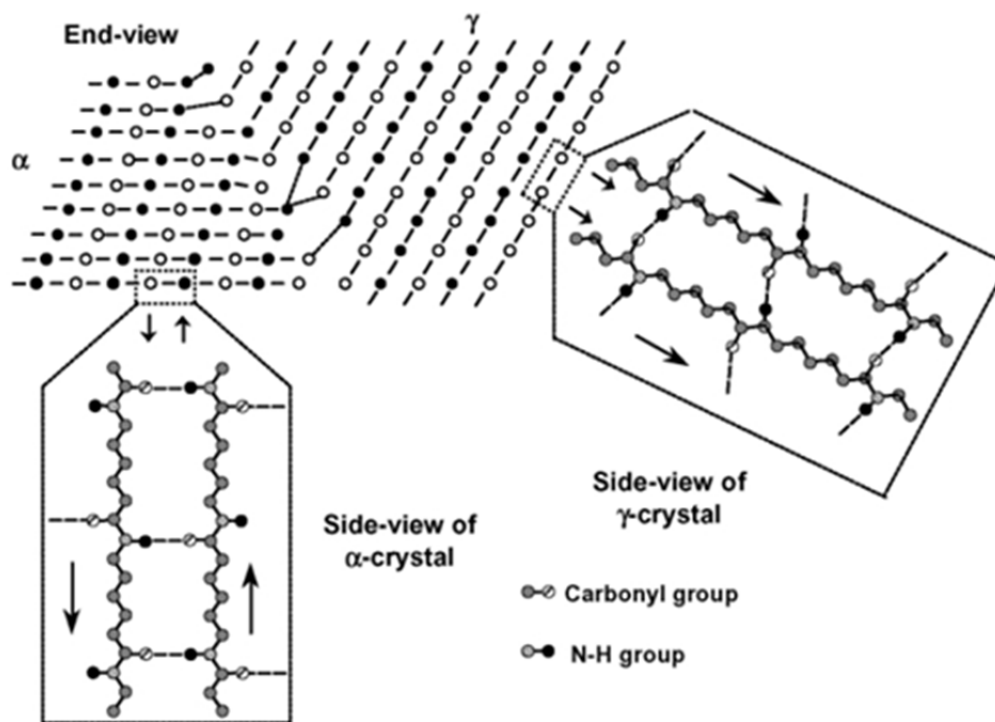


Figure 2-3 Schematic of hydrogen bonding within the α and γ crystalline forms of nylon 6 as seen from end and side-view of each crystal [24].

Poly (m-xylene adipamide) (MXD6) (Figure 2.4) is a semi-crystalline aromatic nylon with a better mechanical performance and barrier property in comparison with PA6 and can be considered as a potential candidate to replace PA6 for some packaging applications.

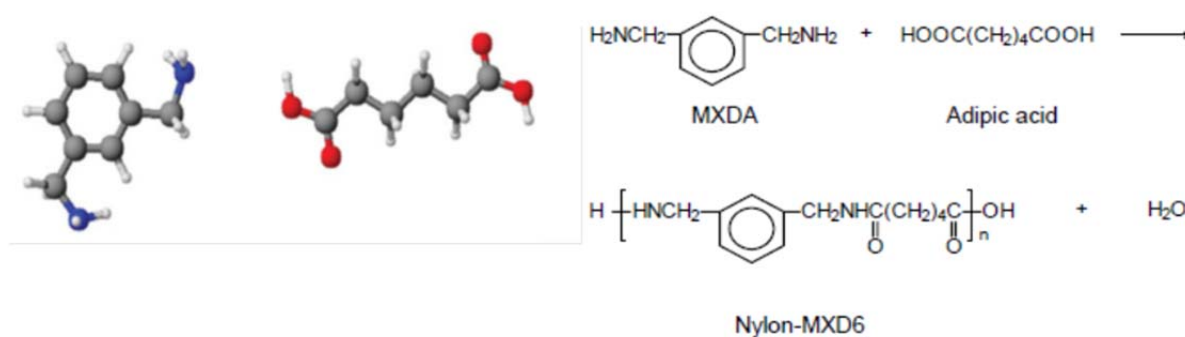


Figure 2-4 Condense polymerization and chemical structure of MXD6 [29].

For MXD6 (Figure 2.5), only one triclinic crystalline phase with the dimensions of $a = 1.201$ nm, $b = 0.483$ nm, $c = 2.98$ nm, $\alpha = 75^\circ$, $\beta = 26^\circ$ and $\gamma = 65^\circ$ is usually formed [30].

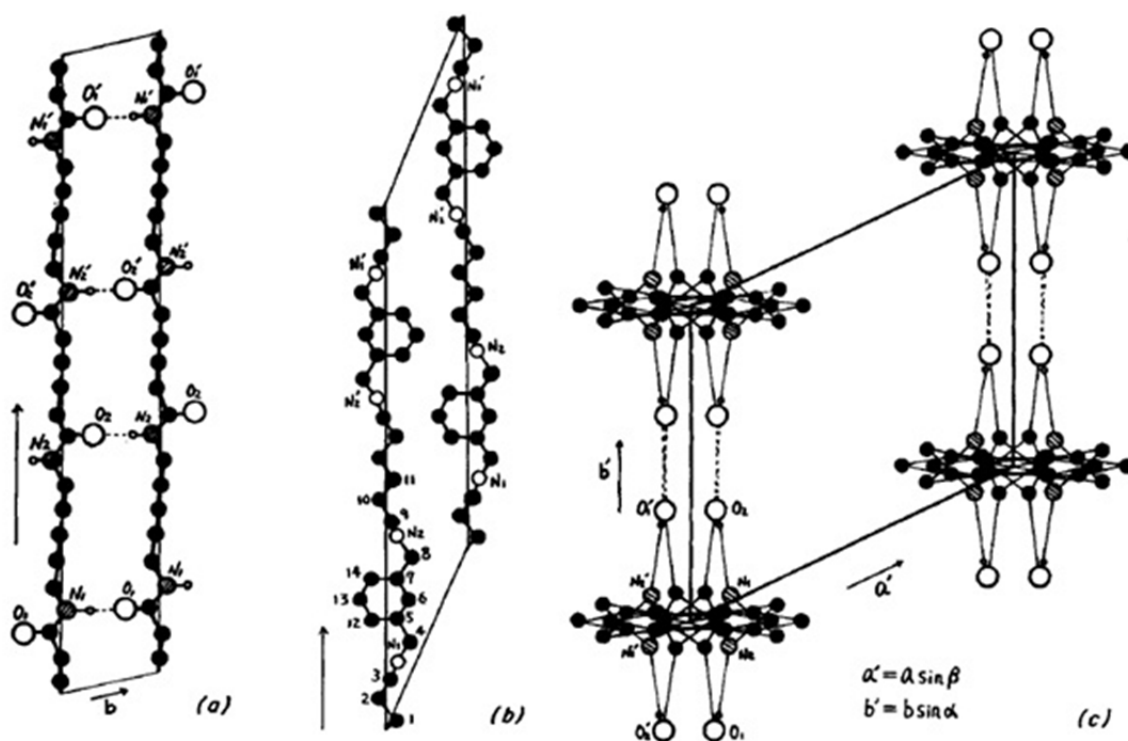


Figure 2-5 Crystal structure of poly (m-xylene adipamide) (MXD6) shown by projection on various planes: (a) the (100) plane; (b) the (120) plane; (c) the plane perpendicular to the c -axis [30].

MXD6 is well known for its excellent gas barrier properties even at the high humidity conditions [3, 4]. Its other features such as thermal stability, high bending strength and ease of stretching and/or thermoforming makes MXD6 in high attention in the film packaging. The gas permeation of MXD6 in contact with water molecules was studied in literature [4, 31]. Hu et al. [4] speculated that it is energetically more favorable for water molecules to form hydrogen bonds with the polymer matrix of MXD6. In fact, the water molecules occupied a part of the free volume in the polymer matrix available for gas diffusion and reduced the amount of the free volume and pathways for the oxygen permeation. Krizan et al. [32] reported that water molecules

compete with permeate gas for excess free volume in the MXD6 polymer matrix. In another study, Buquet [33] showed that a spherulitic water-induced crystallization phase takes place from the water/polymer interface after water immersion at ambient temperature and the presence of these crystals improved the barrier properties of the MXD6.

Some studies have been conducted in order to improve the properties of PA6 by blending with MXD6. The PA6/MXD6 system is a crystalline-crystalline polymer blend and the crystallization of each polymer plays an important role in the phase separation behavior of the blend [34]. Takeda and Paul extensively studied miscibility of PA6 and MXD6 [35-37]. They observed some miscibility of the PA6/MXD6 blends via the amide exchange reaction between these two polyamides. Shibayama et al. [34] showed that the miscibility of PA6/MXD6 blends is a function of the blend composition. Melt blending of PA6 and MXD6 during high-temperature extrusion can lead to a material with a homogeneous melt phase with a single T_g owing to the interchange reactions [37].

2.3 Methods used to improve barrier properties

Since plastic materials are growing fast in food packaging, permeation of oxygen through the package becomes more of an issue. For many products, the presence of a small amount of oxygen in the package is enough to severely affect the quality of the product. Oxygen scavengers are highly reactive with oxygen and can be placed in the interior of the package. There are three basic types of scavengers; iron-based systems, oxidizable polymers, and photo reducible compounds [38]. In the iron-based scavengers, iron reacts with oxygen in the presence of moisture. The oxidizable polymer organic components are catalyzed by a transition metal salt and can be activated by ultraviolet (UV) light. Regardless of which scavenger used, all the scavengers have a finite absorption capacity. Thus, the capacity to absorb oxygen in the package

highly depends on the amount of the scavenger added to the structure and it is limited to the package space. The scavenging rate is typically affected by scavenging concentration, storage conditions (i.e. temperature and relative humidity), and diffusion rate of oxygen to the scavenging component [39]. It should be pointed out that if the packaged item is damaged within one day of exposure to oxygen and it takes multiple days for the scavenger to completely eliminate the oxygen within a package, the scavenger would be completely useless.

Surface modification is one technique to improve barrier properties. Coating of silicon oxide (SiO_x) on polymers has attracted many attentions for the food and medical applications, due to its transparency, water resistance, recyclability, retortability, microwave use and excellent barrier properties. SiO_x coating on polymers such as poly (ethylene terephthalate) (PET), polypropylene (PP), nylon6 (PA6), poly (ethylene naphthalate) (PEN) and polyvinyl alcohols (PVA) films have been reported [40]. Two techniques have been applied for SiO_x coating; physical vapor deposition (PVD) and plasma-enhanced chemical vapor deposition (PECVD). The later technique was more preferable because it can be used to deposit materials at low temperature with excellent coverage in a high deposition rate, which creates better adhesion and less brittle failure [40-43].

Metallization under very high vacuum at high temperature is another technique used to improve barrier properties of the films. This technique was applied to improve barrier properties of films including PET, Polypropylene (PP), Low density polyethylene (LDPE), Polylactic acid (PLA), Polycarbonate (PC) and biaxially oriented nylon6. The main disadvantage of this method is the poor transparency of the metalized films. In fact, the surface modification methods are expensive and are not appropriate for some food packaging industries. Furthermore, crack

formation at the surface during stretching of the coated products can cause a deterioration of barrier properties.

Blending to combine desired properties of different polymers together is another way to improve barrier properties. In blending, the barrier properties are strongly influenced by the morphology of product. The main challenge in blending is to have a favorable morphology at a reasonable cost. Some blends have been developed for high barrier applications in the food packaging industry including EVOH in PP [44], EVOH in PA6 [45], PA6 in PP [46], PA6 in PET [47] or PEN in PET [48].

2.4 Nanocomposites for high barrier packaging

Dispersion of layered silicate clay as an impermeable phase with very high aspect ratio of 10-1000 in a polymer matrix is the chief idea to achieve a remarkable enhancement in gas barrier properties. The impermeable silicate layers create a tortuous path in a polymer matrix and as a consequence, the gas molecules penetrate with more difficulties (Figure 2.6).

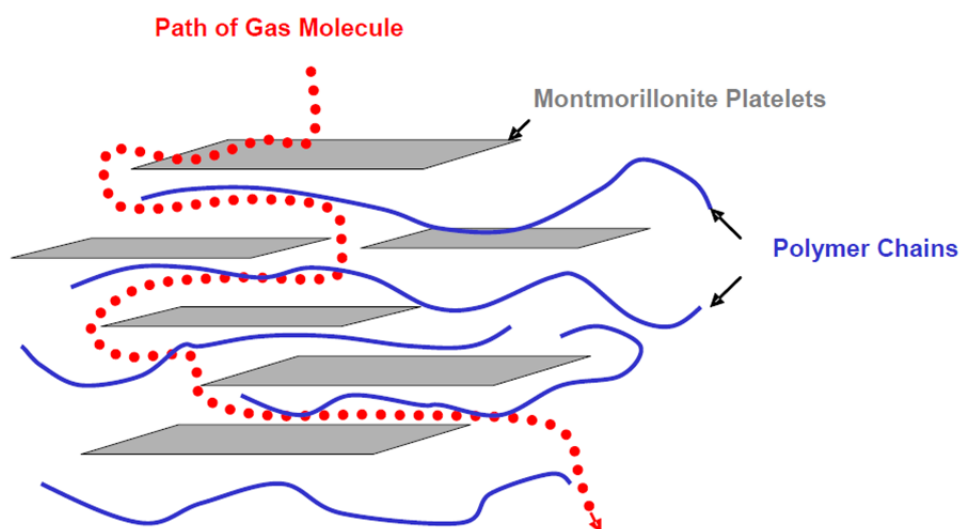


Figure 2-6 Tortuous pathway of gas permeant through nanocomposite [49].

Depending on the strength of the interfacial interaction between polymer and layered silicates, different types of morphologies are possible in nanocomposites including aggregated, intercalated and exfoliated (see Figure 2.7). Improvement of barrier properties of nanocomposites is strongly correlated with the morphology and dispersion state of the nanoclay platelets.

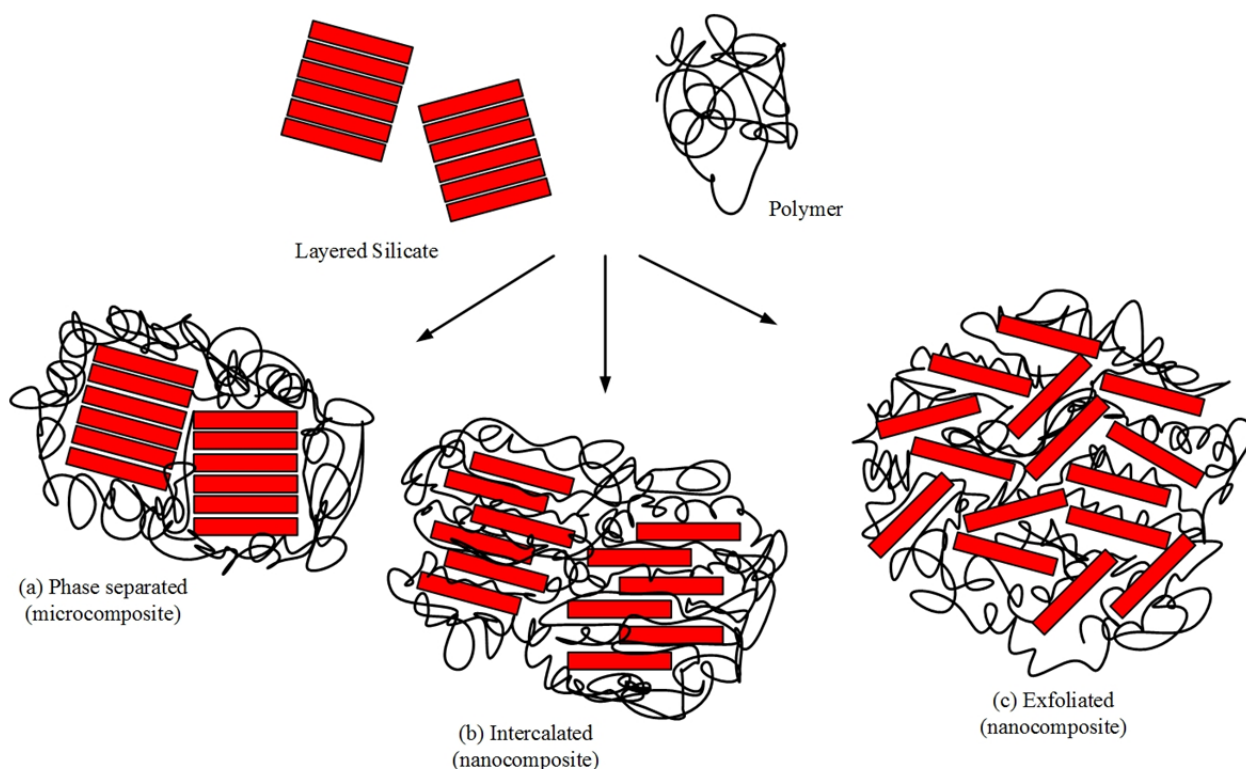


Figure 2-7 Dispersion state of nanoclays in a polymer matrix.

Polymer nanocomposite films containing impermeable lamellar fillers such as montmorillonite have recently received considerable attention in packaging because of improved mechanical and barrier properties [50-52].

During the cast film extrusion process, these nano-platelets could be oriented in the flow direction (Figure 2.8) and subsequently would enhance the gas barrier property of the nanocomposite films [53, 54].

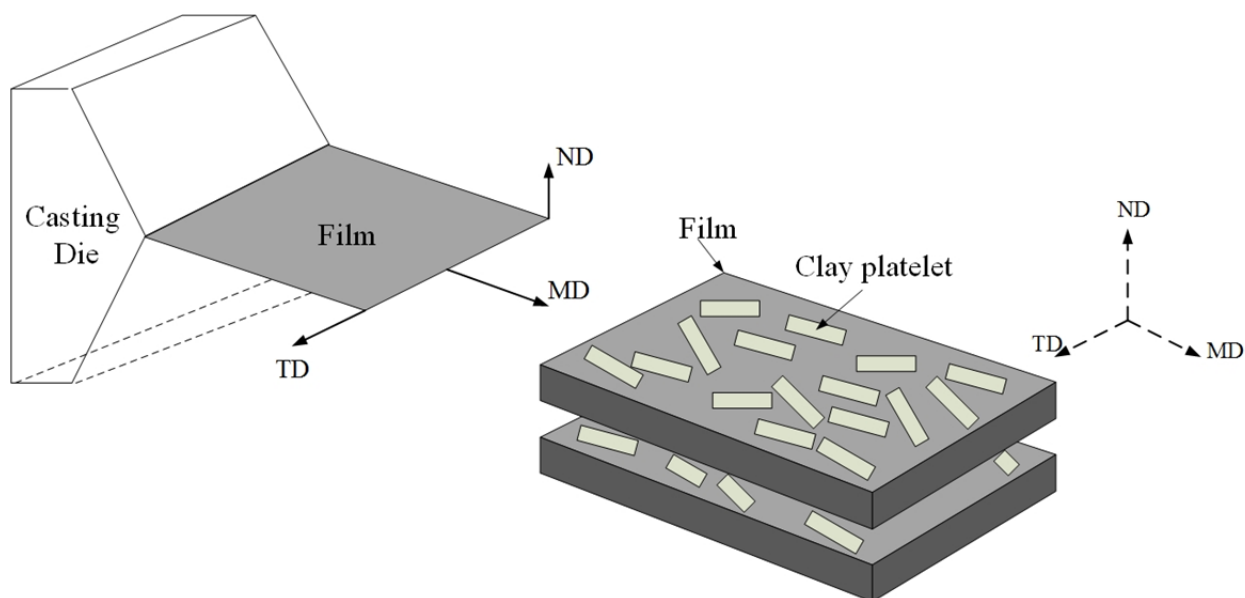


Figure 2-8 Schematic of clay orientation in cast nanocomposite films.

Due to a unique combination of good processability, high mechanical properties and chemical resistance as well as low oxygen permeation, a great interest has arisen in silicate clay nylon 6 nanocomposites [55-62]. Properties of nanocomposite films depend on many factors such as the aspect ratio of fillers, orientation and its degree of exfoliation and dispersion in the matrix, as well as the adhesion at filler-matrix interface. The studies on intercalation and exfoliation of PA6/clay nanocomposites, produced either through in-situ polymerization (Figure 2.9) [56, 63] or melt compounding [57, 64-66] processes, confirmed that the nanoclay particles can be extremely well intercalated and exfoliated in the nylon matrices, hence nanoclay composite films of nylon will have enhanced mechanical and barrier characteristics.

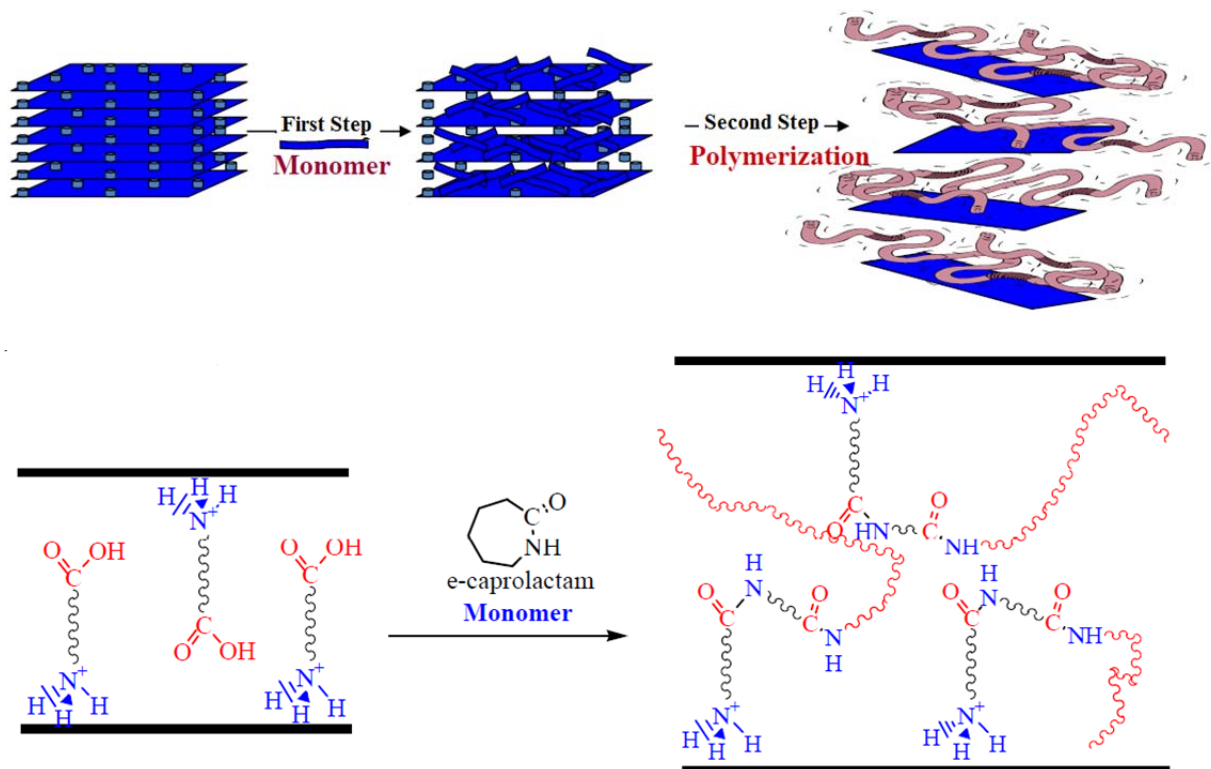


Figure 2-9 Nylon 6 nanocomposite formed through *in-situ* polymerization with modified montmorillonite [49].

The influence of clay platelet content and dispersion state in PA6 nanocomposites on the barrier properties of films were examined by Picard et al. [62]. The barrier properties of nanocomposites with clay contents ranging from 0 to 18 wt. % were investigated. It was found that the relative permeability was independent of the permeant molecule showing that tortuosity has the most important role on improving barrier properties of nanocomposites. It was reported that the crystallinity of PA6 was slightly dependent on the nanocomposite composition [62]. Consequently, the barrier properties have been related to the clay content and dispersion state. Usuki [56] et al. synthesized and characterized nylon 6 nanocomposites using organically modified clay platelets and studied the effect of platelets on the oxygen and water vapor barrier properties of polyamide. The study elucidated how the glass transition temperature of polyamide

decreased with addition of clay platelets. It was found that the water vapor and oxygen permeability of films made from the in-situ polymerized nanocomposites are remarkably reduced in comparison with the neat nylon 6 films. Their study showed that with only adding 2 wt% of montmorillonite, the permeability coefficient of water vapor reduced to less than half of that of polyamide. Thellen et al. [67] also reported a 40% and 30% improvement of oxygen and water vapor barrier properties respectively for melt-extruded PA6 nanocomposite films with incorporation 4 wt% of montmorillonite. In another study with Kojima et al. [68], a better resistance to water permeation of nanocomposite compared with that of neat nylon 6 was reported due to the decrease in diffusion coefficient (D). Pramoda et al. [69] showed that PA6/clay nanocomposite films had higher barrier properties compared to the neat polyamide, and also better thermal stability as well as higher stability in the process compared to neat polyamide grades. A comparative study of in situ polymerized and melt-blended nylon 6 nanocomposite systems by Tung et al. [70] showed a broader organoclay length distribution in synthesized nanocomposites because of extensive damage to the silicate layers in the melt blended samples which had been caused by high shearing forces applied in the extruder. The in situ polymerized nanocomposite exhibited higher melt viscosity and higher tensile ductility than the melt blended nanocomposite, which was reported to be due to improved dispersion and polymer-silicate interactions for that system. In another work by Fornes et al. [58], the effect of nylon molecular weight on the structure of PA6/clay nanocomposites was studied. A better clay exfoliation was observed for the nylon6 with a higher molecular weight due to the higher shear stress involved for the higher molecular weight matrix. A larger barrier improvement was observed for nylon 6 with higher molecular weight due to higher polymer-clay interactions [71]. Yano et al. [72] claimed that by adding only 2 wt % clay into PA6 matrix, the oxygen

permeation reduced by a factor of 2 and by a factor of 10 for 8 wt % clay loading. A reduction of about 40 and 80 % in oxygen transmission rate of nylon 6 at 65 % relative humidity was reported with incorporation of 2 and 8 wt. % clay, respectively, in polymer matrix [49]. Up to 200 % increase in the tensile modulus [73] and 175 % increase in the yield stress [74, 75] have been reported for PA6/clay nanocomposites compared to neat PA6. In general, crystallinity of polyamide nanocomposite is controlled by the type of polyamide matrix, molecular weight, clay concentration and the level of clay exfoliation, and plays an important role in the final properties.

Recently, incorporation of nano-clay in MXD6 nylon has received attention in order to further improve its gas barrier properties [6, 7]. MXD6 nanocomposite containing montmorillonite-layered silicates has been developed by Nanocor and 40% improvement in oxygen barrier over MXD6 film at 0% RH has been reported [76]. Incorporation of different kinds of clay in MXD6 nylon has also received attention [6, 7]. The results suggested that the strong interfacial interaction at the polymer/clay interface causes a reduction in the polymer free volume and, consequently, leads to a dramatic reduction in gas permeation.

2.5 Stretching of polymer films

This technique is based on drawing of a polymer film to improve mechanical and barrier properties. Upon stretching, the polymer chains and filled particles are oriented in the stretching direction, which leads to an increase in the diffusion path of permeant (see Figure 2.10).

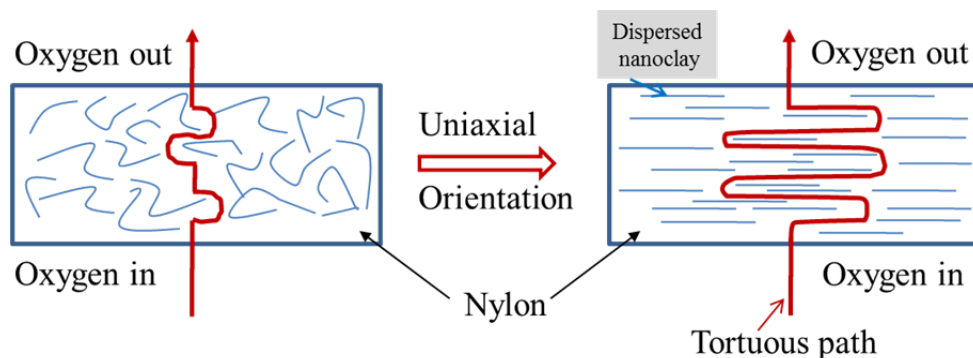


Figure 2-10 Schematic of tortuous diffusion path through precursor and uniaxially stretched of PA6/clay film.

Many attempts have been done to improve the final properties of films by post processing such as uniaxial or biaxial stretching. Stretching can result in a highly oriented film, reduced oxygen permeability [77, 78], improved water vapor barrier [79, 80] and improved mechanical strength and clarity [81-83]. However, it lowers elongation at break [83] and tear resistance along machine direction (MD) [77]. For instance, gas permeability of polypropylene was improved by a factor of 2 after biaxial orientation without sacrificing clarity and toughness of the films [84]. The oxygen diffusivity, solubility and consequently the permeability of poly (ethylene terephthalate) (PET) films were decreased after uniaxial stretching due to a reduction in the amount of excess-hole free volume in the polymer [85]. In another study, it was shown that orientation decreased the permeability of uniaxially stretched PET to almost one-third of the undrawn film [86]. Comparison between the barrier properties of biaxially oriented poly (ethylene terephthalate) / poly(ethylene 2,6-naphthalate) blends with pure PET showed that in the oriented samples (Figure 2.11), the solubility coefficient in a mixture composed of oxygen, nitrogen and carbon dioxide decreased around 50% [87].

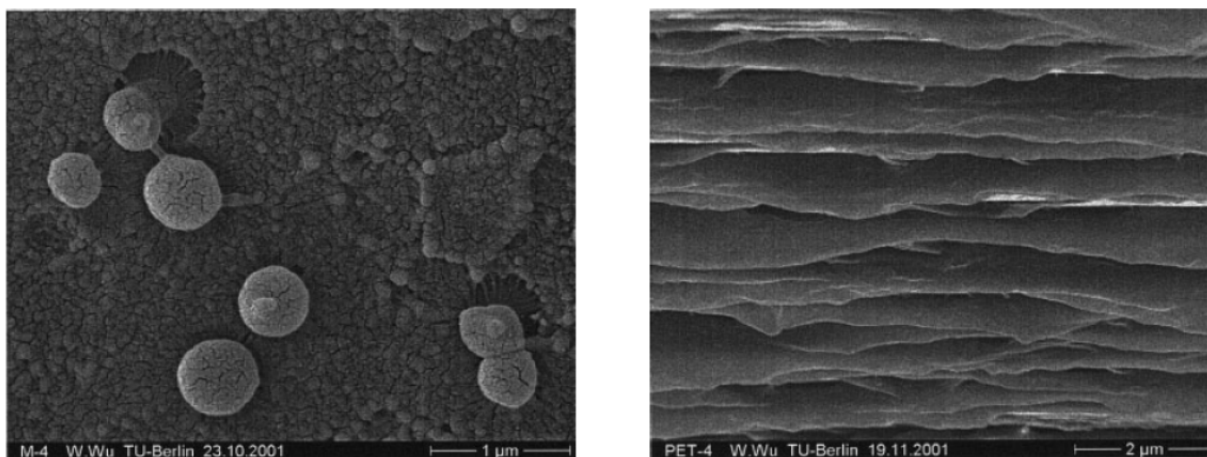


Figure 2-11 (a) SEM micrograph of the fracture surface of an extruded sample of a PET/PEN blend (70/30). (b) SEM micrograph of the tearing fracture surface of a biaxially oriented film of a PET/PEN blend (70/30) [87].

Uniaxial orientation also significantly improved the O_2 and CO_2 barrier properties of poly(ether block amide) (PEBA) copolymers [88]. The molecular motion that facilitates the movement of permeant molecules through a polymer film reduces by the extent of orientation upon stretching process. In fact, molecular orientation leads to a reduction in the diffusion coefficient of gases through polymers. The reduction in gas permeability could be also attributed to an increase in the crystallinity induced during stretching [88]. A study by Doudou et al. [89] showed that the crystallinity of a PET/MXD6 blend film was improved 40% upon uniaxial stretching when draw ratio increased to 5. In fact, the spherical MXD6 particles in PET matrix transformed into platelets with high aspect ratio arrayed in the plane of the film during stretching. Consequently, the diffusion path for gas molecules became more tortuous, resulting in a lower permeability [89]. Another study showed that the transparency of PET/MXD6 blend improved up to 70 % through biaxial orientation [90].

The structural development of nylon films during uniaxial stretching are influenced by initial morphology, molecular orientation, ability to crystallize (i.e. fast or slow crystallization rate), type of crystalline structure and physical state of the material (i.e. glassy, rubbery, partially

molten or fully molten). Additionally, the final properties of stretched films are strongly dependent on processing conditions such as stretching rate, extent of deformation and stretching temperature. The uniaxial stretching of PA6 to a draw ratio of 3 resulted in a 62.5% reduction in the oxygen transmission rate, a 17.4 % improvement in the puncture resistance, and also a 53 % increase in the clarity [53]. It was also reported that, even at a small draw ratio of 1.5, the mechanical strength of PA6/clay increased by 55% [53]. Another study showed that biaxial orientation of PA6 nanocomposite films was 1.5 times more efficient on improving the mechanical properties compared to uniaxial drawing under the same conditions [66].

Depending on the processing conditions and thermomechanical history, different crystalline forms (α and/or γ) may be presented in uniaxially and biaxially stretched PA6 and PA6/clay film [91, 92]. The γ form of PA6 is thermodynamically unstable and is transformed into the α form in plastic drawing [93-96] or thermal annealing [97]. The α form is highly stable and is typically stiffer than the γ form that has higher modulus and yield stress, and lower strain at break [93, 95]. The PA6 films in the mesomorphic γ crystalline form are more ductile than the films in the predominant stable α form. However, a lower orientation of the PA6 α phase compared with the γ phase has been reported after biaxial and uniaxial drawing [93]. The γ phase has a better ability for biaxial drawing so, starting with a PA6 film with a predominant γ phase is recommended to achieve uniform biaxial drawing [93]. The structural evolution analysis of nylon6 nanocomposite films during uniaxial stretching concluded that γ - α phase transition occurs under specific conditions. First, a sufficient extension for the γ phase is required to untwist the chain around the amide group. Second, an adequate molecular mobility is needed to change the stacking in the crystalline structure [54]. Since clay platelets limited the γ - α transformation in uniaxial drawing the PA6/clay film, some residual γ crystal remained after stretching at high draw ratio [98]. As it

can be observed in Figure 2.12, the γ - α strain-induced transition becomes more important in drawing polyamide at high temperatures due to an improvement in the chain mobility of crystals [93, 94].

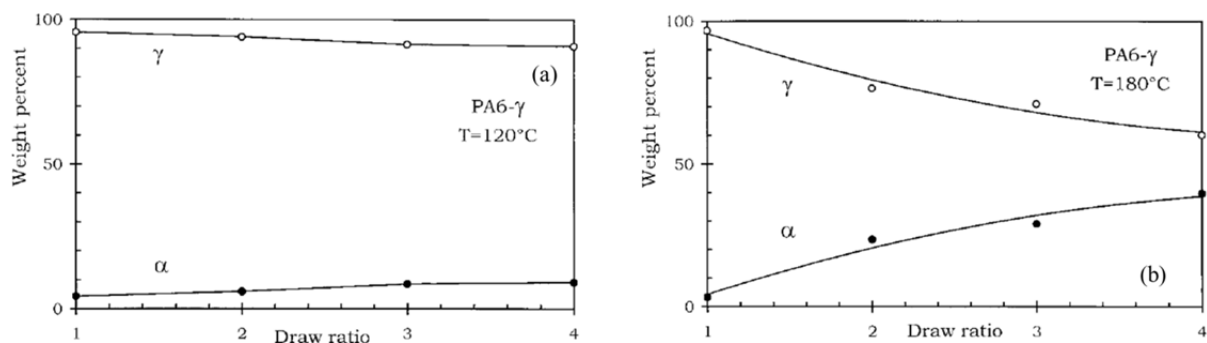


Figure 2-12 Structure evolution as a function of draw ratio for PA6 upon uniaxial stretching (a) at 120 °C and (b) at 180 °C [93].

2.6 Multilayer packaging technologies

Multilayer films having a core layer with good barrier and mechanical properties coextruded between two polyolefin layers have been used in food packaging industry to improve the mechanical performance and the barrier properties. However, combining different polymers in order to have an optimized designed multilayer film structure with excellent gas barrier properties (usually against water vapor and/or oxygen), high mechanical and optical performance, and low cost are a challenge in food packaging industries. Multilayer films are produced for food packaging through lamination (adhesive lamination or extrusion lamination), coating or coextrusion processes. In adhesive lamination technique, the polymer layers are combined using an adhesive material. In extrusion laminations, the layers are adhered together using a molten polymer such as low-density polyethylene (LDPE) [1]. A greater stiffness for the extrusion laminated films than the adhesive laminated ones has been reported, because extrusion lamination allows the layers to be separated further apart [8]. Coextruded multilayer films are

produced through combining polymer melts from different extruders in a feed-block. The simultaneous processing of polymers with different rheological properties is an important issue in coextrusion technique. In order to eliminate interfacial instability and encapsulation [99], or to avoid layer rearrangement caused with high viscosity ratio at adjacent layers [100], material selection is an important step in multilayer technology. One of the most important problems facing multilayer films is the adhesion of layers made of various materials to one another. When working with incompatible materials, a tie layer will most likely be required for adhesion purposes. Therefore, this is a major challenge in industries such as food packaging to achieve a cost optimized structure of multilayer film with high barrier properties and excellent mechanical performances.

Due to the hydrophilic nature of nylon materials, nylons are typically laminated or coextruded between other moisture protective polyolefin in order to improve the oxygen barrier performance [53, 66, 101]. Also, MXD6 can be sandwiched between polyolefin layers such as polyethylene, polypropylene, copolymers of at least two olefins selected from propylene, ethylene, etc. [102]. In those multilayer structures, an adhesive layer is needed to provide adhesion between the gas barrier layer and the polyolefin layer. The multilayer bottles based on MXD6 made by thermoforming showed excellent transparency, heat resistance and gas barrier properties, which could be suitable for high and low water content foodstuffs as well as any kind of hot and cold beverages such as juice and whisky [102].

A multilayer MXD6 with poly (ethylene terephthalate) (PET) was suggested for high barrier carbonated drink bottles [102]. Another study showed that a five-layer packaging film with MXD6 as the oxygen barrier layer and ethylene vinyl acetate copolymer (EVA) as the sealant and moisture barrier layer had acceptable barrier and/or mechanical properties [103]. Some

studies on PA6/MXD6 blends have been conducted to improve the PA6 properties [104, 105]. The influence of multilayer composition and MXD6/PA6 blend ratio on stretching, stretching stress, physical, mechanical properties (i.e. tensile, toughness, tear and impact strength) and gas permeability of biaxially oriented coextruded multilayer films have been investigated [104, 105]. The miscibility of PA6/MXD6 blends was extensively studied [34-36, 106]. PA6/MXD6 system is a crystalline-crystalline polymer blend and crystallization of each polymer plays an important role in the blend phase separation behavior [34]. Takeda and Paul extensively studied miscibility of PA6 and MXD6 [35-37]. They observed miscibility of the PA6/MXD6 blend via the amide exchange reaction between these two polyamides. Shibayama et al. [34] showed that miscibility of PA6/MXD6 blends is a function of blend composition. Melt blending PA6 and MXD6 during high-temperature extrusion can lead to a material with a homogeneous melt phase and a single T_g owing to interchange reactions [37].

Although a large number of barrier thermoplastics are commercially available in the market, they all have their drawbacks, e.g. cost, moisture-sensitivity, opacity or limited mechanical and thermal resistance. Currently, a number of different barrier technologies are being developed and are making their way into the marketplace. There is a desire to use the plastic based flexible packaging materials for different applications, which stimulates the industry to provide new and more efficient barrier solutions.

2.7 The measurement of the permeability of nanocomposites by models

In general, permeability of a permeant through a film depends on many factors, including the nature of the polymer, film's thickness, size and shape of the permeant, pressure and temperature. The chemical structure can also influence the permeability of polymers including polarity, unsaturation, symmetry, lateral chains, steric hindrance, glass transition temperature,

crystallinity, degree of crosslinking, intermolecular interactions, hydrogen bonding, present of comonomers, and orientation.

Steady state condition

The barrier property of a plastic refers to its abilities of transferring something through it. When a film is exposed to a permeant with different concentration in two sides, the permeant pass through the polymer by the net effect from the high concentration to the low concentration side in three steps; the sorption of gas molecules on the surface of film, the diffusion through the polymer, and finally, the desorption of gas from the other surface of the film (Figure 2.13).

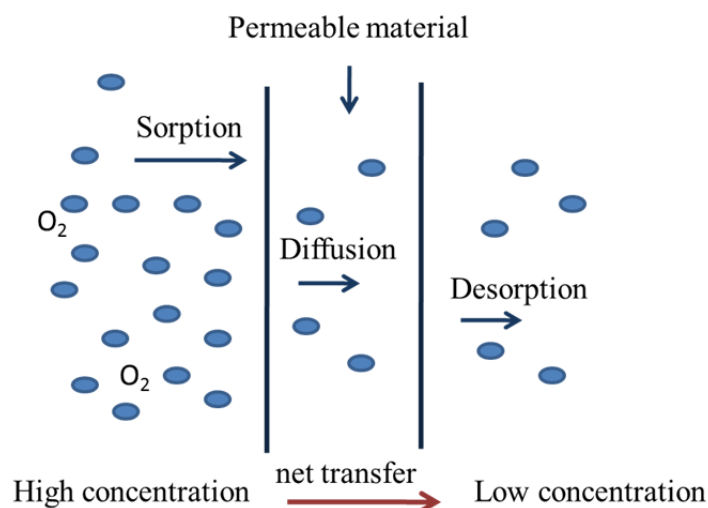


Figure 2-13 Permeation of a substance through a plastic packaging material [107].

Under steady state condition, the permeability coefficient is defined as “*the rate at which a quantity of permeant passes through a unit surface area of polymer in unit time having unit thickness with a unit pressure difference across the sample*” [107]. Mathematically, the permeability coefficient, P (in $\text{mol Pa}^{-1} \text{m}^{-1} \text{s}^{-1}$), is the product of solubility coefficient or solubility, S (in $\text{mol m}^{-3} \text{Pa}^{-1}$), and the diffusion coefficient, D (in $\text{m}^2 \text{s}^{-1}$):

$$P = DS = \frac{Q.L}{A.t.\Delta P} \quad (2.1)$$

Where, P is permeability coefficient, Q is mass of permeant passing through the film, L is film's thickness, A is surface area available for mass transfer, t is time, and ΔP is partial pressure difference for the permeant between two sides.

The main assumptions that are considered in this equation are

1. Partial pressure of permeant inside and outside of the film is constant.
2. Henry's Law represents the relationship between solubility and partial pressure.
3. Diffusion coefficient is independent of permeant concentration.

It should be pointed out that both solubility and diffusivity are affected by temperature.

According to Arrhenius' Law, diffusivity increases by increasing temperature [107].

$$D = D_0 e^{\frac{-E_a}{RT}} \quad (2.2)$$

Where D is the diffusivity at the final temperature (T), D_0 is the diffusivity at the reference temperature, E_a is the activation energy, R is the gas constant and T ($^{\circ}\text{K}$) is the absolute temperature.

Solubility decrease with increasing temperature for gases, while increasing for liquid and solids, so for relatively small temperature ranges, the relationship between permeability constant at different temperature can be explained by an Arrhenius type relationship [107].

$$P_2 = P_1 e^{\left(\frac{E_a}{R}\right)\left[\left(\frac{1}{T_1}\right) - \left(\frac{1}{T_2}\right)\right]} \quad (2.3)$$

Permeability constant for the multilayer can be estimated from the permeability constants of individual layers [107]

$$\frac{L_t}{P_t} = \sum \left(\frac{L_i}{P_i} \right) \quad (2.4)$$

where, L_t is total thickness, L_i is thickness of each layer, P_i is permeability of each layer, P_t is permeability of multilayer.

Permeability constant of miscible blend can be calculated by simplest model as follows [108]:

$$\ln P_t = \Phi_1 \ln P_1 + \Phi_2 \ln P_2 \quad (2.5)$$

Φ : Represents the volume fraction of the component.

For immiscible blends, the relationships are complex. For blends with one continuous phase and the other dispersed as spherical particles the following equation may be used [108]:

$$P_t = \frac{P_c[P_d+2P_c-2\phi_d(P_c-P_d)]}{[P_d+2P_c+\phi_d(P_c-P_d)]} \quad (2.6)$$

where, d is discontinuous phase and c is continuous phase.

By ignoring the effect of filler on the surrounding polymer matrix, the composite solubility coefficient can be described as [109]:

$$S = S_0 (1 - \phi) \quad (2.7)$$

where, S_0 is the solubility coefficient of pure polymer, and ϕ is the volume fraction of dispersed particles. According to the above equations, relative permeability is obtained as:

$$K = \frac{P}{P_0} = (1 - \phi) \frac{D}{D_0} \quad (2.8)$$

where, index “0” indicates the neat polymer. In fact the barrier properties increase in filled polymers, due to combination of two phenomena: reduction of available area for diffusion and addition of travel distance for a permeant.

The simplest model for diffusion of small molecules through a filled matrix has been proposed by Maxwell equation (1881) for impermeable arrayed spheres:

$$K = \frac{1 - \phi}{1 + \frac{\phi}{2}} \quad (2.9)$$

This equation is valid for dilute suspensions, and it is independent of the filler particle size.

Raleigh (1892) suggested the following equation for arrayed infinite cylinders aligned parallel to the surface. This equation is also independent of the size of the cylinders.

$$K = \frac{1 - \phi}{1 + \phi} \quad (2.10)$$

Nielsen (1967) proposed the following relation for permeability of filled polymer systems as a function of aspect ratio and volume fraction of filler:

$$K = \frac{1 - \phi}{1 + \frac{\alpha \phi}{2}} \quad (2.11)$$

where, α is the aspect ratio of fillers. The main assumption in this model was that, plates with rectangular cross section were uniformly dispersed in the polymer matrix. Some attempts have been made to modify this model capable to predict changes in diffusivity particularly at large values of α . Cussler simplified the above equation by proposing a geometric factor, μ , that depends on the shape of the dispersed particles:

$$(K)^{-1} = 1 + \mu \frac{\alpha^2 \phi^2}{1 - \phi} \quad (2.12)$$

Bharadwaj [110] considered sheet orientation and modified Nielsen's model. He applied the following order parameter:

$$S = \frac{1}{2} \langle 3 \cos^2 \theta - 1 \rangle \quad (2.13)$$

Where, θ represents the angle between the normal unit vector of silicate layers and the direction of preferred orientation (Figure 2.14). The angular brackets denote the average over all the dispersed layers.

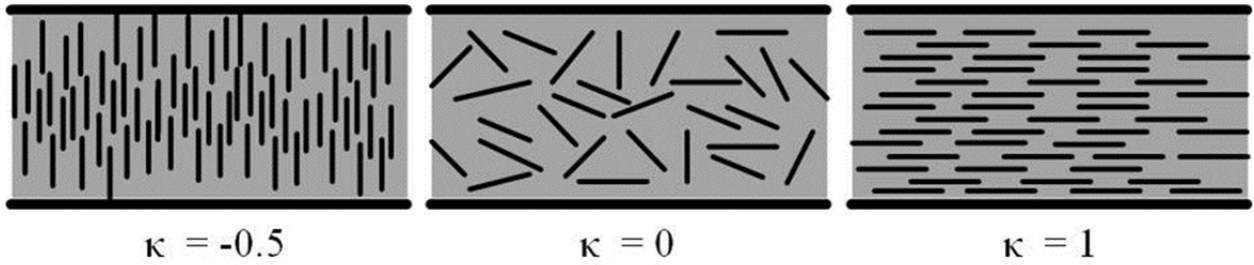


Figure 2-14 Direction of preferred orientation and normal vector of mineral sheets [110].

The relative permeability is given by the following equation:

$$K = \frac{1 - \phi}{1 + \frac{\alpha \phi}{2} \left(\frac{2}{3} \right) \left(S + \frac{1}{2} \right)} \quad (2.14)$$

Falla et al. [50] derived another model based on tortuous path of the diffusion through plates and resistance of the silts against gas diffusion according to aspect ratio of slits as well as the effect of large space between narrow slits. The proposed the relative permeability by:

$$K^{-1} = 1 + \frac{\alpha^2 \phi^2}{1 - \phi} + \frac{\alpha \phi}{\sigma} + \frac{4\alpha \phi}{\pi(1 - \phi)} \ln \left[\frac{\pi \alpha^2 \phi}{\sigma(1 - \phi)} \right] \quad (2.15)$$

The second term of equations, indicate the contribution of the tortuous path of the permeant through the plates. The third term, that involves σ , is reflected the resistance of the slits to diffusion and depends on aspect ratio of slits. The last part represents the restriction from the wide space between the plates into the narrow slits and it depends on α/σ .

Moggride et al. [50] applied a shape factor parameter by considering hexagonal array arrangement and proposed the following parameter:

$$K^{-1} = 1 + \frac{2}{27} \frac{\alpha^2 \phi^2}{1 - \phi} \quad (2.16)$$

The difference due to the platelet-shape is reflected by the coefficient (2/27), which reduces the barrier effectiveness.

Picard et al. [62] considered not only the polydispersity of the width of the filler but also the polydispersity of its thickness:

$$\frac{K_{composite}}{K_{matrix}} = \frac{1-\phi}{\left[1 + \frac{1}{3}\phi \frac{\sum n_i \left(\frac{w_i}{t_i}\right)^2}{\sum n_i \frac{w_i}{t_i}}\right]^2} \quad (2.17)$$

where, w_i and t_i are the width and the thicknesses of the fractions i of the platelets. This model is more appropriate for the cases of high loading of the impermeable phase, where, due to the presence of agglomerates, there is a distribution for the aspect ratio values.

Unsteady state condition

The oxygen diffusion through polymer film can be determined by solution of Fick's second law [32]:

$$\frac{\partial c}{\partial t} = D \frac{\partial^2 c}{\partial x^2} \quad (2.18)$$

For solving of the above equation two boundary conditions and one initial condition are necessary. With the preliminary assumption that Henry's law is valid at atmospheric pressures and ambient temperature for all polymeric materials, we can assume that oxygen concentration at one side of the film which is in the contact with food is zero and in the other side of film, the oxygen concentration is equal to $S.P_0$ [32];

where, S is the solubility coefficient and P_0 is the gas pressure which is constant at both side of film [32]. The concentration of the gas in two sides of the film can be considered for the boundary conditions as $c(x=0, t)=SP_0$ and $c(x=l, t)=0$, while l is film's thickness. The initial condition for the above equation can be considered as $c(x, t=0)=0$. By solving the equation (2.18) based on the boundary and initial conditions consideration, permeant concentration in polymer matrix at t , can be determined by the following equation [111]:

$$c(x, t) = S P_0 \left[\left(1 - \frac{x}{l}\right) - \frac{2}{\pi} \sum_{n=1}^{\infty} \frac{1}{n} \sin\left(\frac{n\pi x}{l}\right) \exp\left(-\frac{n^2 \pi^2 D t}{l^2}\right) \right] \quad (2.19)$$

It should be pointed out that the main assumption for solving the equation (2.18) was that the diffusion coefficient is independent of oxygen concentration and time.

For the film with the thickness of d , the flux density $J(t)$ in ($\text{mol m}^{-2} \text{s}^{-2}$) of the permeant gas when ($t \rightarrow \infty$), J_{∞} depends on the gas pressure, P_0 :

$$J_{\infty} = P \frac{P_0}{d} \quad (2.20)$$

where, the constant of proportionality, P , is the permeability coefficient.

Consequently by replacing $c(x, t)$ in fundamental law of diffusion the following relation between oxygen flux and diffusion coefficient will be obtained:

$$J(t) = \frac{P P_0}{l} \left[1 + 2 \sum_{n=1}^{\infty} (-1)^n \exp(-\pi^2 n^2 D t) \right] / l^2 \quad (2.21)$$

Oxygen flux as a function of time in the each unsteady state cycle of permeation measurement can be obtained from experimental data. The diffusion coefficient, D , is determined from the slope of the straight line of the plot $\left(\frac{Dt}{l^2}\right)$ versus “ t ”. At steady state condition, when ($t \rightarrow \infty$), the oxygen permeation can be measured as:

$$J_{\infty} = D S \frac{P}{l} \quad (2.22)$$

In equation (2.22), the oxygen permeability constant, P , can be determined directly from the steady state values in the permeability experiment.

Generally, literature data for gas transport coefficients (i.e. permeability, diffusion, and solubility coefficients) are changed with polymer parameters such as degree of crystallinity, nature of the polymer, and the thermal and mechanical histories of samples such as orientation. Sorption and diffusion phenomena take place exclusively in the amorphous phase of a semicrystalline polymer and not in its crystalline region. In the most of theoretical models have

been driven in the literature, the effect of crystallinity on the permeability coefficient is not considered. While, the effect of crystallinity on the permeability coefficient of high density polyethylene (HDPE) to oxygen was illustrated and it was shown that $P \times 10^{11}$ decreased from 54.9 (mL.cm.cm⁻².s⁻¹.(cm Hg)⁻¹) at 60% crystallinity to 20.9 at 69% and at 10.6 81% crystallinity [112].

2.8 Originality

Although, few authors have investigated properties of PA6 and MXD6 films, but to our knowledge, no study has been conducted to compare the thermal, crystal structure, rheological, mechanical and barrier properties of PA6 and MXD6 in the presence of nanoclay. Moreover, some studies have been reported on the uniaxial drawing of PA6/clay nanocomposite films [54, 92]. However, there is no published work on the uniaxial drawing of MXD6/clay nanocomposite.

Hence, a fundamental understanding on differences between the microstructure and properties of aliphatic and aromatic nylons and their nanocomposites is crucial for the packaging industry. In this dissertation, first, rheological, thermal, morphology, crystal structure, crystallization rate, mechanical and barrier properties of neat aliphatic (PA6) and aromatic (MXD6) nylons and their in-situ polymerized nanocomposite were studied and compared.

Since post-processing drawing is vastly used in packaging industry, in the next step, the effect of uniaxial stretching on the crystal structure, orientation, mechanical and barrier properties of PA6 and MXD6 in the presence of exfoliated clay were studied. Mostly, one characterization technique has been used in the literature to investigate the orientation of clay and crystalline phase upon stretching, which is not adequate to determine the orientation of all crystal axes of nylon in the presence of clay platelets. In this thesis, both X-ray diffraction and Trichroic Infrared analyses were used to shed light on the orientation of clay, all the crystal phase and amorphous region of the aliphatic and aromatic nylon films upon uniaxial stretching. Our findings showed that in addition to the common γ (200) crystal population (γ_1), an extra γ (020) crystalline population (γ_2) formed during stretching of PA6/clay films. The c -axis of γ_1 crystal population was oriented in the normal and transverse directions (ND and TD), while the c -axis of

γ_2 was aligned in the normal direction (ND), indicating that this later crystal population formed perpendicular to the (001) plane of the clay platelets.

The crystalline and amorphous orientations as well as the clay alignment significantly affect the performance of the stretched films. In the next step of this study, the structural development of the PA6 and MXD6 films in the presence of exfoliated nanoclay during uniaxial stretching was investigated in details and compared. The effect of uniaxial drawing on the morphology, crystal structure and crystallinity, thermal, mechanical and oxygen barrier properties of the polyamide 6 and the MXD6 as well as their in-situ polymerized nanocomposites were studied in this work. In addition, the relative oxygen permeability of the precursor and uniaxially oriented aromatic and aliphatic nanocomposite films has been predicted in this study with the different geometrical models and using the quantitative orientation of the nanoclay particles that was obtained in the previous stage. There is no published work to apply the experimental clay orientation as the orientation parameter in the theoretical models to calculate the relative oxygen permeability of nanocomposites.

Since a multilayer film is mainly used as a food package in industry, at the last step of this project, multilayer films with core layer of aliphatic and aromatic nylons and their in-situ polymerized nanocomposites were produced and thermal, barrier, mechanical and optical properties of the final product were compared. No study has been reported yet to investigate the influence of exfoliated nanoclay in aromatic and aliphatic nylon matrices used in the core layer of coextruded multilayer films on the mechanical and barrier properties.

2.9 Objectives

The main objective of this project is to fundamentally investigate the differences between microstructure and the macro-scale properties of monolayer and multilayer aromatic and aliphatic nylon films and their in-situ polymerized nanocomposites.

To achieve this main objective, the specific objectives of the current work are summarized as follows:

- To establish a fundamental understanding of the rheological and thermal properties, morphology (the extent of nanoclay intercalation and exfoliation), crystallization rate, type of crystalline structure, crystallinity, barrier and mechanical properties of PA6 and MXD6 as well as their in-situ polymerized nanocomposites films.
- Determine the effect of uniaxial stretching on the changes in the clay alignment and the orientation of crystal axes of all the crystalline phases and amorphous region of the aromatic and the aliphatic nylon films and their nanocomposites.
- To establish a fundamental understanding of the effect of uniaxial drawing on the morphology, crystallinity, thermal, mechanical and oxygen barrier properties of the PA6 and the MXD6 as well as their in-situ polymerized nanocomposites.
- To investigate the influence of exfoliated nano-clay filled aromatic and aliphatic nylon matrices used in the core layer of coextruded multilayer films on the mechanical and barrier properties.

CHAPTER 3

METHODOLOGY

To meet the objectives of this thesis, the experiments were divided in four phases (Figure 3.1). The first phase of the project was conducted based on raw material selection and characterization, including thermal and rheological characterization of neat resins and nanocomposites. The first part was also included processing, comprising single layer film extrusion and characterization. In the second step, the precursor films were uniaxially stretched with different draw ratios. The changes in orientation of clay and crystal axes of all the crystalline phases and amorphous region were examined using X-ray diffraction and Trichroic Infrared analyses. Furthermore, the effect of uniaxial drawing on crystal structure, crystallinity, thermal, mechanical and barrier properties of the neat and in-situ polymerized nanocomposites of aromatic and aliphatic nylons were investigated in the second phase. In the third step, the relative oxygen permeability of the precursor and uniaxially oriented nanocomposite films has been predicted with different geometrical models. Furthermore, from the quantitative orientation of the nanoclay particles obtained in the previous stage, the ability of the models to predict the relative oxygen permeability of the nanocomposites and to calculate the effective theoretical clay aspect ratio was investigated. In the last phase, multilayer coextrusion films were prepared and characterized. Five-layer films of aromatic and aliphatic nylons and their nanocomposites (as the core layer) with adjacent tie and LLDPE layers were produced using a multilayer co-extrusion cast process.

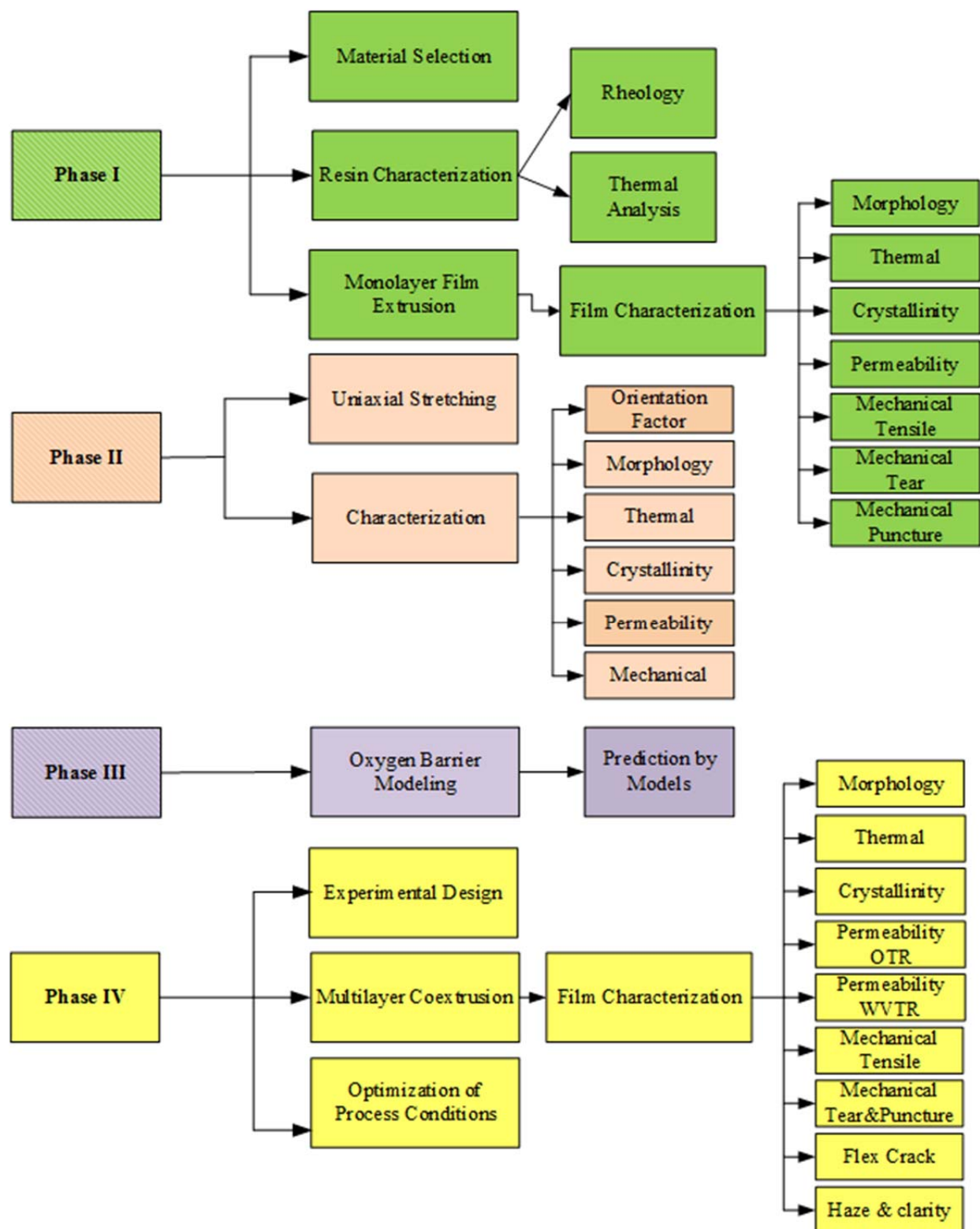


Figure 3-1 Experimental strategy

3.1 Materials

PA6 (Ultramid B36, from BASF) and PA6/clay nanocomposites (Cress-Alon™ NF3040, from CP polymers) were selected as the aliphatic nylon and its nanocomposite, respectively. The NF3040 had 4 wt% montmorillonite with 200 to 300 aspect ratios (reported by the supplier). MXD6 6007 resin and Imperm 103, which is a MXD6 resin nanocomposite with montmorillonite clay supplied by Nanocor (in partnership with Mitsubishi Gas Chemical), were selected as the aromatic nylon and its nanocomposite, respectively. According to Nanocor, the silicate layered montmorillonite content of the Imperm 103 nanocomposite MXD6 is between 3.3 to 3.6 wt% with 200 to 400 aspect ratios. As Linear Low Density Polyethylene (LLDPE) is hydrophobic, it was selected as the outer skin layers of the coextruded multilayer films, which would be in direct contact with atmospheric moisture. LLDPE (Sclair-FP120D from NOVAChemical) was used for the skin layers. A linear low density polyethylene grafted with maleic anhydride (Bynel 4125, from Dupont) was chosen for the tie layers to adhere the nylon core layer to the LLDPE skin layers. A linear low density polyethylene grafted with maleic anhydride (Bynel 4125, from Dupont) was chosen for the tie layers to adhere the nylon core layer to the LLDPE skin layers. Table 3.1 summarizes the materials used in this study and some of their characteristics.

Table 3.1 List of materials used in this study and their main characteristics (reported by suppliers).

Material	Commercial name	Supplier	Nomenclature	Main characteristics
Nylon 6	Ultramid B36	BASF (Freeport, USA)	PA6	$M_n = 18,000 \text{ g.mol}^{-1}$ $\rho = 1.14 \text{ g.cm}^{-3}$ $\eta_r = 3.6$ MFI (275°C/5kg) = 10 g/10 min
Nylon 6/clay	NF3040	CP Polymers (Montebello, USA)	PA6/clay	$\rho = 1.15 \text{ g.cm}^{-3}$ $\eta_r = 3$ MFI (230°C/5kg) = 8.9 g/10 min Clay content = 4 wt%
Aromatic Nylon	MXD6 6007	Mitsubishi Gas Chemical (Colonial Heights, USA)	MXD6	$M_n = 25,000 \text{ g.mol}^{-1}$ $\rho = 1.21 \text{ g.cm}^{-3}$ $\eta_r = 2.7$ MFI (230°C/5kg) = 12 g/10 min
Aromatic Nylon/clay	Imperm 103	Nanocor (Arlington Heights, USA)	MXD6/clay	$\rho = 1.22 \text{ g.cm}^{-3}$ $\eta_r = 2.5$ Clay content = 3.3 to 3.6 wt%
Linear Low Density Polyethylene	Sclair-FP120D	Nova Chemicals (Calgary, Alberta, CANADA)	LLDPE	MFI (190°C/2.16kg) = 1 g/10 min $\rho = 0.92 \text{ g.cm}^{-3}$
Linear Low Density Polyethylene grafted with Maleic Anhydride	Bynel-4125	DuPont (Wilmington, DE, USA)	LLDPE-g-MA	MFI (190°C/2.16kg) = 2.5 g/10 min $\rho = 0.93 \text{ g.cm}^{-3}$

M_n : Number average molecular weight

ρ : Density

η_r : Relative viscosity = (η/η_0) where η_0 is the viscosity of the solvent.

MFI: Melt flow index

3.2 Film preparation

Single-layer cast films of nylon and nylon/clay were prepared using a fully intermeshing co-rotating twin-screw extruder (Leistritz ZSE 18 HP) (Nuremberg, Germany) with 18 mm screw diameter and a length/diameter (L/D) of 40. To minimize degradation, the screw configuration was set to yield a low to medium shear environment during extrusion. The aromatic (i.e. MXD6 and MXD6/clay) and aliphatic nylons (i.e. PA6 and PA6/clay) were dried prior to extrusion in a vacuum oven at 130 °C for 5 h and at 80 °C for 24 h, respectively. The screw speed was 200 rpm and the temperature profile from the hopper to the die was 230/240/245/255/260 °C for the

aliphatic nylons and 235/250/255/260/265 °C for the aromatic ones. The extruder was equipped with a slit die followed by rapid cooling using an air knife. Chill rolls set at ambient temperature were used to stretch the precursor films to obtain 30-70 µm thick films. The precursor films were kept in desiccators (under vacuum) for further characterizations.

The MXD6 compression molding samples were prepared at 270 °C for 9 min, under a purge of nitrogen to obtain 30 to 300 µm thick films. The samples were rapidly cooled in the liquid nitrogen.

The uniaxial stretching was carried out on 5 cm × 1.5 cm × 70 µm precursor films using an Instron (Instron Electro Puls E3000, UK) apparatus equipped with a heating chamber. The uniaxial stretching was performed at 110 °C, an optimized speed of 400 mm/min and draw ratios from 1.5 to 5. The stretching DR is the ratio of the final grip distance (sample's length after stretching) to the initial grip distance (sample's length before stretching). Before drawing, the films were kept at 110 °C in the heating chamber of the tensile machine for 10 min to allow a homogenous temperature distribution. Stress-strain curves (Figure 3.2) exhibited a plateau plastic deformation after the yield point for the stretched films at all draw ratios. All the samples were rapidly air cooled to room temperature and then removed from the clamps for further characterizations. The stress drop after yielding in the engineering stress-strain curves is indicative of the necks typically observed during uniaxial deformation as was addressed by Cakmak and coworkers [113].

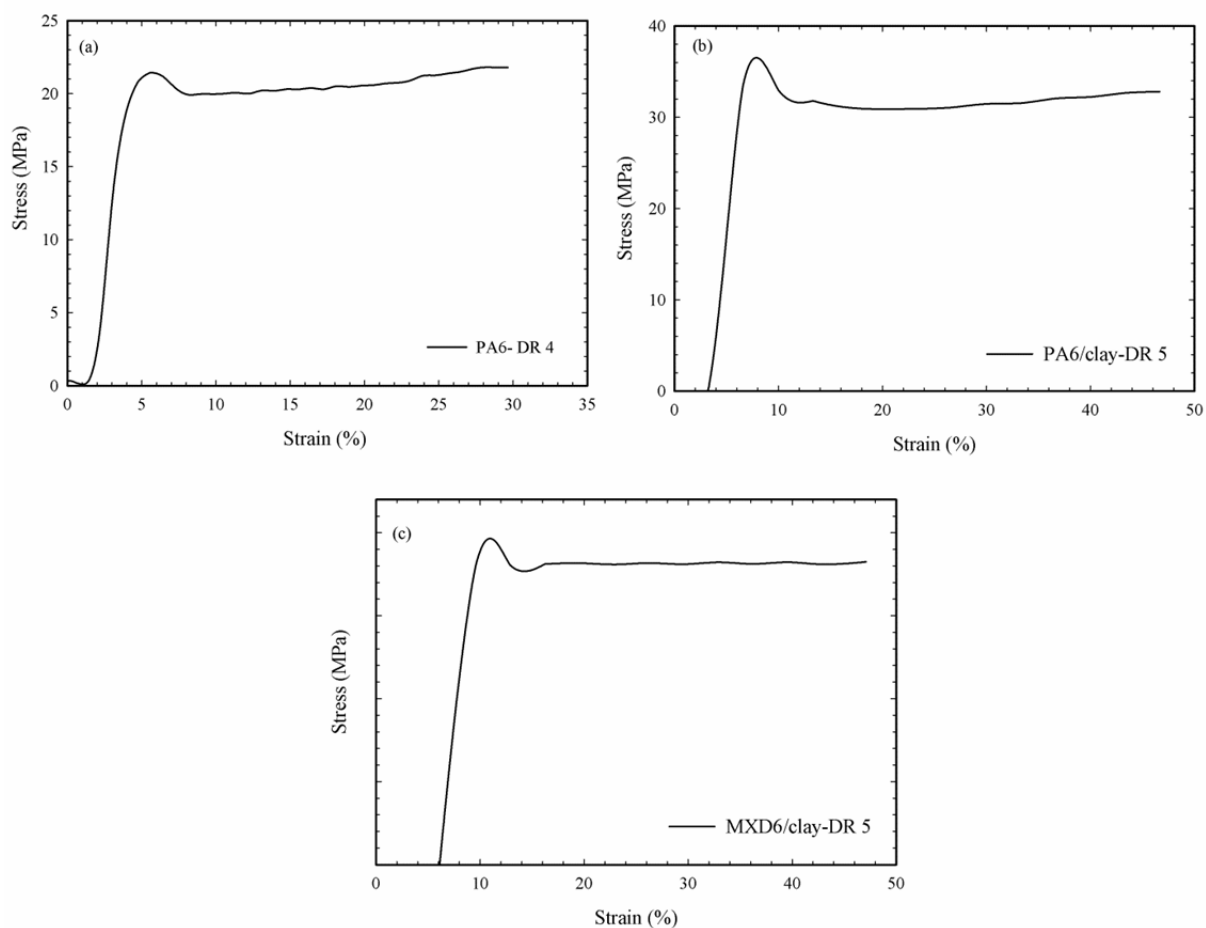


Figure 3-2 Stress-Strain curves for (a) PA6, (b) PA6/clay and (c) MXD6/clay films stretched at 110 °C.

Multilayer films prepared with a co-extrusion cast process had five layers:

- PA6, MXD6 and their nanocomposites as the oxygen barrier layer (core)
- LLDPE as the moisture resistant layers (skins)
- LLDPE-g-MA as the tie layers

The films were prepared using a Labtech Engineering Co-Extrusion Multilayer Line with four single-screw extruders (type LE20-30C) with 20 mm screw diameter and a 30 length/diameter (L/D) ratio. The feed-block with (A/B/C/D/A) design for five-layer and a flat die with 30 cm width were used to process the films. The aromatic (i.e. MXD6 and MXD6/clay) and aliphatic

nylons (i.e. PA6 and PA6/clay) were dried prior to extrusion in a vacuum oven at 130 °C for 5 h and 80 °C for 24 h, respectively. The temperature profile from the hopper to the die was 275/280/280/285 °C for the aliphatic nylons, 280/285/285/290 °C for the aromatic ones, 215/220/225/225 °C for the LLDPE, and 210/215/220/225 °C for the LLDPE-g-MA. The co-extrusion line was equipped with a slit die followed by rapid cooling using an air knife with 13 psi pressure. Chill rolls set at the ambient temperature were used to stretch the films to obtain 100 µm thick films including 35 µm, 10 µm and 45 µm thicknesses in the core, tie and the skin layers respectively. The temperature for die, feed block and connections were set at 280 °C. The die gap was adjusted at 2 mm. The screw speeds were set at 80 rpm, 35 rpm and 30 rpm for the skin, core and tie layer extruders, respectively.

3.3 Characterizations

3.3.1 Rheological properties

Dynamic rheological measurements were conducted using an Advanced Rheometric Expansion System (ARES, TA Instruments) (Rheometric Scientific Inc., USA) strain-controlled rheometer equipped with a conventional oven for temperature control. Small amplitude oscillatory shear (SAOS) deformation was applied using parallel plate geometry of 25 mm in diameter and a gap of 1.2 mm under nitrogen atmosphere. The linear viscoelastic properties of the neat polymers and nanocomposites were measured in the frequency range of 0.06 to 100 rad/sec. Prior to frequency sweep tests, time sweep tests were performed at a frequency of 6.28 rad/s for 20 min to check the thermal stability of the samples. The relaxation spectra for the neat polymers were calculated from linear dynamic experiments. The rheological tests were conducted at 270 and 280 °C for MXD6 and MXD6/clay and at 220, 240 and 260 °C for PA6

and PA6/clay, and LLDPE. In order to avoid the effect of humidity on rheological measurements, nylon pellets and disk samples were dried at 80 °C for 24 h in a vacuum oven and then they were kept in a desiccator. It should also be pointed out that, due to the instability of nylon at high temperatures and long period of time (nearly 45 min) [114], all the frequency sweep tests for nylon and nylon/clay samples have been performed from high to low frequencies.

3.3.2 Thermal analysis

Differential Scanning Calorimetry (DSC) Q1000 (TA Instruments, New-Castle, DE, USA) was used for thermal analysis of the resins and films. Three scanning cycles were conducted under nitrogen atmosphere between 10 to 280 °C under heating and cooling rates of 10 °C/min. At the end of the first heating ramp, the samples were held at 280 °C for 3 min to erase their thermal history before cooling ramp. The melting, crystallinity, and glass transition behavior of the specimens were obtained and discussed. Non-isothermal crystallization of the neat resins as well as their nanocomposites was studied at cooling rates of 5, 10 and 50 °C/min.

The crystallinity (X_c (%)) of the resins was calculated according to the following equation:

$$X_c (\%) = \frac{\Delta H_c}{\Delta H_0(1 - x)} \times 100 \quad (3.1)$$

where x is the percentage of clay, ΔH_c is the enthalpy of crystallization obtained from cooling scan and ΔH_0 is the heat of fusion for 100% crystalline PA6 and MXD6, which are 190 and 175 J/g, respectively [24, 115].

The crystallinity of produced films was calculated according to the following equation:

$$X_c (\%) = \frac{\Delta H_m - \Delta H_{cc}}{\Delta H_0(1 - x)} \times 100 \quad (3.2)$$

where ΔH_m and ΔH_{cc} are the melting and cold crystallization enthalpy obtained from first heating cycle.

The skin layer crystallinity (X_c (%)) was estimated by dividing the heat of fusion of LLDPE resin by 294 J/g [116] (the theoretical value for 100% crystalline polyethylene homopolymer).

Heat fusion of each layer (ΔH_i) is obtained by heat fusion from the heating scan (ΔH_j) divided by weight fraction (wt) of that layer:

$$\Delta H_i = \frac{\Delta H_j}{wt} \quad \text{and} \quad wt = \frac{\frac{\mu_i}{\sum \mu_i} \times \rho_i}{\sum (\frac{\mu_i}{\sum \mu_i} \times \rho_i)} \quad (3.3)$$

where μ_i and ρ_i are the thickness and density of each layer, respectively.

Modulated DSC (MDSC) used for the purpose of deconvolution of the melting endotherm of the LLDPE and cold crystallization exothermic of the aromatic nylon that appear on the film heating ramp. In MDSC, a linear 3 °C/min heating rate, 60 s modulation period, and a ± 0.45 °C temperature amplitude were selected.

The weight percentage of nanofillers was determined by Thermal Gravimetry Analysis (TGA) Q500 (TA Instruments, New-Castle, DE). The samples were heated from 30 to 500 °C at 10 °C/min and from 500 to 800 °C at 50°C/min under helium atmosphere.

3.3.3 X-ray diffraction

Wide angle X-ray diffraction (WAXD) measurements were carried out using Philips X'pert apparatus (Netherlands). The generator was set up at 50 kV and 40 mA and a copper CuK α radiation ($\lambda=1.54 \text{ \AA}$) was selected. The samples were scanned from 1 to 10 degree ($^\circ$) under scanning rate of 0.01 $^\circ$ /s to estimate basal spacing (d_{001}) between the silicate layers and also scanned from 10 to 50 $^\circ$ at 0.04 $^\circ$ /s for exploring nylon crystalline structure.

3.3.4 Morphology

Transmission electron microscopy (TEM) (JEOL JEM-2100F, Japan, operating at 200 kV) was used to observe clay exfoliation and dispersion quality in the aromatic and aliphatic nylon matrices. The specimens were impregnated in epoxy resin and microtomed in the MD-ND plane using an Ultracut FC microtome (Leica, Germany) with a diamond knife. The TEM micrographs were used to measure the average aspect ratio of the dispersed clays. The micrographs were manually digitized using a digitizing table from Wacom and SigmaScan v.5 software (SPSSInc., USA) and a digitizing tablet (Wacom, Japan).

Scanning electron microscopy (SEM) (Hitachi S4700 with a cold field emission gun, FEG-SEM) was used to measure the thickness of layers. The films were broken in liquid nitrogen and were coated with gold.

Spectrum 65 FT-IR polarized microscopic (Spotlight 400, PerkinElmer) (Waltham, MA) was used to investigate the cross section of multilayer films and measure the layer thickness and uniformity. The films were gently stood between the rounded clips, MD plane was vertical and perfectly in parallel with the mold sidewall to avoid possible movement, and then were molded in epoxy. The cross section surfaces of the multilayer films were polished and were scanned under the FTIR microscope.

3.3.5 Barrier property

Oxygen transmission rate (OTR) for the precursor and stretched films in accordance with the D-3985-81 ASTM standard was measured using MOCON OXTRAN (Minneapolis, USA) oxygen permeability tester at 25 °C, 0% relative humidity, and 1 atm pressure. A mixture of 98% nitrogen (N_2) and 2% hydrogen (H_2) was used as the carrier gas and 100% oxygen (O_2) was used

as the test gas. The test was ended when the oxygen flux changed by less than 1% during a 40 min test cycle. The reported data have been normalized (multiplied) by the films' thickness and are an average of four tests.

Water vapor transmission rate (WVTR) for multilayer films in accordance with D-6701 ASTM standard was measured using MOCON AQUATRAN® Model 1 (Minneapolis, USA) water vapor permeability tester at 37.8 °C, 100% relative humidity, and 1 atm pressure.

3.3.6 Mechanical properties

Tensile tests in both machine and transverse directions (MD and TD, respectively) were carried out using INSTRON-3365 (USA). Young modulus, tensile toughness, elongation at break and yield strength of the films were measured according to D 882-02 ASTM standard. Samples with 25 mm width, 250 mm length, and 30 µm thickness were stretched at a rate of 5 mm/min.

The Elmendorf tear resistance of the films was measured in both MD and TD according to ASTM standard D1922 with ProTear (Thwing Albert Instrument Co. USA) testing machine. The specimens cut to 76 mm in width by 63 mm in length (63-mm specimen dimension is the direction of tear).

The puncture resistance was evaluated according to ASTM standard D2582 using 250 N load cell of Instron E3000R6454 (USA). The displacement of the film was recorded against the force (N) and the maximum force was reported as the puncture strength. A needle with 0.5 mm radius was used to pierce the film at a rate of 25 mm/min.

The flex crack resistance of the multilayer films was investigated using a Gelbo Flex Tester (model GFT 392) (Vinatoru, NC, USA) according to the ASTM F392-93 standard. The reported data are the average of pinholes detected in 15 samples, with 280 × 200 mm dimensions, after 900 full flex cycles implemented for 20 minutes.

3.3.7 Optical property

Optical property of the films in the term of Haze values were determined according to D-1003 ASTM standard using a LAMBDA 1050 spectrophotometers from PerkinElmer.

3.3.8 Orientation

To evaluate orientation and monitor crystalline phase formation, infrared spectra of the precursor and stretched films were recorded using a Spectrum 65 FTIR spectrometer from PerkinElmer (Waltham, MA) with a resolution of 4 cm^{-1} and an accumulation of 32 scans over the wavenumber range of 400 to 4000 cm^{-1} . The beam was polarized with a Spectra-Tech zinc selenide wire grid polarizer from Thermo Electron Corp. The details of the technique can be found elsewhere [117]. Spectra were recorded with the polarizer in the vertical machine direction (MD), S_M , and in the horizontal transverse direction (TD), S_T . The films were also tilted by an angle of φ with respect to MD, S_{NT} , and spectrum was recorded with the polarizer in the horizontal direction [92]. The spectra in the normal direction (ND), S_N , can be calculated according to the following equation [92, 118, 119]:

$$S_N = \frac{S_{NT}(1 - \frac{\sin^2 \varphi}{n^2})^{1/2} - S_T(1 - \frac{\sin^2 \varphi}{n^2})}{\sin^2 \varphi / n^2} \quad (3.4)$$

where n is the refractive index and was reported equal to 1.62 for nylon [118, 119] and 1.73 for clay platelets [120, 121] in the NT plane. A value of 45° was chosen for φ [92].

The structurally dependent spectrum, S_0 , is obtained according to:

$$S_0 = \frac{(S_M + S_N + S_T)}{3} \quad (3.5)$$

This is the spectrum of the corresponding isotropic sample. The degree of orientation of a specific molecular chain axis or crystal axis (i) with respect to the film directions (j) can be calculated by [92]:

$$f_{ij} = \frac{D-1}{D+2} \times \frac{2}{3\cos^2\phi-1} \quad (3.6)$$

where D is the dichroic ratio ($D = A_j/A_0$), j is MD, TD, or ND, A_j and A_0 are the absorption peak intensities in the S_j and S_0 spectra, respectively, and ϕ is the angle that the transition moment makes with the polymer chain axis. The latter was taken equal to 0° as mentioned in the Refs [91, 92]. PeakFit v4.06 Software was used for peak fitting of the spectra. In this study, the PA6 crystallographic axes $i = a, b$, and c were defined as the same assignment used by Arimoto et al. [122]. In this assignment, the crystallographic b -axis is considered being parallel to the nylon chain axis which is different from the assignments of Cole et al. [91] who considered the c -axis is being parallel to the chain axis. The thick films, more than $50 \mu\text{m}$ thickness, are unsuitable for structural investigation using transmission infrared spectroscopy since the signal for some peaks become saturated

The crystalline structure and orientation of the crystal axes of nylons as well as the clay platelet alignment were investigated by wide angle X-ray diffraction (WAXD) in the transmission mode with a single-crystal diffractometer AXS X-ray (Bruker, Karlsruhe, Germany) equipped with a Hi-STAR two-dimensional area detector. The generator was set up at 40 kV and 40 mA and the copper CuK α radiation ($\lambda = 1.542 \text{ \AA}$) was selected using a graphite crystal monochromator. The sample to detector distance was fixed at 12 cm and it was scanned from 10 to 50° at $0.04^\circ/\text{s}$. Several film layers were stacked together in order to obtain a total thickness of approximately 2 mm to get the maximum diffraction intensity. For each sample, a transmission diffraction pattern was recorded using a pole figure accessory as the sample was

rotating at a scanning rate of 3° per minute through spherical angles (0° to 360°) with respect to the beam. This allows measuring the intensity of diffraction for a given crystallographic plane (hkl), in order to obtain probability distribution of orientation (normal to hkl plane) with respect to the directions of the sample.

Herman orientation function, f , represents the fraction of polymer chains that are perfectly aligned parallel to the symmetry axis and is calculated according to [123]:

$$f = \frac{1}{2}(3\cos^2\theta_\mu - 1) \quad (3.7)$$

where θ_μ is the angle between the unit cell axes (a , b , and c) and reference axis. The details of calculations can be found elsewhere [123]. The orientation factors from WAXD are mainly due to the crystalline part, therefore no information about the orientation of the amorphous phase can be obtained.

CHAPTER 4

ORGANIZATION OF ARTICLES

The main achievements of this research project are presented in the form of four scientific papers in the following four chapters:

Chapter 5 presents the results of the first paper “*Rheological, crystal structure, barrier and mechanical properties of PA6 and MXD6 nanocomposite films*” that has been published in *Polymer Engineering and Science*. In this work, various properties such as crystal structure, rheological, thermal, barrier and mechanical properties of the PA6, MXD6 and their in-situ polymerized nanocomposites are studied and compared using dynamic rheological tests, XRD, DSC, TGA, oxygen permeability and tensile tests. Dynamic rheological measurements are used to study the thermal stability of the samples, the dispersion state of the nanoclay (i.e. intercalated or exfoliated), the interactions between the polymer and clay, and the relaxation behavior of the resins. The clay dispersion state is also investigated by XRD and TEM. The cast process is employed to prepare the aromatic and aliphatic nylon monolayer films and their nanocomposites. The film structures in details and in relation to the final properties are investigated. The crystalline structure and the crystallinity of the neat PA6 and MXD6 and their nanocomposites are studied by WAXD and DSC. The non-isothermal crystallization rate and the effect of annealing on crystallinity and oxygen transmission of the aromatic and aliphatic nylon films in the presence of clay are compared.

Chapter 6 presents the second article “*X-ray and Trichroic Infrared orientation analyses of uniaxially stretched PA6 and MXD6 nanoclay composite films*” that has been accepted in *Macromolecules*. In this work, the changes in orientation of clay and crystal axes of all the crystalline phases and amorphous region upon uniaxial stretching were examined using X-ray

diffraction and Trichroic Infrared analyses and the results are discussed in details. The clay alignment is measured with three different techniques: FTIR peak deconvolution, FTIR interactive spectral subtraction and X-ray diffraction. WAXD and FTIR analyses are conducted to calculate the orientation of the amorphous phase and all the crystalline populations which are mainly formed in the presence of clay during rapid cooling of the aromatic and aliphatic nylon cast films. The orientation of the crystalline and amorphous phases as well as clay alignment plays an important role in determining the permeability coefficient to diffusing gases through the polymer films. Therefore, those fundamental findings allow us to elucidate the effect of the microstructure of neat and nanocomposite PA6 and MXD6 films on the permeability and mechanical properties.

Chapter 7 presents the third paper “*Effect of uniaxial deformation on thermal, oxygen barrier and mechanical properties of PA6 and MXD6 nanocomposite films*” that has been submitted to *Polymer Engineering and Science*. In this work, the structural development of the aliphatic and the aromatic nylon films and their nanocomposite during uniaxial stretching are investigated and compared. The effect of uniaxial drawing on the morphology, crystallinity, thermal, mechanical and oxygen barrier properties of the polyamide 6 and the MXD6 as well as their in-situ polymerized nanocomposites are studied. In addition, the oxygen permeability and oxygen diffusion through nylon nanocomposite films are predicted with theoretical models and with incorporating structural parameters such as the clay aspect ratio, and the crystalline phase orientation and the clay orientation data that are obtained in the previous Chapter.

Chapter 8 presents the fourth article “*Properties of co-extruded nano-clay filled aliphatic Nylon (PA6)/linear low density polyethylene (LLDPE) and aromatic Nylon (MXD6)/LLDPE multilayer films*” that has been accepted in *Journal of Plastic Film and Sheeting*. In this work, coextruded multilayer films with the PA6 and the MXD6 nylons as well as their in-situ

polymerized nanocomposites, as an oxygen barrier layer (core), and a linear low-density polyethylene (LLDPE) as the moisture barrier layers (skin) with the adjacent tie are produced and characterized. The fundamental findings from the dynamic rheological measurements assisted us to process coextruded multilayer films with a minimum interfacial instability and encapsulation. The effect of microstructure, morphology, orientation, crystal structure and crystallinity of neat and nanocomposite PA6 and MXD6 nylons in the core layer of coextruded multilayer films on the different final properties such as oxygen and water vapor barrier, puncture, tear, flex crack, tensile and optical properties are discussed.

CHAPTER 5

Rheological, Crystal Structure, Barrier and Mechanical

Properties of PA6 and MXD6 Nanocomposite Films¹

Maryam Fereydoon, Seyed H. Tabatabaei and Abdellah Ajji*

CREPEC, Chemical Engineering Department, Ecole Polytechnique,

C.P. 6079, Succ. Centre ville Montreal, QC, H3C 3A7 Canada

Abstract

In this study, rheological, crystal structure, barrier and mechanical properties of polyamide 6 (PA6), poly (m-xylene adipamide) (MXD6) and their in-situ polymerized nanocomposites with 4 wt% clay were studied. The extent of clay intercalation and exfoliation as well as type of crystals, crystallinity and thermal transitions were investigated using X-ray Diffraction (XRD) and Differential Scanning Calorimetry (DSC), respectively. Dynamic rheological measurements revealed that incorporation of nanoclay significantly increases complex viscosity of MXD6 nanocomposites at low frequencies, which was related to the formation of a nanoclay network and exchange reaction between MXD6 chains. The comparative study of dynamic characteristics ($G'(\omega)$ and $G''(\omega)$) for aliphatic and aromatic polyamide nanocomposites with their neat resins as well as the relaxation spectra for both polymer systems confirmed the possibility of the aforementioned phenomena. Although, the crystallinity of MXD6 films was lower compared to PA6 films, the permeability to oxygen was more than 5 times better for the former. Incorporating 4 wt% clay enhanced the barrier property, tensile modulus and yield stress of PA6 and MXD6

¹ Published in *Polymer Engineering and Science*. November 2013. DOI: 10.1002/pen.23813

nanocomposite films in both machine and transverse directions without sacrificing much puncture and tear resistances. The PA6 based films showed higher tear and puncture strength compared to MXD6 films.

Keywords: Nylon, Nanocomposites, Rheology, Crystallization, Barrier

5.1 Introduction

Insufficient barrier properties of commercial thermoplastics to the permeation of atmospheric gases such as oxygen and water vapor are a major problem in the packaging industry. In particular, a high oxygen permeation rate reduces the shelf life of packaged food products which results in higher costs for food processors and retail customers. Multilayer films consisting of a core layer having good barrier and mechanical properties sandwiched between two polyolefin layers is a technique currently used in food packaging industry in order to improve mechanical performance and barrier to oxygen.

Ethylene vinyl alcohol copolymer (EVOH) has high barrier against aroma and oxygen. However, moisture sensitivity of EVOH, especially at high relative humidity (RH), lowers mechanical performance and barrier properties of EVOH films [1]. Also, exposure of EVOH films to high temperatures, such as retort processing, leads to a sharp decrease in oxygen barrier properties at a given relative humidity [2]. In addition, due to fast crystallization kinetics and high rigidity, EVOH cannot be used for thermoforming application [2].

Poly vinylidene chloride (PVDC) is also used as an oxygen barrier [3], however, it is not environmental friendly due to the generation of toxic gases during incineration [4]. Polymer nanocomposite films containing impermeable lamellar fillers such as montmorillonite have recently received considerable attention in packaging because of improved mechanical and barrier properties [5-7]. Poly (ethylene terephthalate) (PET) is used for packaging applications

due to its advantages of high chain stiffness, high glass transition temperature and crystallinity. However, high oxygen and carbon dioxide permeability is a challenge for using PET for beverage packaging. Some effort has been done to enhance gas barrier properties of PET by incorporating layered silicate nanoclay via melt compounding [8] or in-situ polymerization [9]. However, at high processing temperatures required for melt compounding of PET, the organo modifier of nanoclay undergoes thermal degradation resulting in a little effect of nanoparticles on the barrier properties of PET [10, 11]. Other studies also reported a reduction in gas permeability of polyolefin nanoclay composite films, but oxygen permeation is still higher than values of interest in some food packaging applications [12, 13].

Aliphatic nylons such as polyamide 6 (PA6) have been widely used in food packaging. Poly (m-Xylene Adipamide) (MXD6) is a semi-crystalline aromatic nylon with better mechanical performance and barrier property in comparison with PA6 and can be considered as a potential candidate to replace PA6 for some packaging applications. In addition, it is well known that nanoclay particles can be extremely well intercalated and exfoliated in nylon matrices; hence nanoclay composite films of PA6 and MXD6 will have enhanced mechanical and barrier characteristics.

MXD6 nanocomposite containing montmorillonite-layered silicates has been developed by Nanocor and 40% improvement in oxygen barrier over MXD6 film at 0% RH has been reported [14]. Incorporation of different kind of clay in MXD6 nylon has also received attention [15, 16]. The results suggested that strong interfacial interaction at polymer/clay interface causes a reduction in the polymer free volume and, consequently, a dramatic reduction in gas permeation. The gas permeation of MXD6 in contact with water molecules was studied in literature [17, 18]. EVOH barrier to oxygen drops significantly at high relative humidity, whereas that of MXD6

does not deteriorate in high relative humidity environments. Hu et al. [18] speculated that it is energetically more favorable for water molecules to form hydrogen bonds with the polymer matrix of MXD6. In fact, water molecules occupied part of free volume in polymer matrix available for gas diffusion and reduce the amount of free volume and the pathways for oxygen permeation. Krizan et al. [19] reported that water molecules compete with permeate gas for excess free volume in the MXD6 polymer matrix. In another study, Buquet [20] showed that a spherulitic water-induced crystallization phase takes place from the water/polymer interface after water immersion at ambient temperature and this presence of crystals improve the barrier properties of MXD6.

MXD6 can be sandwiched between polyolefin layers such as polyethylene, polypropylene, copolymers of at least two olefins selected from propylene, ethylene, etc. [21]. In those multilayer structures, an adhesive resin layer is needed to provide adhesion between the gas barrier layer and the polyolefin layer. The multilayer containers made by thermoforming showed excellent transparency, heat resistance and gas barrier properties, which could be suitable for high and low water content foodstuffs as well as any kind of hot and cold beverages such as juice and whisky [21].

Some studies have been conducted in order to improve properties of PA6 by blending with MXD6. PA6/MXD6 system is a crystalline-crystalline polymer blend and crystallization of each polymer plays an important role in the phase separation behavior of the blend [22]. Takeda and Paul extensively studied miscibility of PA6 and MXD6 [23-25]. They observed some miscibility of the PA6/MXD6 blend via the amide exchange reaction between these two polyamides. Shibayama et al. [22] showed that miscibility of PA6/MXD6 blends is a function of blend

composition. Melt blending of PA6 and MXD6 during high-temperature extrusion can lead to a material with a homogeneous melt phase and a single T_g owing to interchange reactions [25].

Including blends of MXD6 with PA6 in the core layer of a multi-layer film would significantly enhance the barrier and mechanical performances [21, 26]. MXD6 has higher gas barrier, easier straight line cut in tearing and higher mechanical performance than PA6 and the blended film has better puncture resistance, impact and tear strength than MXD6 [26, 27].

Although a few authors have investigated properties of PA6 and MXD6 nanocomposites, no study has compared the crystal structure, rheological, mechanical and barrier properties of PA6, MXD6 and their nanoclay composite films. A fundamental understanding on differences in the properties of such films would be crucial for packaging industry. In this work, cast films of aromatic and aliphatic nylon monolayer films (18-50 μm) and their nanocomposites were produced to investigate their structures in details and in relation to the final properties.

5.2 Experimental

5.2.1 Materials

Nylon MXD6 6007 resin and Imperm 103, which is a nanocomposite of MXD6 resin with montmorillonite clay supplied by Nanocor, in partnership with Mitsubishi Gas Chemical, were selected. According to Nanocor, silicate layered montmorillonite content of the Imperm 103 nanocomposite MXD6 is between 3.3 to 3.6 wt% with aspect ratios of 200 to 400. Nylon PA6 Ultramid B36 and Cress-Alon™ NF3040, which is a nanocomposite of PA6 were purchased from BASF and CP Polymers, respectively. The montmorillonite content of NF3040 is 4 wt% with aspect ratios of 200 to 300. Table 5.1 summarizes the material used in this study.

Table 5.1 List of materials used in this study and their main characteristics (reported by suppliers).

Material	Commercial name	Supplier	Nomenclature	Main characteristics
Nylon 6	Ultramid B36	BASF (Freeport, USA)	PA6	$M_n = 18,000 \text{ g.mol}^{-1}$ $\rho = 1.14 \text{ g.cm}^{-3}$ $\eta_r = 3.6$ MFI (275°C/5kg) = 10 g/10 min
Nylon 6/clay	NF3040	CP Polymers (Montebello, USA)	PA6/clay	$\rho = 1.15 \text{ g cm}^{-3}$ $\eta_r = 3$ MFI (230°C/5kg) = 8.9 g/10 min Clay content = 4 wt%
Aromatic Nylon	MXD6 6007	Mitsubishi Gas Chemical (Colonial Heights, USA)	MXD6	$M_n = 25,000 \text{ g.mol}^{-1}$ $\rho = 1.21 \text{ g.cm}^{-3}$ $\eta_r = 2.7$ MFI (230°C/5kg) = 12 g/10 min
Aromatic Nylon/clay	Imperm 103	Nanocor (Arlington Heights, USA)	MXD6/clay	$\rho = 1.22 \text{ g.cm}^{-3}$ $\eta_r = 2.5$ Clay content = 3.3 to 3.6 wt%

M_n : Number average molecular weight

ρ : Density

η_r : Relative viscosity = (η/η_0) where η_0 is the viscosity of the solvent.

MFI: Melt flow index

5.2.2 Film Processing

Cast films of neat and layered silicate nanocomposite nylons were prepared using a fully intermeshing co-rotating twin-screw extruder (Leistritz ZSE 18 HP) (Nuremberg, Germany) with 18 mm screw diameter and length/diameter (L/D) of 40. To minimize degradation, the screw configuration was set to yield low to medium shear environment during extrusion. The aromatic nylon resins (i.e. MXD6 and MXD6/clay) as well as the aliphatic ones (i.e. PA6 and PA6/clay)

were dried in a vacuum oven at 130 °C for 5 h and 80 °C for 24 h, respectively. The screw speed was 200 rpm and the temperature profile from the hopper to the die was set at 235/240/250/250/255 °C for PA6 and PA6/clay and 230/240/245/255/260 °C for MXD6 and MXD6/clay. For film preparation, the extruder was equipped with a slit die followed by rapid cooling using an air knife and uniaxial stretching by chill rolls set at ambient temperature. Different draw ratios were applied to produce films with thicknesses in the range of 18 to 50 μm . The produced films were kept in desiccators (under vacuum) for further characterizations.

5.3 Resin and film characterizations

Rheological Properties

Dynamic rheological measurements were conducted using an Advanced Rheometric Expansion System (ARES, TA Instruments) (Rheometric Scientific Inc., USA) strain-controlled rheometer equipped with a conventional oven for temperature control. Small amplitude oscillatory shear (SAOS) deformation was applied using parallel plate geometry of 25 mm in diameter and a gap of 1.2 mm under nitrogen atmosphere. The linear viscoelastic properties of the neat polymers and nanocomposites were measured in the frequency range of 0.06 to 100 rad/sec. Prior to frequency sweep tests, time sweep tests were performed at a frequency of 6.28 rad/s for 20 min to check the thermal stability of the samples. The relaxation spectra for the neat polymers were calculated from linear dynamic experiments. The rheological tests were conducted at 270 and 280 °C for MXD6 and MXD6/clay and at 220, 240 and 260 °C for PA6 and PA6/clay. In order to avoid the effect of humidity on rheological measurements, nylon pellets and disk samples were dried at 80 °C for 24 h in a vacuum oven and then they were kept in a desiccator. It should also be pointed out that, due to the instability of nylon at high

temperatures and long period of time (nearly 45 min) [28], all the frequency sweep tests for nylon and nylon/clay samples have been performed from high to low frequencies.

Thermal analysis

Differential Scanning Calorimetry (DSC) Q1000 (TA Instruments, New-Castle, DE, USA) was used for thermal analysis of the resins and films. Three scanning cycles were conducted between 10 to 260 °C under heating and cooling rates of 10 °C/min. At the end of the first heating ramp, the samples were held at 260 °C for 3 min to erase their thermal history before cooling ramp. The melting, crystallinity, and glass transition behavior of the specimens were obtained and discussed. Non-isothermal crystallization of the neat resins as well as their nanocomposites was studied at cooling rates of 5, 10 and 50 °C/min.

The crystallinity of the resins was calculated according to the following equation:

$$\text{Crystallinity (\%)} = \frac{\Delta H_c}{\Delta H_0(1-x)} \times 100 \quad (5.1)$$

where x is the percentage of clay, ΔH_c is the enthalpy of crystallization obtained from cooling scan and ΔH_0 is the heat of fusion for 100% crystalline PA6 and MXD6, which are 190 and 175 J/g, respectively [29, 30].

The crystallinity of produced films was calculated according to the following equation:

$$\text{Film crystallinity(\%)} = \frac{\Delta H_m - \Delta H_{cc}}{\Delta H_0(1-x)} \times 100 \quad (5.2)$$

where ΔH_m and ΔH_{cc} are melting and cold crystallization enthalpy obtained from first heating cycle.

The weight percentage of nanofillers was determined by Thermal Gravimetry Analysis (TGA) Q500 (TA Instruments, New-Castle, DE). The samples were heated from 30 to 500 °C at 10 °C/min and from 500 to 800 °C at 50°C/min under helium atmosphere.

X-ray diffraction

Wide angle X-ray diffraction (WAXD) measurements were carried out using Philips X'pert apparatus (Netherlands). The generator was set up at 50 kV and 40 mA and a copper CuK α radiation ($\lambda=1.54056 \text{ \AA}$) was selected. The samples were scanned from 1 to 10 degree ($^{\circ}$) under scanning rate of 0.01 $^{\circ}$ /s to estimate basal spacing (d_{001}) between the silicate layers and also scanned from 10 to 50 $^{\circ}$ at 0.04 $^{\circ}$ /s for exploring nylon crystalline structure.

Morphology

Transmission electron microscopy (TEM) (JEOL JEM-2100F, Japan, operating at 200 kV) was used to observe clay dispersion quality in the aromatic and aliphatic nylon matrices. To evaluate the orientation of silicate platelets, microtoming was performed along the machine direction. For cutting, the specimens were impregnated in epoxy resin and microtomed by using an Ultracut FC microtome (Leica, Germany) with a diamond knife. TEM micrographs were used to measure the average aspect ratio of the dispersed clays and the free-path spacing distance between clay layers. The micrographs were manually digitized using a digitizing table from Wacom and SigmaScan v.5 software (SPSSInc., USA) and a digitizing tablet (Wacom, Japan).

Barrier property

Oxygen transmission rate (OTR) in accordance with the D-3985-81 ASTM standard was measured using MOCON OXTRAN (Minneapolis, USA) oxygen permeability tester at 25 $^{\circ}$ C, 0% relative humidity, and 1 atm pressure. A mixture of 98% nitrogen (N_2) and 2% hydrogen (H_2) was the carrier gas and 100% oxygen (O_2) was used as the test gas. The test was ended when the oxygen flux changed by less than 1% during a 40 min test cycle. The reported data have been normalized (multiplied) by the films' thickness and are an average of four tests.

Mechanical properties

Tensile tests in both machine and transverse directions (MD and TD, respectively) were carried out using INSTRON-3365 (USA). Young modulus, tensile toughness, elongation at break and yield strength of the films were measured according to D 882-02 ASTM standard. Samples with 25 mm width, 250 mm length, and 30 μm thickness were stretched at a rate of 5 mm/min.

The Elmendorf tear resistance of the films was measured in both MD and TD according to ASTM standard D1922 with ProTear (Thwing Albert Instrument Co. USA) testing machine. The specimens were cut to 76 mm in width by 63 mm in length (63-mm specimen dimension is the tear direction). The puncture resistance was evaluated according to ASTM standard D2582 using 250 N load cell of Instron E3000R6454 (USA). The displacement of the film was recorded against the force (N) and the maximum force was reported as the puncture strength. A needle with 0.5 mm radius was used to pierce the film at a rate of 25 mm/min.

5.4 Results and discussion

5.4.1 Rheological characterization

The viscoelastic properties of the *in-situ* polymerized aromatic and aliphatic nylon/clay nanocomposites were measured and compared with the neat nylons. The linear viscoelastic properties of nanocomposites are strongly correlated with the dispersion state of the nanoclays, either intercalated or exfoliated [31]. In addition, linear viscoelastic measurements are known to well represent the network structure created by nanoparticles and consequently describe the meso-scale dispersion level of the nanoclays in the polymer matrix. The linear viscoelastic zones were fulfilled at 10 % strain for the neat resins and 1 % strain for the nanocomposites.

Thermal Stability (Time Sweep experiments)

Thermal stability of the samples was explored via dynamic time sweep test. The storage modulus (G') of PA6 and MXD6 as well as their nanocomposites as a function of time are shown in Figures 5.1 (a) and (b), respectively.

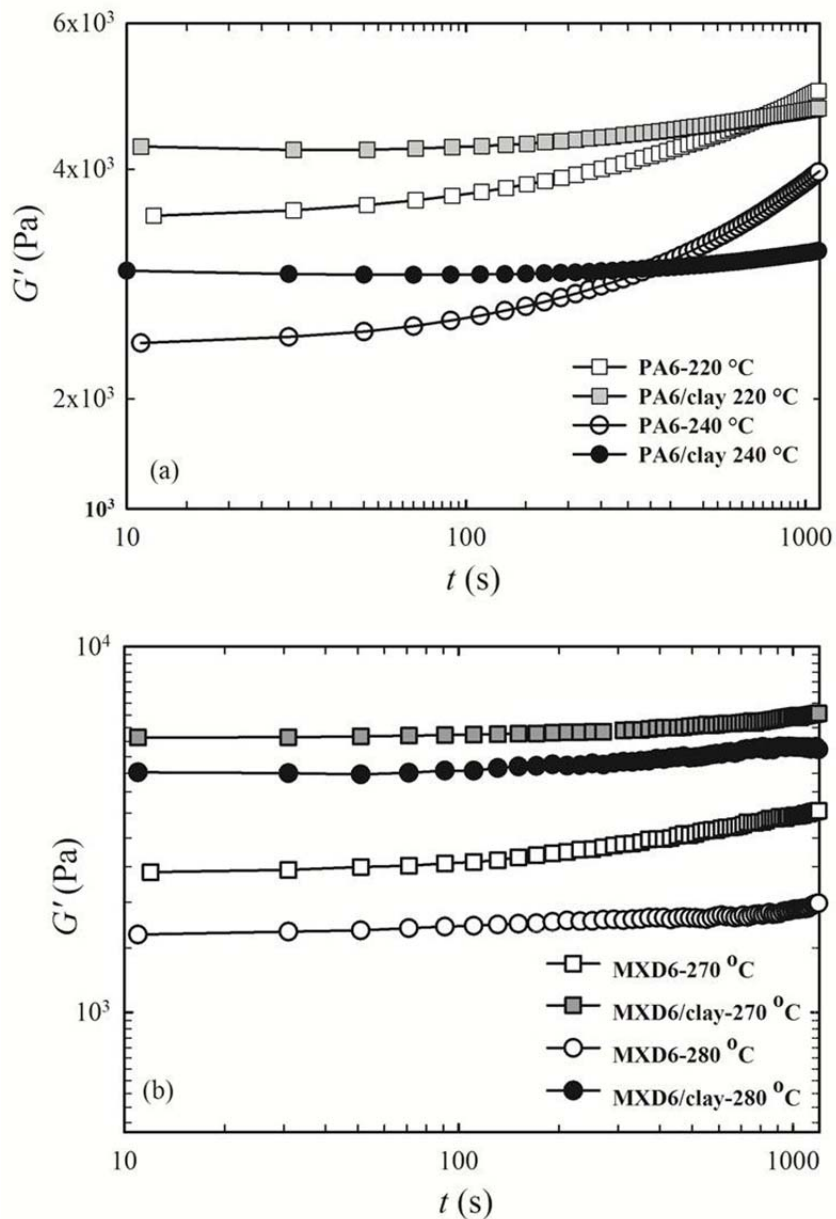


Figure 5-1 Storage modulus (G') vs. time for (a) PA6 and PA6/clay at 220 and 240 °C and (b) MXD6 and MXD6/clay at 270 and 280 °C; $\omega = 6.28$ rad/s.

After 20 min, the storage modulus increased by 63% and 16% at 220 ° C for PA6 and PA6/clay, respectively, and enhanced by 48% and 16% at 270 ° C for MXD6 and MXD6/clay, respectively, suggesting possible interchange reaction occurring in both neat and nanoclay composite nylons. The possibilities of interchange reactions for polyamides have been reported by other researchers as well [23, 24, 32]. In addition to the interchange reactions, because of the presence of carboxylic and amine functional end groups, it is expected that some polycondensation reactions occur between polyamide chains, resulting in the formation of longer chains. However, for nylon nanocomposites, it is noted that the rate of increase of storage modulus (G') with time is lower than the pure ones. In nylon/clay nanocomposites, in addition to the interchange and polycondensation reactions, due to the strong interaction between the silicate platelets and nylon chains as well as the clay particle-particle interactions, a secondary network structure can be also created by clay platelets. It has been reported that the network structure created in nylon/clay nanocomposite is mostly due to the ionic bond strength between the OH- of silicate layers and terminal ammonium ion, $-NH_3^+$, of nylon [33]. The network structure created by the silicate platelets may yield a particular spatial inhibition between the nylon chains, which reduces the amount of interchange reactions in comparison with the neat polymers. These can explain the lower increase rate of the storage modulus (G') with time for both PA6/clay and MXD6/clay compared to the neat polymers.

Dynamic Frequency Sweep

The complex shear viscosities (η^*) as a function of frequency at different temperatures for the aliphatic and aromatic nylons are plotted in Figures 5.2 (a) and (b), respectively. The higher complex viscosity of the nanocomposite compared to the neat matrix in the low frequency region suggests strong interactions between the polymer and clay. Such interactions in nanocomposites

hinder the motion of polymer chains and cause the increase in viscosity. Unlike the neat resins that show the Newtonian plateau at low frequencies, the nanocomposites display a pronounced shear thinning behavior.

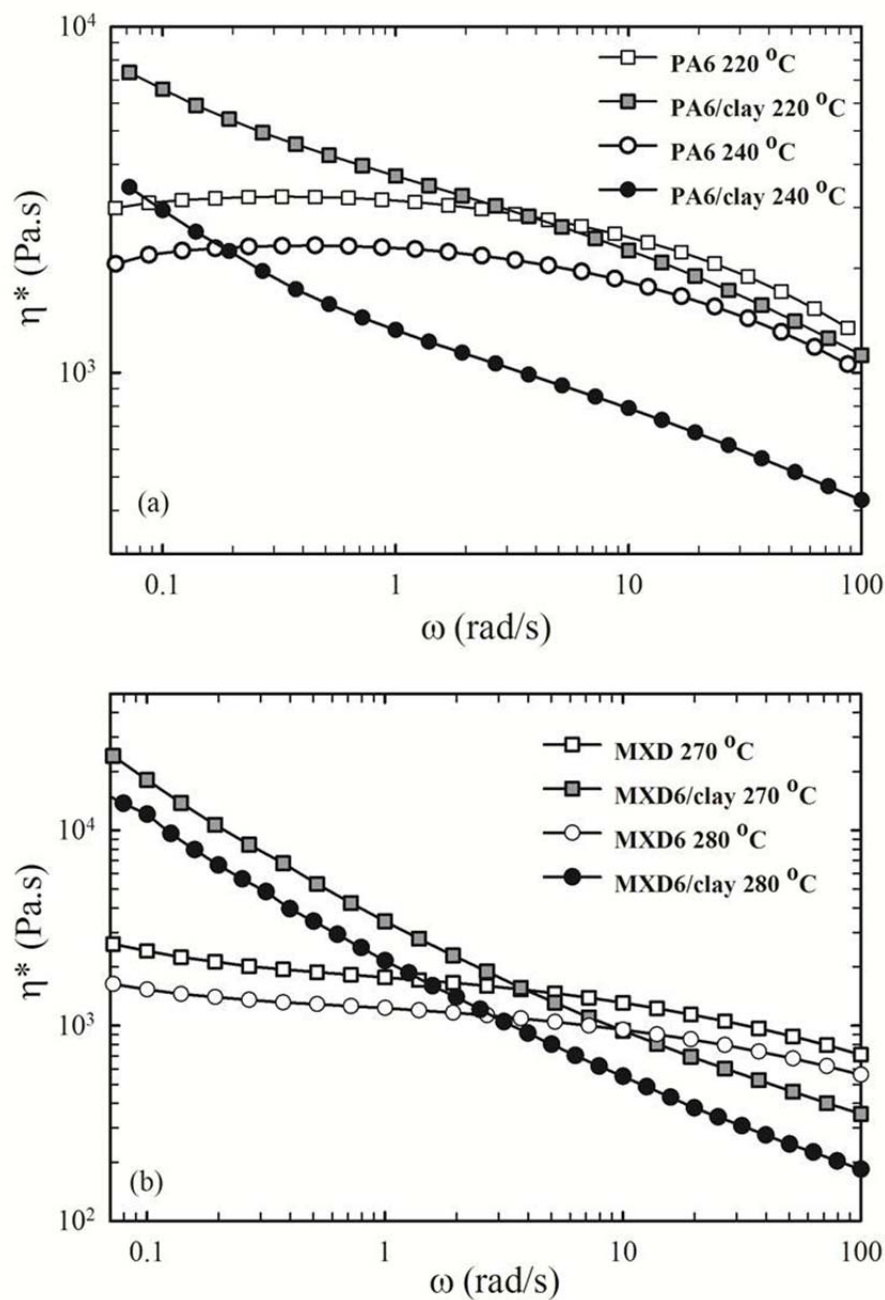


Figure 5-2 Complex viscosity (η^*) vs. frequency for (a) PA6 and PA6/clay at 220 and 240 °C and (b) MXD6 and MXD6/clay at 270 and 280 °C.

This behavior could be related to strong particle-matrix or particle-particle interactions that dominate at low frequencies and create a secondary network structure, which breaks down at higher frequencies. Ren et al. [34] also reported a similar frequency dependency of the complex viscosity for neat PA6 and PA6/clay, in which complex viscosity behavior of neat PA6 markedly differed from that of the nanocomposite system. Similar solid like behavior was also observed for other polymer nanocomposites as well [7, 35-37]. Comparing Figures 5.2 (a) and (b), it is clear that shear thinning behavior of MXD6/clay nanocomposite is more prominent and occurs at lower frequencies compared to PA6/clay, probably due to stronger polymer-particle interactions in the former and a different extent of exfoliation.

The obtained results indicated that incorporation of clay caused a significant increase in complex viscosity of the MXD6 nanocomposites at low frequencies. While presence of clay brought about a reduction in viscosity of the PA6, which was more obvious at higher temperatures and frequencies, and was reported by other authors [38]. It was claimed that slip between the PA6 matrix and the exfoliated organoclay platelets caused the reduction of melt viscosity in the PA6 nanocomposites. Another possibility is that the silicate clay somehow caused matrix degradation in PA6 at that processing temperature in the presence of clay [39, 40], while in MXD6 nanocomposite, a network structure formed due to strong interaction between clay platelets and polymer caused the increase in complex viscosity [16].

The storage and loss moduli as a function of frequency at different temperatures for the PA6 and MXD6 as well as for the nanoclay composites are presented in Figure 5.3.

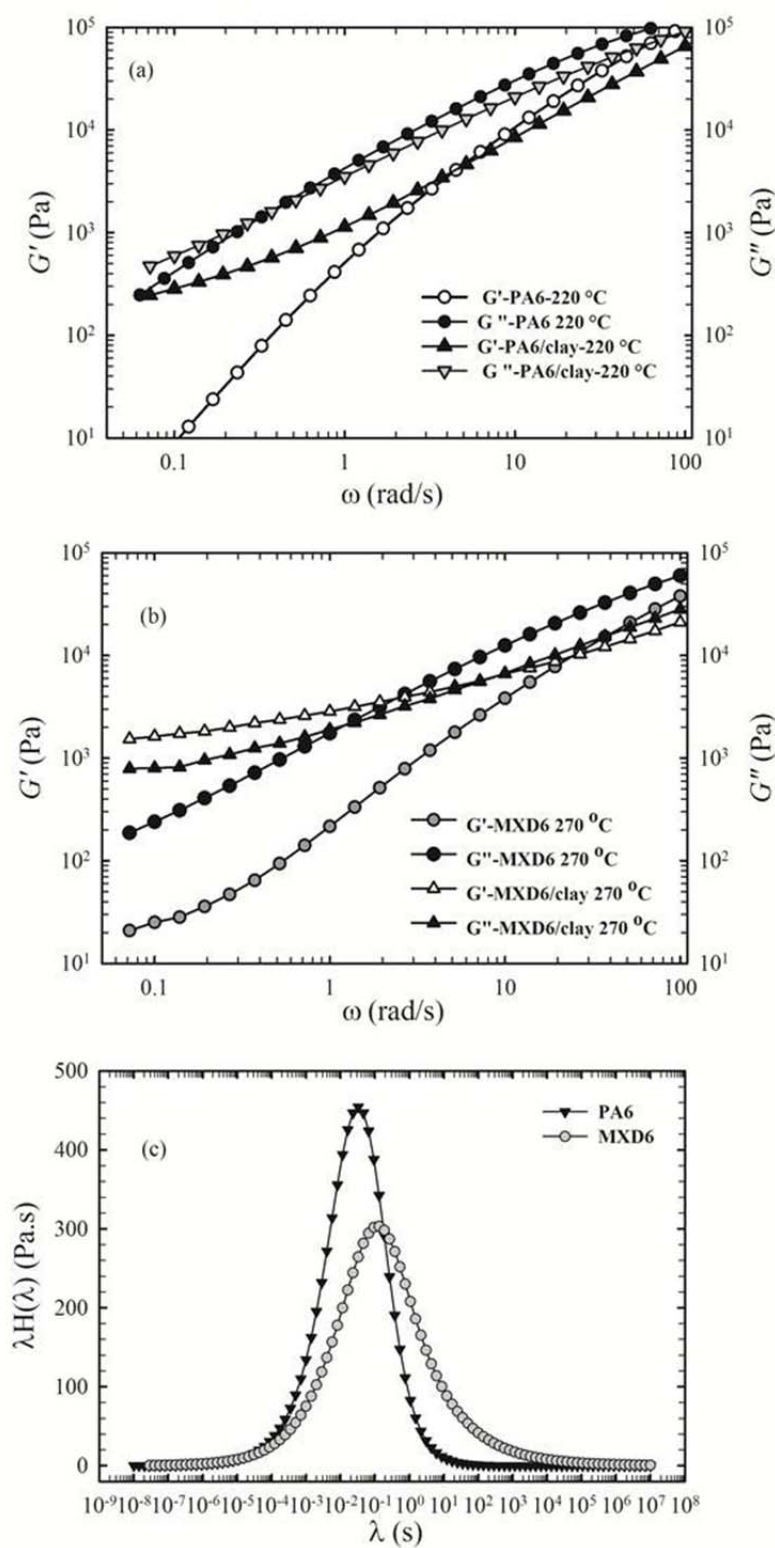


Figure 5-3 Storage modulus (G') and Loss modulus (G'') vs. frequency for (a) PA6 and PA6/clay at 220 °C and (b) MXD6 and MXD6/clay at 270 °C. (c) Weighted relaxation spectra for the neat PA6 and neat MXD6 obtained from dynamic frequency data.

The high storage modulus in the low frequencies for the PA6/clay and MXD6/clay nanocomposites indicates high clay dispersion in the polymer matrix [41]. The frequency dependence of the storage and loss moduli at low frequencies, which corresponds to the liquid-like behavior of polymers, can be modeled using a single-relaxation-time model in the terminal zone such as the Maxwell fluid power law model where $G' \sim \omega^2$ and $G'' \sim \omega^1$ [33]. The power-law frequency dependence of G' and G'' in the terminal zone for the PA6, PA6/clay, MXD6 and MXD6/clay are listed in Table 5.2.

Table 5.2 Power-law frequency dependency of G' and G'' in the terminal zone.

Sample	G'	G''
PA6-220 °C	1.80	1.00
PA6/clay-220 °C	1.11	0.84
PA6-240 °C	1.41	0.89
PA6/clay-240 °C	0.75	0.74
MXD6-270 °C	1.20	0.82
MXD6/clay- 270 °C	0.36	0.52
MXD6-280 °C	1.06	0.85
MXD6/clay-280 °C	0.34	0.49

For the aliphatic nylon, at low frequencies and 240 °C, the power law indexes for the storage and loss moduli are smaller than 2 and 1, respectively. In addition, the terminal zone for G' is not observed for the PA6 nor PA6/clay. These data are in a good agreement with the results obtained by Ayer et al. and other researchers for PA6 nanoclay composites [28]. This behavior was interpreted as due to the presence of fluctuating particulate network [42]. The non-terminal behavior of G' and G'' for polymer clay nanocomposites has also been investigated by Krishnamoort et al. [31, 33, 43]. For PA6/montmorillonite nanocomposites, they suggested that strong interaction between the polymer matrix and clay particles forms a percolated filler network structure that leads to a significant increase in the relaxation time, which causes a shift

in the terminal relaxation to very low frequencies. They speculated that uncompleted relaxation of polymer chains contributed to the solid-like response at low frequencies. In other words, solid-like character in polymer/clay nanocomposites is a result of the percolated structure of layered silicates network. For the aromatic nylon, at low frequencies and 270 °C, it is clear that more deviation from the Maxwell behavior is observed. Non-terminal low-frequency rheological behavior was also reported for EVOH/Cloisite nanocomposite [44], polypropylene nanoclay composite [37], and carbon black-filled elastomers [45]. The plateau observed for G' at the low frequency region for the MXD6/clay is an indication of its solid-like behavior at low deformation rate due to the strong interaction of the well dispersed clay platelets in the MXD6 matrix.

The weighted relaxation spectra evaluated from dynamic moduli (G' , G'' , ω) using the NLREG (nonlinear regularization) software are plotted in Figure 5.3 (c). The area under the curve is equal to the zero shear viscosity (η_0) [28]. The intermolecular entanglement and interaction have the main effect on the relaxation behavior of the resins. The longer relaxation time for MXD6 ($\lambda=0.132$ s) compared to PA6 ($\lambda=0.033$ s) is attributed to the higher molecular weight as well as higher intermolecular interactions of the former. Due to a pronounced shear thinning behavior of nanocomposites (see Figure 5.2), it was impossible to calculate spectra of PA6/clay and MXD6/clay. These data will be used to discuss the crystallization behavior of the films.

5.4.2 Dispersion state by XRD and TEM

X-ray diffraction profiles at low diffraction angles are depicted in Figure 5.4. No characteristic basal reflection is observed for nanoclay composites, indicating that nanoparticles are completely exfoliated due to the interactions between the polar polymer chains and nanoclays [42]. The strong shear thinning behavior of complex viscosity at low frequencies as well as the

frequency dependence of the storage and loss moduli (see Figures 5.2 and 5.3), are related to the solid like behavior and exfoliation state of nylon nanocomposite.

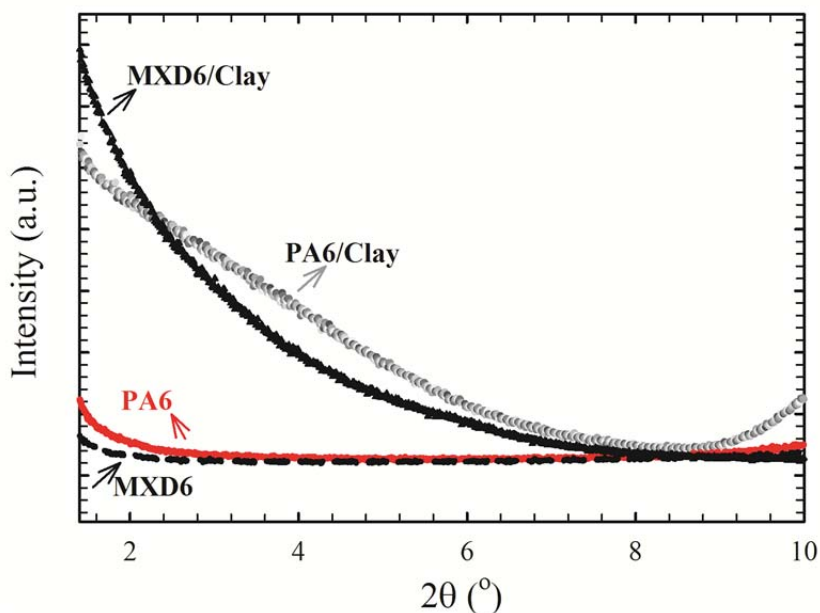


Figure 5-4 X-ray diffraction patterns for neat nylons and nanocomposites.

TEM micrographs for the PA6/clay and MXD6/clay nanocomposite films are shown in Figure 5.4. A high level of clay dispersion and exfoliation for both aromatic and aliphatic nylon matrices is observed, confirming the XRD results. The low magnification images of Figures 5.5 (a) and 5.5 (d) reveal that clay particles are uniformly dispersed in the PA6 and MXD6, respectively. The higher magnification images (Figures 5.5 (c) and 5.5 (f)) show that the nanoclay particles are well exfoliated in the PA6 and MXD6, respectively. They also show that the individual layers are perfectly aligned in the flow direction. Since the interfacial area between the polymer matrix and nanoclay is high, a large interaction between polymer matrix and silicate platelets could be expected. The significant increase in the complex viscosity of nanocomposite at low frequencies is related to the network structure forms due to uniform distribution of clay platelets.

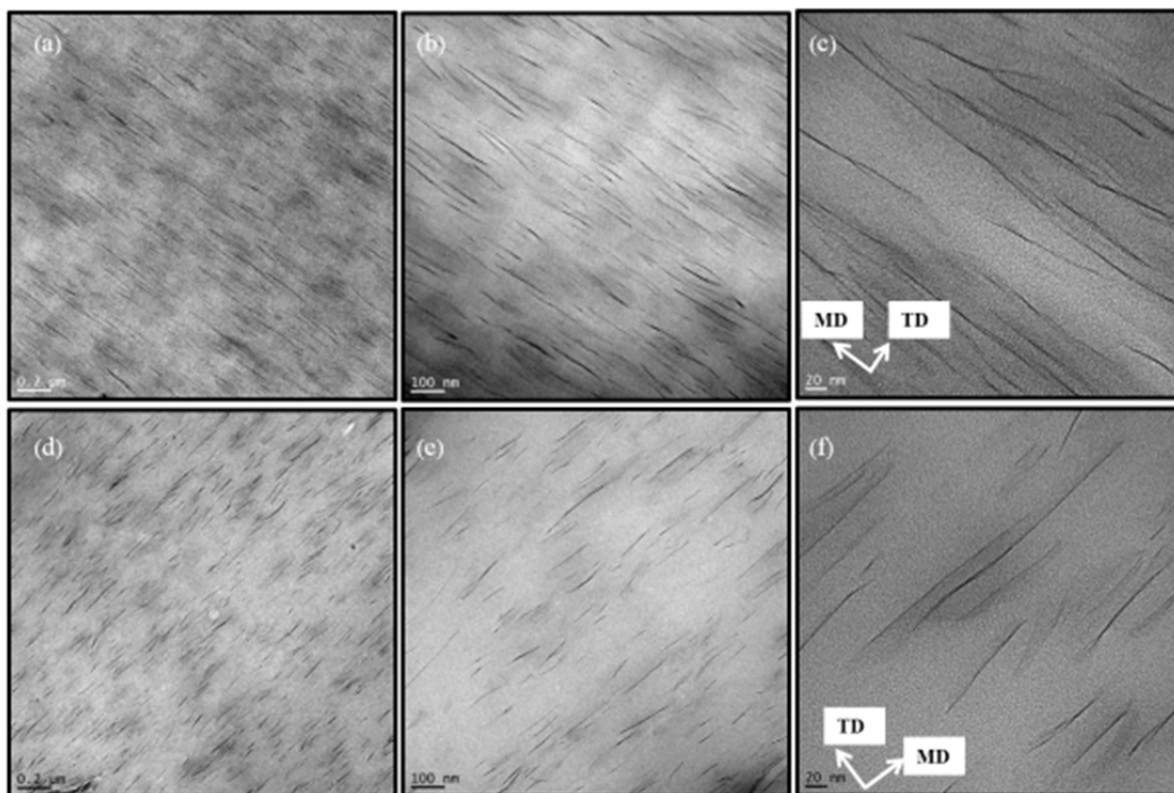


Figure 5-5 TEM micrographs for (a, b, c) PA6/clay nanocomposite films and (d, e, f) MXD6/clay nanocomposite films.

5.4.3 Crystal structure

From literature [30], PA6 could have two major crystalline phases: α and γ . The α phase has monoclinic unit cells with the dimensions of $a=0.956$, $b=1.724$, $c=0.801$ nm and $\beta=67.5^\circ$, where the hydrogen bonds are formed between the anti-parallel chains. The γ phase has a pseudo hexagonal structure with the dimensions of $a=0.472$, $c=1.688$ nm and $\gamma=120^\circ$, where the twisted chains allow formation of the hydrogen bonds between parallel chains [30, 46]. It has been shown that PA6 crystalline structure depends strongly on processing conditions [44, 47-49]. In general, lower temperature and faster cooling rate promote γ crystal of PA6 while higher crystallization temperature and slow cooling rate create more α crystal. For MXD6, only one

triclinic crystalline phase with the dimensions of $a=1.201$ nm, $b=0.483$ nm, $c=2.98$ nm, $\alpha=75^\circ$, $\beta=26^\circ$ and $\gamma=65^\circ$ is usually formed [50].

The crystalline structure and crystallinity of neat PA6, MXD6 and their nanocomposites were investigated by wide angle X-ray diffraction (WAXD) and differential scanning calorimetry (DSC). Figure 5.6 shows the diffraction intensity profiles for compressed molded samples prepared with a hot press as well as for film samples made by cast extrusion.

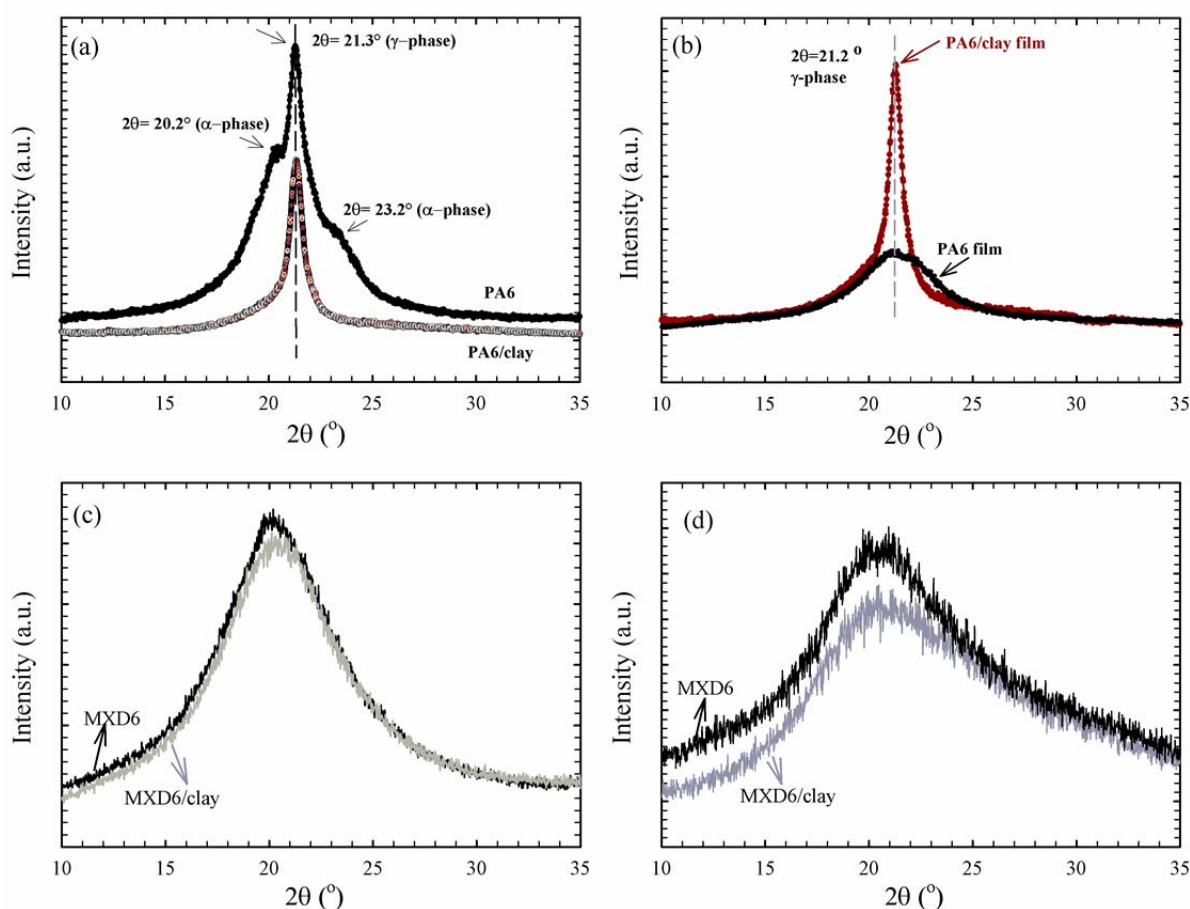


Figure 5-6 XRD patterns for (a) compressed molded neat PA6 and PA6/clay nanocomposites, (b) neat PA6 and PA6/clay nanocomposite films, (c) compressed molded neat MXD6 and MXD6/clay nanocomposites and (d) neat MXD6 and MXD6/clay nanocomposite films.

In Figure 5.6 (a), coexisting α and γ phases are seen for the compression molded PA6 whereas only γ phase can be detected for PA6/clay. The major diffraction peak at $2\theta=21.3^\circ$ corresponds to

the γ crystalline structure [30] and the two small diffraction peaks at $2\theta=20.2^\circ$ and 23.2° are related to the α crystalline phase of PA6 [51]. Our results are in good agreement with the findings of other researchers who showed that γ phase is dominant for PA6/clay composite films [7, 30, 48, 51, 52]. The crystalline structure of the PA6 films produced by cast extrusion process reveals the existence of only γ crystalline phase, as demonstrated in Figure 5.6 (b). This confirms that processing conditions could significantly impact PA6 crystalline structure. In addition, introduction of clay into PA6 drastically increased the formation of γ phase crystals in both molded and cast film samples.

For compressed molded MXD6, the X-ray patterns for the neat and nanoclay composite samples are almost the same, as depicted in Figure 5.6 (c). The MXD6 films shows a much wider diffraction peak compared to PA6 and also the diffraction profiles for the neat MXD6 and its nanocomposite films are almost the same (Fig. 5.6 (d)). A wide diffraction peak between $2\theta=15$ to 25° with maximum intensity at 20.7° is related to the amorphous phase and indicates low crystallinity for MXD6 and MXD6/clay.

Figure 5.7 shows the heating and cooling DSC thermograms for neat and nanocomposite films.

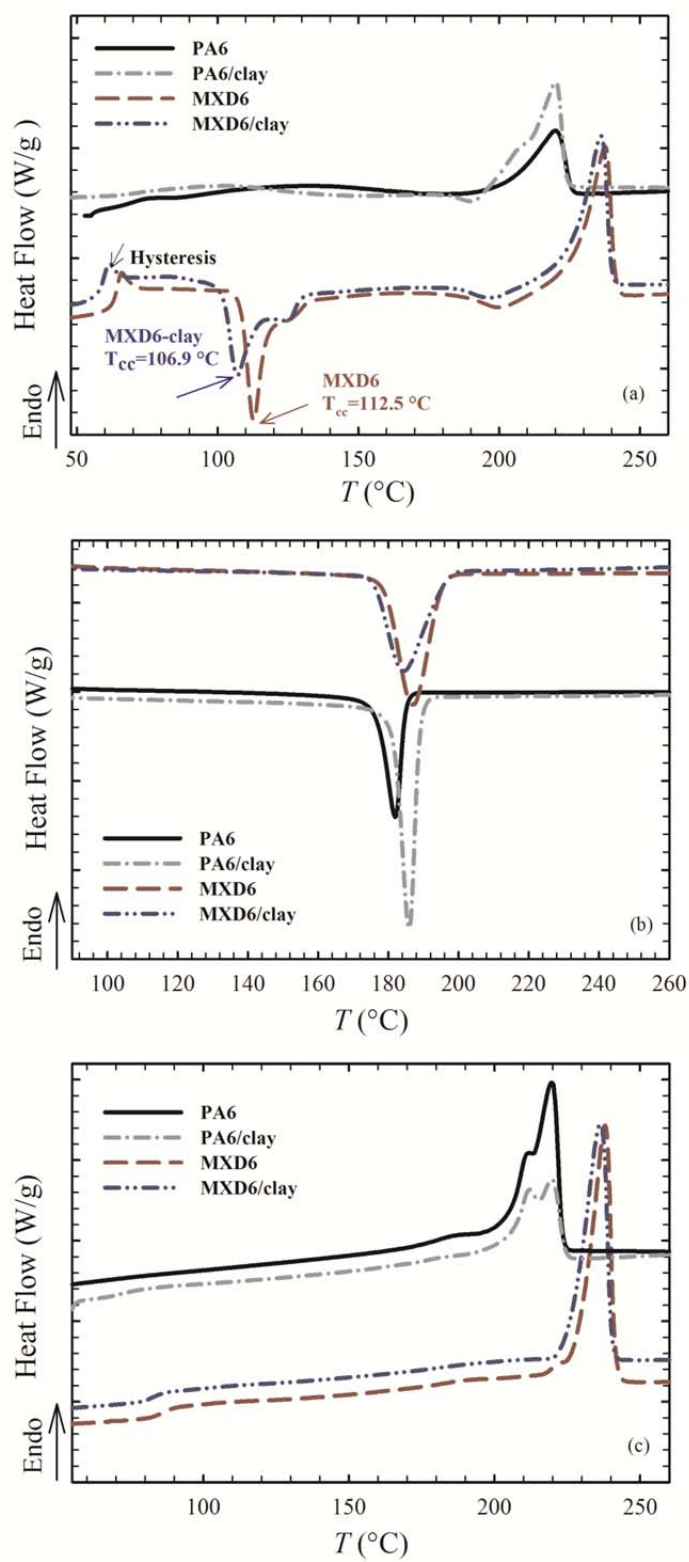


Figure 5-7 DSC thermograms for PA6, PA6/clay, MXD6 and MXD6/clay films; (a) first heating ramp, (b) cooling (crystallization) ramp and (c) second heating ramp.

In Figure 5.7 (a), the endothermic peak at 220 °C in the first heating ramp of the PA6 is due to the melting of the α -form crystals. A sharp peak at 220 °C and a small shoulder at 212 °C are seen in the first heating cycle of PA6/clay film which are associated with the melting of thermally stable α and less stable γ crystalline phases, respectively. Magniez et al. [53] suggested that the clay nanoparticles act as heterogeneous nucleating sites, which can create a different crystalline phase than the polymer matrix. The DSC results show coexisting α and γ crystals in PA6/clay nanocomposite whereas the XRD results revealed the presence of only γ phase. This can be explained by formation of the γ crystalline phase during film processing and conversion of the γ -form into the α -form during the DSC heating scan [54]. On the other hand, since the γ crystalline form of PA6 is thermodynamically unstable, it is completely converted to α crystalline form prior to final melting in the DSC heating scan. Addition of clay in PA6 facilitates the production of aligned arrays of H-bonded sections that act as stable γ nuclei, capable of remaining intact in the melt state for longer periods of time. Presence of clay also affects thermal memory and stress histories that remain present in the sample after processing and consequently caused dissimilarity in DSC heating scan of PA6/clay compared to PA6.

In Figure 5.7 (a), it should be pointed out that a small exothermic peak at 190 °C appears in the first heating scan of PA6/clay film, which is attributed to the slight cold crystallization of the oriented films. Cold crystallization exothermic peaks in the first heating scans of MXD6 and MXD6/clay are observed in the range of 104-134 °C and 97-131 °C, respectively (Figure 5.7 (a)), which are in agreement with the results obtained by Seif et al [55]. During film processing, orientation of MXD6 chains takes place such that they can act as nucleating sites for further crystallization by increasing temperature. Additionally, the MXD6 films exhibit an extra hysteresis peak at about 61 °C probably due to physical relaxation, such as residual orientation

relaxation, as also reported elsewhere [56]. A small peak with an exothermic heat of 13.8 J/g at 200 °C, just below the endothermic peak, in the first heating cycle of the MXD6 film is attributed to the crystalline reorganization of the polymer matrix [29]. The cooling cycle presented in Figure 5.7 (b) was used to calculate the crystallinity of each sample after erasing thermal history, while the first DSC cycle was used to obtain the amount of crystallinity present in the film. The second heating thermograms for the neat PA6 and PA6/clay clearly show coexistence of α and γ -phase crystals (see Figure 5.7 (c)). No exothermic peak in the reheating curves can be observed (see Figure 5.7 (c)).

The crystallization temperature (T_c), melting point (T_m), cold crystallization temperature (T_{cc}), glass transition temperature (T_g), resin crystallinity ($X_{c, resin}$), and film crystallinity ($X_{c, film}$) are listed in Table 5.3.

Table 5.3 Thermal properties of PA6, MXD6, and PA6/clay and MXD6/clay resins and films.

	T_c (°C)	T_m (°C)	T_{cc} (°C)	T_g (°C)	$X_{c, resin}$ (%)	$X_{c, film}$ (%)
PA6	180.0	212.0, 220.0	-	50	25 ± 1	24 ± 0.5
PA6/clay	186.6	210.6, 220.0	-	50	40 ± 1	37 ± 1
MXD6	187.7	237.0	112.5	83	31 ± 1	4 ± 1
MXD6/clay	184.0	236.0	106.9	85	33 ± 1	9 ± 1

In general, crystallinity of polyamide based nanocomposite is controlled by the type of polyamide matrix, molecular weight, clay concentration, and the level of clay exfoliation. From Table 5.3, crystallinity of the PA6/clay and MXD6/clay are much higher than their neat

polymers. In addition, crystallinity of neat and nanocomposite MXD6 films is quite low, which is in agreement with the XRD results of Figure 5.6 (c). However, the crystallinity of MXD6 resins obtained from the second heating cycle is drastically higher than the MXD6 films, indicating that processing conditions, particularly cooling rate, have a significant effect on the level of crystallinity, which will be discussed in more details later.

To study the effect of annealing on crystallinity, PA6 and MXD6 as well as their nanocomposites were annealed at 150 °C for 30 min. The XRD patterns for the annealed films are demonstrated in Figure 5.8.

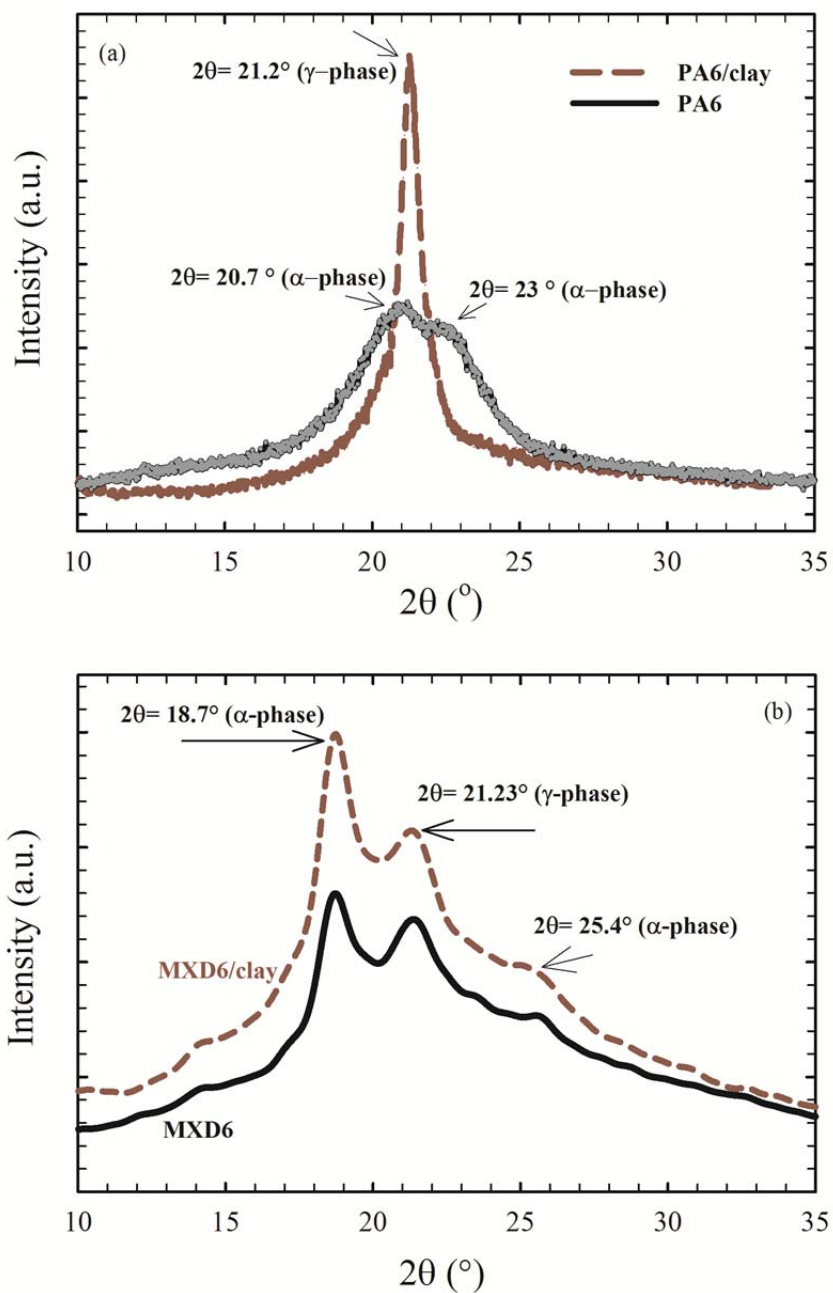


Figure 5-8 XRD patterns for (a) annealed neat PA6 and PA6/clay nanocomposite films and (b) annealed neat MXD6 and MXD6/clay nanocomposite films; annealing at 150 $^{\circ}\text{C}$ for 30 min.

It is obvious that, in contrast to the results shown in Figure 5.6 (b), PA6 and PA6/clay films do not exhibit a similar polymorphic behavior when they are annealed at high temperature. The γ

phase is the dominant crystalline phase for annealed PA6/clay films whereas the fraction of γ phase significantly decreases and more stable α phase becomes the predominant crystal structure for annealed PA6 films, which are in agreement with previous works [57, 58]. The reason that γ phase becomes dominant for annealed PA6/clay films is probably because of the presence of layered silicate, which induces the heterophase nucleation of γ phase [59].

Three major diffraction peaks are observed in the XRD patterns of the MXD6 and MXD6/clay films annealed at 150 °C as depicted in Figure 5.8 (b). A sharp peak at 18.7° and a small peak at 25.4° are representative of α -phase and the sharp peak at 21.23° is indicative of γ -phase. Formation of both γ and α crystals in MXD6 as a result of hydrogen bonds between the fully extended chains was also reported elsewhere [50]. This indicates that the crystallization behavior of MXD6 is strongly affected by the thermal history, annealing and crystallization temperature [29].

Figure 5.9 (a) shows the first DSC heating thermograms for the samples before and after annealing at 150 °C for 30 min.

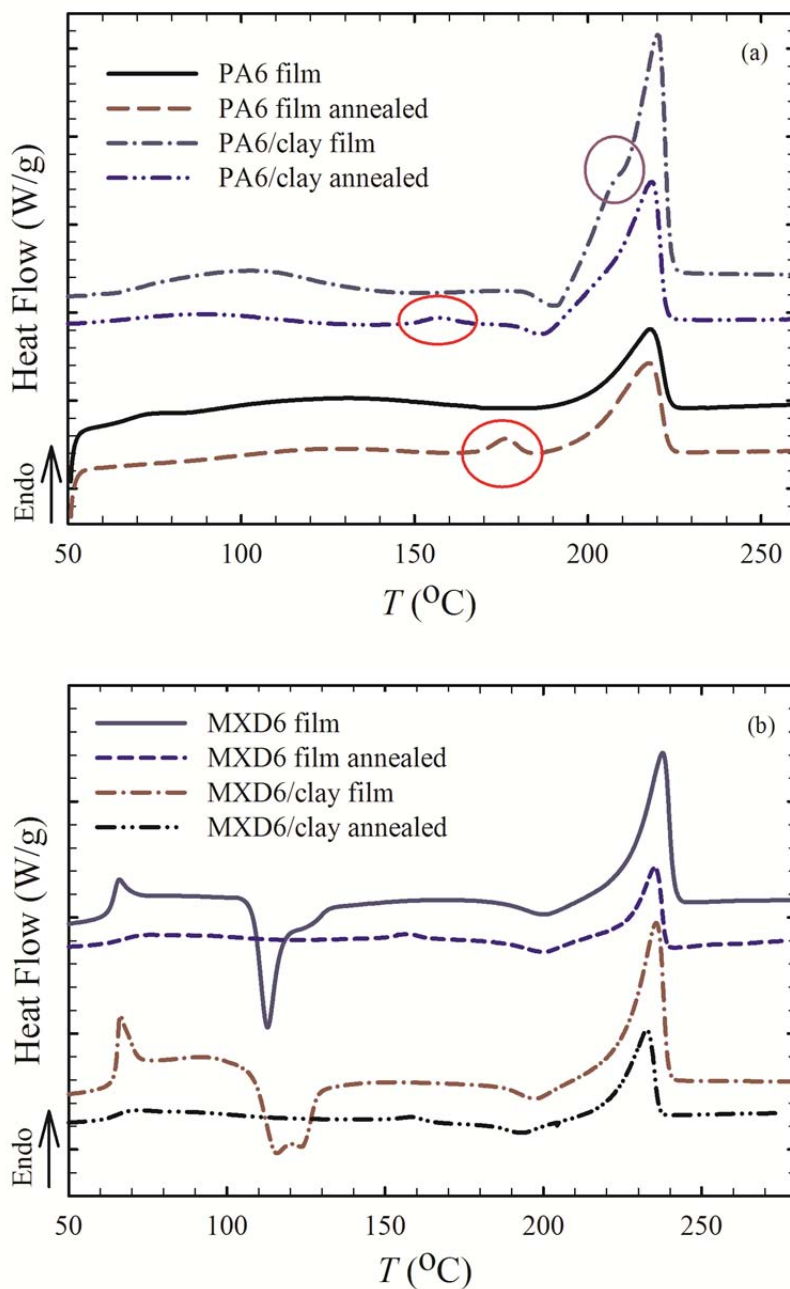


Figure 5-9 First DSC heating thermograms for (a) PA6 and PA6/clay films and (b) MXD6 and MXD6/clay films before and after annealing at 150 $^{\circ}\text{C}$ for 30 min.

For annealed PA6 and PA6/clay films, in addition to the presence of sharp endothermic peaks at 220 $^{\circ}\text{C}$, which are due to the melting of α -form crystals, other small endothermic peaks are also detected at 175 $^{\circ}\text{C}$ and 160 $^{\circ}\text{C}$, respectively. These additional peaks can be attributed to the

formation of small crystals during annealing [49]. They were also related by some authors [57] to an enthalpy relaxation process of the interphase between the crystalline and amorphous phases, which can be induced by isothermal crystallization or annealing process. A remarkable feature in Figure 5.9 (a) is the appearance of a somewhat broad and less pronounced endothermic shoulder around 212 °C for non-annealed PA6/clay film, which is associated with the melting of γ -form crystals. After annealing, this shoulder completely disappears due to the conversion of γ -crystal phase to the more thermodynamically stable α -crystal phase. DSC thermograms for the neat MXD6 and MXD6/clay films, before and after annealing at 150 °C for 30 min, are shown in Figure 5.9 (b). It is clear that the cold crystallization behavior observed for non-annealed MXD6 and MXD6/clay films disappear after annealing. For non-annealed MXD6 films, the partially oriented polymer chains act as nucleating sites for further crystallization at high temperature. For annealed MXD6 films, all crystals are formed during annealing; hence no extra crystals can be formed during the heating ramp in DSC. In Figure 5.9 (b), it is also obvious that the small endothermic hysteresis peak for the non-annealed MXD6 films observed at low temperature of 61 °C disappears after annealing.

5.4.4 Non-Isothermal crystallization

Since during the solidification stage in film casting, non-isothermal crystallization takes place, therefore, it is important to evaluate the non-isothermal crystallization rate of the samples at different cooling rates. The relative crystallinity, $X_R(t)$, as a function of time, t , can be expressed as [53]:

$$X(t) = \frac{X_c(t)}{X_c(t_\infty)} = \frac{\int_{t_0}^t \left(\frac{dH}{dt}\right) dt}{\int_{t_0}^{t_\infty} \left(\frac{dH}{dt}\right) dt} = \frac{\Delta H_t}{\Delta H_\infty} \quad (5.3)$$

where t_o and t_∞ are the start and end time of crystallization, respectively, dH/dt is the rate of enthalpy, ΔH_t is the enthalpy at time t and ΔH_∞ is the total enthalpy at the end of crystallization. The relative crystallinity versus time at different cooling rates is presented in Figure 10. In addition, the enthalpy of fusion, ΔH , total crystallinity, X_{tot} , onset crystallization temperature, T_o , and half time of crystallization, $t_{1/2}$, are reported in Table 5.4.

Table 5.4 Enthalpy of fusion, ΔH , total crystallinity, X_{tot} , onset crystallization temperature, T_o , and half time of crystallization, $t_{1/2}$, for the PA6, PA6/clay, MXD6 and MXD6/clay.

Samples	Cooling rate (°C/min)	ΔH (J/g)	X_{tot} (%)	T_o (°C)	$t_{1/2}$ (sec)
PA6	5	48.8	25.7	187.0	88
	10	45.8	24.1	186.6	51
	50	41.2	21.7	175.5	17
PA6/clay	5	74.4	37.6	196.5	87
	10	68.7	34.7	193.0	49
	50	57.1	28.8	181.8	12
MXD6	5	59.0	33.7	205.0	144
	10	54.7	31.2	200.0	101
	50	48.5	27.7	184.8	43
MXD6/clay	5	57.0	31.5	196.7	132
	10	52.0	28.8	194.0	92
	50	47.0	26.1	179.0	39

At low cooling rates, it takes a longer time for the polymer chains to form crystallites and adjust themselves in the appropriate conformation. In Figure 5.10, a lower transition at the early stage of crystallization appears for low cooling rates, due to the slow rates of crystallization.

Also, it is obvious that the rate of crystallization for the MXD6 is much slower than the PA6. Non-Isothermal crystallization behavior of polymers at high cooling rates is more representative of the cast film process.

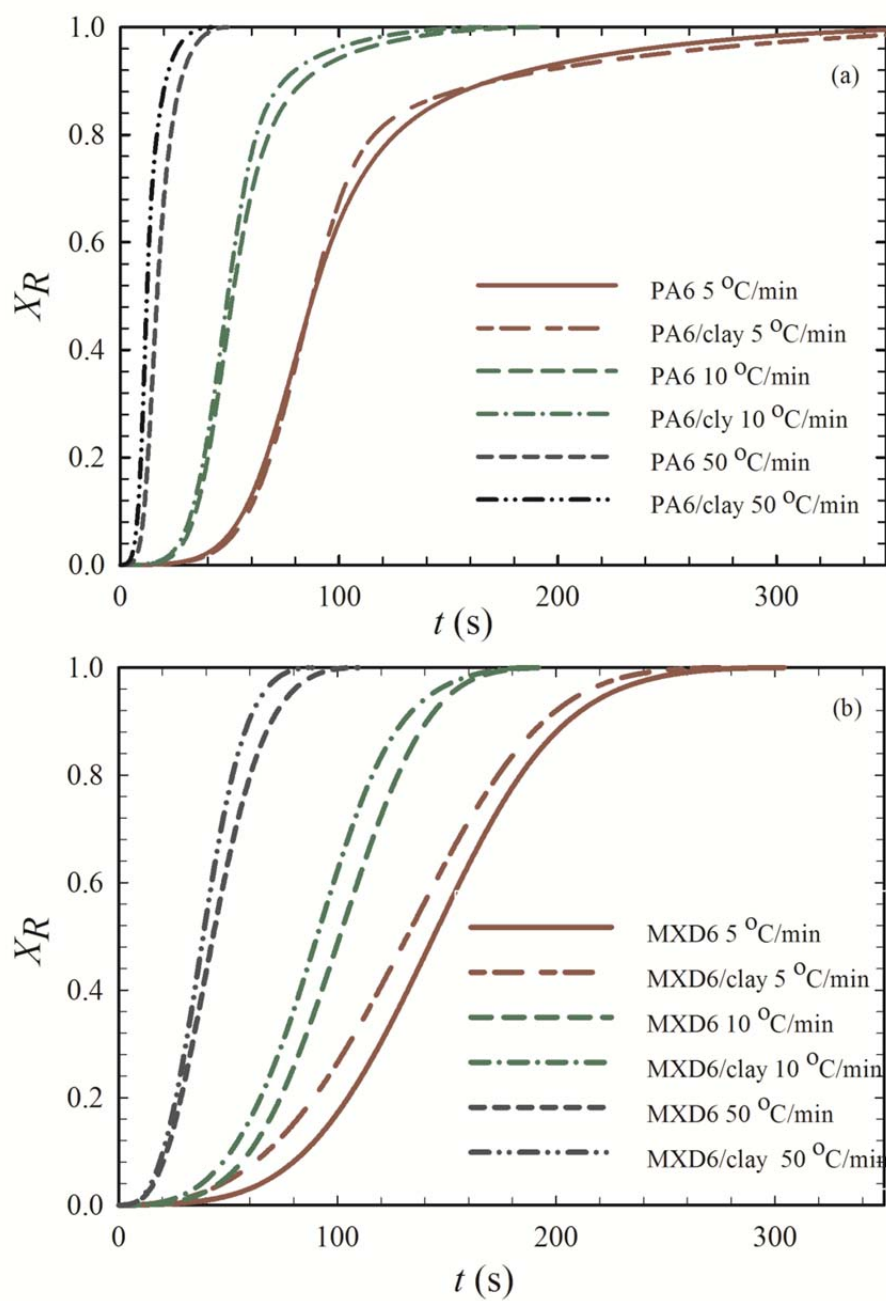


Figure 5-10 Relative crystallinity vs. time at different cooling times for (a) PA6 and PA6/clay and (b) MXD6 and MXD6/clay.

These results show that at high cooling rates (e.g. 50 °C/min) $t_{1/2}$ for PA6 and PA6/clay was 17 sec and 12.2 sec respectively, whereas $t_{1/2}$ for the MXD6 and MXD6/clay was 43 sec and 39 sec respectively. In addition, since clay layers act as nucleating sites, the rate of crystallization at a chosen cooling rate is higher for the PA6/clay and MXD6/clay compared to the PA6 and MXD6.

The data reported in Table 5.4 show that MXD6 has a low rate of crystallization. Additionally, as discussed in Figure 5.3, MXD6 has very long relaxation time compared to PA6. Since in the cast extrusion process, films are cooled rapidly, therefore, the processing time scale is much shorter than the crystallization characteristic time and, as a result, a low amount of crystals are formed for MXD6 and MXD6/clay films. These can explain the results reported in Table 5.3 as why the level of crystallinity was much lower for the MXD6 and MXD6/clay films compared to their resins.

5.4.5 Thermal degradation

Thermal degradation of polymers, particularly during film and thermoforming processes, is an important concern. In such processes, it is necessary that the polymer to be thermally stable at high processing temperatures in order to avoid any loss of original properties. The thermal stability of the nylon based resins was studied using thermo gravimetric analysis (TGA), as depicted in Figure 5.11.

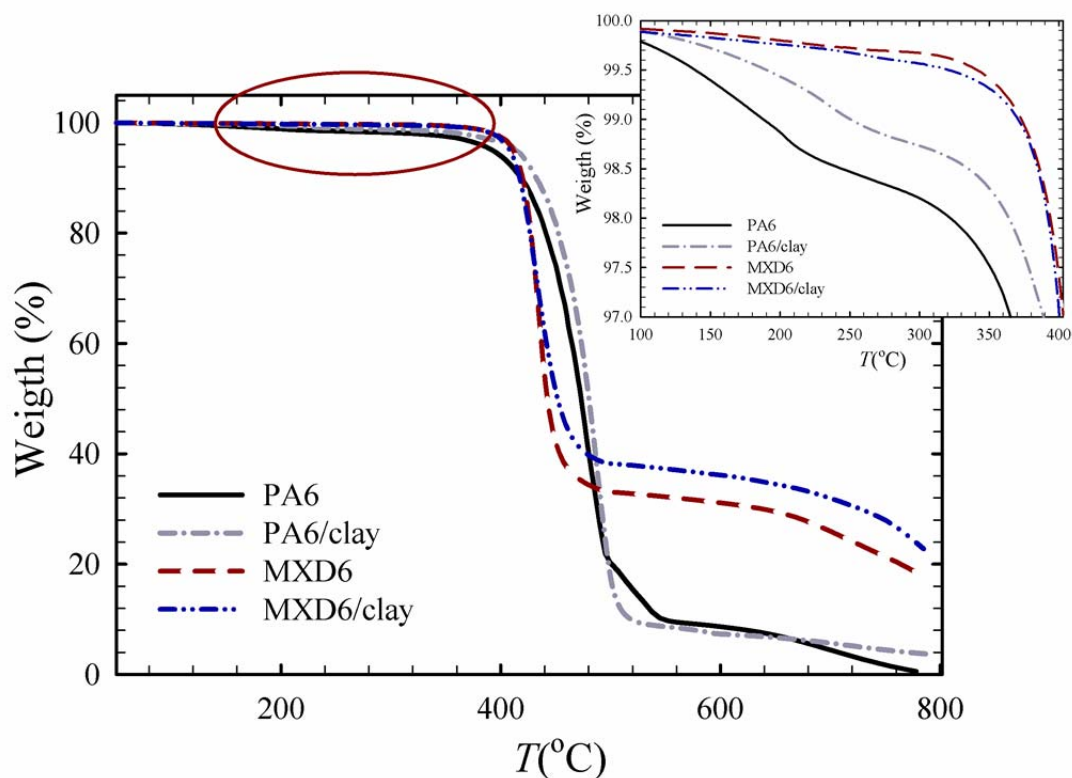


Figure 5-11 Thermal gravimetric curves for PA6, PA6/clay, MXD6, and MXD6/clay.

Below 400 °C, MXD6 is more stable compared to PA6. The temperatures corresponding to 0% (T_o , onset of decomposition temperature), 5% (T_5), 10% (T_{10}), 20% (T_{20}), and 50% (T_{50}) weight losses are listed in Table 5.5. The temperature for maximum weight loss, T_{max} , is the main criteria for thermal stability of resins and nanocomposites, which can be obtained from the derivative thermograms [60].

Table 5.5 Temperatures at different percentage of weight loss for PA6, MXD6, and nanocomposites.

	T_o (°C)	T_5 (°C)	T_{10} (°C)	T_{20} (°C)	T_{50} (°C)	T_{max} (°C)
PA6	331	399	420	441	473	470
PA6/clay	364	413	432	452	480	487
MXD6	340	411	420	428	442	436
MXD6/clay	320	408	417	427	452	432

The onset degradation temperature is about 30 °C higher for the PA6/clay nanocomposite with 4 wt% clay content than that for the neat PA6. This indicates that the PA6/clay nanocomposite has greater thermal stability than the pure PA6, which is in agreement with the previous observations obtained by Pramoda et al. [61]. However, the thermal stability of MXD6/clay nanocomposite is lower than pure MXD6. In fact, decomposition of MXD6/clay occurs at lower temperature than for neat MXD6, which confirms the findings of Zabaleta et al. [62] who reported that the weight loss onset temperature decreased by addition of modified organoclays (e.g. Cloisite 30B and Cloisite 20A) to an amorphous nylon. They concluded that the higher thermal stability of pure amorphous nylon in comparison with nylon nanocomposite is due to the degradation of the clay modifier at high temperatures. It was also mentioned that the catalytic activity of the montmorillonite organoclay could accelerate degradation of the neat nylon.

5.4.6 Oxygen permeability

As discussed earlier, the main demand for aromatic nylon comes from high barrier application. PA6 and PA6/clay nanocomposites have been vastly used in packaging applications due to their relatively low oxygen permeation. MXD6 has recently received more attention due to its much better barrier characteristics, less moisture sensitivity and higher glass transition and melting temperatures. The oxygen transmission rates (OTR) normalized by film thickness for the PA6 and MXD6 thin films as well as their nanocomposites before and after annealing at 150 °C for 30 min are shown in Figure 5.12.

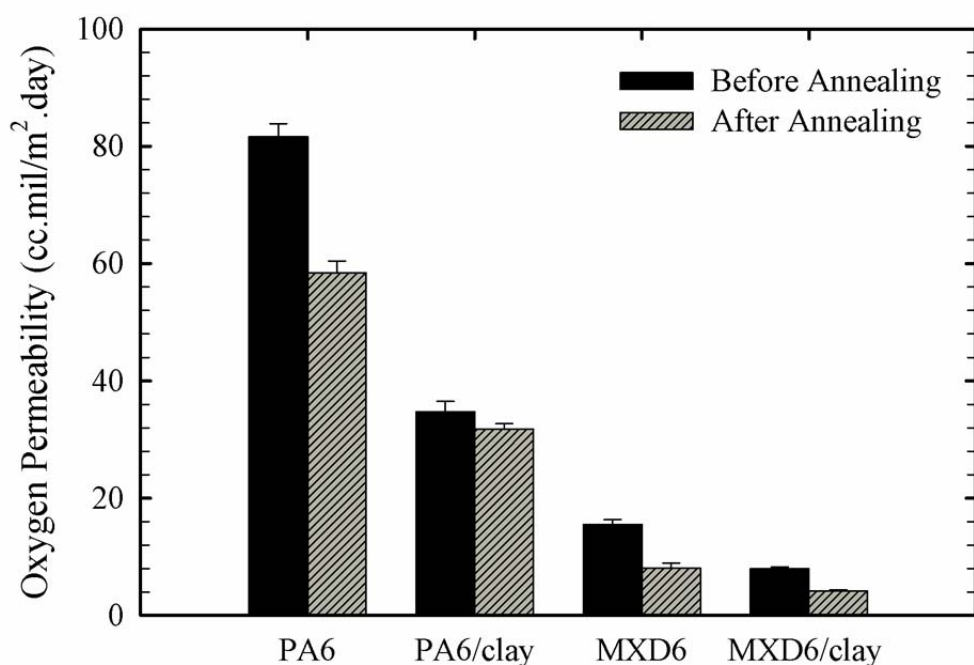


Figure 5-12 Oxygen permeation through neat PA6 and MXD6 as well as their nanocomposites films (30 μm) before and after annealing.

Adding 4 wt% clay into PA6 reduced its permeability to oxygen by about 40%. According to Picard et al. [63], the oxygen barrier property of a PA6/clay nanocomposite improved by about 45%. The barrier property of MXD6 film was more than five times better than that of PA6 film

processed under the same conditions. In addition, incorporating clay in MXD6 improved oxygen barrier by 46%, in a good agreement with the finding of Thellen et al. [64] who reported 42% reduction in the oxygen permeability of MXD6 nanocomposites. Annealing improved the oxygen barrier of PA6, PA6/clay, MXD6 and MXD6/clay by 28%, 10%, 42 % and 44.5 %, respectively. The level of crystallinity for the films before and after annealing is presented in Figure 5.13.

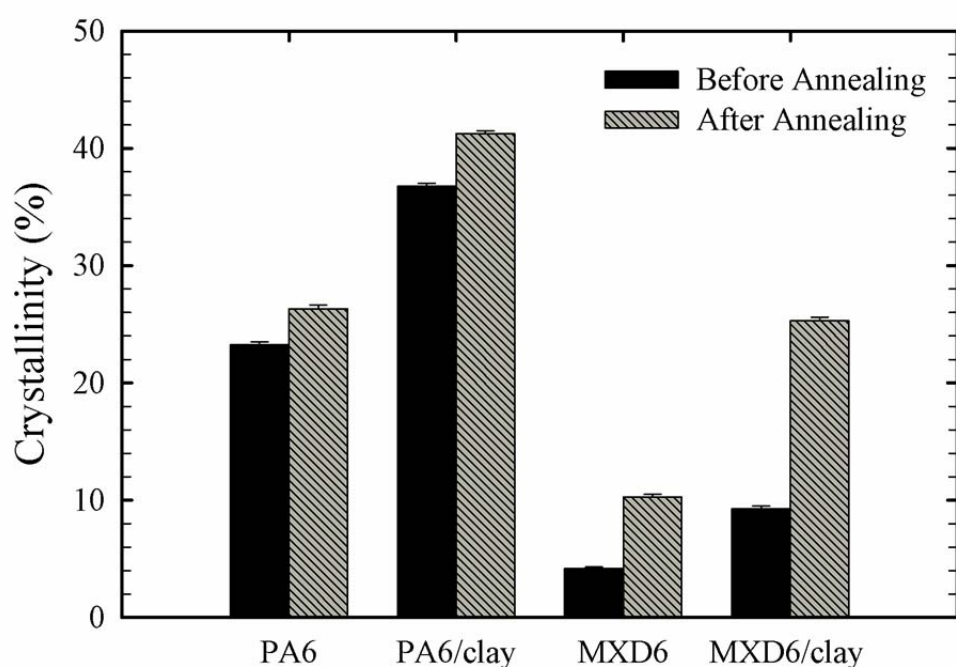


Figure 5-13 Crystallinity of neat PA6 and MXD6 as well as their nanocomposites films (30 μm) before and after annealing.

PA6 films show greater crystallinity than MXD6 and also the clay incorporation enhances films crystallinity. Additionally, annealing increases crystallinity, which is more pronounced for the MXD6 compared to the PA6. It should be mentioned that MXD6 films show better barrier property in spite of their low level of crystallinity (see Table 5.3). It is known that gas diffusion in polymers is strongly dependent on free volume, which is the volume that is not occupied by

polymer chains. In fact, in the diffusion process, a gas molecule should find its way through the free volume from hole to hole. Free space between polymer chains can be formed due to insufficient chain packing. The amount of free volume for polymers depends on crystallinity, crystalline orientation and more importantly on polymer chain interaction and, as consequence, chain packing. In literature [15, 65], the free volume of MXD6 was reported to be 13.6 % less than that of PA6. This indicates that, although PA6 has higher crystallinity than MXD6 (see Table 5.3), MXD6 chains are more packed than those of PA6 and as a consequence, MXD6 has much lower oxygen transmission rate. It was shown that small changes in free volume significantly affect the physical properties of a polymer, such as gas diffusion coefficient [66]. It has been also reported that adding clay in a polymer matrix would increase free volume [15, 65]. From these observations, it can be concluded that the diffusion coefficient in polymer nanocomposites depends on tortuosity, orientation and free volume. These parameters can be in competition. The increase or decrease of the diffusion coefficient in polymer nanocomposites by clay addition depends on which of these parameters becomes dominant. The aspect ratio of the clay in nanocomposite systems can be used as a factor representing tortuosity. TEM micrographs, which were shown and discussed in Figure 5.5, were used to estimate the average aspect ratio of the clay, ϕ , which is the ratio of the length (l) to the thickness (t) of clay particles as shown in Figure 5.14. Although the average clay aspect ratio for MXD6/clay is about 35 and for PA6/clay is 64 (based on the analysis of the results of ca. 500 calculated ratios), MXD6/clay showed significantly better barrier property, which is attributed to its lower free volume and more packed chains.

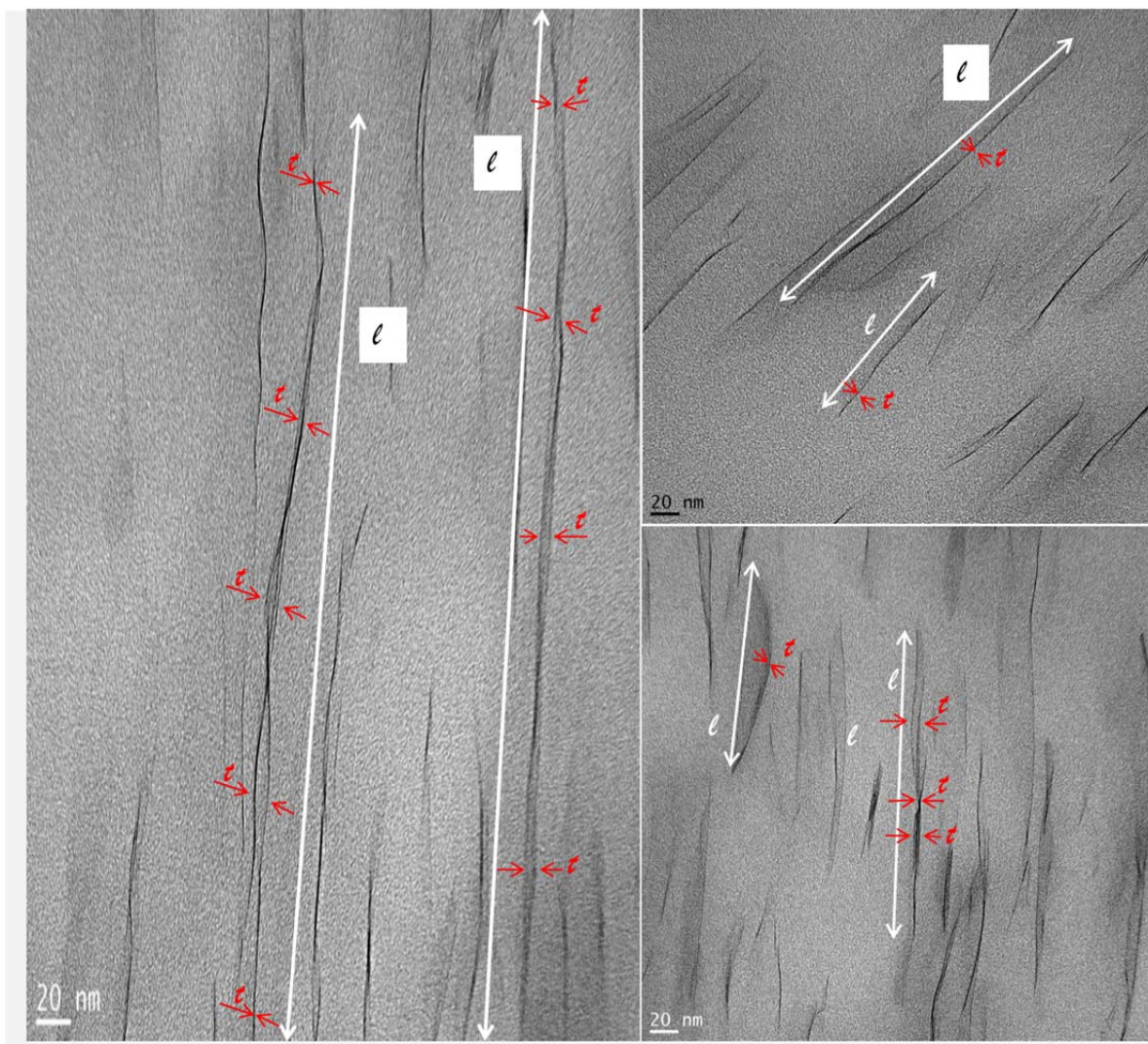


Figure 5-14 Measuring the aspect ratio of the clay layers for PA6/clay by image analysis. Silicate layers are laid in machine direction (MD).

5.4.7 Mechanical properties

The tensile properties of the films in both machine and transverse directions (MD and TD, respectively) are summarized in Table 5.6. Incorporation of 4 wt% clay improved the Young's modulus of the MXD6 film by almost 18 % and 30 % in MD and TD, respectively. Addition of clay also enhanced the yield stress by 17 % in MD and 15 % in TD, but the elongation at break

decreased significantly. Similar behaviors were observed for PA6 as well, confirming the results obtained by Poisson et al. [67] for 2 wt% nanoclay composite films produced by film blowing.

Table 5.6 Young's modulus, yield stress and elongation at break for the 30 μm films in MD and TD.

	Young's Modulus (MPa)	Yield Stress (MPa)	Elongation at Break (%)	Toughness (J/m ³)
PA6-MD	2760 \pm 136	38 \pm 4	250 \pm 20	10922 \pm 800
PA6-TD	2167 \pm 20	27 \pm 3	210 \pm 16	3318 \pm 300
PA6/clay-MD	3233 \pm 100	58 \pm 4	108 \pm 21	8304 \pm 360
PA6/clay-TD	2771 \pm 50	40 \pm 5	77 \pm 13	6313 \pm 260
MXD6-MD	3685 \pm 100	62 \pm 8	50 \pm 8	741 \pm 125
MXD6-TD	3146 \pm 45	48 \pm 4	2.3 \pm 0.2	67 \pm 15
MXD6/clay-MD	4333 \pm 131	70 \pm 5	2.4 \pm 0.2	406 \pm 67
MXD6/clay-TD	4088 \pm 178	60 \pm 5	1.37 \pm 0.3	32 \pm 28

The MXD6 shows much larger Young's modulus and tensile strength compared to the PA6. Although crystallinity of the PA6 films was higher than that for the MXD6, both barrier and mechanical properties of the MXD6 film were better than those of the PA6. This can be explained by higher interaction of the aromatic chains compared to the aliphatic ones as discussed previously. The mechanical performances of PA6 films reveal that PA6 has the advantage of more flexibility than MXD6, and as a result, higher elongation at break and toughness.

It should be pointed out that for both aromatic and aliphatic nylons, the modulus and yield strength is slightly higher in MD than in TD, which is attributed to the chain orientation in machine direction due to stretching and fast cooling in the cast film processing [68].

The tear resistance of the neat nylons and their nanocomposite films, in both MD and TD, are presented in Figure 5.15.

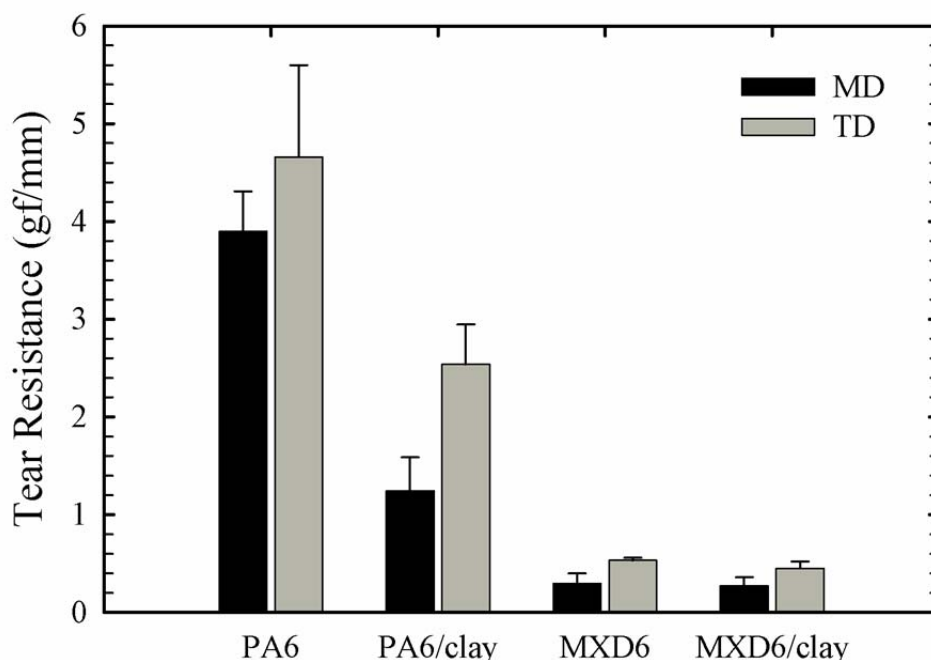


Figure 5-15 Tear resistance for PA6, PA6/clay, MXD6 and MXD6/clay films (30 μm) in MD and TD.

The nanoclay composite films showed lower tear resistance compared to the neat polymers, which was also reported for other nanocomposites [69-71]. The resistance to tear propagation for neat polymers in TD is higher than in MD due to partial orientation of the polymer chains in the flow direction. This phenomenon becomes more significant for the nanocomposite films, which is attributed to the combined effect of chains orientation and nanoclay platelets with high aspect ratio in MD. In addition, the tear resistance of the PA6 is higher than that of the MXD6 due to

the higher crystallinity of the former. The puncture resistance of nylon and nanocomposite films is shown in Figure 5.16.

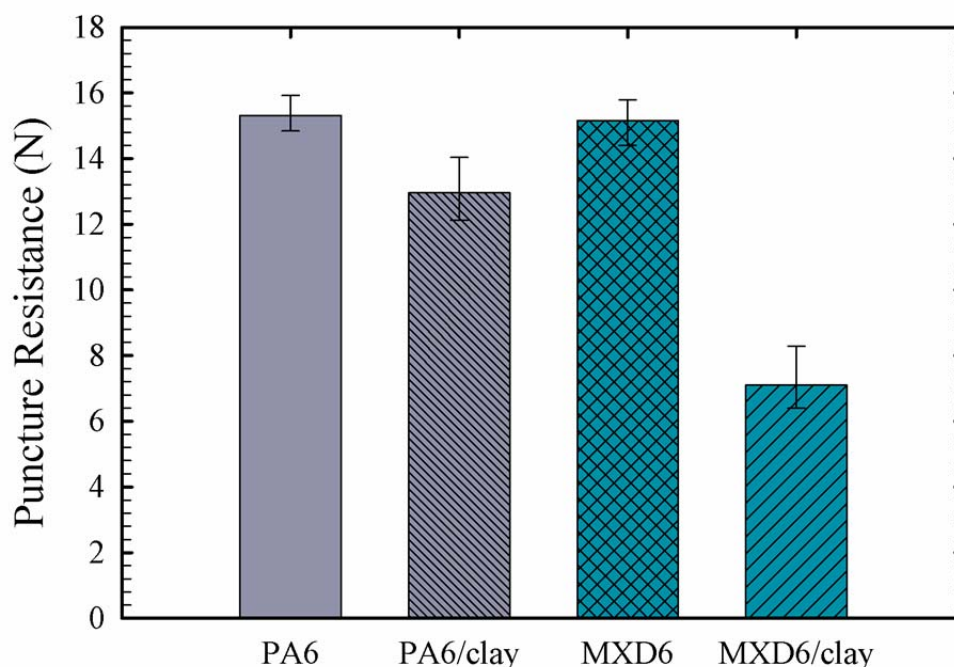


Figure 5-16 Puncture resistance for PA6, PA6/clay, MXD6 and MXD6/clay films (30 μm).

The puncture resistance of the films is reduced by adding clay. This could be related to the strong interfacial adhesion between the clay surface and nylon as well as to the slip between the nylon matrix and exfoliated clay platelets. Moreover, nylon/clay is more brittle because of the higher level of crystallinity compared to neat nylon. This brittleness induced by addition of nanoparticles to the polymer leads to the reduction in elongation at break, and hence puncture resistance. The puncture resistance of MXD6 film is reduced by 54% by clay addition. It has been also reported that puncture resistance of PET/clay nanocomposite was reduced by 60% in comparison with the neat PET [69].

5.5 Conclusions

In this study, rheological, crystal structure, thermal, mechanical and barrier properties of PA6 and MXD6 and their in-situ polymerized nanocomposites were investigated. The findings can be summarized as follows:

- The rheological results showed that the storage modulus increases with time, which was attributed to amide interchange reactions and polycondensation between nylon chains. The shear thinning behavior of MXD6/clay nanocomposite was more prominent and occurred at lower frequencies compared to PA6/clay, because of the stronger interactions in the former. The low frequency plateau in G' for MXD6/clay was an indication of its solid-like behavior at low deformation rate due to the strong interaction of well dispersed clay platelets with MXD6 nylon chains. The longer relaxation time for MXD6 was related to its higher intermolecular interactions compared to PA6.
- The XRD measurements, in agreement with the rheological measurements and TEM observations, showed completely exfoliated nanoparticles in both PA6 and MXD6 matrices.
- The γ crystalline phase was dominant in the aliphatic nylon films and its content increased with nanoparticles incorporation.
- Adding clay drastically increased the rate of crystallization, particularly for MXD6. Longer relaxation time of MXD6 compared to PA6 resulted in slower rate of crystallization and lower crystallinity in the former.
- Annealing improved oxygen barrier and crystallinity of PA6 and MXD6 as well as their nanocomposite films and this was more pronounced for the latter. The γ crystalline phase was dominant for annealed PA6/clay films whereas this crystalline form significantly

transformed to more stable α phase for annealed PA6 films. In addition, annealing caused formation of γ and α crystals in MXD6 and its nanocomposite film.

- MXD6 showed five times better oxygen barrier compared to PA6. Due to the stronger polymer chain interaction of MXD6, there is lower amount of free volume and gas diffusion path for MXD6 compared to PA6. Incorporating clay in PA6 and MXD6 enhanced oxygen barrier by 40 % and 46 %, respectively.
- MXD6 showed much larger Young's modulus and tensile strength compared to PA6. Elongation at break and toughness was higher for PA6 than for MXD6 due to the higher flexibility of PA6. For both aromatic and aliphatic nylons, the modulus and yield strength were slightly higher in MD than in TD, which was attributed to chain orientation in machine direction in the cast film processing. Adding clay to nylon improved the mechanical performance without sacrificing tear strength and puncture resistance.

5.6 Acknowledgment

Financial support from NSERC (Natural Science and Engineering Research Council of Canada) and of the industrial partners of 3SPack Chair is gratefully acknowledged. We also thank Dr. Tie Lan and Nanocor, Inc. for donating the Imperm resin used in this work.

5.7 References

1. Z. Zhang, I.J. Britt, and M.A. Tung, *J. Appl. Polym. Sci.* 82, 1866 (2001).
2. J.M. Lagarón, E. Giménez, B. Altava, V. Del-Valle, and R. Gavara, *Macromol. Symp.* 198, 473 (2003).
3. H.S. Tamber, *PVDC as a barrier material in packaging applications*, 1998, SME: Dearborn, MI, United States.
4. T.-H. Hsieh and K.-S. Ho, *J. Polym. Sci., Part A: Polym. Chem.* 37, 3269 (1999).
5. G. Choudalakis and A.D. Gotsis, *Eur. Polym. J.* 45, 967 (2009).
6. M. Alexandre and P. Dubois, *Mater. Sci. Eng., R.* 28, 1 (2000).
7. A. Okada and A. Usuki, *Macromol. Mater. Eng.* 291, 1449 (2006).
8. H. Ghasemi, P.J. Carreau, M.R. Kamal, and J. Uribe-Calderon, *Polym. Eng. Sci.* 51, 1178 (2011).
9. M. Yin, C. Li, G. Guan, X. Yuan, D. Zhang, and Y. Xiao, *Polym. Eng. Sci.* 49, 1562 (2009).
10. C.H. Davis, L.J. Mathias, J.W. Gilman, D.A. Schiraldi, J.R. Shields, P. Trulove, T.E. Sutto, and H.C. Delong, *J. Polym. Sci. Pol. Phys.* 40, 2661 (2002).
11. S.A. Jabarin and E.A. Lofgren, *Polym. Eng. Sci.* 24, 1056 (1984).
12. S.H. Tabatabaei and A. Ajji, *J. Appl. Polym. Sci.* 124, 4854 (2012).
13. M. Kato, H. Okamoto, N. Hasegawa, A. Tsukigase, and A. Usuki, *Polym. Eng. Sci.* 43, 1312 (2003).
14. J.C. Tie Lan, Ying Liang, Jerry Qian, and Peter Maul, *Nanocor Technical Paper, Nanocor Inc., Arlington Heights, USA, 2001.*, (2001).

15. A. Ammala, S.J. Pas, K.A. Lawrence, R. Stark, R.I. Webb, and A.J. Hill, *J. Mater. Chem.* 18, 911 (2008).
16. A. Ammala, A.J. Hill, K.A. Lawrence, and T. Tran, *J. Appl. Polym. Sci.* 104, 1377 (2007).
17. J.M. Lagarón, E. Giménez, R. Gavara, and J.J. Saura, *Polymer*. 42, 9531 (2001).
18. Y.S. Hu, S. Mehta, D.A. Schiraldi, A. Hiltner, and E. Baer, *J. Polym. Sci. Pol. Phys.* 43, 1365 (2005).
19. J.C.C. T.D. Krizan, P.S. Blatz, W.J. Koros (Ed.), *Barrier Polymers and Structures*, American Chemical Society, Washington, DC., 111 (1990).
20. C.L. Buquet, B.B. Doudou, C. Chappey, E. Dargent, and S.p. Marais, *J. Phys. Chem. B.* 113, 3445 (2009).
21. Tomomichi Kanda and A. Mori, *Gas-Barrier Multi-Layer Structure in Kanagawa2007*, Mitsubishi Gas Chemical Company Inc., Tokyo (JP): Japan.
22. M. Shibayama, K. Uenoyama, J.I. Oura, and S. Nomura, *Polymer*. 36, 4811 (1995).
23. Y. Takeda and D.R. Paul, *Polymer*. 33, 3899 (1992).
24. Y. Takeda and D.R. Paul, *Polymer*. 32, 2771 (1991).
25. Y. Takeda, H. Keskkula, and D.R. Paul, *Polymer*. 33, 3394 (1992).
26. M. Takashige and T. Kanai, *Int. Polym. Proc.* 20, 100 (2005).
27. M. Takashige, T. Kanai, and T. Yamada, *Int. Polym. Proc.* 19, 147 (2004).
28. R.K. Ayyer and A.I. Leonov, *Rheol. Acta.* 43, 283 (2004).
29. B. Doudou, E. Dargent, and J. Grenet, *J. Therm. Anal. Calorim.* 85, 409 (2006).
30. T.D. Fornes and D.R. Paul, *Polymer*. 44, 3945 (2003).

31. R. Krishnamoorti and K. Yurekli, *Current Opinion in Colloid & Interface Science*. 6, 464 (2001).
32. P.S. Walia, R.K. Gupta, and C.T. Kiang, *Polym. Eng. Sci.* 39, 2431 (1999).
33. R. Krishnamoorti and E.P. Giannelis, *Macromolecules*. 30, 4097 (1997).
34. J. Ren, B.F. Casanueva, C.A. Mitchell, and R. Krishnamoorti, *Macromolecules*. 36, 4188 (2003).
35. S. Abbasi, P. Carreau, A. Derdouri, and M. Moan, *Rheol. Acta*. 48, 943 (2009).
36. K.M. Lee and C.D. Han, *Macromolecules*. 36, 7165 (2003).
37. W. Lertwimolnun and B. Vergnes, *Polymer*. 46, 3462 (2005).
38. J.W. Cho and D.R. Paul, *Polymer*. 42, 1083 (2001).
39. G. Filippone, N.T. Dintcheva, F.P. La Mantia, and D. Acierno, *Polymer*. 51, 3956 (2010).
40. T.D. Fornes, P.J. Yoon, and D.R. Paul, *Polymer*. 44, 7545 (2003).
41. John M. Dealy and K.F. Wissbrun, *Melt rheology and its role in plastics processing, theory and applications* (1999), Dordrecht, The Netherlands: Kluwer Academic Publishers.
42. T.D. Fornes, P.J. Yoon, H. Keskkula, and D.R. Paul, *Polymer*. 42, 09929 (2001).
43. S.R. Liang Xu, Mahesh Thopasridharan, Jiaxiang Ren, Devon A Shipp and Ramanan Krishnamoorti, *Nanotechnology*. 16, S514 (2005).
44. K.M. Lee and C.D. Han, *Macromolecules*. 36, 7165 (2003).
45. K. Yurekli, R. Krishnamoorti, M.F. Tse, K.O. McElrath, A.H. Tsou, and H.C. Wang, *J. Polym. Sci. Pol. Phys.* 39, 256 (2001).
46. Y. Li and W.A. Goddard, *Macromolecules*. 35, 8440 (2002).

47. Y. Zhang, Y. Zhang, S. Liu, A. Huang, Z. Chi, J. Xu, and J. Economy, *J. Appl. Polym. Sci.* 120, 1885 (2011).
48. M.N. Bureau, J. Denault, K.C. Cole, and G.D. Enright, *Polym. Eng. Sci.* 42, 1897 (2002).
49. X. Liu and C. Breen, *Macromol. Rapid Commun.* 26, 1081 (2005).
50. T. Ota, M. Yamashita, O. Yoshizaki, and E. Nagai, *J. Polym. Sci. Pol. Phys.* 4, 959 (1966).
51. V. Miri, S. Elkoun, F. Peurton, C. Vanmansart, J.M. Lefebvre, P. Krawczak, and R. Seguela, *Macromolecules.* 41, 9234 (2008).
52. T.X. Liu, Z.H. Liu, K.X. Ma, L. Shen, K.Y. Zeng, and C.B. He, *Compos. Sci. Technol.* 63, 331
53. K. Magniez, B.L. Fox, and M.G. Looney, *J. Polym. Sci. Pol. Phys.* 47, 1300 (2009).
54. Y.P. Khanna and W.P. Kuhn, *J. Polym. Sci. Pol. Phys.* 35, 2219 (1997).
55. S. Seif and M. Cakmak, *Polymer.* 51, 3762 (2010).
56. L.H. Sperling, *Introduction to Physical Polymer Science.*(2006), New Jersey: John Wiley & Sons, Inc.
57. X.-Y. Zhao and B.-Z. Zhang, *J. Appl. Polym. Sci.* 115, 1688 (2010).
58. L. Penel-Pierron, C. Depecker, R. Seguela, and J.M. Lefebvre, *J. Polym. Sci. Pol. Phys.* 39, 484 (2001).
59. X.Y. Zhao, *Polym. Int.* 58, 469 (2009).
60. R.D. Davis, J.W. Gilman, and D.L. VanderHart, *Polym. Degrad. Stab.* 79, 111 (2003).
61. K.P. Pramoda, T. Liu, Z. Liu, C. He, and H.J. Sue, *Polym. Degrad. Stab.* 81, 47 (2003).
62. A. Zabaleta, I. González, J.I. Eguiazabal, and J. Nazabal, *Polym. Eng. Sci.* 51, 1428 (2011).

63. E. Picard, A. Vermogen, J.F. Gérard, and E. Espuche, *Journal of Membrane Science*. 292, 133 (2007).
64. C. Thellen, S. Schirmer, J.A. Ratto, B. Finnigan, and D. Schmidt, *Journal of Membrane Science*. 340, 45 (2009).
65. P. Winberg, M. Eldrup, N.J. Pedersen, M.A. van Es, and F.H.J. Maurer, *Polymer*. 46, 8239 (2005).
66. G. Choudalakis, A.D. Gotsis, H. Schut, and S.J. Picken, *Eur. Polym. J.* 47, 264 (2011).
67. C. Poisson, J. Guerengomba, M.-F. Lacrampe, P. Krawczak, B. Gupta, V. Miri, and J.-M. Lefebvre, *Polym. Polym. Compos.* 16, 349 (2008).
68. S.H. Tabatabaei, P.J. Carreau, and A. Ajji, *Polymer*. 50, 4228 (2009).
69. H. Ghasemi, P.J. Carreau, M.R. Kamal, and S.H. Tabatabaei, *Polym. Eng. Sci.* 52, 420 (2012).
70. Y. Lin, A. Hiltner, and E. Baer, *Polymer*. 51, 5807 (2010).
71. R.K. Shah, R.K. Krishnaswamy, S. Takahashi, and D.R. Paul, *Polymer*. 47, 6187 (2006).

CHAPTER 6

X-ray and Trichroic Infrared Orientation Analyses of Uniaxially Stretched PA6 and MXD6 Nanoclay Composite Films²

Maryam Fereydoon, Seyed H. Tabatabaei and Abdellah Aji*

*3SPack NSERC-Industry Chair, Chemical Engineering Department, Polytechnique Montreal,
C.P. 6079, Succ. Centre ville, Montreal, QC, Canada H3C 3A7*

(* All correspondence should be addressed to: abdellah.ajji@polymtl.ca

Abstract

Cast films of aliphatic (PA6) and aromatic (MXD6) nylons and their in-situ polymerized nanocomposites with 4 wt% clay were prepared by extrusion process and rapid cooling using an air knife. The precursor films were then uniaxially stretched at 110 °C with draw ratios varying from 1.5 to 5. The changes in orientation of clay and crystal axes of all the crystalline phases and amorphous region were examined using X-ray diffraction and Trichroic Infrared analyses. The clay alignment was measured with three different techniques: FTIR peak deconvolution, FTIR interactive spectral subtraction and X-ray diffraction. It was found that the clay platelets are mainly oriented in the machine direction (MD) and their orientation improved upon uniaxial stretching. X-ray analysis showed that γ crystals (designated as γ_1) of both nylons were mainly formed during rapid cooling of cast films. However, only the PA6/clay films showed an extra γ crystal population (designated as γ_2). WAXD and FTIR analyses revealed that the *c*-axis of γ_1 crystal population was oriented in the normal and transverse directions (ND and TD), while the *c*-axis of γ_2 was aligned in the normal direction (ND), indicating that this later crystal population

² Published in *Macromolecules*. February 2014. DOI: 10.1021/ma402466c

formed perpendicular to the (001) plane of the clay platelets. The orientation of γ_1 and γ_2 crystal populations increased after uniaxial deformation. The MXD6 showed very little crystallinity due to its higher stiffness and low relaxation rate of the aromatic chains. The amorphous region had a lower orientation in the nanocomposite films due to the spatial hindrance caused by the presence of clay platelets.

Keywords: PA6, MXD6, Clay, Uniaxial Stretching, Orientation, Crystallinity.

6.1 Introduction

Nylon is an engineering thermoplastic used extensively in food packaging due to its high stiffness, toughness, tensile strength, flex crack and puncture resistance as well as low oxygen transmission rate. In the past two decades, incorporating silicate nano-layers with high aspect ratio (such as modified montmorillonite) into nylon matrices has received significant attention to improve mechanical and barrier performances¹⁻⁶. During the cast film extrusion process, these nano-platelets could be oriented in the flow direction and subsequently enhance the gas barrier properties of the nylon nanocomposite films⁷.

The structural development of nylon films during uniaxial stretching are influenced by initial morphology, molecular orientation, ability to crystallize (i.e. fast or slow crystallization rate), type of crystalline structure and physical state of material (i.e. glassy, rubbery, partially molten or fully molten). In addition, the final properties of stretched films are strongly dependent on the processing conditions such as drawing rate, extent of deformation and stretching temperature. Stretching can result in a highly oriented film, which reduces the oxygen permeability⁸ and improves the tensile strength, modulus, puncture resistance and clarity⁹. However, it lowers the elongation at break¹⁰ and tear resistance along the machine direction (MD)^{8, 11, 12}.

Polyamide 6 (PA6) displays a polymorphism crystalline behavior and depending on the processing conditions and thermo-mechanical history, different crystalline forms (i.e. α , γ and β) may be observed in the uniaxially and biaxially oriented PA6 and PA6/clay films^{13, 14}. The monoclinic α form, with the H-bonds lying between antiparallel chains, has a planar zigzag conformation with (002) crystalline plane and it is promoted under slow cooling from the melt state¹⁵⁻¹⁸. The α form is the most thermally stable crystalline phase of PA6. The pseudo-hexagonal γ phase, with the H-bonds linking parallel chains, has a twisted chain conformation with (200) planes and can be developed under rapid cooling^{15, 17}. The thermodynamically unstable mesomorphic β form has a random distribution of the H-bond layers normal to the chain axis with (020) planes and can be generated by quenching PA6¹⁹. The β structure can be transformed into the α form during drawing²⁰ or thermal annealing¹⁹. The α phase typically shows higher stiffness (modulus) and yield stress, but has lower elongation at break than the β and γ forms^{20, 21}. The structural evolution analysis of nylon6 nanocomposite films during uniaxial stretching revealed that the γ - α phase transition occurs under specific conditions^{19, 20}. First, a sufficient extension for the γ phase is required to untwist the chains around the amide groups. Second, an adequate molecular mobility is needed to change stacking in the crystalline structure^{22, 23}. The γ - α strain-induced transition becomes more important in drawing polyamide at high temperatures because of the improvement in chain mobility of crystals^{20, 23}.

The effect of clay platelets on the crystallization of nylon has been studied extensively in the literature^{16, 17, 24, 25}. It was found that depending on the amount of shear and elongation induced during the process, the PA6 γ crystals could align themselves either parallel or perpendicular to the clay platelets²⁶. Fong et al.²⁷ showed that the crystalline units of PA6 orient perpendicular to the clay platelets in the PA6/clay fibers obtained from the electro-spinning process.

Poly (m-Xylene adipamide) (MXD6) is a semi-crystalline aromatic nylon, which has better mechanical performance and oxygen barrier property in comparison with PA6. Our recent study²⁸ showed that although the crystallinity of MXD6 films was much lower than PA6 films, however, the oxygen barrier was five times better for the former. It was found that due to the stronger polymer chain interaction of MXD6, there was lower amount of free volume and gas diffusion path for MXD6 compared to PA6. Additionally, MXD6 showed longer relaxation time and much larger Young's modulus and tensile strength than that of PA6 due to its higher intermolecular interactions. In another study²⁹, it was revealed that the gas permeation of MXD6 in contact with water molecules does not deteriorate.

The gas barrier property of poly (ethylene terephthalate) (PET) blends with poly (m-Xylene adipamide) MXD6 was studied by Prattipati et al.³⁰. The oxygen permeability of PET drastically decreased with adding only 10 wt% of MXD6. Adding a small amount of sodium 5-sulfoisophthalate (SIPE) as compatibilizer to the PET matrix before blending with MXD6 showed a significant improvement in the oxygen barrier property of the blends. This was attributed to a better compatibility between the two polymers in the presence of SIPE, which reduced the domain size of the nylon distributed in the PET matrix. Another study showed that in a PET/MXD6 blend, the crystallinity of PET film increased by about 40% upon uniaxial stretching when draw ratio increased to 5³¹. During stretching, the spherical MXD6 particles in the PET matrix were transformed into platelets with high aspect ratios. Consequently, the diffusion path for gas molecules became more tortuous, resulting in a lower permeability³¹. Hu et al.³² revealed that the transparency of PET/MXD6 blends improved up to 70% through biaxial orientation.

Although a few authors have investigated the structure of PA6/clay nanocomposite films upon uniaxial and biaxial drawing ^{14, 22}, there is no report on comparison between the crystalline structure and orientation of uniaxially oriented aliphatic and aromatic nylon nanocomposite films. Moreover, most studies used only one technique to measure the clay and crystalline orientation of nylon nanocomposites, which is not enough to obtain the orientation of the crystal axes of all the crystalline phases of nylon in the presence of clay platelets. In this study, the effect of uniaxial drawing on the orientation of the clay, crystal axes of all the crystalline phases and amorphous region of the polyamide 6 (PA6), poly (m-xylene adipamide) (MXD6) and their in-situ polymerized nanocomposites with 4 wt% clay were studied using X-ray diffraction and Trichroic Infrared analyses.

6.2 Experimental

6.2.1 Materials

PA6 (Ultramid B36, from BASF) and PA6/clay nanocomposites (Cress-Alon™ NF3040, from CP polymers) were selected as the aliphatic nylon and its nanocomposite, respectively. The montmorillonite content of NF3040 is 4 wt% with aspect ratios of 200 to 300. MXD6 6007 resin and Imperm 103, which is a nanocomposite of MXD6 resin with montmorillonite clays, supplied by Nanocor (in partnership with Mitsubishi Gas Chemical) were selected as the aromatic nylon and its nanocomposite, respectively. According to Nanocor, the silicate layered montmorillonite content of the Imperm 103 nanocomposite MXD6 is between 3.3 to 3.6 wt% with aspect ratios of 200 to 400. The main characteristics of the materials used in this study are listed in Table 6.1.

Table 6.1 Main characteristics of materials used in this study.

Material	Commercial name	Supplier	Nomenclature	Main characteristics
Nylon 6	Ultramid B36	BASF (Freeport, USA)	PA6	$M_n = 18,000 \text{ g.mol}^{-1}$ $\rho = 1.14 \text{ g.cm}^{-3}$ $\eta_r = 3.6$ MFI (275°C/5kg) = 10 g/10 min
Nylon 6/clay	NF3040	CP Polymers (Montebello, USA)	PA6/clay	$\rho = 1.15 \text{ g.cm}^{-3}$ $\eta_r = 3$ MFI (230°C/5kg) = 8.9 g/10 min Clay content = 4 wt%
Aromatic Nylon	MXD6 6007	Mitsubishi Gas Chemical (Colonial Heights, USA)	MXD6	$M_n = 25,000 \text{ g.mol}^{-1}$ $\rho = 1.21 \text{ g.cm}^{-3}$ $\eta_r = 2.7$ MFI (230°C/5kg) = 12 g/10 min
Aromatic Nylon/clay	Imperm 103	Nanocor (Arlington Heights, USA)	MXD6/clay	$\rho = 1.22 \text{ g.cm}^{-3}$ $\eta_r = 2.5$ Clay content = 3.3 to 3.6 wt%

M_n : Number average molecular weight

ρ : Density

η_r : Relative viscosity = (η/η_0) where η_0 is the viscosity of the solvent.

MFI: Melt flow index

6.2.2 Film preparation

Cast films of nylon and nylon/clay materials were prepared using a fully intermeshing co-rotating twin-screw extruder (Leistritz ZSE 18 HP) with 18 mm screw diameter and length/diameter (L/D) of 40. To minimize degradation, the screw configuration was set to yield low to medium shear environment during extrusion. The aromatic (i.e. MXD6 and MXD6/clay) and aliphatic nylon resins (i.e. PA6 and PA6/clay) were dried prior to extrusion in a vacuum oven at 130 °C for 5 h and at 80 °C for 24 h, respectively. The screw speed was 200 rpm and the temperature profile from the hopper to the die was 230/240/245/255/260 °C for the aliphatic nylons and 235/250/255/260/265 °C for the aromatic ones. The extruder was equipped with a slit die followed by rapid cooling using an air knife. Chill rolls set at ambient temperature were used

to stretch the extrudate to obtain 60-70 μm thick films. The precursor films were kept in desiccators (under vacuum) for the further characterizations.

The uniaxial stretching was carried out on 5 cm \times 1.5 cm \times 70 μm precursor films using an Instron (Instron Electro Puls E3000, UK) apparatus equipped with a heating chamber. The drawing was performed at 110 $^{\circ}\text{C}$, an optimized speed of 400 mm/min and draw ratios from 1.5 to 5. Before drawing, the films were kept at 110 $^{\circ}\text{C}$ in the heating chamber of the tensile machine for 10 min to allow a homogenous temperature distribution. Stress-strain curves (data are not shown) exhibited a plateau plastic deformation after the yield point for the stretched films at all draw ratios. All the samples were rapidly air cooled to room temperature and then removed from the clamps for further characterizations.

6.3 Characterization

To evaluate orientation and monitor crystalline phase formation, infrared spectra of the precursor and stretched films were recorded using a Spectrum 65 FTIR spectrometer from PerkinElmer (Waltham, MA) with a resolution of 4 cm^{-1} and an accumulation of 32 scans over the wavenumber range of 400 to 4000 cm^{-1} . The beam was polarized with a Spectra-Tech zinc selenide wire grid polarizer from Thermo Electron Corp. Spectra were recorded with the polarizer in the vertical machine direction (MD), S_M , and in the horizontal transverse direction (TD), S_T . The films were also tilted by an angle of φ with respect to MD, S_{NT} , and spectrum was recorded with the polarizer in the horizontal direction¹⁴. The spectra in the normal direction (ND), S_N , can be calculated according to the following equation^{14, 33, 34}:

$$S_N = \frac{S_{NT} \left(1 - \frac{\sin^2 \varphi}{n^2}\right)^{1/2} - S_T \left(1 - \frac{\sin^2 \varphi}{n^2}\right)}{\sin^2 \varphi / n^2} \quad (6.1)$$

where n is the refractive index and was reported equal to 1.62 for nylon^{33, 34} and 1.73 for clay platelets^{35, 36} in the NT plane. A value of 45° was chosen for ϕ ¹⁴.

The structurally dependent spectrum, S_0 , is obtained according to:

$$S_0 = \frac{(S_M + S_N + S_T)}{3} \quad (6.2)$$

This is the spectrum of the corresponding isotropic sample. The degree of orientation of a specific molecular chain axis or crystal axis (i) with respect to the film directions (j) can be calculated by¹⁴:

$$f_{ij} = \frac{D-1}{D+2} \times \frac{2}{3\cos^2\phi-1} \quad (6.3)$$

where D is the dichroic ratio ($D = A_j/A_0$), j is MD, TD, or ND, A_j and A_0 are the absorption peak intensities in the S_j and S_0 spectra, respectively, and ϕ is the angle that the transition moment makes with the polymer chain axis. The latter was taken equal to 0° as mentioned in the Refs^{13, 14}. PeakFit v4.06 Software was used for peak fitting of the spectra. In this study, the PA6 crystallographic axes $i = a, b$, and c were defined as the same assignment used by Arimoto et al.³⁷. In this assignment, the crystallographic b -axis is considered being parallel to the nylon chain axis which is different from the assignments of Cole et al.¹³ who considered the c -axis is being parallel to the chain axis.

The crystalline structure and orientation of the crystal axes of nylons as well as the clay platelet alignment were investigated by wide angle X-ray diffraction (WAXD) in the transmission mode with a single-crystal diffractometer AXS X-ray (Bruker, Karlsruhe, Germany) equipped with a Hi-STAR two-dimensional area detector. The generator was set up at 40 kV and 40 mA and the copper CuK α radiation ($\lambda = 1.542 \text{ \AA}$) was selected using a graphite crystal monochromator. The sample to detector distance was fixed at 12 cm and it was scanned

from 10 to 50° at 0.04 °/s. Several film layers were stacked together in order to obtain a total thickness of approximately 2 mm to get the maximum diffraction intensity. For each sample, a transmission diffraction pattern was recorded using a pole figure accessory as the sample was rotating at a scanning rate of 3° per minute through spherical angles (0° to 360°) with respect to the beam. This allows measuring the intensity of diffraction for a given crystallographic plane (hkl), in order to obtain probability distribution of orientation (normal to hkl plane) with respect to the directions of the sample.

Herman orientation function, f , represents the fraction of polymer chains that are perfectly aligned parallel to the symmetry axis and is calculated according to³⁸:

$$f = \frac{1}{2}(3\cos^2\theta_\mu - 1) \quad (6.4)$$

where θ_μ is the angle between the unit cell axes (a , b , and c) and reference axis. The details of calculations can be found elsewhere³⁸. The orientation factors from WAXD are mainly due to the crystalline part, therefore no information about the orientation of the amorphous phase can be obtained.

Transmission electron microscopy (TEM) (JEOL JEM-2100F, Japan, operating at 200 kV) was used to observe clay exfoliation and dispersion quality in the aromatic and aliphatic nylon matrices. The specimens were impregnated in epoxy resin and microtomed in the MD-ND plane using an Ultracut FC microtome (Leica, Germany) with a diamond knife.

6.4 Results and Discussion

The surface (MD-TD plane) and cross-section (MD-ND plane) WAXD patterns of the precursor and stretched (DR=4) aliphatic nylon and the corresponding nanocomposite films are presented in Figure 6.1.

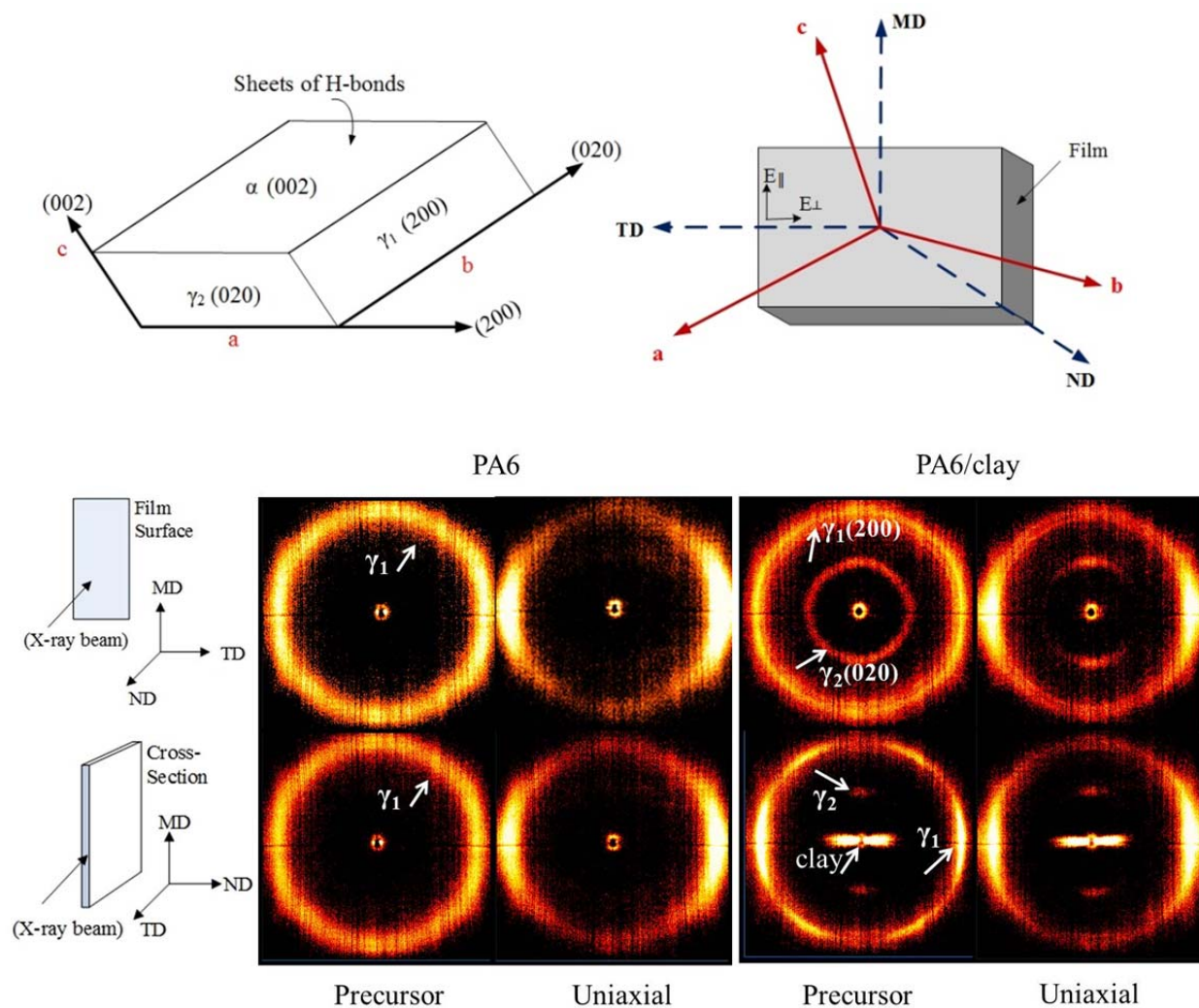


Figure 6-1 Surface (MD-TD plane) and cross-section (MD-ND plane) 2D WAXD patterns for precursor and stretched (DR=4) PA6 and PA6/clay films.

The Debye-Scherrer diffraction ring, represents the (200) crystalline reflection of the precursor and stretched nylon films. The smaller ring corresponds to the (020) crystallographic plane and is only seen for the PA6/clay films. The latter is related to the heterogeneous nucleation of the PA6 crystals on the surface of the clay platelets, which creates another crystal population with different orientation (it will be discussed later). Due to the low crystallinity and impossible separation of the γ phase contribution from the amorphous phase, the pole figures for the MXD6 films are not shown here. In the cross section patterns of the nanocomposite films, the

oriented streak diffraction at small angles along the meridian, (001) plane, are attributed to the preferential orientation of the clay platelets in the flow direction and parallel to the film surface.

To shed light on the effect of stretching on orientation of the aliphatic and aromatic nylons films and their nanocomposites, the FTIR and WAXD techniques were both used in order to completely measure the orientation of the clay, crystalline and amorphous phases. The results are presented in the following three sections.

6.4.1 Effect of Stretching on Orientation of Clay

In addition to the clay alignment, the degree of exfoliation and intercalation of clay platelets in the polymer matrix have significant impacts on the performance of the nanocomposite films³. In Figure 6.2, no peak was observed in the diffraction intensity profiles of the precursor PA6/clay and MXD6/clay films at low diffraction angles, indicating that the dispersed clays have been exfoliated. The TEM micrographs in Figure 6.2 also display individual dispersed silicate layers in both the aliphatic and aromatic nylon nanocomposite films, confirming exfoliation of the nanoparticles.

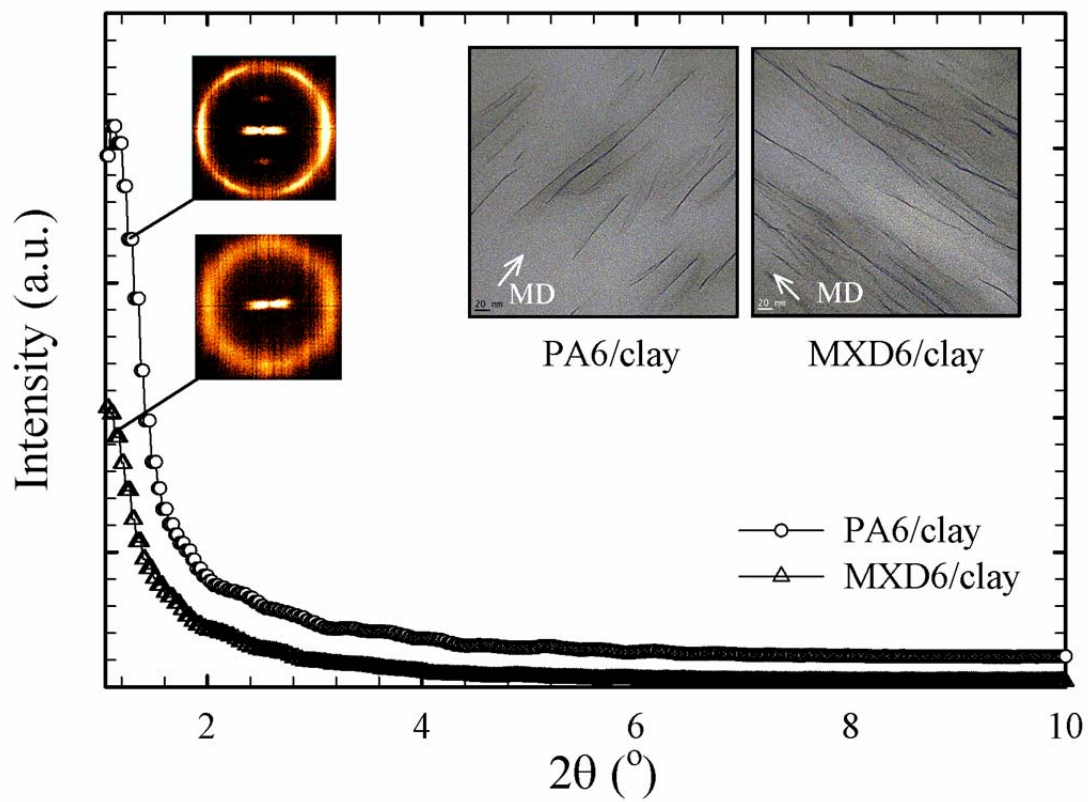


Figure 6-2 Diffraction intensity profiles for PA6/clay and MXD6/clay films in the MD-ND plane.

Clay platelets have a high tendency to orient themselves in the flow direction during cast film process^{39, 40}, due to their planar structure with high aspect ratios²². The clay orientation can be analyzed quantitatively from WAXD pole figures of the (001) plane. The pole figure for the normal to the (001) plane of the clay in the precursor and stretched (DR=4) PA6/clay and MXD6/clay films are depicted in Figure 6.3. A significant orientation of the *c*-axis of the clays along ND indicates that the clay platelets have been aligned in the MD-TD plane, which is consistent with those reported for the other uniaxial oriented nanocomposites^{9, 22, 41}. The 3D cone curvature of the clay orientation (see Figure 6.3) becomes narrower, sharper and more concentrated in the center for the drawn films, implying more orientation.

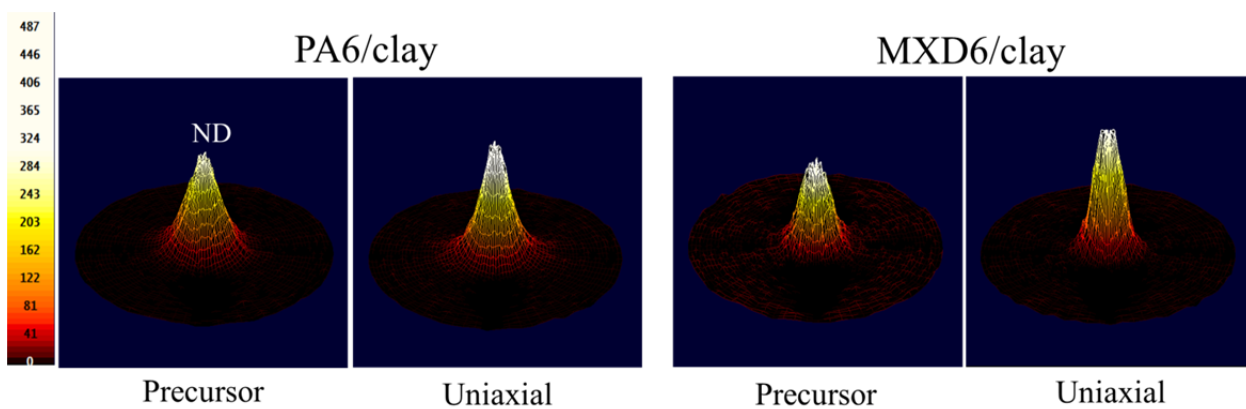
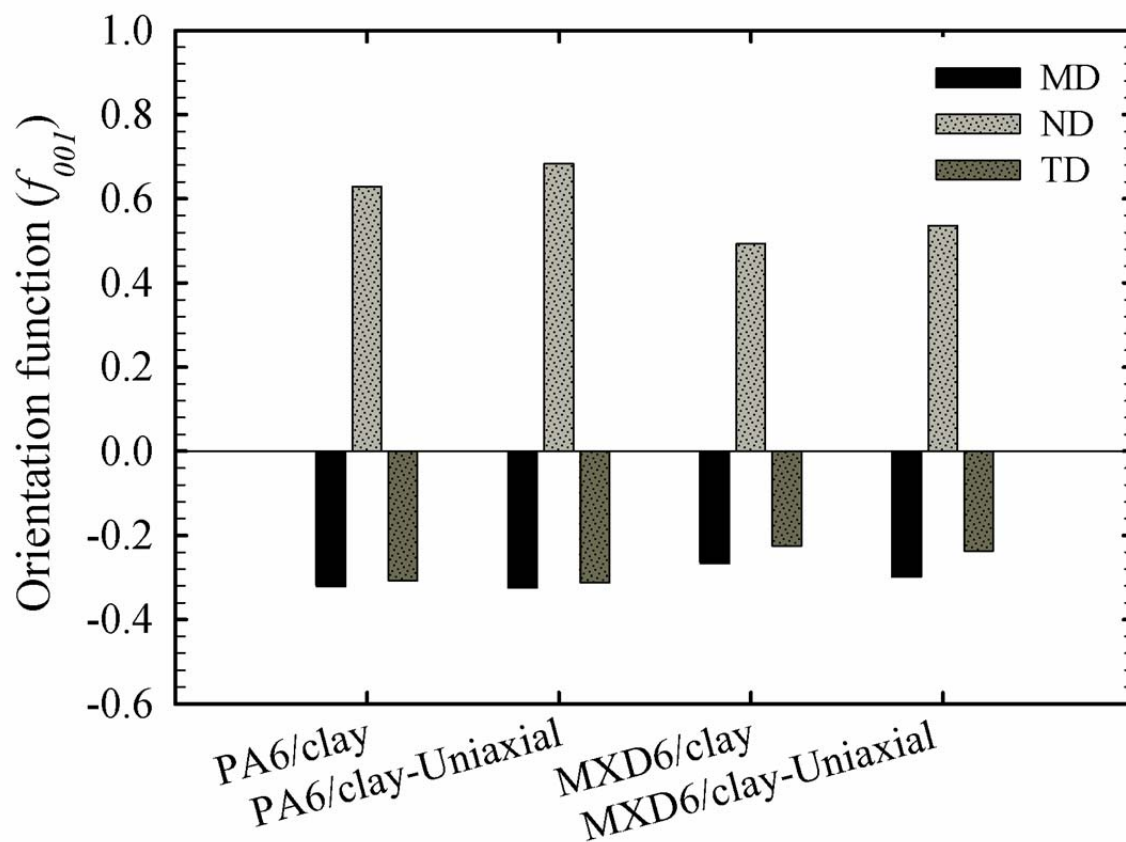


Figure 6-3 Herman orientation function (f_{001}) and pole figure of the (001) plane of clay along MD, TD, and ND for precursor and stretched (DR=4) PA6/clay and MXD6/clay films.

The clay platelets alignment in MD for the PA6/clay film is greater than that for the MXD6/clay film. In fact, the ability of the silicate layers to be oriented under shear flow is

highly dependent on the processing temperature, molecular weight of polymers, polymer/clay interactions and rheological properties of the polymer matrix^{42, 43}. In our recent study²⁸, using rheological characterizations, it was shown that there is a stronger interaction between the aromatic nylon chains and silicate layers compared to the aliphatic nylon. A higher MXD6/clay interaction combined with a low crystallinity of the MXD6 can possibly be the reason for observing a lower clay orientation in comparison with the aliphatic nylons. In addition, in Figure 6.3, it is clear that the clay orientation in MD is not affected significantly by stretching. This indicates that hot stretching has less impact on the clay orientation than the crystal orientation, which will be discussed with more details in the next section.

The infrared absorption peaks of the silicate layers were qualitatively and quantitatively analyzed based on the silicon-oxygen network of the hexagonal symmetry theory proposed by Farmer et al.⁴⁴. The “tilted film” transmission infrared spectroscopy method was used to characterize the clay platelets orientation in the precursor and stretched PA6/clay and MXD6/clay films⁴⁴. The clay orientation could be determined from the Si-O stretching bands in the spectral region of 970-1200 cm^{-1} ^{41, 45}. The four detected Si-O stretching band peaks of the PA6/clay and MXD6/clay films at the wavenumbers of 1114, 1084, 1044, and 1014 cm^{-1} are shown in Figures 6.4 and 6.5, respectively.

The second peak (II) in Figure 6.4b is related to the transition dipole moment of the apical oxygen atom perpendicular to the (001) plane of clay (out-plane vibration); while the other Si-O peaks (i.e. I, III and IV) are pertinent to the transition dipole moment of the basal oxygen atoms laid on the surface of the clay parallel to the (001) plane (in-plane vibrations)^{14, 35, 36, 41, 46}. The peak at 1100 cm^{-1} has likewise overlap with the PA6 peaks, thus cannot be considered for measuring clay orientation³⁶.

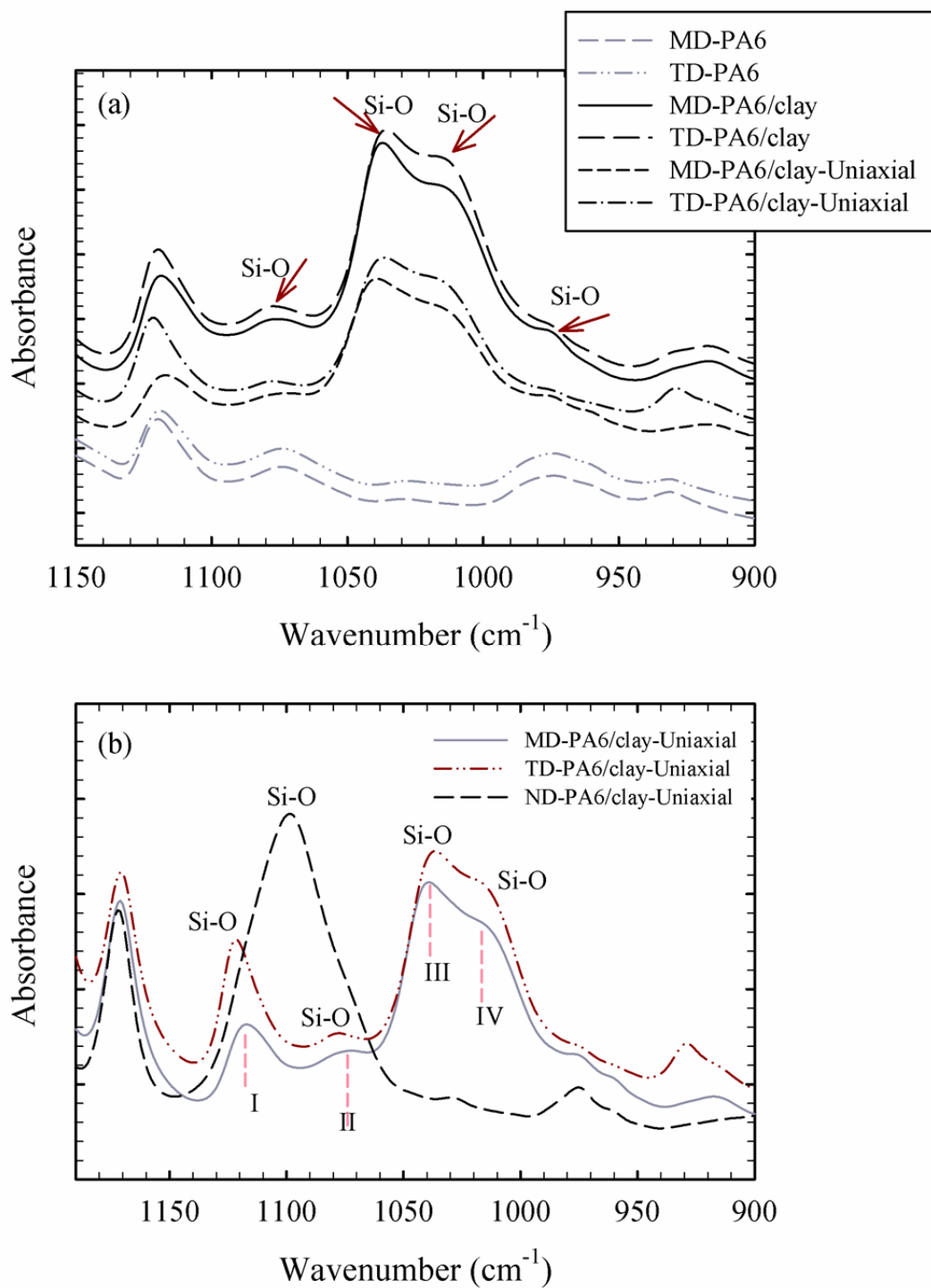


Figure 6-4 (a) Trichroic FTIR spectra along MD, TD and calculated ND in the Si-O stretching region for precursor and stretched (DR=4) PA6 and PA6/clay. (b) The four peaks for the Si-O stretching bonds of silicate layers in MD, TD and ND spectra in oriented PA6/clay film.

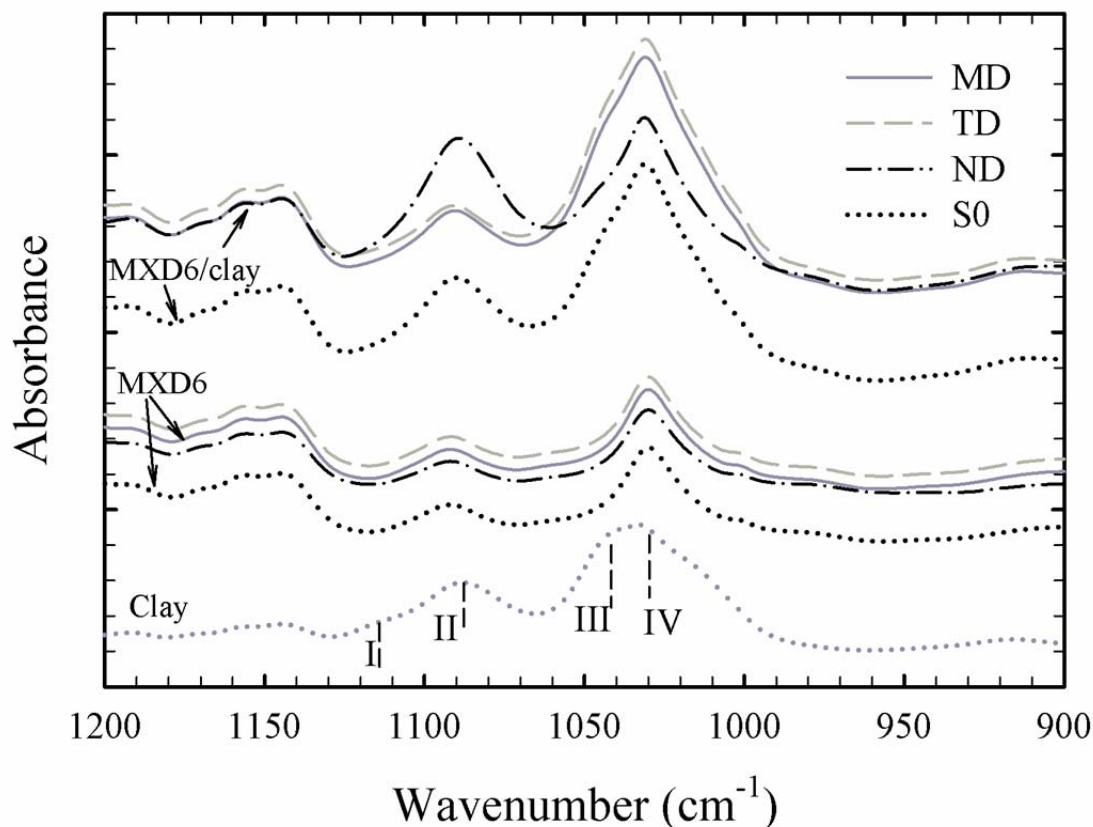


Figure 6-5 Trichroic FTIR spectra along MD, TD, calculated ND and structural factor spectrum (S0) for MXD6 film, MXD6/clay film and nanoclay spectrum obtained by subtraction.

In Figure 6.4b, for the PA6/clay films, a strong out-of-plane vibration (peak II) is observed in ND. In contrast, the intensity of the in-plane vibrations (peaks I, III and IV) are weak in ND. This confirms that the silicate layers are mainly oriented in MD during the cast film extrusion. In fact, when the incident beam in FTIR is perpendicular to the surface of the film (i.e. MD or TD), the out-plane absorption band (peak II) is expected to be absent or weak^{14, 35, 41}. Therefore, the out-plane vibration (peak II) was used to calculate the Herman orientation factor of the *c*-axis of the clay platelets with respect to the normal direction, f_{cN} , of the film surface (see Eq. 6.3). To calculate the orientation of the clay platelets from the peak fitting data, two different approaches

were used; First, the dichroic ratios, A_j/A_{o_2} were calculated based on the areas under the peaks IIa and IIb after deconvolution⁴⁷ using PeakFit v4.06 Software, as shown in Figure 6.6.

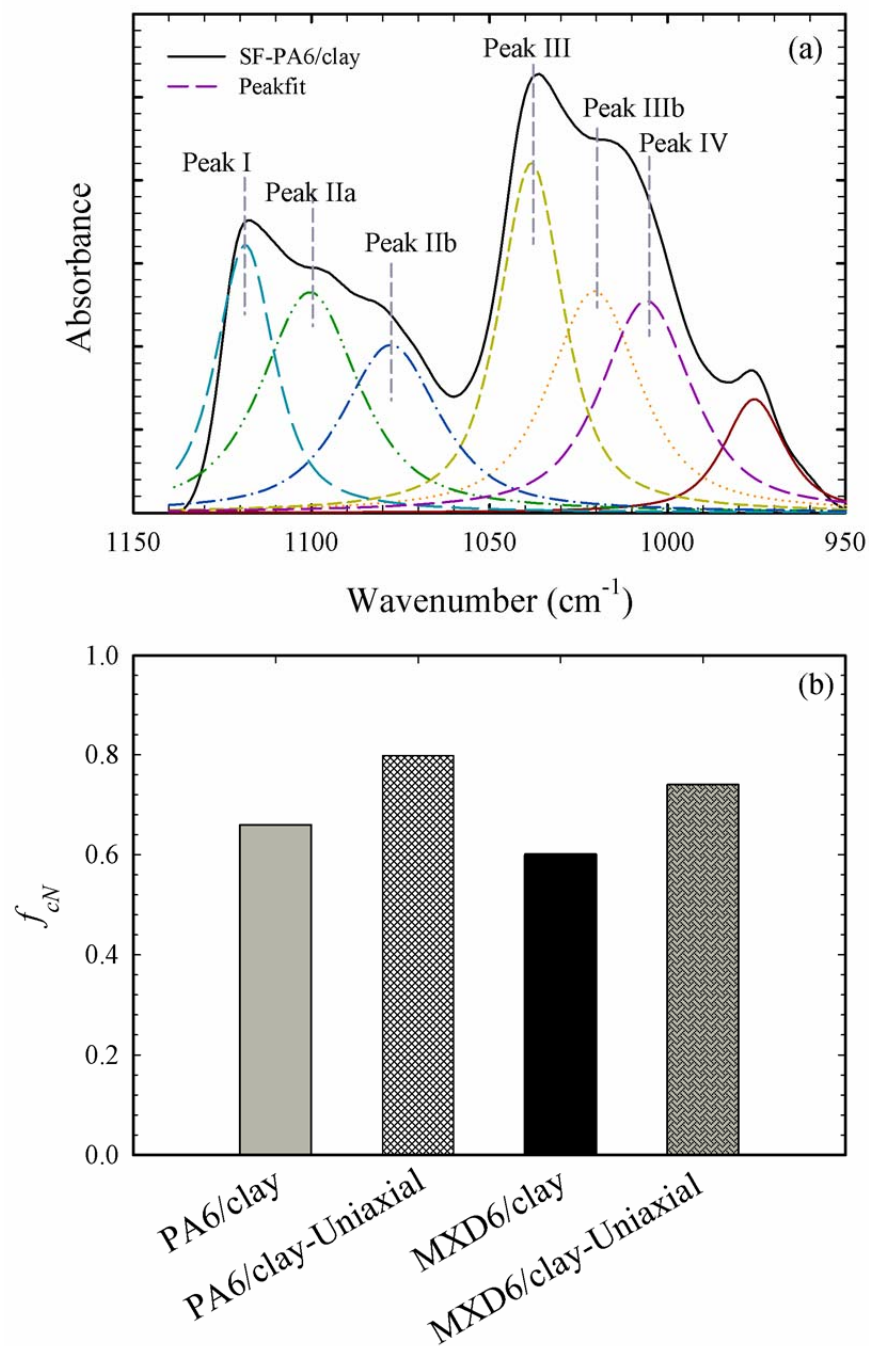


Figure 6-6 (a) Peak fitting for the FTIR structural spectrum (SF) of clay. (b) Herman orientation function of clay obtained with peak fitting method for precursor and stretched (DR=4) PA6/clay and MXD6/clay nanocomposite films.

As seen, stretching slightly improves the orientation of the clay platelets. Second, using an interactive spectral subtraction method⁴¹, the dichroic ratios, A_j/A_{o_z} were determined by interactively subtracting the S_N spectrum from the structural factor spectrum, S_o , and adjusting the subtraction factor until the peak II disappears (see Figure 6.7).

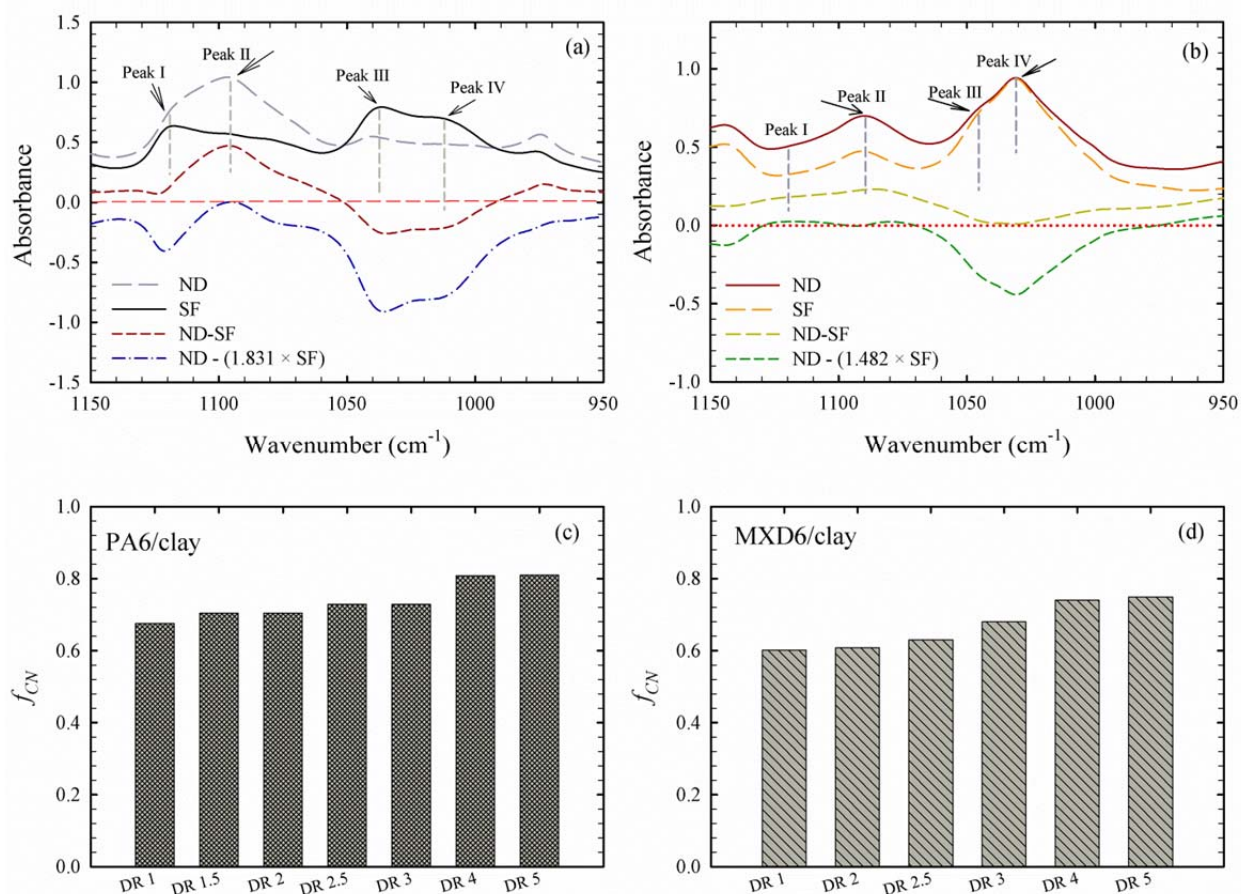


Figure 6-7 (a) and (b) Illustration of subtraction procedure for PA6/clay and MXD6/clay films. (c) and (d) Herman orientation function of clay versus draw ratio obtained by subtraction method for precursor and stretched PA6/clay and MXD6/clay.

Due to the broadness of the clay peaks, it was difficult to completely eliminate the peak II and it required many trials to adjust the subtraction factor. The orientation functions obtained by this approach are presented in Figures 6.7c and 6.7d. These results are close to those obtained from

the peak fitting method. As seen in Figure 6.7, uniaxial deformation slightly improves the orientation of the clay platelets in the flow direction for the both nylon nanocomposite films. It should be mentioned that the clay orientation results obtained by FTIR are slightly higher than those obtained by the WAXD technique; however the trends are quite similar (see Figure 6.3).

6.4.2 Effect of Stretching on Orientation of Nylons Crystalline Phase

The surface (MT plane) and cross section (MN plane) WAXD intensity profiles of the precursor and stretched (DR=4) aliphatic and aromatic nylon films are presented in Figure 6.8.

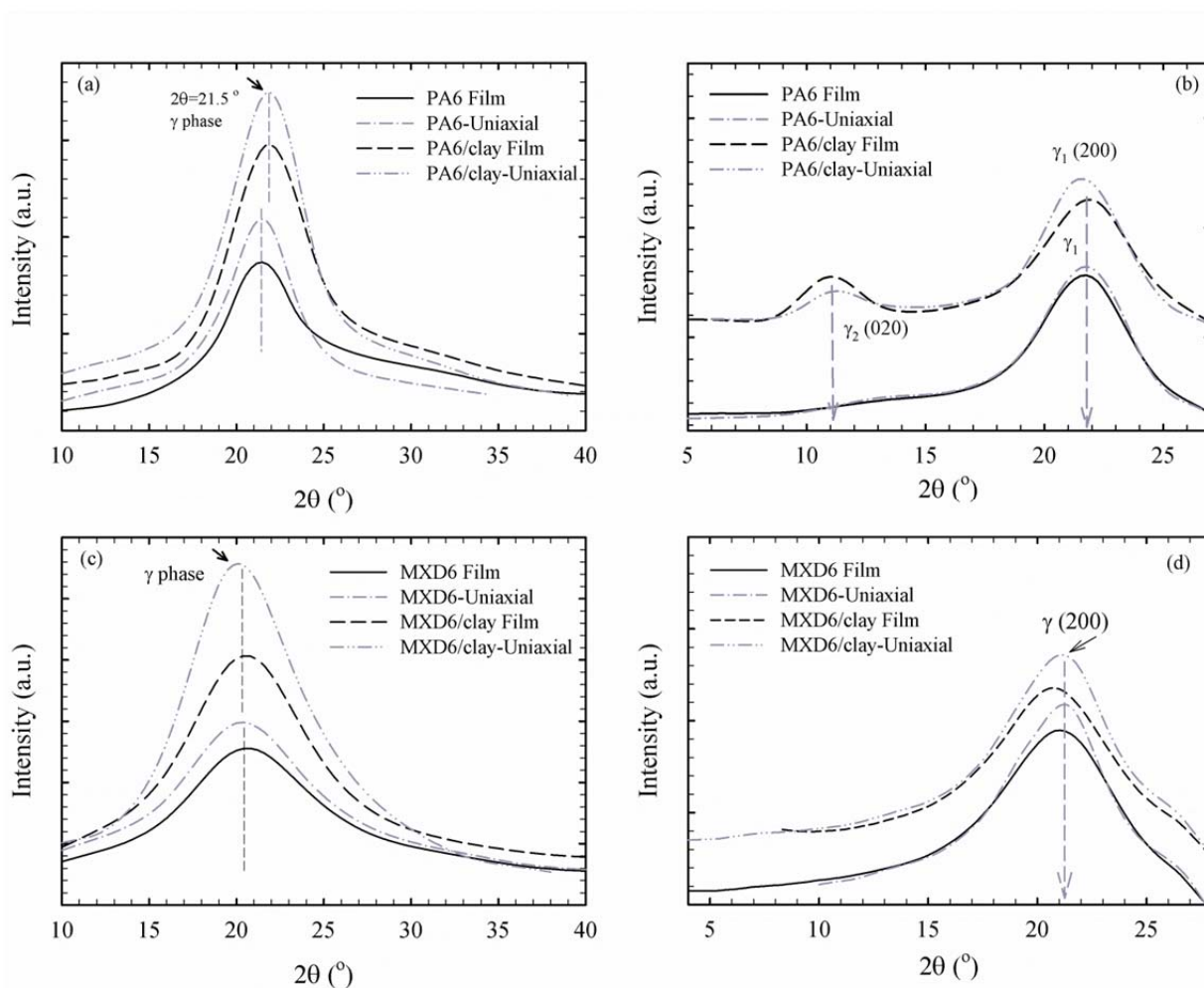


Figure 6-8 Diffraction intensity profiles along MD-TD plane (a) and (c), and MD-ND plane (b) and (d) for precursor and stretched (DR=4) PA6, PA6/clay, MXD6 and MXD6/clay films.

A major diffraction peak at $2\theta = 21.5^\circ$, corresponding to the γ (200) crystal plane^{23, 48}, is observed for all the nylon films. The formation of the γ crystalline structure is a result of fast cooling with air knife after the cast extrusion process^{15, 47, 49}. As shown in Figure 6.8, the precursor and stretched (DR=4) PA6/clay display an additional diffraction peak at $2\theta = 11.2^\circ$, which is attributed to the γ (020) crystal plane⁵⁰. Two populations of γ crystals having different orientations with regards to the oriented clay platelets were observed in the PA6/clay films. The presence of γ (020) reflection in PA6/clay films has also been reported elsewhere^{22, 51, 52}. Henceforth, the γ (200) and γ (020) diffraction peaks in the PA6/clay films in this study are assigned as γ_1 and γ_2 , respectively. As it was observed in Figure 6.1, the diffraction rings before stretching indicate a random distribution of the γ crystal unit cells, hence a low crystalline phase orientation. Upon stretching, diffraction arcs that are sharper and more concentrated in the center are observed, implying more crystalline alignment. The crystalline orientation can be analyzed quantitatively from the WAXD pole figures of the (200) and (020) planes. The pole figures of the γ_1 (200) crystal population plane for the precursor and stretched (DR=4) PA6 and PA6/clay films are illustrated in Figure 6.9. In our recent study²⁸, it was shown that the MXD6 has a lower rate of crystallization and a much longer relaxation time compared to the PA6, which result in a very low level of crystallinity for the former. In the WAXD analysis, employing deconvolution or comparative methods did not allow the separation of the γ phase contribution from the amorphous phase.

The Herman orientation function values of the γ_1 crystal population plane, f_{200} , obtained from the pole figures are displayed in Figure 6.9. These results show that the a -axis of the γ_1 crystal population plane is oriented in TD and ND and its alignment significantly increases upon uniaxial deformation. According to Arimoto et al.³⁷, the hydrogen bonded sheets that build up

between parallel twisted-chains of the γ -form are laying within (200) planes, corresponding to the prominent X-ray reflection.

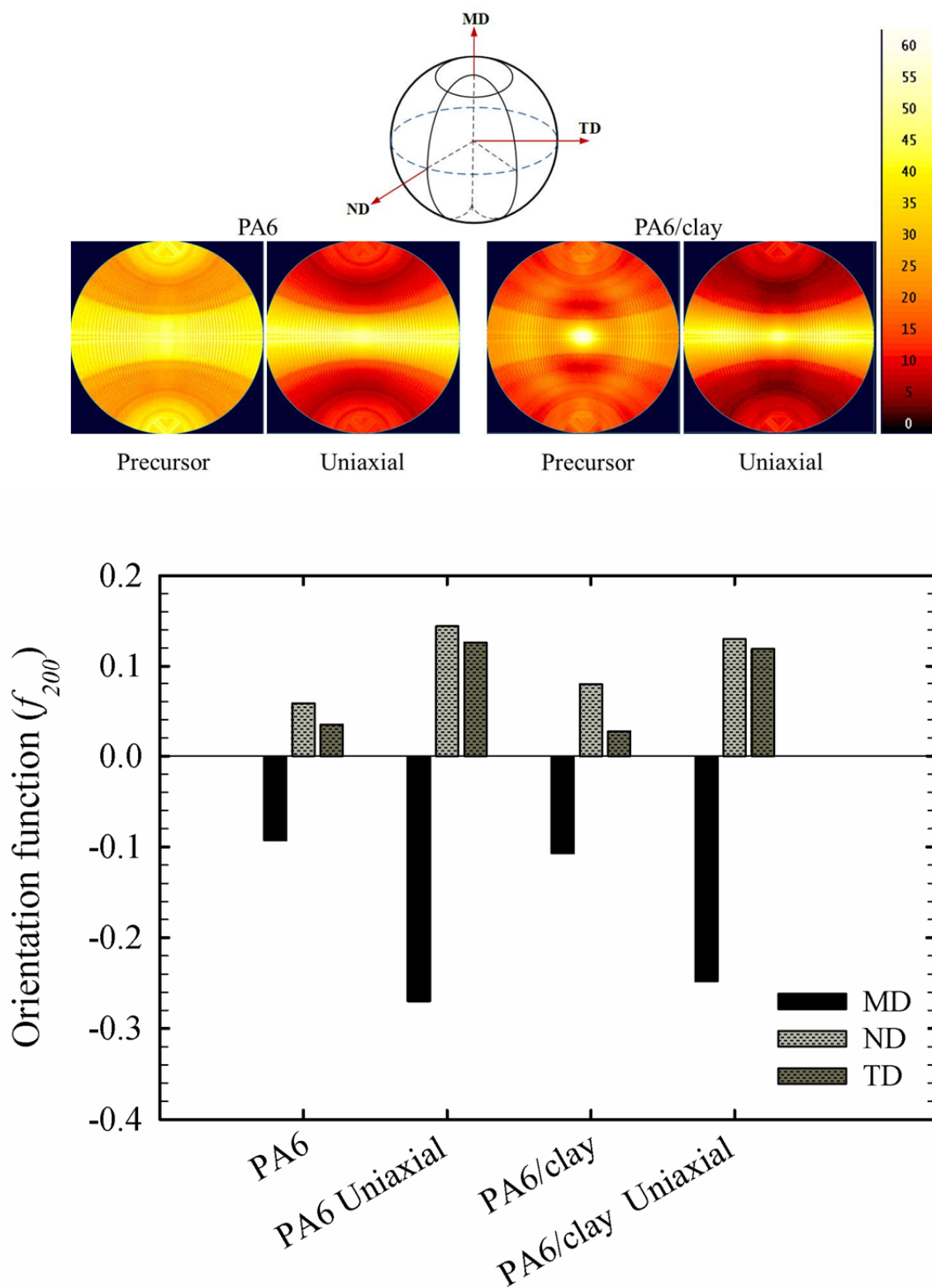


Figure 6-9 Pole figure and Herman orientation function (f_{200}) of the (200) plane of γ_1 crystal population along MD, TD, and ND for precursor and stretched (DR=4) PA6 and PA6/clay films.

FTIR is a powerful technique to measure the orientation functions for the b and c axes of the γ_1 crystal population. The FTIR spectra of the precursor and stretched (DR=4) PA6 and PA6/clay films are illustrated in Figure 6.10.

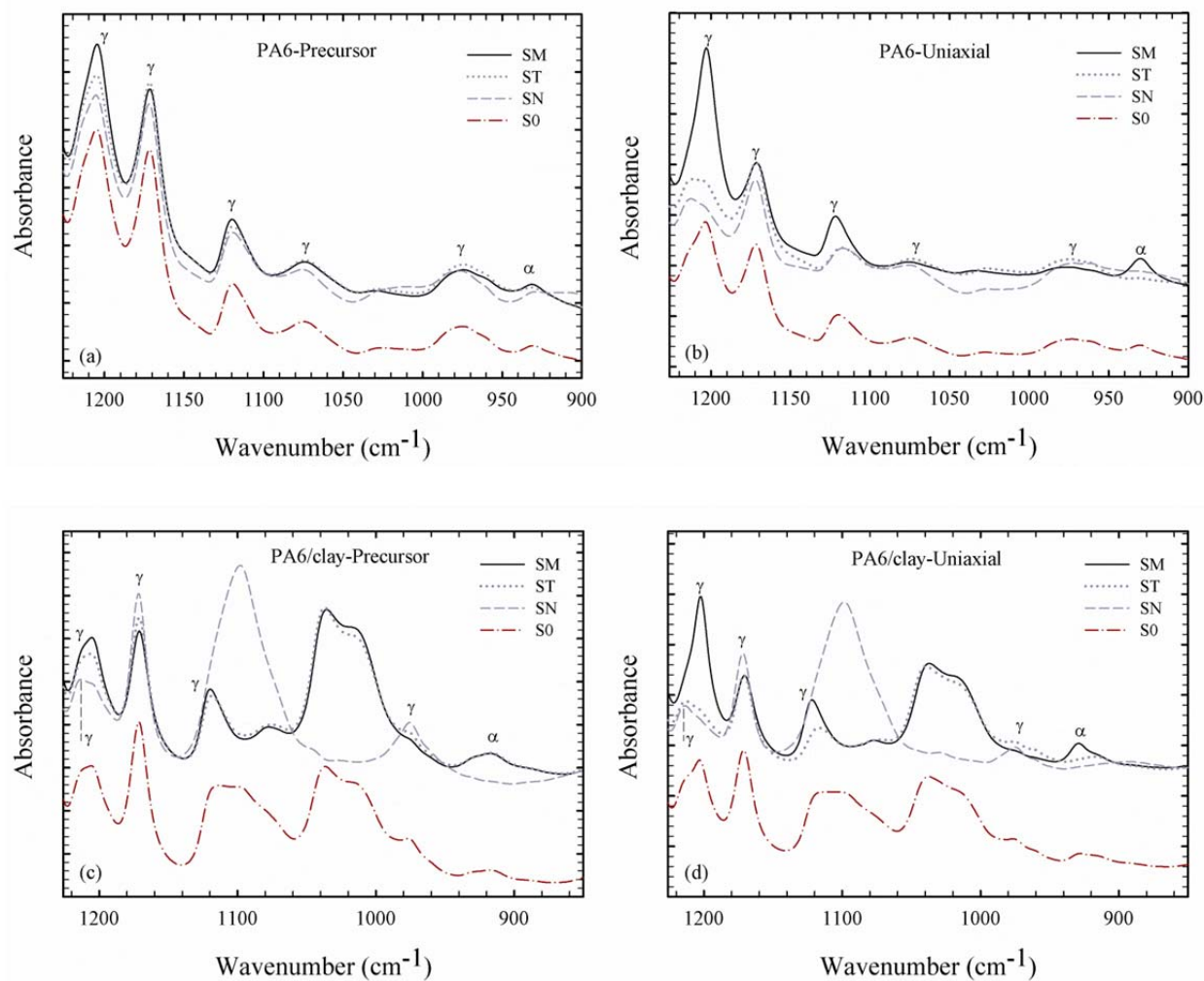


Figure 6-10 FTIR spectra of α and γ phases along MD, TD, calculated ND and structural factor spectrum (S0) for precursor and stretched (DR=4) PA6 and PA6/clay films.

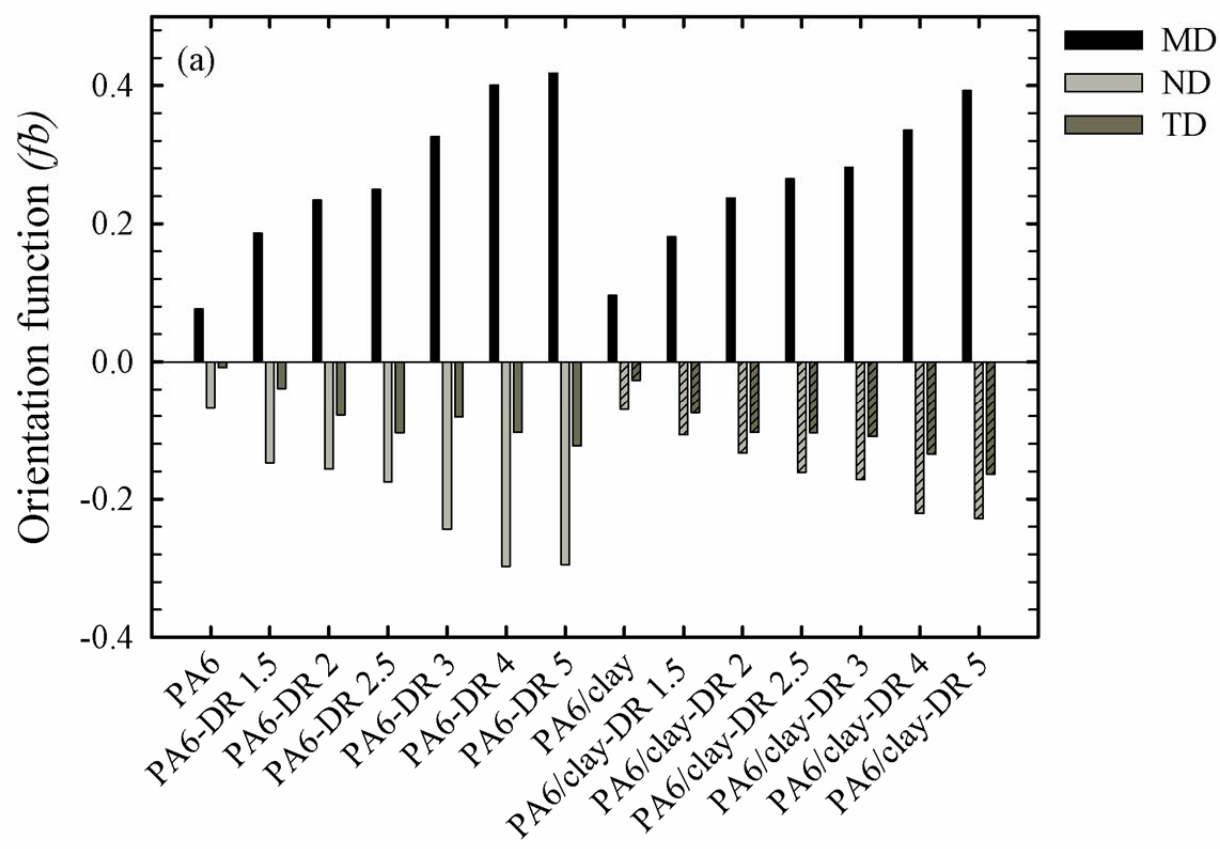
A small peak at the wavenumber of 930 cm^{-1} observed in MD for all the films is a characteristic of the C=O-NH in-plane vibration along the molecular chain³³ and is assigned to the α phase^{13, 14, 19, 36, 48}. Comparing the FTIR spectra in MD with those in TD and ND suggests that this very small population of the α crystals (the α phase was not detected by WAXD) tend to

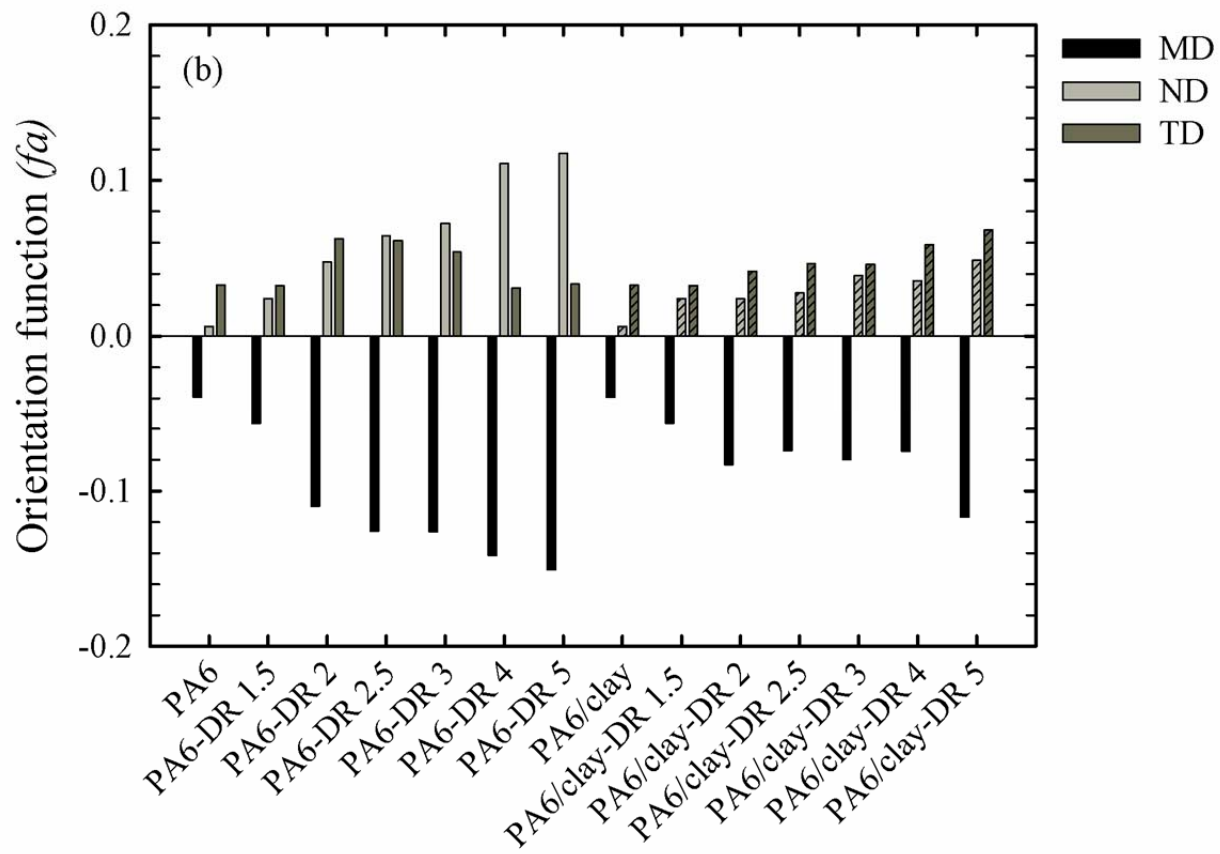
lay parallel to the plane of the film and become more oriented after stretching^{13, 33}. The band absorption at 930 cm⁻¹ is stronger in the machine direction compared to the transverse and normal directions. The difference becomes more pronounced for the uniaxially oriented films. Since the transition moment of the band at 930 cm⁻¹ is parallel to the plane of the hydrogen bonded sheets formed by the α conformation, then the higher value of absorption in MD compared to ND and TD suggests that the hydrogen-bonded sheets in the α phase tend to lay down parallel to the plane of the film and the level of orientation increases by stretching. A high degree of chain alignment of the α phase along the drawing direction at high draw ratios was also reported elsewhere^{13, 33}. According to the WAXD results presented in Figure 6.8, the γ phase is the main notable crystalline structure in the precursor and stretched aliphatic and aromatic nylon film. Therefore, the emphasis of this study is on the orientation of the γ conformation.

The trichroic peak at 1214 cm⁻¹ (related to the CH₂ twisting vibration) has a transition moment parallel to the hydrogen bonded sheets of the γ_1 crystal population³³. As shown in Figure 6.10, this peak has higher intensity in the MD spectrum and becomes stronger after stretching, indicating that the b -axis (parallel to the polymer chain) is oriented more in MD than in TD and ND. This peak was used to measure the orientation function of the b -axis using both Eq. 6.3 and the deconvolution peak fitting technique discussed in the previous section. The trichroic peak at 730 cm⁻¹ (related to the N-H out-of-plane vibration, not shown in Figure 6.10) with a transition moment normal to the hydrogen bonded sheets of the γ_1 crystal population was used to measure the orientation function of the a -axis. The Herman orientation function for the c -axis was calculated from the orthogonality relation:

$$f_{cj} = -f_{bj} - f_{aj} \quad (6.5)$$

The orientation functions for all the axes of the γ_1 crystal population are reported in Figure 6.11.





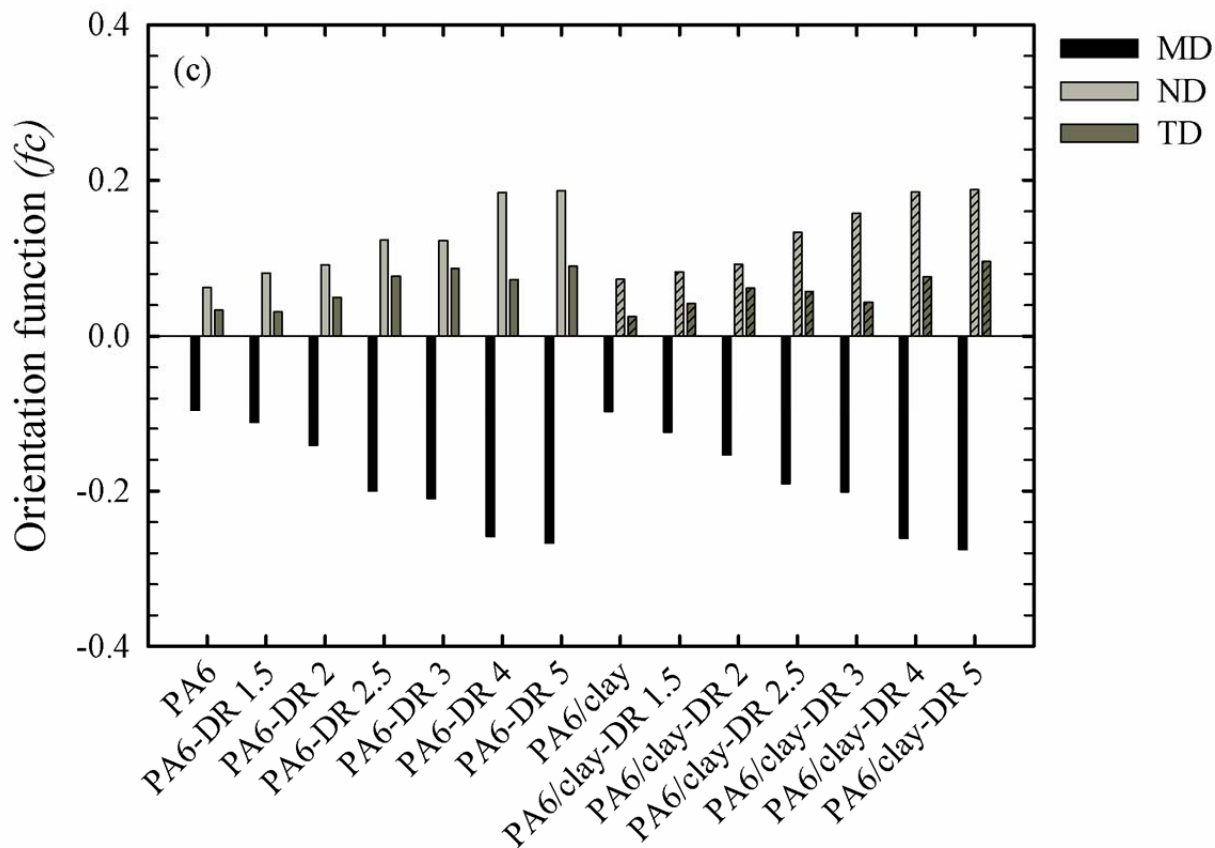


Figure 6-11 Orientation functions of γ_1 crystal population (a) b -axis, (b) a -axis, and (c) c -axis for precursor and stretched PA6 and PA6/clay films.

It is obvious that the b -axis orientation in MD significantly increases by increasing draw ratio. In addition, the b -axis alignment of the PA6/clay films was slightly lower in MD compared to the PA6 films. The precursor films (i.e. DR=1) exhibit the a -axis alignment in both TD and ND with a tendency to orient towards TD. However, after stretching, the a -axis of the PA6 films shows more orientation in ND, especially at high draw ratios. This could be associated to tilting the hydrogen-bonded sheets and their alignment in parallel to the film surface through uniaxial deformation. The a -axis orientation in ND for the PA6/clay is less than that of the PA6 films. It seems that the clay platelets reduce the mobility of the crystal segments and limit the phase

orientation^{7, 16, 45}. Moreover, the presence of the clay platelets decreases the formation of the γ phase hydrogen-bonded sheets^{36, 41, 53}. The c -axis of the precursor films is aligned in both ND and TD with a tendency to orient in ND. After stretching, the c -axis orients more in both TD and ND and takes a position closer to ND. The FTIR results confirm the a -axis orientation function values of the γ_1 crystal population obtained from the WAXD orientation analysis presented in Figure 6.9.

The FTIR spectra of the aromatic nylon films display no preferential alignment in any direction, as depicted in Figure 6.12.

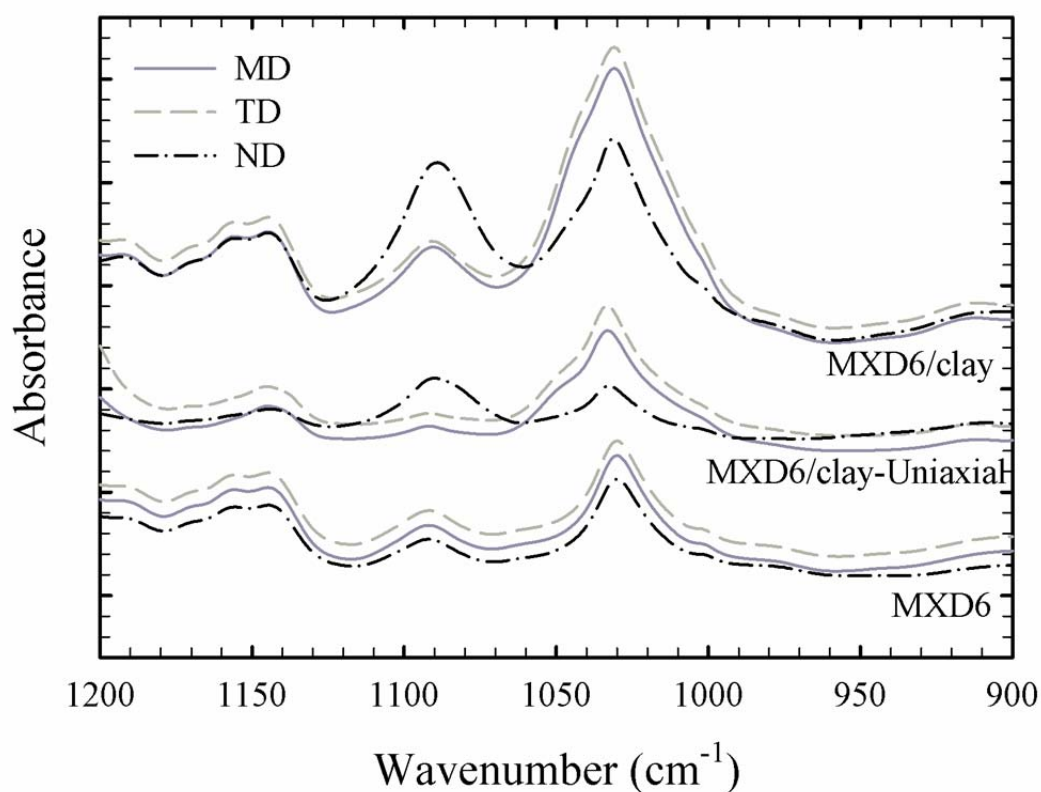


Figure 6-12 Trichroic FTIR spectra for precursor and stretched (DR=4) MXD6 and MXD6/clay films along MD, TD and ND.

In other words, FTIR was not sensitive enough to record any changes in the intensity of the peaks with respect to the film coordinates. The low crystallinity and orientation of the MXD6

could be related to the high level of stiffness of the molecular chains or low relaxation time due to the strong intermolecular entanglement and interaction, which were discussed in our previous work²⁸. In the cast extrusion process, the films were cooled rapidly and therefore, the processing time scale was much shorter than the crystallization characteristic time of the MXD6, resulting in a very low crystallinity²⁸. In Figure 6.12, only the MXD6/clay films show sensitivity to stretching in the trichroic peak at 1083 cm^{-1} . The orientation function values of the MXD6/clay films measured based on the peak at 1083 cm^{-1} are depicted in Figure 6.13. Clearly, the small crystalline phase of the MXD6/clay (induced by the presence of the clay) becomes more oriented upon uniaxial stretching.

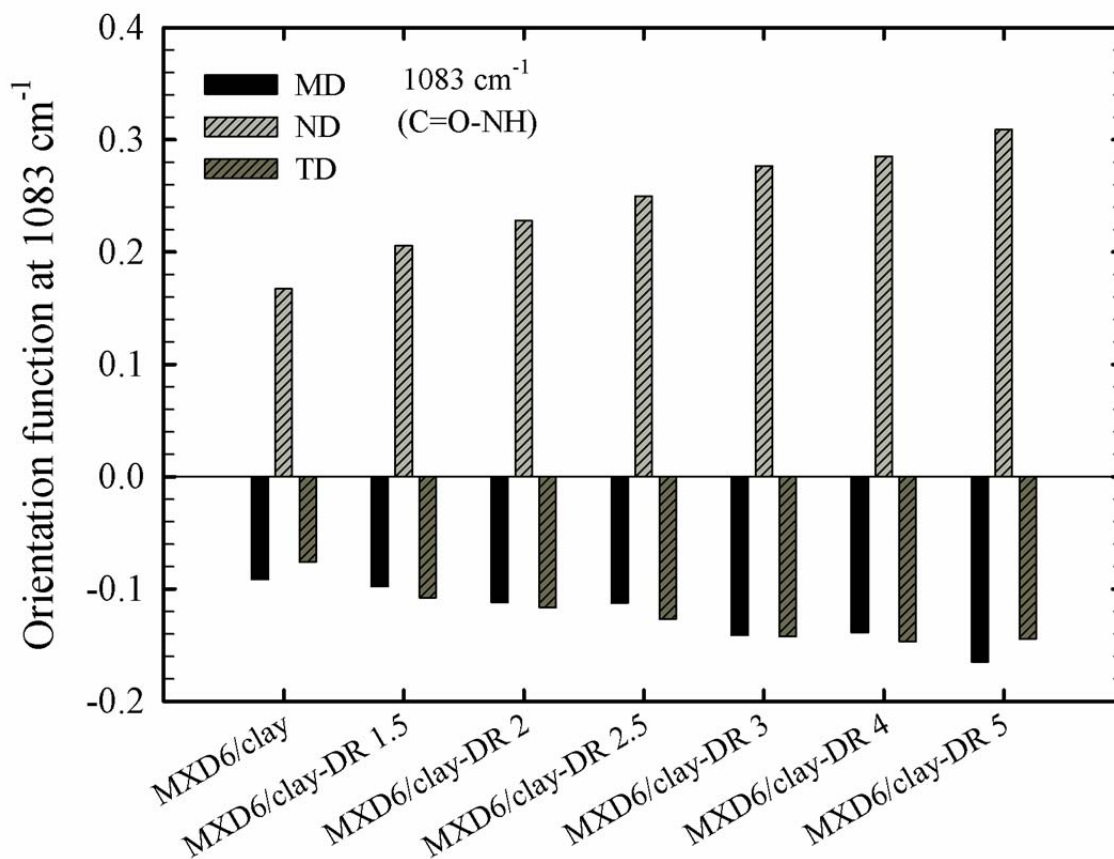


Figure 6-13 Orientation function of amorphous phase from the Trichroism of the peaks at 1083 cm⁻¹ for precursor and stretched MXD6/clay films.

As discussed earlier, the PA6/clay films show a diffraction peak associated with the γ_2 crystal population in the WAXD results (see Figures 6.1 and 6.8). The orientation of the γ_2 crystal population was calculated from the WAXD pole figures of the (020) plane of the crystals in the PA6/clay films and is presented in Figure 6.14. The b -axis of the γ_2 crystal population is preferentially oriented along MD. This orientation increases drastically after uniaxial stretching. The stretched PA6/clay film at DR of 4 has almost three times larger orientation function than the precursor PA6/clay film. The b -axis orientation of the γ_2 crystal population along TD decreased significantly upon uniaxial drawing.

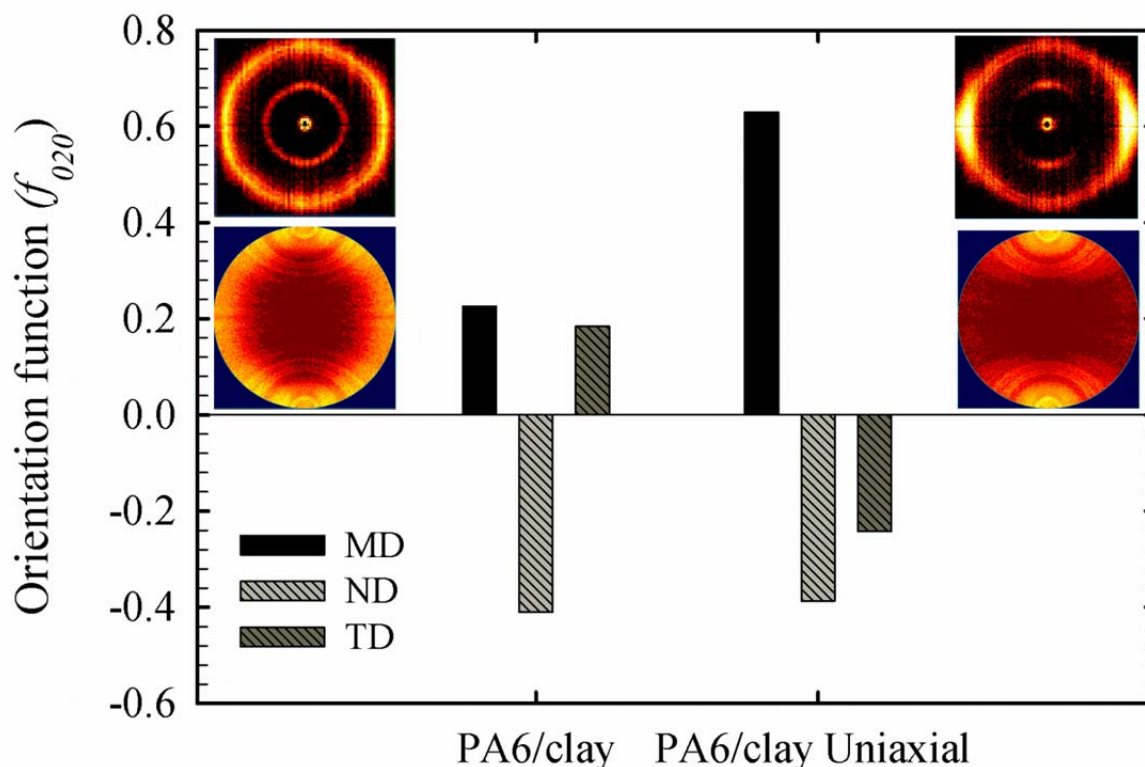
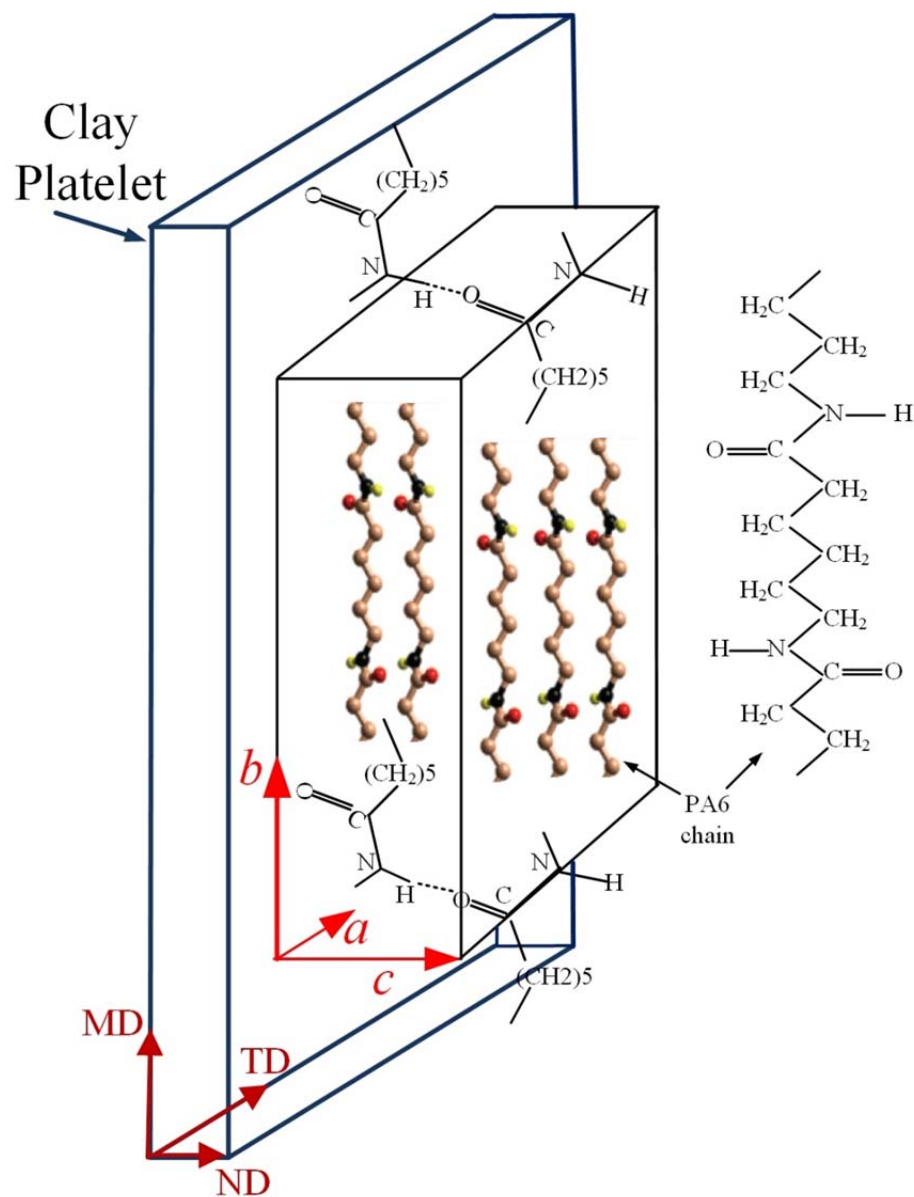


Figure 6-14 Herman orientation function (f_{020}) of the 020 plane of γ_2 crystal population along MD, TD and ND for precursor and stretched (DR=4) PA6/clay films.

It can be concluded that the γ_2 crystal population is oriented in the TD-ND plane of the precursor or stretched PA6/clay films. It is believed that the γ_2 crystal population were attached to the clay platelets via their amide groups, while the hydrogen bonded (C=O–NH) standing up onto the clay platelets (see Figure 6.15 top). In other words, the γ_2 crystal population in the PA6/clay films has a b -axis parallel to MD and a c -axis parallel to the normal vector of the clay plane due to the epitaxial arrangement of the γ_2 population unit cells in the nylon nanocomposites^{15, 16, 22, 44}. This is a different orientation from the γ_1 crystal population.

The FTIR technique was also used to analyze the crystallographic texturing of the γ_2 crystal population. The trichroic peak at 975 cm^{-1} is attributed to the C=O–NH in-plane vibration bond of the γ crystals and was used to calculate the orientation function of the c -axis for the γ_2 crystal

population using Eq. 3 and the deconvolution peak fitting technique^{13, 16, 33, 41, 53, 54}. As illustrated in Figure 6.15, the c -axis of the γ_2 crystal population is strongly aligned in ND of the PA6/clay film (i.e. parallel to the normal vector of the clay plane), which is in agreement with the WAXD results.



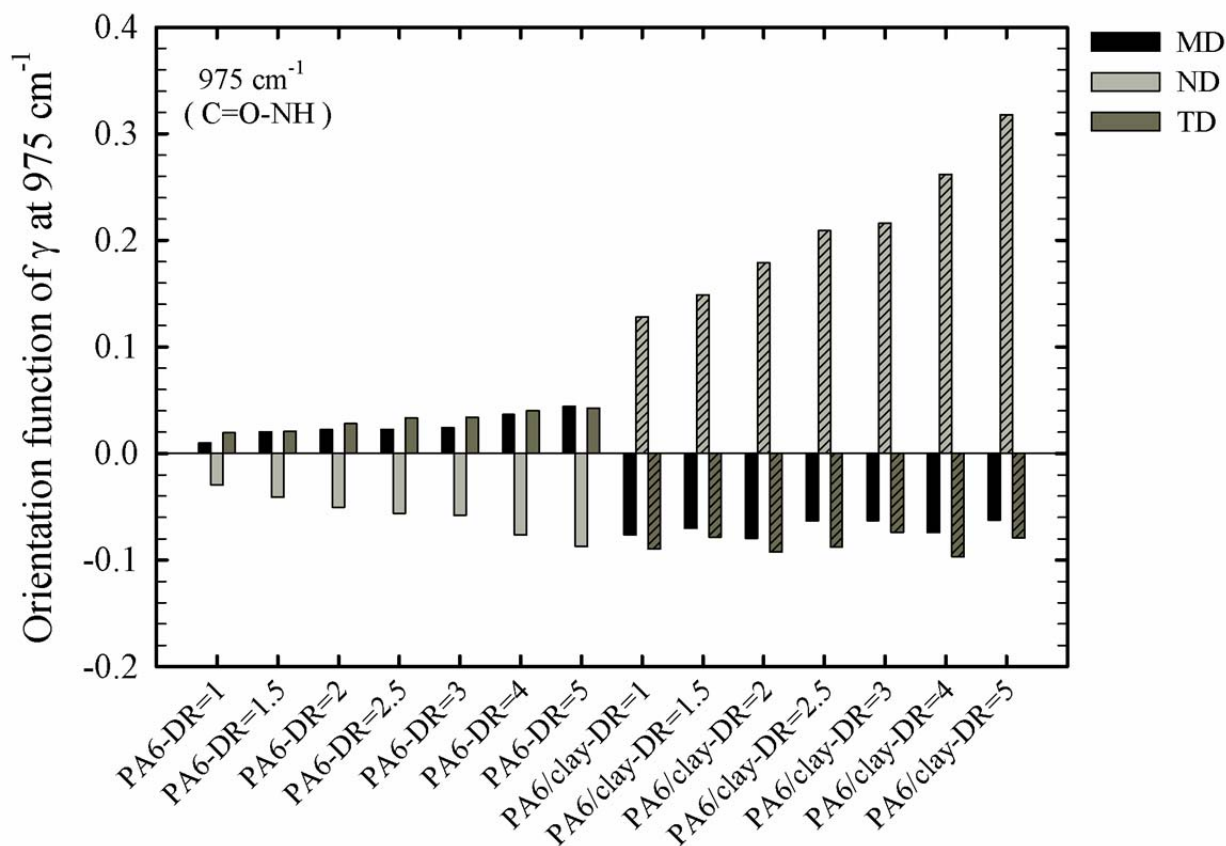


Figure 6-15 (Top) Schematic of γ_2 (020) texturing parallel to the clay platelet. The monomer unit of the PA6 chain has been inspired from Ref. ⁵⁸. (Bottom) Orientation function of γ_2 crystal population from the Trichroism of the peaks at 975 cm⁻¹ for precursor and stretched PA6 and PA6/clay films.

Based on the WAXD patterns and FTIR results, schematic models are proposed in Figure 6.16 to describe the crystallization mechanism of the PA6 in the presence of clay platelets. As illustrated, the γ_1 population crystal units are aligned in the flow direction (MD) and in the presence of clay, another population of crystals, γ_2 , forms perpendicular to the clay surface. The *c*-axis of the γ_1 population crystal unit cells aligns in ND and TD (see Figure 6.11) while the *c*-axis of the γ_2 population crystal units is parallel to ND (see Figure 6.15).

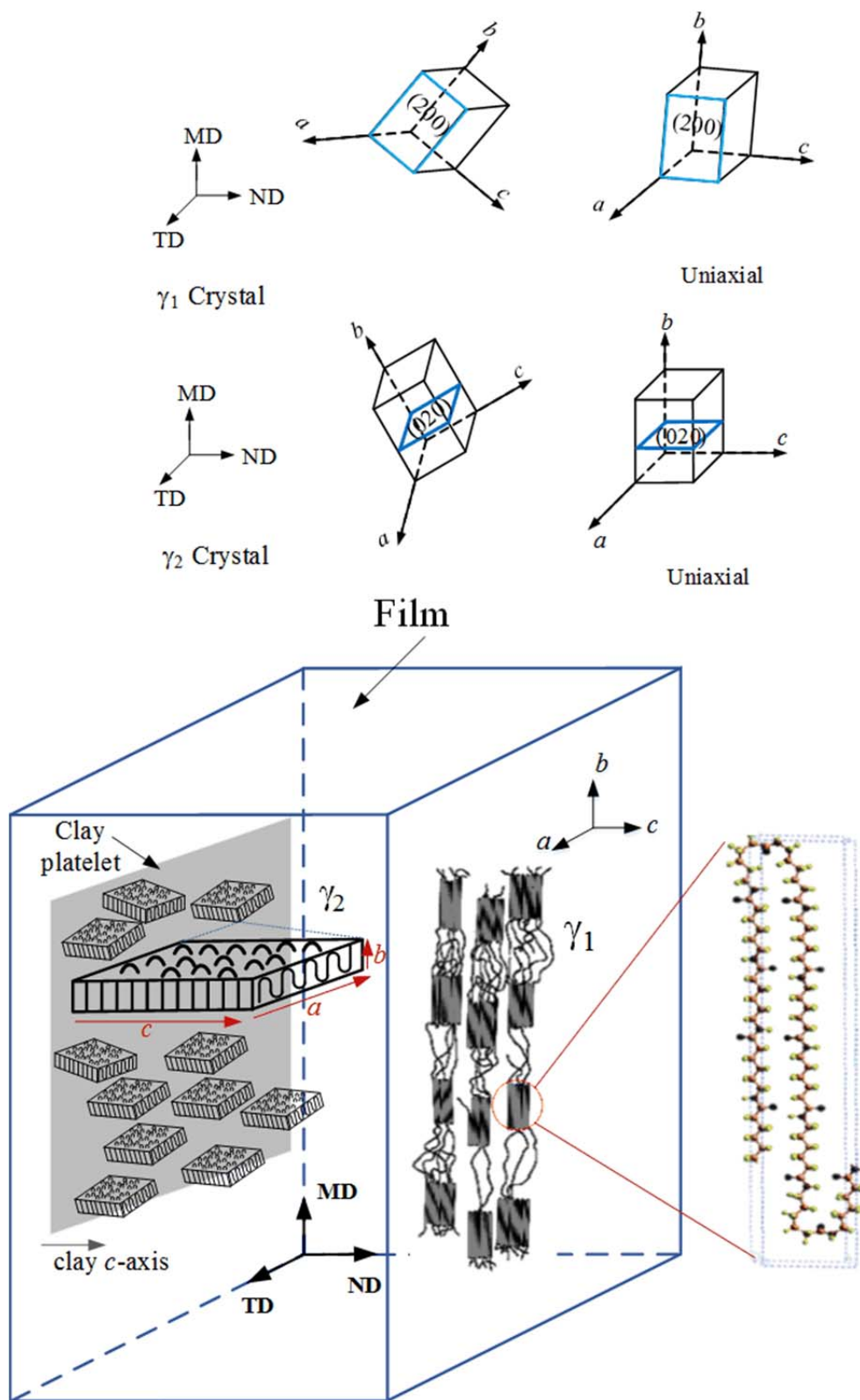


Figure 6-16 (Top) Models for crystalline unit cell orientation of precursor and stretched PA6 and PA6/clay films. (Bottom) Schematics of clay, γ_1 and γ_2 crystal alignments in PA6/clay film.

6.4.3 Effect of Stretching on Orientation of Amorphous Phase

The Trichroic infrared analysis was also used to study the effect of stretching on the orientation of the amorphous region. The trichroic peak at 1120 cm^{-1} (C-C stretching) is attributed to the amorphous phase^{55, 56} and was used to determine the orientation of the amorphous region (using Eq. 6.3) in both the precursor and stretched PA6 and PA6/clay films. Figure 6.17 shows that the amorphous orientation of the precursor films (i.e. DR=1) is quite low compared to the stretched ones due to the increase in the chain motions of the amorphous region during stretching.

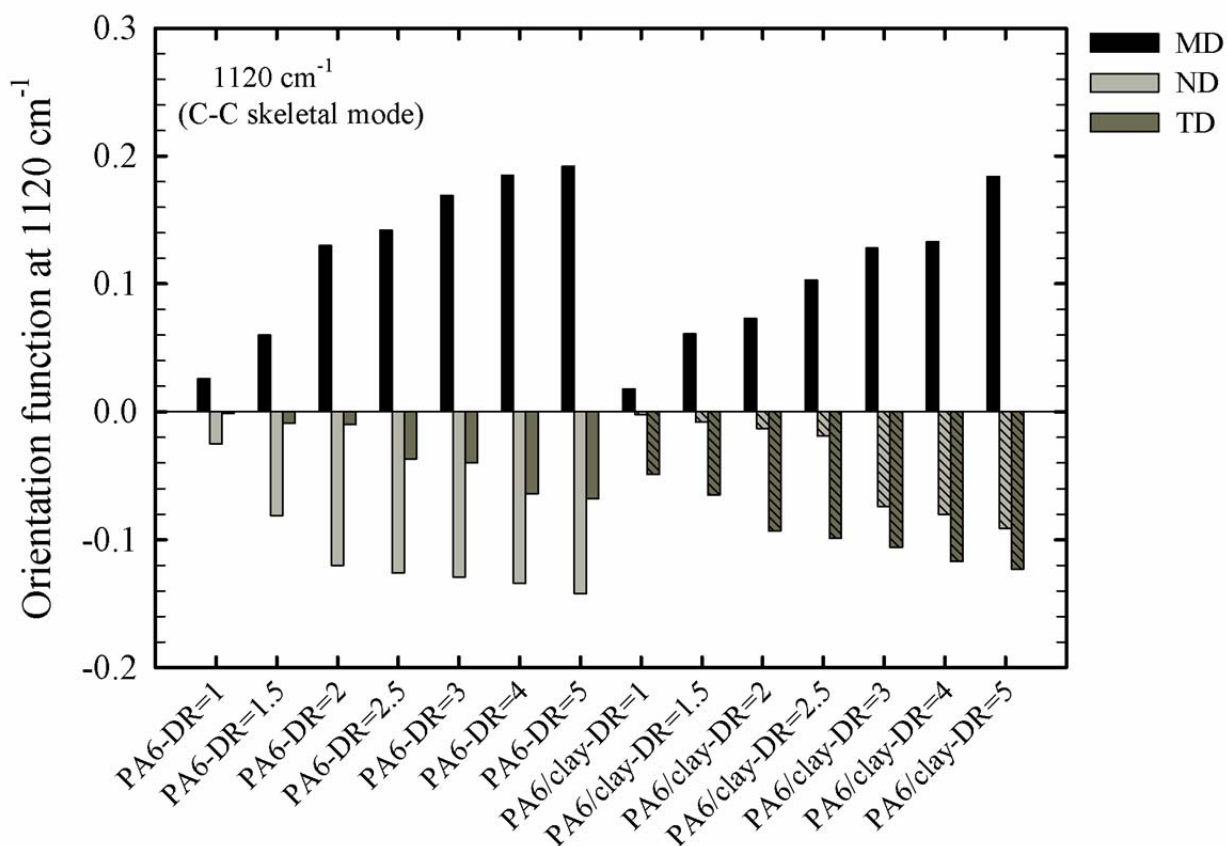


Figure 6-17 Orientation function of amorphous phase from the Trichroism of the peaks at 1120 cm^{-1} for precursor and stretched PA6 and PA6/clay films.

The orientation of the amorphous region in the PA6 films is slightly higher than that of the PA6/clay films, which is related to the spatial hindrance in the vicinity of the clay platelets. It should be mentioned that, as expected, the orientation of the amorphous phase is much lower than the crystalline phase after uniaxial deformation. Considering the Trichroic peak at 1120 cm^{-1} for the MXD6 presented in Figure 6.12, it is clear that the MXD6 amorphous orientation values (are not shown here) are very low compared to the PA6.

Orientation of the crystalline and amorphous phases as well as clay alignment plays an important role in determining the permeability coefficient to diffusing gases through the polymer films. Higher orientation results in a lower diffusion coefficient and hence lower permeability. Our results showed that upon uniaxial stretching, the chain alignment and clay orientation improved significantly; therefore, a significant improvement in the gas barrier property of the stretched films is expected to be obtained. The effect of uniaxial drawing on crystallinity, thermal, mechanical and barrier properties of PA6, MXD6 and their nanocomposites was investigated in our recent study⁵⁷. A significant enhancement in the Young's modulus and tensile strength of the uniaxially stretched aliphatic and aromatic nylons was observed.

6.5 Conclusions

In this study, cast films of the PA6 and MXD6 and their in-situ polymerized nanocomposites were produced and rapidly cooled using an air knife. The precursor films were then uniaxially stretched at $110\text{ }^{\circ}\text{C}$ with draw ratios varying from 1.5 to 5. The effect of uniaxial stretching on the orientation of the clay and crystal axes of all nylons crystalline phases as well as the amorphous region was investigated using X-ray diffraction and Trichroic Infrared analyses. The clay orientation was measured with three different techniques: FTIR peak deconvolution, FTIR interactive spectral subtraction, and X-ray diffraction. Our findings showed that the clay platelets

were mainly oriented in MD and their orientation was slightly increased after uniaxial deformation. The WAXD and FTIR results showed that, during cast extrusion process with rapid cooling, the γ crystal population (designated γ_1 here) was mainly formed. Only the PA6/clay films showed a second γ crystal population (designated γ_2) and which was related to the formation of crystals on the surface of the clay platelets. The c -axis of the γ_1 crystal population was oriented in ND and TD, while the c -axis of the γ_2 crystal population was aligned in ND. It was concluded that the γ_2 crystal population were formed perpendicular to the (001) plane of the clay platelets. The orientation of both the γ_1 and γ_2 crystal populations increased upon uniaxial stretching. A small amount of the α phase crystals in the aliphatic nylons was found by FTIR and their orientation improved after uniaxial deformation. Also, the aromatic nanoclay composite films showed a small amount of crystalline phase induced by the presence of the clay. Finally, the amorphous phase showed a lower orientation in the nanocomposite films, which was explained by the spatial hindrance caused by the presence of the clay platelets.

6.6 Acknowledgments

The authors would like to thank NSERC (Natural Science and Engineering Research Council of Canada) and the industrial partners of 3SPack Chair Saputo and Prolamina for funding this project and financial support.

6.7 References

1. Cho, J.W. and D.R. Paul, *Nylon 6 nanocomposites by melt compounding*. Polymer, 2001. 42(3): p. 1083-1094.
2. Fornes, T.D., et al., *Nylon 6 nanocomposites: the effect of matrix molecular weight*. Polymer, 2001. 42(25): p. 09929-09940.
3. Mohanty, S. and S.K. Nayak, *Mechanical, thermal and viscoelastic behavior of nylon 6/clay nanocomposites with cotreated montmorillonites*. Polymer-Plastics Technology and Engineering, 2007. 46(4): p. 367-376.
4. Yeh, J.-T., et al., *Oxygen barrier and blending properties of blown films of blends of modified polyamide and polyamide-6 clay mineral nanocomposites*. Applied Clay Science, 2009. 45(Compendex): p. 1-7.
5. Usuki, A., et al., *Characterization and properties of nylon 6. Clay hybrid*. 1990, ACS: Washington, DC, USA. p. 651-652.
6. Picard, E., et al., *Barrier properties of nylon 6-montmorillonite nanocomposite membranes prepared by melt blending: Influence of the clay content and dispersion state: Consequences on modelling*. Journal of Membrane Science, 2007. 292(1-2): p. 133-144.
7. Sadeghi, F. and A. Ajji, *Structure, Mechanical and Barrier Properties of Uniaxially Stretched Multilayer Nylon/Clay Nanocomposite Films*. International Polymer Processing, 2012. 5: p. 565-573.
8. Tabatabaei, S.H., P.J. Carreau, and A. Ajji, *Structure and properties of MDO stretched polypropylene*. Polymer, 2009. 50(16): p. 3981-3989.
9. Tabatabaei, S.H. and A. Ajji, *Crystal structure and orientation of uniaxially and biaxially oriented PLA and PP nanoclay composite films*. Journal of Applied Polymer Science, 2012. 124(6): p. 4854-4863.
10. Tabatabaei, S.H., P.J. Carreau, and A. Ajji, *Microporous membranes obtained from PP/HDPE multilayer films by stretching*. Journal of Membrane Science, 2009. 345(1-2): p. 148-159.
11. Sadeghi, F., et al., *Properties of uniaxially stretched polypropylene films: effect of drawing temperature and random copolymer content*. Canadian Journal of Chemical Engineering, 2010. 88(6): p. 1091-1098.
12. Zhang, X.M., et al., *Oriented structure and anisotropy properties of polymer blown films: HDPE, LLDPE and LDPE*. Polymer, 2004. 45(1): p. 217-229.
13. Cole, K.C., et al., *Biaxial deformation of polyamide-6: Assessment of orientation by means of infrared trichroism*. Polymer Engineering and Science, 2004. 44(2): p. 231-240.

14. Cole, K.C., J. Denault, and M.N. Bureau, *Infrared spectroscopy studies of structure and orientation in clay-reinforced polyamide-6 nanocomposites*. Macromolecular Symposium, 2004. 205(1): p. 47-60.
15. Miri, V., et al., *Crystallization Kinetics and Crystal Structure of Nylon6-Clay Nanocomposites: Combined Effects of Thermomechanical History, Clay Content, and Cooling Conditions*. Macromolecules, 2008. 41(23): p. 9234-9244.
16. Maiti, P. and M. Okamoto, *Crystallization Controlled by Silicate Surfaces in Nylon 6-Clay Nanocomposites*. Macromolecular Materials and Engineering, 2003. 288(5): p. 440-445.
17. Liu, X. and C. Breen, *High-Temperature Crystalline Phases in Nylon 6/Clay Nanocomposites*. Macromolecular Rapid Communications, 2005. 26(13): p. 1081-1086.
18. Shishan, W., et al., *The structure and properties of PA6/MMT nanocomposites prepared by melt compounding*. Polymer Engineering and Science, 2004. 44(11): p. 2070-2074.
19. Penel-Pierron, L., et al., *Structural and mechanical behavior of nylon 6 films part I. Identification and stability of the crystalline phases*. Journal of Polymer Science Part B: Polymer Physics, 2001. 39(5): p. 484-495.
20. Penel-Pierron, L., et al., *Structural and mechanical behavior of nylon-6 films. II. Uniaxial and biaxial drawing*. Journal of Polymer Science Part B: Polymer Physics, 2001. 39(11): p. 1224-1236.
21. Seguela, R., *On the Strain-Induced Crystalline Phase Changes in Semi-Crystalline Polymers: Mechanisms and Incidence on the Mechanical Properties*. Journal of Macromolecular Science, Part C, 2005. 45(3): p. 263-287.
22. Yalcin, B., et al., *Molecular origins of toughening mechanism in uniaxially stretched nylon 6 films with clay nanoparticles*. Polymer, 2008. 49(6): p. 1635-1650.
23. Miri, V., et al., *Strain-induced disorder–order crystalline phase transition in nylon 6 and its miscible blends*. Polymer, 2007. 48(17): p. 5080-5087.
24. Devaux, E., S. Bourbigot, and A. El Achari, *Crystallization behavior of PA-6 clay nanocomposite hybrid*. Journal of Applied Polymer Science, 2002. 86(10): p. 2416-2423.
25. Bureau, M.N., et al., *The role of crystallinity and reinforcement in the mechanical behavior of polyamide-6/clay nanocomposites*. Polymer Engineering and Science, 2002. 42(9): p. 1897-1906.
26. Kojima, Y., et al., *Novel preferred orientation in injection-molded nylon 6-clay hybrid*. Journal of Polymer Science Part B: Polymer Physics, 1995. 33(7): p. 1039-1045.
27. Fong, H., et al., *Generation of electrospun fibers of nylon 6 and nylon 6-montmorillonite nanocomposite*. Polymer, 2002. 43(3): p. 775-780.

28. Fereydoon, M., S.H. Tabatabaei, and A. Ajji, *Rheological, crystal structure, barrier, and mechanical properties of PA6 and MXD6 nanocomposite films*. Polymer Engineering & Science, 2013. published online: p. n/a-n/a.
29. Ammala, A., et al., *Poly(m-xylene adipamide)-montmorillonite nanocomposites: effect of organo-modifier structure on free volume and oxygen barrier properties*. Journal of Materials Chemistry, 2008. 18(8): p. 911-916.
30. Prattipati, V., et al., *Improving the transparency of stretched poly(ethylene terephthalate)/polyamide blends*. Journal of Applied Polymer Science, 2006. 99(1): p. 225-235.
31. Ben Doudou, B., E. Dargent, and J. Grenet, *Relationship between draw ratio and strain-induced crystallinity in uniaxially hot-drawn PET-MXD6 films*. Journal of Plastic Film & Sheeting, 2005. 21(3): p. 233-251.
32. Hu, Y.S., et al., *Improving transparency of stretched PET/MXD6 blends by modifying PET with isophthalate*. Polymer, 2005. 46(14): p. 5202-5210.
33. Sibilgia, J.P., *Orientation in nylon 6 films as determined by the three-dimensional polarized infrared technique*. Journal of Polymer Science Part A-2: Polymer Physics, 1971. 9(1): p. 27-42.
34. Garton, A., D.J. Carlsson, and D.M. Wiles, *Molecular Orientation Measurements in Polymers by Infrared Spectral Subtraction*. Appl. Spectrosc., 1981. 35(4): p. 432-435.
35. Holmgren, A. and X. Yang, *A Polarized Fourier Transform Infrared Spectrometry Attenuated Total Reflection Study of Bentonite Settled onto Magnetite*. The Journal of Physical Chemistry C, 2008. 112(42): p. 16609-16615.
36. Loo, L.S. and K.K. Gleason, *Fourier Transform Infrared Investigation of the Deformation Behavior of Montmorillonite in Nylon-6/Nanoclay Nanocomposite*. Macromolecules, 2003. 36(8): p. 2587-2590.
37. Arimoto, H., et al., *Crystal structure of the γ -form of nylon 6*. Journal of Polymer Science Part A: General Papers, 1965. 3(1): p. 317-326.
38. Cullity, B.D. and S.R. Stock, *Elements of X-Ray Diffraction*. 2 ed. 2001, New Jersey: Prentice Hall.
39. Bafna, A., et al., *3D Hierarchical orientation in polymer-clay nanocomposite films*. Polymer, 2003. 44(4): p. 1103-1115.
40. Usuki, A., et al., *Three-Dimensional Observation of Structure and Morphology in Nylon-6/Clay Nanocomposite*. Nano Letters, 2001. 1(5): p. 271-272.

41. Cole, K.C., F. Perrin-Sarazin, and G. Dorval-Douville, *Infrared Spectroscopic Characterization of Polymer and Clay Platelet Orientation in Blown Films Based on Polypropylene-Clay Nanocomposite*. *Macromolecular Symposia*, 2005. 230(1): p. 1-10.
42. Krishnamoorti, R., J. Ren, and A.S. Silva, *Shear response of layered silicate nanocomposites*. *Journal of Chemical Physics*, 2001. 114(11): p. 4968-4973.
43. Wang, X., et al., *Unusual Rheological Behavior of Liquid Polybutadiene Rubber/Clay Nanocomposite Gels: The Role of Polymer–Clay Interaction, Clay Exfoliation, and Clay Orientation and Disorientation*. *Macromolecules*, 2006. 39(19): p. 6653-6660.
44. Farmer, V.C. and J.D. Russell, *The infra-red spectra of layer silicates*. *Spectrochimica Acta*, 1964. 20(7): p. 1149-1173.
45. Na, B., et al., *Suppressed molecular orientation in nylon 6/clay nanocomposite at large strain: Role of microvoiding*. *Journal of Polymer Science Part B: Polymer Physics*, 2010. 48(5): p. 514-519.
46. Cole, K.C., *Use of Infrared Spectroscopy To Characterize Clay Intercalation and Exfoliation in Polymer Nanocomposites*. *Macromolecules*, 2007. 41(3): p. 834-843.
47. Galeski, A., A.S. Argon, and R.E. Cohen, *Deconvolution of x-ray diffraction data to elucidate plastic deformation mechanisms in the uniaxial extension of bulk nylon 6*. *Macromolecules*, 1991. 24(13): p. 3945-3952.
48. Clarey, M., et al. *Removal of impurities from clay where purified clay is useful as filler in plastics involves centrifuging followed by ion-exchanging the clay to replace monovalent cations for multivalent cations in the clay interlayer*. 1998 18 Apr 2000; Available from: <Go to ISI>://DIIDW:2000349243.
49. Zhao, X.-y., *Thermal history dependence of polymorphic transformation of polyamide 6/silicate nanocomposites*. *Polymer International*, 2009. 58(5): p. 469-474.
50. Ho, J.-C. and K.-H. Wei, *Induced $\gamma \rightarrow \alpha$ Crystal Transformation in Blends of Polyamide 6 and Liquid Crystalline Copolyester*. *Macromolecules*, 2000. 33(14): p. 5181-5186.
51. Yebra-Rodriguez, A., et al., *Influence of processing conditions on the optical and crystallographic properties of injection molded polyamide-6 and polyamide-6/montmorillonite nanocomposites*. *Applied Clay Science*, 2011. 51(4): p. 414-418.
52. Poisson, C., et al., *Mechanical, optical and barrier properties of PA6/nanoclay-based single- And multilayer blown films*. *Polymers and Polymer Composites*, 2008. 16(6): p. 349-358.
53. Wu, Q., X. Liu, and L.A. Berglund, *FT-IR spectroscopic study of hydrogen bonding in PA6/clay nanocomposites*. *Polymer*, 2002. 43(8): p. 2445-2449.

54. Sallem-Idrissi, N., et al., *Trichroic infrared analysis of the strain-induced structural changes in the PA6 layer of PA6/PE multilayer films under biaxial drawing*. *Polymer*, 2009. 50(24): p. 5812-5823.
55. Vasanthan, N., *Determination of Molecular Orientation of Uniaxially Stretched Polyamide Fibers by Polarized Infrared Spectroscopy: Comparison of X-ray Diffraction and Birefringence Methods*. *Appl. Spectrosc.*, 2005. 59(7): p. 897-903.
56. Kimura, N., et al., *Molecular Orientation and Crystalline Structure of Aligned Electrospun Nylon-6 Nanofibers: Effect of Gap Size*. *Macromolecular Materials and Engineering*, 2010. 295(12): p. 1090-1096.
57. Fereydoon, M., S.H. Tabatabaei, and A. Aji, *Effect of Uniaxial Deformation on Thermal, Oxygen Barrier and Mechanical Properties of PA6 and MXD6 Nanocomposite Films*. has been submitted to *Polymer Engineering & Science*, 2013: p. n/a-n/a.
58. Li, Y. and W.A. Goddard, *Nylon 6 Crystal Structures, Folds, and Lamellae from Theory*. *Macromolecules*, 2002. 35(22): p. 8440-8455.

CHAPTER 7

Effect of Uniaxial Deformation on Thermal, Oxygen Barrier and Mechanical Properties of PA6 and MXD6 Nanocomposite Films³

Maryam Fereydoon, Seyed H. Tabatabaei and Abdellah Aji*

3SPack NSERC-Industry Chair, CREPEC, Chemical Engineering Department, Polytechnique Montreal, C.P. 6079, Succ. Centre ville, Montreal, QC, Canada H3C 3A7

(* All correspondence should be addressed to: abdellah.ajji@polymtl.ca

Abstract

In this study, the effect of uniaxial stretching on the thermal, oxygen barrier and mechanical properties of aliphatic (PA6) and aromatic (MXD6) nylon films as well as their in-situ polymerized nanocomposites with 4 wt% clay were studied. Cast films were prepared by extrusion process and rapidly cooled using an air knife. The precursor films were uniaxially stretched at 110 °C with draw ratios varying from 1.5 to 5. DSC results showed that the cold crystallization temperature (T_{cc}) of the uniaxially stretched MXD6 and MXD6/clay films drastically shifted to the lower temperatures when draw ratio increased. The aromatic nylon films had lower oxygen permeability than those of the aliphatic films, due to more rigidity and chain packing. However, the oxygen permeability of the stretched films increased with draw ratio (DR) up to a critical value for each sample, while further stretching resulted in a reduction in the oxygen permeation. This phenomenon was related to the changes in free volume upon uniaxial stretching. The ability of different geometrical models to describe the experimental relative permeability data was investigated. A model that took into account clay orientation was the most

³ Submitted to *Polymer Polymer Engineering and Science*.

successful one to predict the oxygen barrier characteristics of the stretched nanocomposites at high draw ratios. The Young's modulus and tensile strength of the aliphatic and aromatic nylons increased with uniaxial deformation, while the flexibility and elongation at break of the former decreased with increasing DR. In contrast, the flexibility of the stretched MXD6 improved remarkably (ca. 25 times) compared to the precursor film (DR=1) when the draw ratio increased to 1.5. This could be related to the effect of hot stretching on the enhancement of polymer chains relaxation and mobility at low draw ratios.

Keywords: Nylons, Nanocomposites, Uniaxial Stretching, Crystallization, Oxygen Permeability, Modeling, Mechanical Properties.

7.1 Introduction

Improving the barrier properties of commercial thermoplastics to the permeation of atmospheric gases such as oxygen or water vapor, and consequently increasing the shelf-life of food products, is one of the main challenges in the packaging industry.

Many attempts have been done to improve the final properties of films by post processing such as uniaxial or biaxial stretching. Stretching can result in a highly oriented film, reduced oxygen permeability [1, 2], improved water vapor barrier [3, 4] and improved mechanical strength and clarity [5-7]. However, it lowers elongation at break [7] and tear resistance along machine direction (MD) upon uniaxial stretching [1]. For instance, gas permeability of polypropylene was improved by a factor of 2 after biaxial orientation without sacrificing clarity and toughness of the films [8]. The oxygen diffusivity, solubility and consequently its permeability, were reduced for Poly (ethylene terephthalate) (PET) films after uniaxial stretching, due to a reduction in the amount of excess-hole free volume in the polymer [9]. In another study, it was shown that orientation decreased the permeability of uniaxial stretched PET

to almost one-third of the undrawn film [10]. Uniaxial orientation also significantly improved the O₂ and CO₂ barrier properties of poly (ether block amide) (PEBA) copolymers [11]. The molecular motion that facilitates the movement of permeant molecules through a polymer film reduces by the extent of orientation upon stretching process. In fact, molecular orientation leads to a reduction in the diffusion coefficient of gases through polymers. The reduction in gas permeability could be also attributed to an increase in the crystallinity induced during stretching [11].

Polyamide 6 (PA6) as an aliphatic engineering thermoplastic is extensively used in food packaging due to its high stiffness, toughness, tensile strength, flex crack and puncture resistance as well as low oxygen transmission rate. The structural development of nylon films during uniaxial stretching are influenced by initial morphology, molecular orientation, ability to crystallize (i.e. fast or slow crystallization rate), type of crystalline structure and physical state of the material (i.e. glassy, rubbery, partially molten or fully molten). Additionally, the final properties of stretched films are strongly dependent on processing conditions such as stretching rate, extent of deformation and stretching temperature. The uniaxial stretching of PA6 to a draw ratio of 3 resulted in a 62.5% reduction in the oxygen transmission rate, a 17.4 % improvement in the puncture resistance, and also a 53 % increase in the clarity [12].

In the past two decades, incorporating silicate nano-layers having high aspect ratio (such as montmorillonite) into nylon matrices has received attention to improve mechanical and barrier performance of nylon products [13-18]. During the cast film extrusion process, these nano-platelets could be oriented in the flow direction and subsequently enhance the gas barrier performance of the nylon nanocomposite films [12, 19]. It was also reported that, even at a small draw ratio of 1.5, the mechanical strength of PA6/clay increased by 55% [12]. Another study

showed that biaxial orientation of PA6 nanocomposite films was 1.5 times more efficient on improving the mechanical properties compared to uniaxial drawing the same conditions [20].

Poly (m-Xylene Adipamide) (MXD6) is a semi-crystalline aromatic nylon with better mechanical performance, barrier property, high temperature resistance and less moisture sensitivity in comparison with PA6 [21]. According to our recent study [21], the crystallinity of MXD6 films was lower compared to PA6 films, however, the permeability to oxygen was more than 5 times better for the former. MXD6 showed much larger Young's modulus and tensile strength compared to PA6 film. Thus, MXD6 could be considered as a potential candidate to replace PA6 for some packaging applications.

A study showed that the crystallinity of a PET/MXD6 blend film was improved 40% upon uniaxial stretching when draw ratio increased to 5 [22]. In fact, the spherical MXD6 particles in PET matrix transformed into platelets with high aspect ratio arrayed in the plane of the film during the stretching. Consequently, the diffusion path for gas molecules became more tortuous, resulting in a lower permeability [22]. Another study showed that the transparency of PET/MXD6 blend improved up to 70 % through biaxial orientation [23].

Although few authors have investigated the structure of PA6/clay nanocomposite films upon uniaxial and biaxial drawing [19, 24]; but to our knowledge, no effort has been dedicated to study the stretching of MXD6/clay nanocomposite films. Additionally, no comparison between the structure, mechanical and barrier properties of uniaxially oriented aliphatic (PA6) and aromatic (MXD6) nylon nanocomposite films has yet been made.

In our previous study, the changes in orientation of clay, crystalline phase and amorphous region of uniaxially stretched aliphatic and aromatic nylons and their nanocomposite films were examined [25]. It was found that the clay platelets are mainly oriented in the machine direction

(MD) and their orientation improved upon uniaxial stretching. Our findings indicated the c -axis of γ_1 crystal population was oriented in the normal and transverse directions (ND and TD), while the c -axis of γ_2 was aligned in the normal direction (ND), indicating that this later crystal population formed perpendicular to the (001) plane of the clay platelets [25]. The orientation of γ_1 and γ_2 crystal populations increased after uniaxial deformation. Finally, the amorphous phase showed a lower orientation in the nanocomposite films compared to neat samples.

In this study, the effect of uniaxial drawing on crystal structure, thermal, mechanical and barrier properties of polyamide 6 (PA6), poly (m-xylene adipamide) (MXD6) and their in-situ polymerized nanocomposites with 4 wt% clay were investigated. Furthermore, the oxygen relative permeability of the precursor and uniaxially oriented nanocomposite films has been determined with different geometrical models. From the quantitative orientation of the nanoclay particles obtained from our previous study [25], the ability of the models to describe the effective theoretical aspect ratio of the clay is discussed.

7.2 Experimental

7.2.1 Materials

PA6 (Ultramid B36, from BASF) and PA6/clay nanocomposites (Cress-Alon™ NF3040, from CP polymers) were selected as the aliphatic nylon and its nanocomposite, respectively. The montmorillonite content of NF3040 is 4 wt% with aspect ratios of 200 to 300 (reported by the supplier). MXD6 6007 resin and Imperm 103, which is a nanocomposite of MXD6 resin with montmorillonite clays, supplied by Nanocor (in partnership with Mitsubishi Gas Chemical) were selected as the aromatic nylon and its nanocomposite, respectively. According to Nanocor, the silicate layered montmorillonite content of the Imperm 103 nanocomposite MXD6 is between

3.3 to 3.6 wt% with aspect ratios of 200 to 400. The main characteristics of the materials used in this study are listed in Table 7.1.

Table 7.1 Main characteristics of materials used in this study (reported by suppliers).

Material	Commercial name	Supplier	Nomenclature	Main characteristics
Nylon 6	Ultramid B36	BASF (Freeport, USA)	PA6	$M_n = 18,000 \text{ g.mol}^{-1}$ $\rho = 1.14 \text{ g.cm}^{-3}$ $\eta_r = 3.6$ MFI (275°C/5kg) = 10 g/10 min
Nylon 6/clay	NF3040	CP Polymers (Montebello, USA)	PA6/clay	$\rho = 1.15 \text{ g cm}^{-3}$ $\eta_r = 3$ MFI (230°C/5kg) = 8.9 g/10 min Clay content = 4 wt%
Aromatic Nylon	MXD6 6007	Mitsubishi Gas Chemical (Colonial Heights, USA)	MXD6	$M_n = 25,000 \text{ g.mol}^{-1}$ $\rho = 1.21 \text{ g.cm}^{-3}$ $\eta_r = 2.7$ MFI (230°C/5kg) = 12 g/10 min
Aromatic Nylon/clay	Imperm 103	Nanocor (Arlington Heights, USA)	MXD6/clay	$\rho = 1.22 \text{ g.cm}^{-3}$ $\eta_r = 2.5$ Clay content = 3.3 to 3.6 wt%

M_n : Number average molecular weight

ρ : Density

η_r : Relative viscosity = (η/η_0) where η_0 is the viscosity of the solvent.

MFI: Melt flow index

7.2.2 Film preparation

The cast films of nylon and nylon/clay materials were prepared using a fully intermeshing co-rotating twin-screw extruder (Leistritz ZSE 18 HP) (Nuremberg, Germany) with 18 mm screw diameter and a length/diameter (L/D) of 40. To minimize degradation, the screw configuration was set to yield a low to medium shear environment during extrusion. The aromatic (i.e. MXD6 and MXD6/clay) and aliphatic nylons (i.e. PA6 and PA6/clay) were dried prior to extrusion in a

vacuum oven at 130 °C for 5 h and at 80 °C for 24 h, respectively. The screw speed was 200 rpm and the temperature profile from the hopper to the die was 230/240/245/255/260 °C for the aliphatic nylons and 235/250/255/260/265 °C for the aromatic ones. The extruder was equipped with a slit die followed by rapid cooling using an air knife. Chill rolls set at ambient temperature were used to stretch the precursor films to obtain 60-70 µm thick films. The precursor films were kept in desiccators (under vacuum) for further characterizations.

The uniaxial stretching was carried out on 5 cm × 1.5 cm × 70 µm precursor films using an Instron (Instron Electro Puls E3000, UK) apparatus equipped with a heating chamber. The uniaxial stretching was performed at 110 °C, an optimized speed of 400 mm/min and draw ratios from 1.5 to 5. Before drawing, the films were kept at 110 °C in the heating chamber of the tensile machine for 10 min to allow a homogenous temperature distribution. Stress-strain curves (data are not shown) exhibited a plateau plastic deformation after the yield point for the stretched films at all draw ratios. All the samples were rapidly air cooled to room temperature and then removed from the clamps for further characterizations.

7.3 Characterization

Thermal analysis

Differential Scanning Calorimetry (DSC) Q1000 (TA Instruments, New-Castle, DE, USA) was used for thermal analysis of the films. The scanning cycle was conducted between 10 to 280 °C under heating rates of 10 °C/min. The melting, crystallinity, and glass transition behavior of the specimens were obtained and discussed.

The crystallinity of the produced films was calculated according to the following equation:

$$X_c (\%) = \frac{\Delta H_m - \Delta H_{cc}}{\Delta H_0(1 - x)} \times 100 \quad (7.1)$$

where x is the percentage of the clay, ΔH_m and ΔH_{cc} are the melting and cold crystallization enthalpy obtained from the heating scan and ΔH_o is the heat of fusion for 100% crystalline PA6 and MXD6, which are taken as 190 and 175 J/g, respectively [18, 26].

The weight percentage of nanofillers was determined by Thermal Gravimetric Analysis (TGA) Q500 (TA Instruments, New-Castle, DE). The samples were heated from 30 to 500 °C at 10 °C/min and from 500 to 800 °C at 50°C/min under helium atmosphere.

X-ray diffraction

Wide angle X-ray diffraction (WAXD) measurements were carried out using Philips X'Pert X-ray apparatus (Netherlands). The generator was set up at 50 kV and 40 mA and a copper $\text{CuK}\alpha$ radiation ($\lambda=1.54 \text{ \AA}$) was selected. The samples were scanned from 10 to 50° at 0.04 °/s for exploring nylon crystalline structure.

Morphology

Transmission electron microscopy (TEM) (JEOL JEM-2100F, Japan, operating at 200 kV) was used to observe clay exfoliation and dispersion quality in the aromatic and aliphatic nylon matrices. The specimens were impregnated in epoxy resin and microtomed in the MD-ND plane using an Ultracut FC microtome (Leica, Germany) with a diamond knife. The TEM micrographs were used to measure the average aspect ratio of the dispersed clays. The micrographs were manually digitized using a digitizing table from Wacom and SigmaScan v.5 software (SPSSInc., USA) and a digitizing tablet (Wacom, Japan).

Barrier property

Oxygen transmission rate (OTR) for the precursor and stretched films in accordance with the D-3985-81 ASTM standard was measured using MOCON OXTRAN (Minneapolis, USA) oxygen permeability tester at 25 °C, 0% relative humidity, and 1 atm pressure. A mixture of 98%

nitrogen (N_2) and 2% hydrogen (H_2) was used as the carrier gas and 100% oxygen (O_2) was used as the test gas. The test was ended when the oxygen flux changed by less than 1% during a 40 min test cycle. The reported data have been normalized (multiplied) by the films' thickness and are an average of four tests.

Mechanical properties

Tensile tests in both machine and transverse directions (MD and TD, respectively) were carried out using INSTRON-3365 (USA). Young modulus, tensile toughness, elongation at break and yield strength of the films were measured according to D 882-02 ASTM standard. Samples with 25 mm width, 250 mm length, and 30 μm thickness were stretched at a rate of 5 mm/min.

7.4 Results and Discussion

7.4.1 Nanoclay dispersion

No peak in the cross-section diffraction intensity profiles of the precursor and stretched (DR=4) PA6/clay and MXD6/clay films at low 2θ (below 10°) are observed (Figure 7.1a).

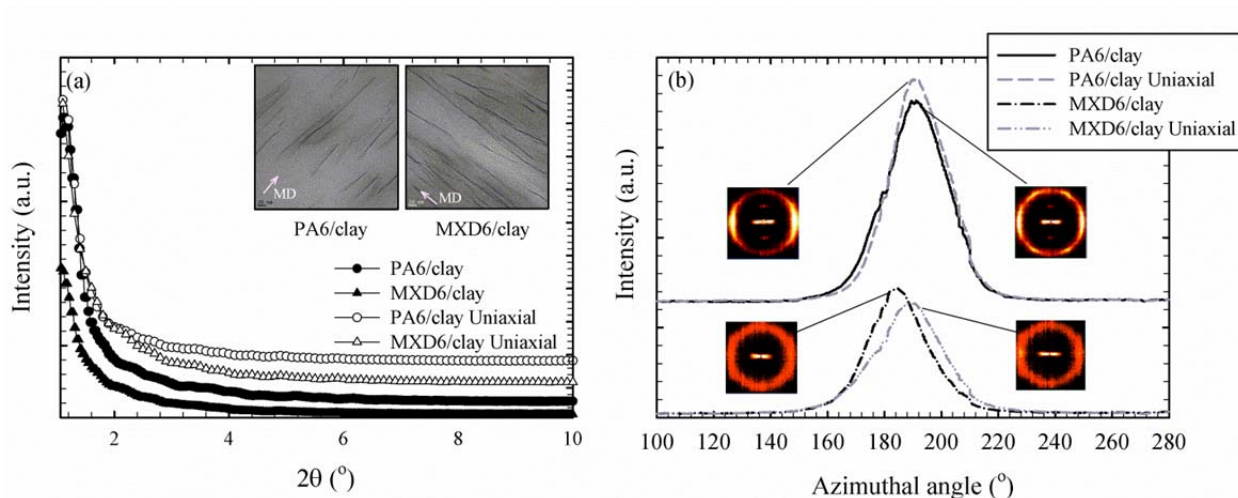


Figure 7-1 (a) TEM micrographs and cross-section diffraction intensity profiles for precursor stretched (DR=4) PA6/clay and MXD6/clay in MD-ND plane. (b) 2D WAXD patterns and azimuthal intensity profiles at 2θ of the 001 clay reflection plane for precursor and stretched (DR=4) PA6/clay and MXD6/clay.

This indicates that the dispersed clay in the nylon nanocomposite films are close to the state of exfoliation [27, 28], which is attributed to the good affinity between the nylon matrices and clay platelets [14]. In addition, the PA6 and MXD6 nylons were in-situ polymerized in the presence of clay. The TEM micrographs in Figure 7.1a display the individual dispersed silicate layers in both the aliphatic and aromatic nylon nanocomposite films, confirming the XRD results. Also, it is clear that the individual layers are perfectly aligned in the machine direction (MD). Clay platelets have a high tendency to orient themselves in the flow direction during the cast film process [29, 30], due to their planar structure with a high aspect ratio [19]. The qualitative comparison between the nanoclay orientation of the precursor and stretched samples

can be better shown when the intensity is plotted as a function of the azimuthal angle. Figure 7.1b shows a noticeable peak at the azimuthal angle of 180° . The azimuthal angle is 0 or 180° along the equator and 90 or 270° along the meridian. This also confirms that the silicate layers are oriented in the flow direction in both the precursor and stretched PA6/clay and MXD6/clay films. The full width at half maximum (FWHM) is 25.8 and 27.3 for the precursor PA6/clay and MXD6/clay films, respectively, and reduced to 22.6 and 23.7 for the uniaxially drawn films, implying a higher orientation of the clay platelets in the stretched samples.

7.4.2 Crystallinity

The crystalline structure and crystallinity of the precursor and stretched PA6, MXD6 and their nanocomposites films were investigated by wide angle X-ray diffraction (WAXD) and differential scanning calorimetry (DSC). Polyamide 6 (PA6) displays a polymorphic crystalline behavior [21] and depending on the processing conditions and its thermo-mechanical history, different crystalline forms (i.e. α and γ) have been reported in uniaxially and biaxially oriented PA6 and PA6/clay films [31-33].

The diffractograms of the precursor and stretched aliphatic and aromatic nylon films obtained from wide angle X-ray diffraction (WAXD) are presented in Figure 7.2.

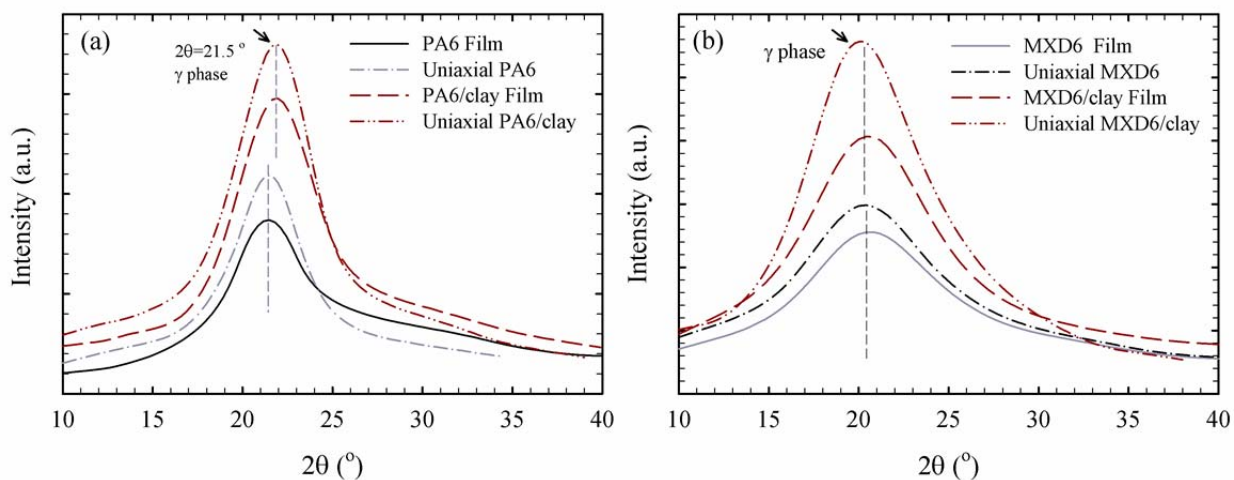


Figure 7-2 XRD patterns for precursor and stretched (DR=4) (a) PA6 and PA6/clay, and (b) MXD6 and MXD6/clay films.

A major diffraction peak at $2\theta = 21.5^\circ$ corresponding to the γ (200) crystalline phase [34, 35] is observed for both the precursor and stretched aliphatic nylon films. The formation of the γ crystalline structure is a result of fast cooling with air knife right after die exit [28, 36]. The aromatic nylon shows a much wider diffraction peak compared to the aliphatic one. The wide diffraction peak between $2\theta = 15$ to 25° with a maximum intensity at 20.7° is related to the amorphous phase of the MXD6. The precursor and stretched MXD6/clay films reveal almost the same diffraction peak and a very little crystallinity due to high rigidity and low relaxation rate of the aromatic chains [21].

To analyze the thermal behavior of the precursor and stretched nylon films, DSC experiments were performed and the thermograms of the first heating scans are presented in Figures 7.3 and 7.4.

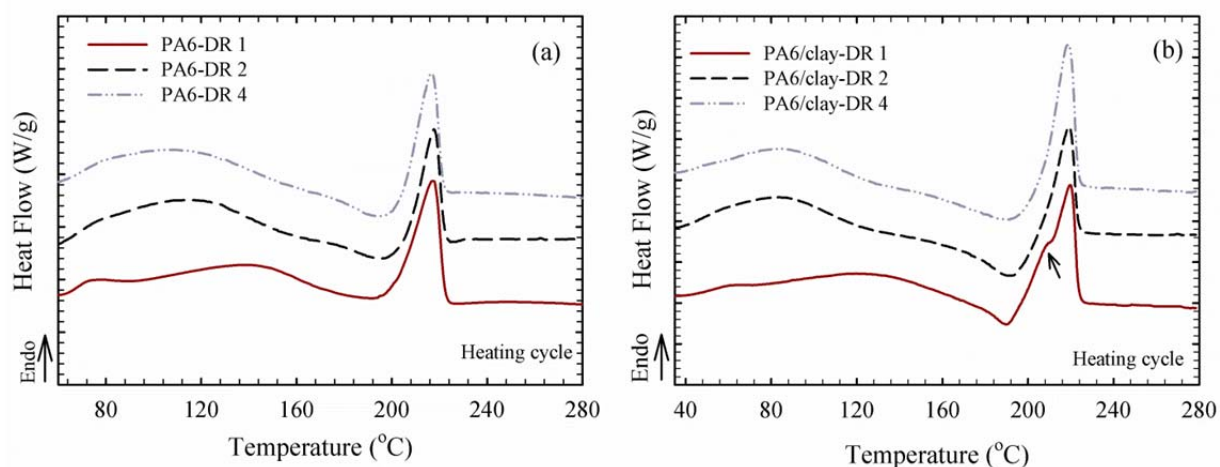


Figure 7-3 First heating ramp of DSC thermograms for precursor and stretched (a) PA6, and (b) PA6/clay films.

The endothermic peak at 220 °C in the first heating ramp of the precursor and stretched PA6 films (Figure 3a) is due to the melting of the α -form crystals. A sharp peak at 220 °C and a small shoulder at 212 °C are seen in the first heating cycle of the precursor PA6/clay film (Figure 7.3b). These are associated with the melting of the thermally stable α and less stable γ crystalline phases, respectively [28]. Magniez et al. [37] suggested that the clay nanoparticles act as heterogeneous nucleating sites, which can create a different crystalline phase than the polymer matrix. The DSC results show coexisting α and γ crystals in the precursor PA6/clay nanocomposite whereas the XRD results revealed the presence of only γ phase. This can be explained by the formation of the γ crystalline phase during the cast film processing with fast air cooling and their transformation to the more stable α -form during the DSC heating scan [38]. In other words, since the γ crystalline form of the precursor PA6 is thermodynamically unstable, it is completely converted to the α crystalline form prior to the final crystal melting in the DSC heating scan. The addition of clay in the PA6 facilitates the formation of the aligned arrays of H-bonded sections that act as stable γ nuclei, capable of remaining intact in the melt state for longer periods of time [32, 33]. The DSC results show coexisting α and γ crystals in the precursor

PA6/clay nanocomposite and the presence of only γ phase in the uniaxially stretched PA6/clay samples (Figure 7.3b). Structural evolution analysis of nylon6 nanocomposite films during uniaxial stretching concluded that the γ - α phase transition occur under specific conditions [33]. First, a sufficient extension for the γ phase is required to untwist the chain around the amide group. Second, an adequate molecular mobility is needed to change the stacking in the crystalline structure [19]. The γ - α strain-induced transition becomes more important in drawing polyamide at high temperatures due to the improvement in chain mobility of crystals [33, 34]. A wide exothermic peak at 80 °C appears in the first heating scan of the uniaxially stretched PA6 and PA6/clay films, which could be attributed to the chain relaxation of the oriented films above the glass transition temperature (T_g) [33].

In our previous study [21], a cold crystallization exothermic peak in the first heating scan of precursor MXD6 and MXD6/clay was observed in the range of 104-134 °C and 97-131 °C respectively, which is in a good agreement with the results reported in other studies [26, 39]. The cold crystallization exothermic peaks of the uniaxially stretched MXD6 and MXD6/clay films are depicted in Figure 7.4.

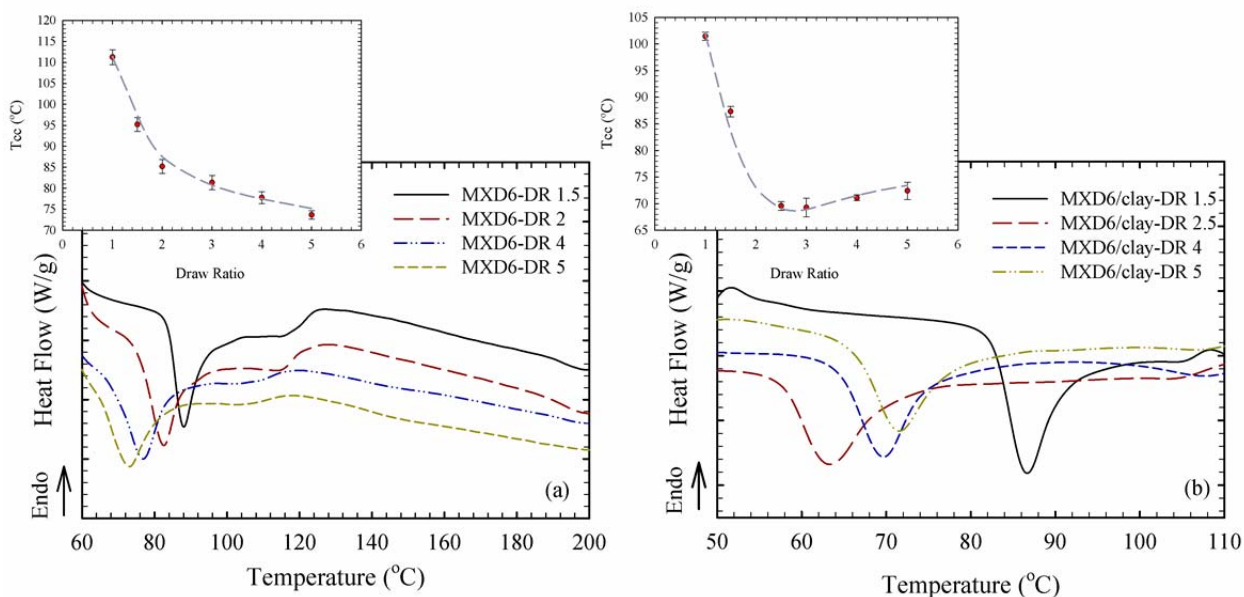


Figure 7-4 First heating ramp of DSC thermograms for precursor and stretched (a) MXD6, and (b) MXD6/clay films.

The cold crystallization temperatures (T_{cc}) lowers with increasing draw ratios. This is in accordance with the results reported for biaxially stretched MXD6 [22]. During film processing, orientation of the MXD6 chains takes place such that they can act as nucleating sites for further crystallization by increasing temperature [40]. Additionally, the presence of clay in the matrix provides more nucleating sites, hence, the cold crystallization of the precursor MXD6/clay is lower compared to the neat sample. It should be noted that at all drawing ratios, the shape of the cold crystallization peak remains the same in both the precursor and stretched films. Increasing draw ratio up to 4 shifted the cold crystallization temperature of the stretched MXD6 film below the T_g (i.e. 83 °C), of the precursor film, which was also reported for biaxially drawn MXD6 [22]. This phenomenon becomes more dominant in the stretched MXD6/clay films (Figure 7.4b). The plot of the cold crystallization temperature as a function of draw ratio for the MXD6/clay films shows two domains (Figure 7.4b). The cold crystallization temperature (T_{cc}) first decreases

when draw ratio increases up to 3 and then it raises with further increasing DR. Increasing the cold crystallization temperature after a certain critical draw ratio was also observed for poly(ethylene terephthalate) (PET) films upon uniaxial [41] and biaxial [22] stretching. The existence of pre-orientation of the molecular chains is an important factor contributing to the decreases in the thermal cold crystallization. In our recent study [25], it was shown that the crystalline orientation function of the neat and nanocomposite aromatic and aliphatic nylon films increased upon uniaxial drawing. The partially oriented polymer chains act as nucleating sites for further crystallization at high temperature. It was shown that the presence of clay in the MXD6 improved the orientation of the polymer chains [25], which act as the nucleating sites for further cold crystallization in the first heating ramp of DSC. At the draw ratios higher than 3, it seems that the ability of the chains to crystallize during the DSC heating cycle decreases for the stretched MXD6/clay films. It has been suggested that the presence of water molecules during stretching has a significant influence on the crystallinity of uniaxially stretched MXD6/clay films [41]. In the other words, the strain-induced crystalline phase can appear during the uniaxial deformation of the MXD6/clay above a critical draw ratio. It can be concluded that with the presence of moisture in the drawn MXD6/clay films, the enthalpy of the extra-cold crystallization reduces at high draw ratios. The same phenomenon was reported during the uniaxial drawing of Poly(ethylene terephthalate) films [41]. It has been reported that moisture does not affect the crystallinity of the drawn films but it can be trapped in the polymer crystallites, and as a result hinders the growth of a part of the crystalline phase and modify their crystalline size [41]. It has also been reported that water molecules can restrict the molecular orientation and shift the cold crystallization temperature to the higher values [42].

The crystallinity (X_c) of the precursor and stretched PA6 and MXD6 as well as their nanocomposite films obtained from DSC and Eq. 1 is presented in Figure 7.5.

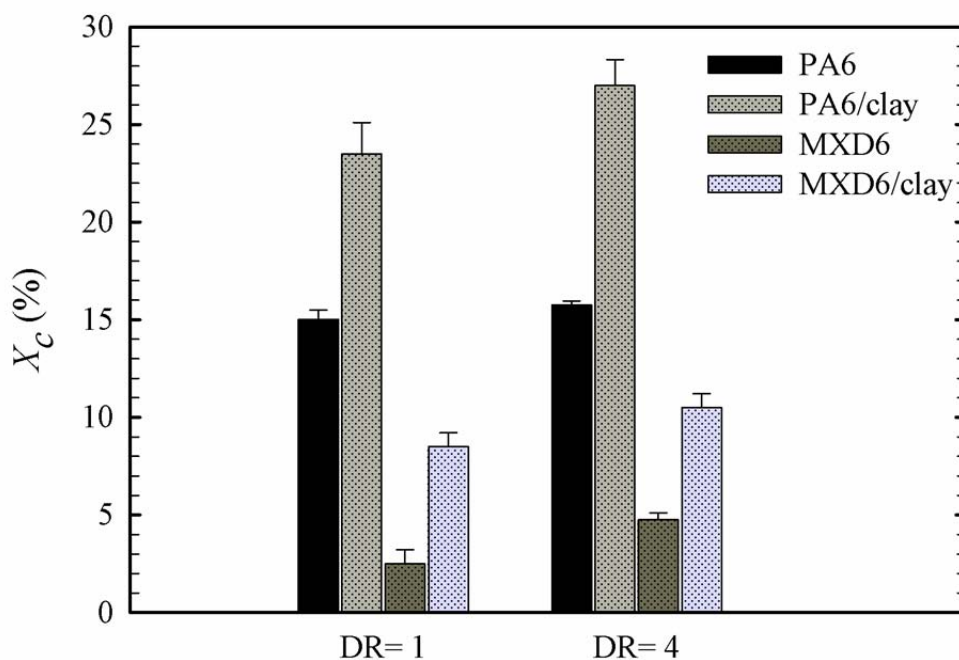


Figure 7-5 Crystallinity of precursor and stretched (DR=4) PA6 and MXD6 and their nanocomposites films.

The crystallinity of the precursor and stretched PA6/clay and MXD6/clay are higher than their neat polymers. It could be related to the fact that the clay platelets initiate a heterogeneous nucleation that leads to an increase in the crystallinity of the nanocomposite samples. In general, the crystallinity of nylon based nanocomposite is controlled by the type of nylon matrix, molecular weight, clay concentration, and level of clay exfoliation [27, 43-45]. For the precursor and stretched MXD6 and MXD6/clay films, the level of crystallinity is quite low because of very long relaxation time of the MXD6 chains, which was discussed in details in our previous study [21]. In Figure 7.5, it is obvious that the degree of crystallinity for the oriented nylons and nanocomposites slightly improves upon uniaxial stretching.

7.4.3 Oxygen Permeation

The permeability coefficient is representative of the barrier capability of a polymer film. In the steady state conditions, it is defined as the rate at which a quantity of a permeant gas passes through a unit area of a film having unit thickness in unit time under a unit pressure difference between both sides of the film [46]. The permeation coefficient (P) is a function of the diffusion coefficient (D) and the solubility coefficient (S). It also depends on the temperature and concentration difference for the permeant gas between the two sides of the polymer film. At a given temperature and steady state condition, the permeability coefficient (P) can be expressed by the equation that relates the permeability constant to diffusivity and solubility, i.e. [47]:

$$P = DS \quad (7.2)$$

Without considering the effect of filler on the surrounding polymer matrix and assuming strong interaction between the dispersed filler and polymer matrix, the solubility coefficient in a nanocomposite can be expressed as [47]:

$$\frac{S}{S_0} = (1 - \phi) \quad (7.3)$$

where S_0 is the solubility coefficient of the neat polymer and ϕ is the volume fraction of the dispersed filler. The silicate layers in nylon/clay composite films act as impermeable obstacles and create a more tortuous path in the polymer matrix. Consequently, the diffusing gas molecules have to penetrate with more difficulty through the composite film. As a result, the diffusion coefficient in the nanocomposite is reduced and can be obtained according to the following equation [47]:

$$D = D_0/\tau \quad (7.4)$$

where D_0 is the diffusion coefficient in the neat polymer, D is the diffusion coefficient of the nanocomposite and τ is the tortuosity factor.

According to the above equations, the relative permeability can be expressed as a function of tortuosity (τ) and volume fraction of the silicate layers (\emptyset) [47]:

$$K = \frac{P_{nanocomposite}}{P_0} = \frac{(1 - \emptyset)}{\tau} \quad (7.5)$$

where P_0 is the permeability coefficient of the neat polymer and P is the nanocomposite permeability coefficient. Several analytical and numerical models have been proposed to describe or predict the tortuosity parameter and permeability of the nanocomposites [48-50]. The main models are summarized in Table 7.2. Three different geometries of impermeable fillers have been considered in the models: disks, hexagonal flakes and ribbons.

The volume fraction of clay in the nylon/clay nanocomposites can be calculated as:

$$\emptyset = \frac{wt\% \text{ clay}}{100} \times \frac{\rho_{nanocomposite}}{\rho_{clay}} \quad \text{where} \quad \frac{\rho_{nanocomposite}}{100} = \frac{wt\% \text{ clay}}{\rho_{clay}} + \frac{100 - wt\% \text{ clay}}{\rho_{matrix}} \quad (7.6)$$

In this study, the reported clay density of 2.75 g/ml and 2.65 g/ml were used for the PA6/clay [51] and MXD6/clay films [52, 53], respectively. The density values of the aromatic and aliphatic nylon and nylon/clay are reported in Table 7.1. The exact clay content in each system was measured after overnight burning a known amount of the sample at a high temperature of 800°C. The clay content (an average of three samples) of the PA6/clay and MXD6/clay is 3.02 and 2.38 wt%, respectively. This corresponds to the clay volume fractions of $\emptyset = 0.0129$ and $\emptyset = 0.0112$ for the PA6/clay and MXD6/clay, respectively. The theoretical aspect ratio (ϕ) expected for a single clay in the perfect exfoliated state and completely oriented in the melt flow direction (orientation factor = 1) was assumed to be 150 for Montmorillonite [54]. The predicted relative oxygen permeability obtained from various models with considering the experimental value of the clay volume fractions and theoretical aspect ratios are summarized in Table 7.2.

Table 7.2 Predicted relative permeability (K) obtained from different models for PA6/clay and MXD6/clay.

Model	Tortuosity parameter (τ)	Model parameters	$(K)_{PA6/clay}$	$(K)_{MXD6/clay}$
Nielson (1967) [55]	$1 + \left(\frac{\varphi\phi}{2}\right)$	Ribbons-infinite length	0.50	0.54
Cussler (1988) [56]	$1 + \left(\frac{\lambda}{4}\right) \left[\frac{(\varphi\phi)^2}{1 - \phi}\right]$	Ribbons-infinite length- $\lambda=1$	0.51	0.59
Cussler (2001) [57]	$1 + \left(\frac{\lambda}{4}\right) \left[\frac{(\varphi\phi)^2}{1 - \phi}\right]$	Ribbons-infinite length with equal probability of alignment and misalignment- $\lambda=1/2$	0.67	0.74
Cussler (2003) [58]	$1 + \left(\frac{\lambda}{4}\right) \left[\frac{(\varphi\phi)^2}{1 - \phi}\right]$	Randomly oriented Hexagonal flask $\lambda=2/27$	0.92	0.94
Cussler (2004) [59]	$\left(1 + \left(\frac{\varphi\phi}{3}\right)\right)^2$	Randomly distributed Rectangular Flask- infinite length-	0.36	0.41
Fredrickson (1999) [60]	$4 \left[\frac{1 + x + 0.1245 x^2}{(2 + x)}\right]^2$	$x = \frac{\pi x\phi}{2 \ln\left(\frac{\phi}{2}\right)}$	0.58	0.62
Gusev (2001) [61]	$exp\left[\left(\frac{\varphi\phi}{3.47}\right)^{0.71}\right]$	Dispersed disk-randomly orientated without overlapping	0.51	0.55
Bharadwaj (2001) [49]	$1 + \frac{\varphi\phi}{2} \left(\frac{2}{3}\right) \left(\kappa + \frac{1}{2}\right)$	Ribbons-infinite length- $\kappa=1$	0.50	0.54
Bharadwaj (2001) [49]	$1 + \frac{\varphi\phi}{2} \left(\frac{2}{3}\right) \left(\kappa + \frac{1}{2}\right)$	Ribbons-infinite length- Randomly oriented $\kappa = 0$	0.75	0.78

$(\phi_{PA6/clay} = 0.0129 \quad \phi_{MXD6/clay} = 0.0112 \text{ and } \varphi = 150)$

λ : Geometrical factor that depends on the shape of dispersed fillers.

κ : An orientation function that depends on the angle between the normal vector of clays and the direction of the preferred orientation.

As it can be seen, the K values predicted from most of the models are close to the experimental values for the precursor films ($K_{PA6/clay} = 0.487$ and $K_{MXD6/clay} = 0.577$), except for those obtained from the models with a random orientation assumption of fillers. Among the above models, the Bharadwaj model, which assumes ribbons fillers with an infinite length perfectly oriented parallel to the films surface ($\kappa=1$), seems a capable model to predict the

relative oxygen permeability. It should be mentioned that fully exfoliation and dispersion of fillers are the preliminary assumption of the model. As the morphology of the nanocomposites might be partially intercalated, the difference between the experimentally measured and the theoretically calculated K is reasonable. Additionally, even if the impermeable clays are parallel to the film surface, their alignment is not perfect. By considering the clay Herman orientation function obtained from our recent study [25] as the real orientation parameter (κ) in the Bharadwaj model, the calculated relative permeability from the model will be more consistent with the experimental values, which will be more discuss later.

TEM micrographs were used to estimate the average aspect ratio, ϕ , which is the ratio of the length (l) to the thickness (t) of the clay particles as illustrated in Figure 7.6. The histogram of the image analysis shows that the average clay aspect ratio for the PA6/clay is ca. 80 and for the MXD6/clay is ca. 45 (based on analysis of the results of ca. 300 calculated ratios). The calculated clay silicate aspect ratios obtained from the TEM analysis of the nanocomposite films are much lower than the theoretical value ($\phi=150$). It is speculated that due to the high shear rate in the extrusion process, the clays were broken, which was also reported in the literature [18, 62]. It is also possible to predict the effective aspect ratio of the nanoclay from the models and it will be discussed later.

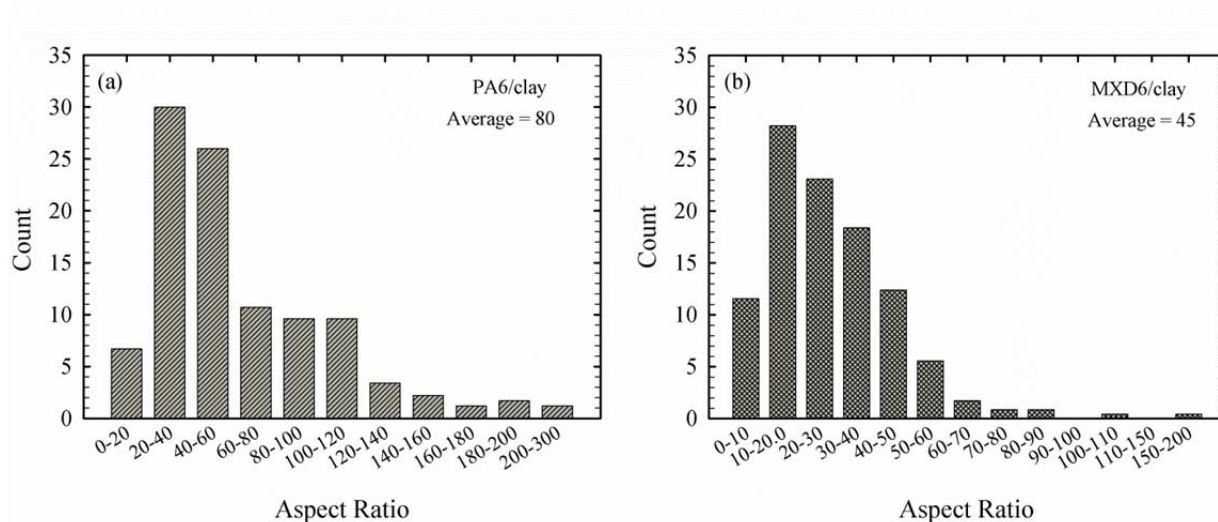


Figure 7-6 Histogram of calculated aspect ratio for (a) PA6/clay and (b) MXD6/clay films.

The measured oxygen permeability of the precursor and stretched PA6 and MXD6 as well as their nanocomposite films are depicted in Figure 7.7.

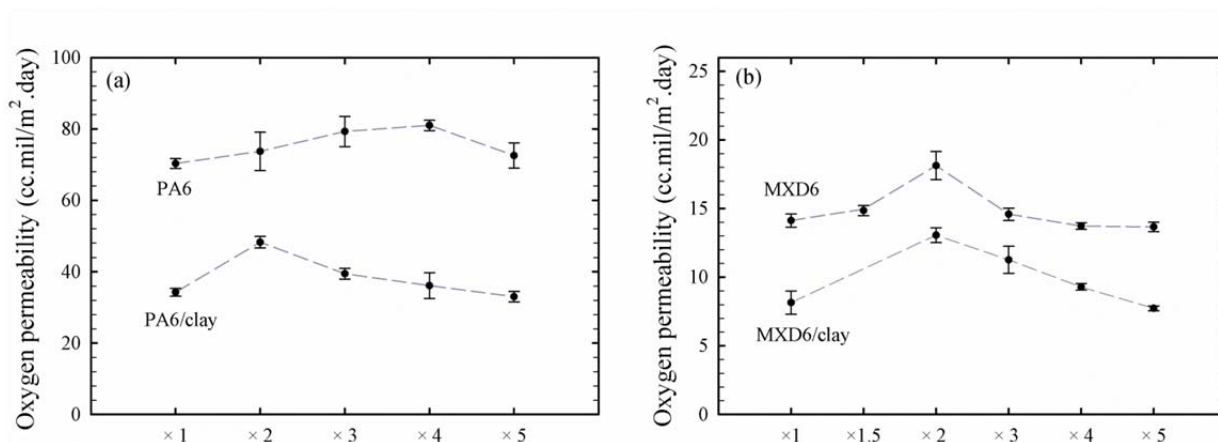


Figure 7-7 Oxygen permeation versus draw ratio for (a) PA6 and PA6/clay (b) MXD6 and MXD6/clay films.

The barrier property of the precursor MXD6 film (DR=1) is more than five times better than that of the precursor aliphatic PA6 film. Moreover, incorporating clay in the PA6 and MXD6 improves the oxygen barrier by ca. 40%, which was also discussed extensively in a previous study [21]. The precursor MXD6/clay (DR=1) shows significantly better barrier property, which is attributed to its lower free volume and more packed chains compared to the PA6/clay film

[21]. From Figure 7.7, the oxygen permeability of the stretched films increases with increasing draw ratio up to a critical value for each sample, while further stretching resulted in a reduction in the oxygen permeation. This behavior was also observed for water vapor permeability through polypropylene (PP) films prepared by biaxial [3] and uniaxial stretching [4, 63]. The results presented in Figure 7.7 appear to be inconsistent with the free volume concepts for gas permeability [64]. It seems that among the controlling factors in the gas permeation through the films (i.e. thickness, crystallinity, orientation and tortuosity path of permeant gas), the free volume plays an important role. In fact, during hot stretching of either the aliphatic or aromatic nylon films at low draw ratios, the chain mobility increases [65] and as a result, the chain entanglements reduces and, accordingly, the free volume and gas permeation increases. After a critical draw ratio, the amorphous and crystalline chains alignment along the drawing direction increase. Therefore, a more packed structure of the polymer chains at higher draw ratio lowers the free volume and results in a reduction in the gas permeation.

As it was discussed above, the Bharadwaj model could successfully predict the relative permeability of the precursor films. The predicted relative permeability of the stretched films obtained by the Bharadwaj model is summarized in Table 7.3. The clay volume fraction (\emptyset) and the aspect ratio (ϕ) of the silicate layers were assumed to be the same as above values and the Herman orientation function of the clay (κ) obtained from the experiments for the precursor and stretched films [25] entered for the κ parameter in the Bharadwaj model.

Table 7.3 Predicted relative permeability (K) values from the Bharadwaj model for PA6/clay and MXD6/clay.

	Herman orientation function of clay (κ)	Tortuosity parameter (τ)	(K) = P/P_0 model	(K) = P/P_0 experiments
PA6/clay-DR 1	0.676	1.76	0.56	0.49
PA6/clay-DR 2	0.705	1.78	0.56	0.65
PA6/clay-DR 3	0.729	1.79	0.55	0.50
PA6/clay-DR 4	0.808	1.84	0.54	0.47
PA6/clay-DR 5	0.810	1.85	0.55	0.46
MXD6/clay-DR 1	0.601	1.60	0.62	0.58
MXD6/clay-DR 2	0.608	1.61	0.61	0.72
MXD6/clay-DR 3	0.680	1.65	0.60	0.77
MXD6/clay-DR 4	0.740	1.68	0.59	0.67
MXD6/clay-DR 5	0.749	1.69	0.58	0.57

($\phi_{\text{PA6/clay}} = 0.0129$), ($\phi_{\text{MXD6/clay}} = 0.0112$), and ($\phi = 150$)

κ : Herman orientation function of the clays obtained with experiments [25]

The relative oxygen permeability of ($K_{\text{PA6/clay}}=0.55$ and $K_{\text{MXD6/clay}}=0.58$) for the stretched films with draw ratio of 5 are close to our experimental value ($K_{\text{PA6/clay}}=0.46$ and $K_{\text{MXD6/clay}}=0.57$). The relative oxygen permeability of the oriented films reveal that the experimental data and the predicted values obtaining from the theoretical models are closer for the aromatic nanocomposite films compared to the aliphatic ones. This is due to the lower level of crystallinity and orientation in the former which was discussed in our recent work [25]. In the other words, crystallinity and crystal orientation play important roles in the permeability performances of the oriented films due to an increase in the tortuous diffusion pathway, which are not considered in the theoretical models.

Aspect ratio of the nanoclay platelets reflects the contribution of the tortuous path of the diffusant through the nanocomposite films. It is difficult to obtain the effective aspect ratio (ϕ) of

the clay in the nanocomposites. However, it is possible to calculate the theoretical effective φ value of the nanoclay with considering the actual clay orientation and using geometrical models. The effective φ of the clays in the precursor and stretched (DR=5) PA6/clay and MXD6/clay films were calculated using the Bharadwaj's model and experimental Herman orientation function of the clay (κ) obtained from our previous study [25]. In Figure 7.8, the predicted relative oxygen permeability (K) as a function of the clay orientation parameter (κ) and the clay aspect ratio (φ) are plotted. It should be noted that the curves were obtained with considering the average experimental volume fractions of clay (\emptyset).

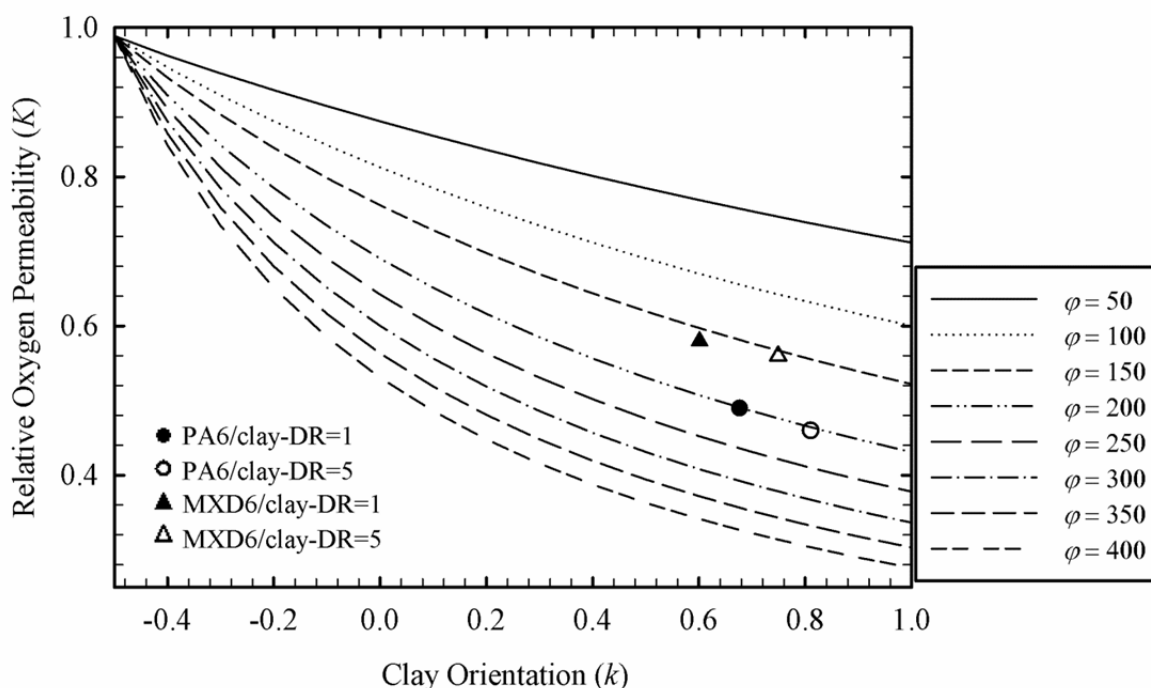


Figure 7-8 Predictions of the Bharadwaj's model for relative oxygen permeability (K) as a function of clay orientation parameter (κ) and clay aspect ratio (φ) with considering the experimental clay volume fractions (\emptyset). Square and triangle symbols are experimental values for relative oxygen permeability for precursor (DR=1) and stretched (DR=5) PA6/clay and MXD6/clay films, respectively.

The values obtained for the theoretical effective φ of the MXD6 and PA6 nanocomposites are about 150 and 200, respectively, which are much higher than the average φ measured from the

TEM analysis (see Figure 7.6). This is probably attributed to the fact that the clay platelet thickness and lengths were inappropriately estimated by the TEM observations of the samples. Moreover, the model tends to significantly overestimate the calculated aspect ratios in comparison with the experimental ones. A similar observation was also reported by Picard et al. [18].

To establish a relationship between the oxygen transmission rate (OTR) and the thickness of the nylon films, the amorphous MXD6 films at various thicknesses were prepared by compression molding and quenched in the liquid nitrogen. In Figure 7.9a, the OTR through the MXD6 films decreases nonlinearly with increasing thickness due to the higher tortuosity diffusion path and more residence time of the oxygen molecules in the thicker films, confirming the results of Tzeng et al. [66]. The oxygen transmission rate of the uniaxially stretched PA6 and MXD6 films as a function of thickness presented in Figure 7.9b and 7.9c show a nonlinear polynomial behavior with one order of magnitude more than the molded MXD6 film. This is probably due to formation of micro voids during fast uniaxial deformation, which facilitates permeation of oxygen through the oriented films.

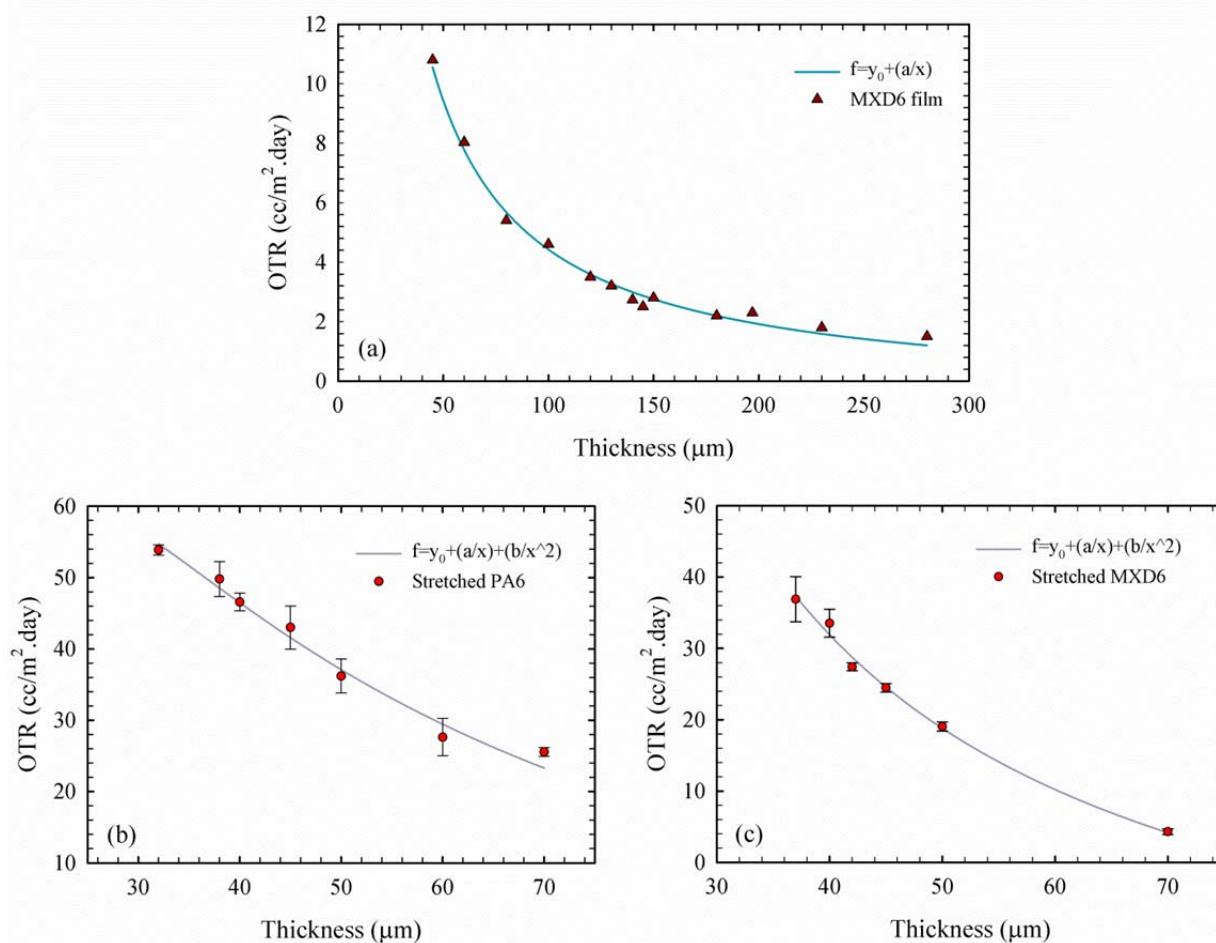


Figure 7-9 Oxygen transmission rate as a function of thickness for (a) MXD6 film, (b) stretched PA6, and (c) stretched MXD6 films.

7.4.4 Mechanical Properties

It is well established that the structure of the crystalline and amorphous phases influences strongly the mechanical properties of the films. The tensile properties (i.e. Young's Modulus, tensile strength, and elongation at break) of the precursor and stretched films are shown in Figures 7.10-12.

The incorporation of 4 wt% clay improves the MD Young's modulus of the precursor (DR=1) aliphatic and aromatic nylon films by ca. 30% and 33%, respectively (Figure 7.10). Furthermore,

the Young's modulus of the PA6 (Figure 7.10a) and PA6/clay (Figure 7.10b) films increases upon uniaxial stretching up to 105% and 125 %, respectively.

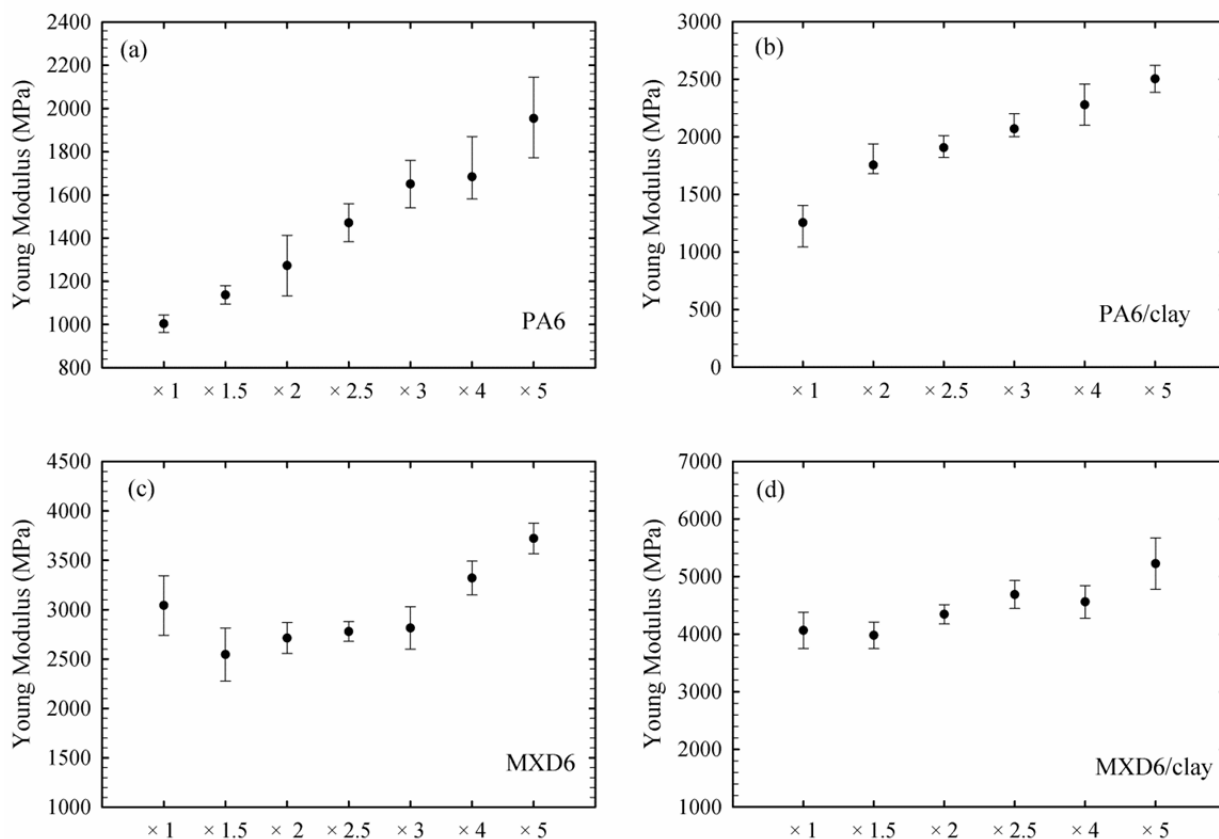


Figure 7-10 Young's modulus as a function of draw ratio for (a) PA6, (b) PA6/clay, (c) MXD6, and (d) MXD6/clay film.

The Young's modulus enhancement after the uniaxial stretching is less significant for the aromatic nylons compared to the aliphatic ones. Only 27% and 37% increase of the Young's modulus at DR of 5 was observed for the stretched MXD6 (Figure 7.10c) and MXD6/clay (Figure 7.10d) films, respectively. It should be noted that the precursor and stretched MXD6 and MXD6/clay films show a larger Young's modulus than the PA6 and PA6/clay films. Although the crystallinity of the PA6 films is higher than that for the MXD6 (see Figure 7.5), however, the barrier and mechanical properties of the MXD6 films are better than those of the PA6. As

discussed above, this could be explained by more rigidity and packing of the aromatic chains of the MXD6 [21] compared to the PA6. A larger increase in the Young's modulus upon uniaxial stretching of the aliphatic nylons compared to that of the aromatic nylon films could also be interpreted to the higher level of crystallinity (Figure 7.5) and more alignment of the crystalline and amorphous phases of the former [25]. The aromatic MXD6 has a longer relaxation time, a higher intermolecular interaction [21] and a lower orientation [25] than the aliphatic PA6. The Young's modulus as a function of draw ratio for the MXD6 films shows a different behavior than the other samples (Figure 7.10c). As seen, the modulus at first decreases at relatively low draw ratios (up to DR=2.5) and then increases. This behavior has also been observed for oriented polyethylene and propylene [67, 68]. It was suggested that this could be related to the chain morphology transformation during uniaxial deformation. Upon uniaxial stretching at low draw ratios, the polymer chains relax and the chain entanglements decrease. In other words the chain relaxation causes a reduction in the Young's modulus at lower draw ratios. With further stretching, orientation and crystallinity start to increase monotonically (data are not shown), leading to a higher stiffness. In Figure 7.11, the tensile strength of the aliphatic and aromatic nylon films and their nanocomposites increase during uniaxial drawing.

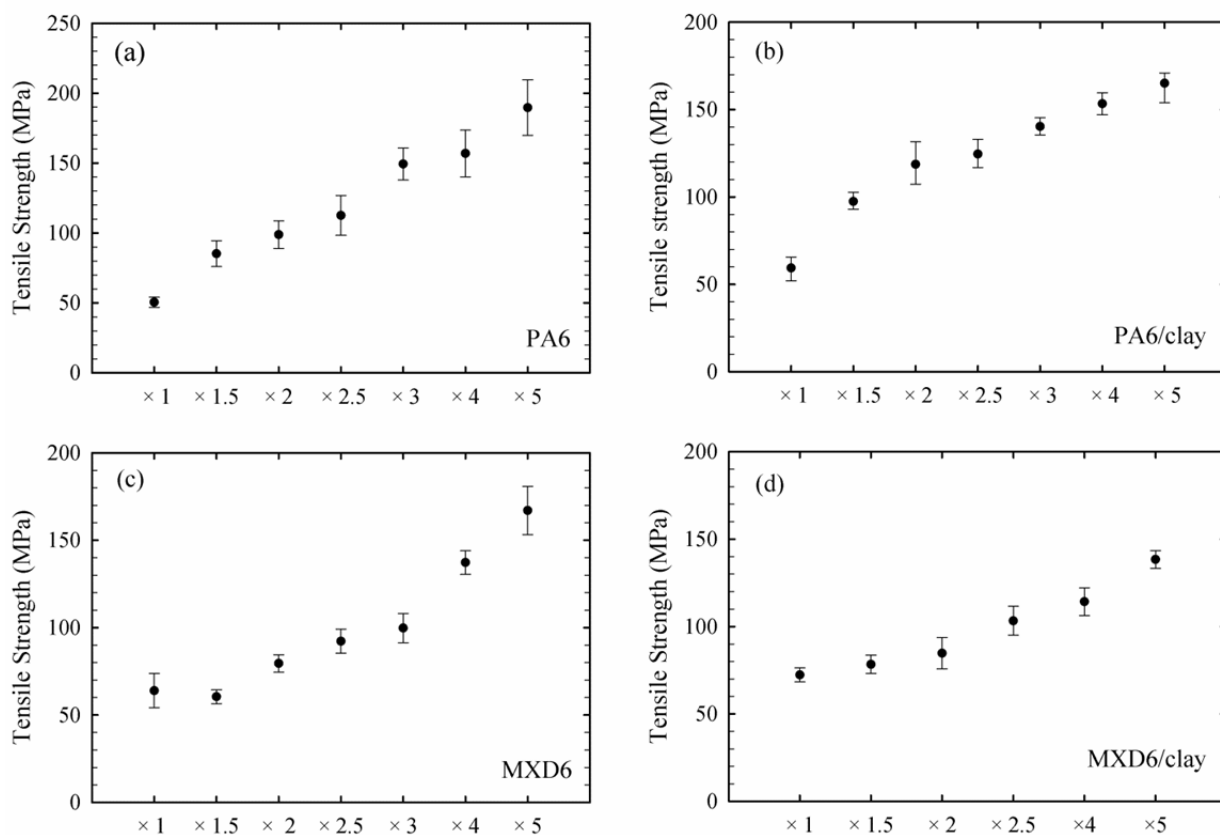


Figure 7-11 Tensile strength as a function of draw ratio for (a) PA6, (b) PA6/clay, (c) MXD6, and (d) MXD6/clay film.

The tensile strength of the stretched (DR=5) PA6 (Figure 7.11a) and PA6/clay films (Figure 7.11b) improve by about 207% and 185 %, respectively, upon uniaxial stretching. The tensile strength of the MXD6 (Figure 11c) and MXD6/clay (Figure 7.11d) films enhanced by 240% and 95% at draw ratio of 5, respectively. It can be also seen that the addition of the clay led to a ca. 18% and 23% increase in the tensile strength of the precursor (DR=1) PA6 and MXD6, respectively. More improvement in the tensile properties of the uniaxial drawn PA6/clay than the stretched MXD6/clay films could be explained by more alignment of the crystalline and amorphous phases of PA6 as well as higher clay orientation in the former [25].

The improvement in the mechanical properties of the oriented PA6 and PA6/clay along MD was however accompanied by a significant reduction in the elongation at break (Figures 12a & b).

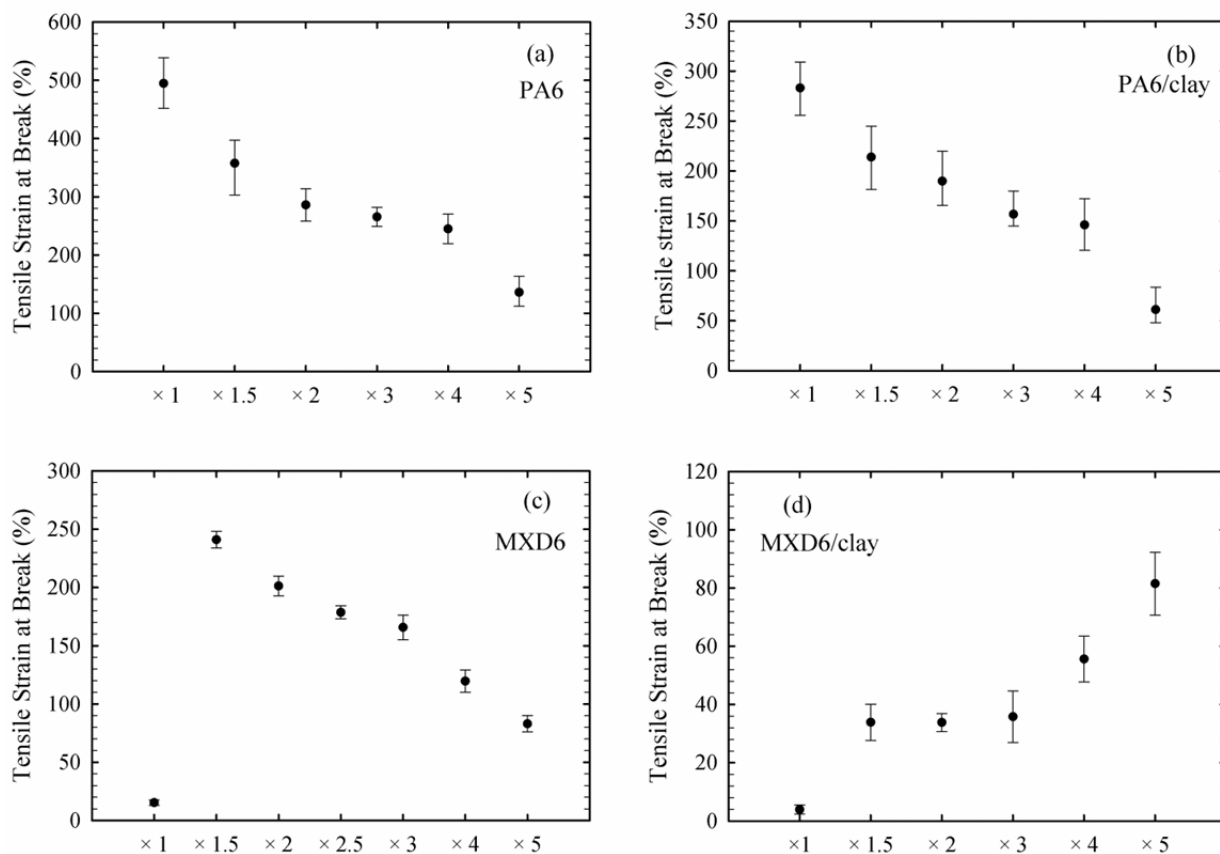


Figure 7-12 Tensile strain at break as a function of draw ratio for (a) PA6, (b) PA6/clay, (c) MXD6, and (d) MXD6/clay film.

A same behavior was also reported for oriented PE and PP [69, 70]. In contrast, upon a small uniaxial deformation (at DR=1.5), the flexibility of the stretched MXD6 improves remarkably (ca. 25 times) compared to the precursor film (DR=1) (Figure 7.12c). The same phenomenon was also observed in the biaxially oriented polystyrene (PS) where stretching enhanced tensile strength and elongation at break significantly and simultaneously up to a critical draw ratio [71]. The flexibility of the MXD6/clay film was monotonically improved (ca. 27 times) upon uniaxial

stretching up to DR=5 (Figure 7.12d). The mobility of the rigid chains in the MXD6 is relatively low and they are extremely packed due to their high intermolecular interaction. Hot stretching at low draw ratio, help the polymer chains to relax and increase their mobility. Consequently, the flexibility of the aromatic nylon films significantly increases while the Young's modulus and tensile strength decrease (see Figures 7.10c and 7.11c). Further extension increases the molecular alignment along the stretching direction and as a result, the tensile strength and modulus increase and flexibility decreases. This is in a good agreement with the oxygen permeability results as discussed earlier (see Figure 7.7). In the MXD6/clay films, the effect of clay in preventing molecular packing after relaxation could explain the increase in the flexibility.

7.5 Conclusions

In this study, the effect of uniaxial drawing on crystal structure, thermal, mechanical and barrier properties of the PA6 and MXD6 and their in-situ polymerized nanocomposite films were studied. The findings can be summarized as follows:

- The cold crystallization temperature (T_{cc}) of the uniaxially stretched MXD6 and MXD6/clay films drastically shifted to the lower temperatures with draw ratio. T_{cc} first decreased with draw ratio up to 3, and then increased upon further stretching. This behavior was attributed to the existence of water molecules during stretching which caused the reduction the enthalpy of the extra-cold crystallization. Nevertheless, the level of crystallinity of the oriented films increased.
- The oxygen permeability of the stretched films increased with draw ratio up to a critical value for each sample, while further stretching resulted in a reduction in oxygen permeation. At low draw ratios, the chain mobility increased, resulting in less chain entanglements and accordingly more free volume. At higher draw ratios (beyond the

critical value), the more packed structure of polymer chains lowered the free volume and resulted in a reduction in the gas permeation.

- Bharadwaj model based on perfect orientation of the impermeable phase was the most appropriate to calculate the relative oxygen permeability of precursor films. With considering the experimental clay orientation as the order parameter, that model was successful to predict the oxygen barrier characteristics of the oriented nanocomposite films.
- The theoretical effective aspect ratio calculated from model was not in consistence with the experimental average values determined by the morphological analysis. Nevertheless, the model generally overestimated the theoretical value of the clay aspect ratio.
- The Young's modulus of the PA6 and PA6/clay films increased significantly upon uniaxial stretching. The Young's modulus enhancement after uniaxial deformation was less significant for the aromatic nylons.
- The elongation at break of the PA6 and PA6/clay films reduced with draw ratio. In contrast, upon a small uniaxial deformation, the flexibility of the stretched MXD6 improved remarkably (ca. 25 times) compared to the precursor film. This behavior was related to the changes in the chain mobility and orientation of the aromatic nylon upon uniaxial drawing.

7.6 Acknowledgment

Financial support from NSERC (Natural Science and Engineering Research Council of Canada) and of the industrial partners of 3SPack Chair Saputo and Prolamina is gratefully acknowledged.

7.7 References

1. Tabatabaei, S.H., P.J. Carreau, and A. Ajji, *Structure and properties of MDO stretched polypropylene*. *Polymer*, 2009. 50(16): p. 3981-3989.
2. Lin, Y.J., et al., *Oxygen permeability of biaxially oriented polypropylene films*. *Polymer Engineering & Science*, 2008. 48(4): p. 642-648.
3. Chu, F. and Y. Kimura, *Structure and gas permeability of microporous films prepared by biaxial drawing of β -form polypropylene*. *Polymer*, 1996. 37(4): p. 573-579.
4. Tabatabaei, S.H., P.J. Carreau, and A. Ajji, *Microporous membranes obtained from polypropylene blend films by stretching*. *Journal of Membrane Science*, 2008. 325(2): p. 772-782.
5. Soon, K., et al., *Morphology, barrier, and mechanical properties of biaxially deformed poly(ethylene terephthalate)-mica nanocomposites*. *Polymer Engineering & Science*, 2012. 52(3): p. 532-548.
6. Abu-Zurayk, R. and E. Harkin-Jones, *The influence of processing route on the structuring and properties of high-density polyethylene (HDPE)/clay nanocomposites*. *Polymer Engineering & Science*, 2012. 52(11): p. 2360-2368.
7. Tabatabaei, S.H., P.J. Carreau, and A. Ajji, *Microporous membranes obtained from PP/HDPE multilayer films by stretching*. *Journal of Membrane Science*, 2009. 345(1-2): p. 148-159.
8. Lin, Y., A. Hiltner, and E. Baer, *Nanolayer enhancement of biaxially oriented polypropylene film for increased gas barrier*. *Polymer*, 2010. 51(24): p. 5807-5814.
9. Liu, R.Y.F., et al., *Oxygen-barrier properties of cold-drawn polyesters*. *Journal of Polymer Science Part B-Polymer Physics*, 2002. 40(9): p. 862-877.
10. Qureshi, N., et al., *Oxygen-barrier properties of oriented and heat-set poly(ethylene terephthalate)*. *Journal of Polymer Science Part B: Polymer Physics*, 2000. 38(13): p. 1679-1686.
11. Armstrong, S., et al., *Gas permeability of melt-processed poly(ether block amide) copolymers and the effects of orientation*. *Polymer*, 2012. 53(6): p. 1383-1392.
12. Sadeghi, F. and A. Ajji, *Structure, Mechanical and Barrier Properties of Uniaxially Stretched Multilayer Nylon/Clay Nanocomposite Films*. *International Polymer Processing*, 2012. 27(5): p. 565-573.
13. Cho, J.W. and D.R. Paul, *Nylon 6 nanocomposites by melt compounding*. *Polymer*, 2001. 42(3): p. 1083-1094.

14. Fornes, T.D., et al., *Nylon 6 nanocomposites: the effect of matrix molecular weight*. Polymer, 2001. 42(25): p. 09929-09940.
15. Mohanty, S. and S.K. Nayak, *Mechanical, thermal and viscoelastic behavior of nylon 6/clay nanocomposites with cotreated montmorillonites*. Polymer-Plastics Technology and Engineering, 2007. 46(4): p. 367-376.
16. Yeh, J.-T., et al., *Oxygen barrier and blending properties of blown films of blends of modified polyamide and polyamide-6 clay mineral nanocomposites*. Applied Clay Science, 2009. 45(Compendex): p. 1-7.
17. Usuki, A., et al., *Characterization and properties of nylon 6. Clay hybrid*. 1990, Publ by ACS: Washington, DC, USA. p. 651-652.
18. Picard, E., et al., *Barrier properties of nylon 6-montmorillonite nanocomposite membranes prepared by melt blending: Influence of the clay content and dispersion state: Consequences on modelling*. Journal of Membrane Science, 2007. 292(1-2): p. 133-144.
19. Yalcin, B., et al., *Molecular origins of toughening mechanism in uniaxially stretched nylon 6 films with clay nanoparticles*. Polymer, 2008. 49(6): p. 1635-1650.
20. Poisson, C., et al., *Mechanical, optical and barrier properties of PA6/nanoclay-based single- And multilayer blown films*. Polymers and Polymer Composites, 2008. 16(6): p. 349-358.
21. Fereydoon, M., S.H. Tabatabaei, and A. Ajji, *Rheological, crystal structure, barrier, and mechanical properties of PA6 and MXD6 nanocomposite films*. Polymer Engineering & Science, 2013: p. n/a-n/a.
22. Ben Doudou, B., E. Dargent, and J. Grenet, *Relationship between draw ratio and strain-induced crystallinity in uniaxially hot-drawn PET-MXD6 films*. Journal of Plastic Film & Sheeting, 2005. 21(3): p. 233-251.
23. Hu, Y.S., et al., *Improving transparency of stretched PET/MXD6 blends by modifying PET with isophthalate*. Polymer, 2005. 46(14): p. 5202-5210.
24. Cole, K.C., J. Denault, and M.N. Bureau, *Infrared spectroscopy studies of structure and orientation in clay-reinforced polyamide-6 nanocomposites*. Macromolecular Symposium, 2004. 205(1): p. 47-60.
25. Fereydoon, M., S.H. Tabatabaei, and A. Ajji, *X-ray and Trichroic Infrared Orientation Analyses of Uniaxially Stretched PA6 and MXD6 Nanoclay Composite Films*. Macromolecules, 2013: p. n/a-n/a.
26. Doudou, B., E. Dargent, and J. Grenet, *Crystallization and melting behaviour of poly(m-xylene adipamide)*. Journal of Thermal Analysis and Calorimetry, 2006. 85(2): p. 409-415.

27. Maiti, P. and M. Okamoto, *Crystallization Controlled by Silicate Surfaces in Nylon 6-Clay Nanocomposites*. *Macromolecular Materials and Engineering*, 2003. 288(5): p. 440-445.
28. Miri, V., et al., *Crystallization Kinetics and Crystal Structure of Nylon6-Clay Nanocomposites: Combined Effects of Thermomechanical History, Clay Content, and Cooling Conditions*. *Macromolecules*, 2008. 41(23): p. 9234-9244.
29. Bafna, A., et al., *3D Hierarchical orientation in polymer-clay nanocomposite films*. *Polymer*, 2003. 44(4): p. 1103-1115.
30. Usuki, A., et al., *Three-Dimensional Observation of Structure and Morphology in Nylon-6/Clay Nanocomposite*. *Nano Letters*, 2001. 1(5): p. 271-272.
31. Cole, K.C., et al., *Biaxial deformation of polyamide-6: Assessment of orientation by means of infrared trichroism*. *Polymer Engineering and Science*, 2004. 44(2): p. 231-240.
32. Penel-Pierron, L., et al., *Structural and mechanical behavior of nylon 6 films part I. Identification and stability of the crystalline phases*. *Journal of Polymer Science Part B: Polymer Physics*, 2001. 39(5): p. 484-495.
33. Penel-Pierron, L., et al., *Structural and mechanical behavior of nylon-6 films. II. Uniaxial and biaxial drawing*. *Journal of Polymer Science Part B: Polymer Physics*, 2001. 39(11): p. 1224-1236.
34. Miri, V., et al., *Strain-induced disorder-order crystalline phase transition in nylon 6 and its miscible blends*. *Polymer*, 2007. 48(17): p. 5080-5087.
35. Clarey, M., et al. *Removal of impurities from clay where purified clay is useful as filler in plastics involves centrifuging followed by ion-exchanging the clay to replace monovalent cations for multivalent cations in the clay interlayer*. 1998 18 Apr 2000; Available from: <Go to ISI>://DIIDW:2000349243.
36. Galeski, A., A.S. Argon, and R.E. Cohen, *Deconvolution of x-ray diffraction data to elucidate plastic deformation mechanisms in the uniaxial extension of bulk nylon 6*. *Macromolecules*, 1991. 24(13): p. 3945-3952.
37. Magniez, K., B.L. Fox, and M.G. Looney, *Nonisothermal crystallization behavior of poly(m-xylene adipamide)/montmorillonite nanocomposites* *Journal of Polymer Science Part B: Polymer Physics*, 2009. 47(13): p. 1300-1312
38. Khanna, Y.P. and W.P. Kuhn, *Measurement of crystalline index in nylons by DSC: Complexities and recommendations*. *Journal of Polymer Science Part B: Polymer Physics*, 1997. 35(14): p. 2219-2231.
39. Seif, S. and M. Cakmak, *Stress - Optical behavior of Poly(m-xylylenediamine adipamide) (Nylon MXD6): Influence of molecular weight*. *Polymer*, 2010. 51(16): p. 3762-3773.

40. Sperling, L.H., *Introduction to Physical Polymer Science*. 4 ed. 2006, New Jersey: John Wiley & Sons, Inc.
41. Dargent, E., et al., *Effect of water molecules on crystallization during uniaxial drawing of poly(ethylene terephthalate) films*. *Journal of Applied Polymer Science*, 2000. 77(5): p. 1056-1066.
42. Hu, Y.S., et al., *Effect of water sorption on oxygen-barrier properties of aromatic polyamides*. *Journal of Polymer Science Part B: Polymer Physics*, 2005. 43(11): p. 1365-1381.
43. Liu, X. and C. Breen, *High-Temperature Crystalline Phases in Nylon 6/Clay Nanocomposites*. *Macromolecular Rapid Communications*, 2005. 26(13): p. 1081-1086.
44. Devaux, E., S. Bourbigot, and A. El Achari, *Crystallization behavior of PA-6 clay nanocomposite hybrid*. *Journal of Applied Polymer Science*, 2002. 86(10): p. 2416-2423.
45. Bureau, M.N., et al., *The role of crystallinity and reinforcement in the mechanical behavior of polyamide-6/clay nanocomposites*. *Polymer Engineering and Science*, 2002. 42(9): p. 1897-1906.
46. Selke, S.E.M., J.D. Culter, and R.J. Hernandez, *Plastics Packaging Properties, Processing, Applications, and Regulations*, ed. 2nd. 2004: Hanser.
47. Selke, S.E.M., *Understanding Plastic packaging Technology*. 1997: New York, Hanser.
48. Takahashi, S., et al., *Gas barrier properties of butyl rubber/vermiculite nanocomposite coatings*. *Polymer*, 2006. 47(9): p. 3083-3093.
49. Bharadwaj, R.K., *Modeling the Barrier Properties of Polymer-Layered Silicate Nanocomposites*. *Macromolecules*, 2001. 34(26): p. 9189-9192.
50. Choudalakis, G. and A.D. Gotsis, *Permeability of polymer/clay nanocomposites: A review*. *European Polymer Journal*, 2009. 45: p. 967-984.
51. Liang, Y., T. Lan, and S. Omachinski, *Manufacture of nanocomposite composition, by forming intercalating composition comprising specific amount of purified sodium smectite clay that contains specific amount of sodium ions, and lactam ring-containing monomer or oligomer*. US2005256244.
52. Lan, T., H.T. Cruz, and A.S. Tomlin, *Intercalates formed by co-intercalation of onium ion spacing/coupling agents and monomer, oligomer or polymer MXD6 nylon intercalants and nanocomposites prepared with the intercalates*. 2001, US6232388.
53. Lan, T., H.T. Cruz, and A.S. Tomlin, *Nanocomposite compositions used to decrease oxygen permeability of films or sheets of matrix polymer and to deliver active materials e.g. cosmetics, hair care and pharmaceutical agents*. 2001, US6232388-B1.

54. Lu, C.S. and Y.W. Mai, *Influence of aspect ratio on barrier properties of polymer-clay nanocomposites*. Physical Review Letters, 2005. 95(8).
55. Nielsen, L.E., *Models for the Permeability of Filled Polymer Systems*. Journal of Macromolecular Science: Part A - Chemistry, 1967. 1(5): p. 929-942.
56. Cussler, E.L., et al., *Barrier membranes*. Journal of Membrane Science, 1988. 38(Compendex): p. 161-174.
57. Yang, C., W.H. Smyrl, and E.L. Cussler, *Flake alignment in composite coatings*. Journal of Membrane Science, 2004. 231(1-2): p. 1-12.
58. Moggridge, G.D., et al., *Barrier films using flakes and reactive additives*. Progress in Organic Coatings, 2003. 46(4): p. 231-240.
59. Lape, N.K., E.E. Nuxoll, and E.L. Cussler, *Polydisperse flakes in barrier films*. Journal of Membrane Science, 2004. 236(1): p. 29-37.
60. Fredrickson, G.H. and J. Bicerano, *Barrier properties of oriented disk composites*. Journal of Chemical Physics, 1999. 110(4): p. 2181-2188.
61. Gusev, A.A. and H.R. Lusti, *Rational design of nanocomposites for barrier applications*. Advanced Materials, 2001. 13(21): p. 1641-1643.
62. Ghasemi, H., et al., *Properties of PET/clay nanocomposite films*. Polymer Engineering and Science, 2012. 52(2): p. 420-430.
63. Tabatabaei, S.H., P.J. Carreau, and A. Ajji, *Microporous membranes obtained from PP/HDPE multilayer films by stretching*. Journal of Membrane Science, 2009. 345(1-2): p. 148-159.
64. Winberg, P., et al., *Free volume sizes in intercalated polyamide 6/clay nanocomposites*. Polymer, 2005. 46(19): p. 8239-8249.
65. Min, U., C.S. Yoon, and J.-H. Chang, *Characterizations of transparent polyimide nanocomposite films with various equibiaxial stretching ratios: Optical transparency, morphology, and oxygen permeability*. Journal of Applied Polymer Science, 2012. 126(S2): p. E2-E11.
66. Tzeng, P., C.R. Maupin, and J.C. Grunlan, *Influence of polymer interdiffusion and clay concentration on gas barrier of polyelectrolyte/clay nanobrick wall quadlayer assemblies*. Journal of Membrane Science, 2014. 452(0): p. 46-53.
67. Sadeghi, F., et al., *Properties of uniaxially stretched polypropylene films: effect of drawing temperature and random copolymer content*. Canadian Journal of Chemical Engineering, 2010. 88(6): p. 1091-1098.

68. Aji, A. and M.M. Dumoulin, *Rolling and Roll-Drawing of Semi-Crystalline Thermoplastics*, in *Solid Phase Processing of Polymers*. 2000, Carl Hanser Verlag GmbH & Co. KG. p. . p. 258-295.
69. Tabatabaei, S.H., P.J. Carreau, and A. Aji, *Effect of processing on the crystalline orientation, morphology, and mechanical properties of polypropylene cast films and microporous membrane formation*. *Polymer*, 2009. 50(17): p. 4228-4240.
70. Tabatabaei, S.H., et al., *Effect of machine direction orientation conditions on properties of HDPE films*. *Journal of Plastic Film & Sheeting*, 2009. 25(3-4): p. 235-249.
71. Zhang, X. and A. Aji, *Biaxial orientation behavior of polystyrene: Orientation and properties*. *Journal of Applied Polymer Science*, 2003. 89(2): p. 487-496.

CHAPTER 8

Properties of co-extruded nanoclay-filled aliphatic nylon (PA6)/linear low-density polyethylene and aromatic nylon (MXD6)/linear low-density polyethylene multilayer films⁴

Maryam Fereydoon, Seyed H. Tabatabaei and Abdellah Ajji*

CREPEC, Chemical Engineering Department, Ecole Polytechnique,

C.P. 6079, Succ. Centre ville Montreal, QC, H3C 3A7 Canada

(* All correspondence should be addressed to: abdellah.ajji@polymtl.ca

Abstract

In this study, coextruded multilayer films with aliphatic (PA6) and aromatic (MXD6) nylons as well as their in-situ polymerized nanocomposites with 4 wt% nanoclay, as an oxygen barrier layer (core), and a linear low-density polyethylene (LLDPE) as a moisture barrier layer (skin) were produced and characterized. Five-layer films were prepared by cast coextrusion and rapidly cooled using an air knife. Dynamic rheological measurements showed that the selected materials can be coextruded with a minimum interfacial instability between the melt flows in the feed block. Type of crystals, crystallinity and thermal transitions of layers were investigated using Differential Scanning Calorimetry (DSC) and modulated DSC (MDSC). The mechanical, optical, oxygen and water vapor barrier properties of the coextruded multilayer films were measured and discussed. Although the crystallinity of the MXD6 layer in the multilayer films was lower compared to the PA6 layer, the impermeability to oxygen and water vapor was much better for the former multilayer films. In addition, substituting the neat PA6 and MXD6 by their nanocomposites improved the oxygen barrier of the multilayer films by more than 50%. The

⁴ Published in *Journal of Plastic Film and Sheeting*. February 2014. DOI:10.1177/8756087914528348

series resistance model was not able to predict the barrier properties of the multilayer films due to the difference in polymer behavior for the single layer and multilayer, and boundary adjacent layer effects. The coextruded PA6/LLDPE multilayer films showed higher toughness, tear and flex crack resistance compared to the MXD6/LLDPE samples. The pristine MXD6 based multilayer film showed a lower haze compared to the PA6 films due to very little crystallinity in the former.

Keywords:

Coextrusion, Multilayer Films, MXD6, PA6, Nanocomposite, Barrier, Mechanical Properties

8.1 Introduction

Insufficient barrier properties of commercial thermoplastics to the permeation of atmospheric gases such as oxygen and water vapor are a major problem in the packaging industry. In particular, a high oxygen permeation rate reduces the shelf life of packaged food products, which results in higher costs for food processors and retail customers. Multilayer films having a core layer with good barrier and mechanical properties coextruded between two polyolefin layers have been used in food packaging industry to improve the mechanical performance and the barrier properties. However, combining different polymers in order to have an optimized designed multilayer film structure with excellent gas barrier properties (usually against water vapor and/or oxygen), high mechanical and optical performance, and low cost is a challenge in food packaging industries. Processing polymers simultaneously with different rheological properties is an important issue in the coextrusion process. To eliminate interfacial instability and encapsulation ^{1, 2}, or layer rearrangement caused by the high viscosity ratio of adjacent layers ³, the material selection is a crucial step in making a multilayer structure. Therefore, this is a major

challenge in industries such as food packaging to obtain a cost optimized multilayer film with a high barrier property and excellent mechanical performance.

Aliphatic nylons such as polyamide 6 (PA6) have been widely used in food packaging due to its remarkable barrier and mechanical properties. In the past two decades, a great interest has arisen in silicate clay polyamide 6 nanocomposites due to the unique combination of good processability, high mechanical properties and chemical resistance as well as low oxygen permeation⁴⁻⁶. There are several studies on intercalation and exfoliation of polyamide 6/clay nanocomposites either through an in-situ polymerization process^{5, 7} or melt compounding⁸⁻¹¹. The property enhancement in nanocomposites strongly depends on many factors including the filler aspect ratio, orientation, degree of exfoliation and dispersion in the matrix as well as adhesion at the filler-matrix interface. The main problem of polyamide nanocomposites is that relative humidity increases the oxygen permeation of nylon films. There are several studies that confirmed dramatic changes in the barrier property of nylon films with moisture^{12, 13}. Due to the hydrophilic nature of nylon materials, nylons are typically laminated or coextruded between other moisture protective polyolefins in order to improve the oxygen barrier performance^{11, 14, 15}.

Poly (m-xylene adipamide) (MXD6) is a semi-crystalline aromatic nylon with higher mechanical performance, temperature resistance, oxygen barrier and less moisture sensitivity in comparison with PA6¹⁶ and can be considered as a potential candidate to replace PA6 for some packaging applications. MXD6 is well known for its excellent gas barrier properties even at high humidity conditions^{12, 17}. MXD6's other advantages are thermal stability, high bending strength and ease of stretching and/or thermoforming. Recently, incorporating nano-clay in MXD6 nylon has received attention in order to further improve its gas barrier properties^{18, 19}. A multilayer MXD6 with poly (ethylene terephthalate) (PET) was suggested for high barrier carbonated drink

bottles²⁰. Another study showed that a five-layer packaging film with MXD6 as the oxygen barrier layer and ethylene vinyl acetate copolymer (EVA) as the sealant and moisture barrier layer had acceptable barrier and/or mechanical properties²¹. Our recent study¹⁶ showed that although the crystallinity of MXD6 films was much lower than the PA6 films, the oxygen barrier was five times better for the MXD6 films. It was found that due to the stronger polymer chain interaction of the MXD6, there was a lower free volume and gas diffusion path for the MXD6 compared to the PA6. Additionally, the MXD6 showed longer relaxation time and much larger Young's modulus and tensile strength than the PA6 due to its higher intermolecular interactions. Elongation at break and toughness was higher for the PA6 than for the MXD6 due to its higher flexibility. Some PA6/MXD6 blending studies have been conducted to improve the PA6 properties. The miscibility of PA6/MXD6 blends was extensively studied²²⁻²⁵. PA6/MXD6 system is a crystalline-crystalline polymer blend and crystallization of each polymer plays an important role in the blend phase separation behavior²². Takeda and Paul extensively studied miscibility of PA6 and MXD6²⁴⁻²⁶. They observed miscibility of the PA6/MXD6 blend via the amide exchange reaction between these two polyamides. Shibayama et al.²² showed that miscibility of PA6/MXD6 blends is a function of blend composition. Melt blending PA6 and MXD6 during high-temperature extrusion can lead to a material with a homogeneous melt phase and a single T_g owing to interchange reactions²⁶. Blending MXD6 with PA6 in biaxially oriented multilayer films was proposed for the open-easiness property and the easy straight line cut application^{27,28}.

The subject of multilayer coextrusion is very extensive, and many aspects have been investigated with several authors; including equipment design²⁹⁻³¹, fluid mechanics and multilayer flow analysis³²⁻³⁵, interfacial defects^{36,37} and processing conditions optimization³⁷,

³⁸. Some important works have been made by C.D. Han ³² and Dooley ^{29, 39} on the issues of equipment design, fluid mechanics and numerical analysis of multilayer flows. Multilayer equipment introduced by Cloeren Company has been analyzed based on the finite element method by Mitsoulis and his coworkers ^{31, 40}. Their work was used by the industry routinely for analyzing and improving multilayer coextrusion designs. However, these issues of fluid mechanics analysis and the design of multilayer flows and equipment is not the subject discussed in our study.

No study has compared the performances of multilayer films incorporating PA6, MXD6 and their nanocomposites as the high oxygen barrier layer and LLDPE as the water vapor resistance layer. A fundamental understanding on the differences in the properties of such films would be very important for packaging applications. In this work, five-layer films (100 μm) of aromatic and aliphatic nylons and their nanocomposites (as the core layer) with adjacent tie and LLDPE layers were produced using a multilayer co-extrusion cast process. The crystal structure, thermal, optical, mechanical and barrier properties of the multilayer films were studied in detail.

8.2 Experimental

8.2.1 Materials

PA6 (Ultramid B36, from BASF) and PA6/clay nanocomposites (Cress-AlonTM NF3040, from CP polymers) were selected as the aliphatic nylon and its nanocomposite, respectively. The NF3040 had 4 wt% montmorillonite with 200 to 300 aspect ratios (reported by the supplier). MXD6 6007 resin and Imperm 103, which is a MXD6 resin nanocomposite with montmorillonite clay supplied by Nanocor (in partnership with Mitsubishi Gas Chemical), were selected as the aromatic nylon and its nanocomposite, respectively. According to Nanocor, the

silicate layered montmorillonite content of the Imperm 103 nanocomposite MXD6 is between 3.3 to 3.6 wt% with 200 to 400 aspect ratios. As Linear Low Density Polyethylene (LLDPE) is hydrophobic, it was selected as the outer skin layers of the coextruded multilayer films, which would be in direct contact with atmospheric moisture. LLDPE (Sclair-FP120D from NOVAChemical) was used for the skin layers. A linear low density polyethylene grafted with maleic anhydride (Bynel 4125, from Dupont) was chosen for the tie layers to adhere the nylon core layer to the LLDPE skin layers. Table 8.1 summarizes the materials used in this study and some of their characteristics.

Table 8.1 Materials used in this study and their main characteristics (reported by the suppliers).

Material	Commercial name	Supplier	Nomenclature	Main characteristics
Nylon 6	Ultramid B36	BASF (Freeport, USA)	PA6	$M_n = 18,000 \text{ g.mol}^{-1}$ $\rho = 1.14 \text{ g.cm}^{-3}$ $\eta_r = 3.6$ MFI (275°C/5kg) = 10 g/10 min
Nylon 6/clay	NF3040	CP Polymers (Montebello, USA)	PA6/clay	$\rho = 1.15 \text{ g cm}^{-3}$ $\eta_r = 3$ MFI (230°C/5kg) = 8.9 g/10 min Clay content = 4 wt%
Aromatic Nylon	MXD6 6007	Mitsubishi Gas Chemical (Colonial Heights, USA)	MXD6	$M_n = 25,000 \text{ g.mol}^{-1}$ $\rho = 1.21 \text{ g.cm}^{-3}$ $\eta_r = 2.7$ MFI (230°C/5kg) = 12 g/10 min
Aromatic Nylon/clay	Imperm 103	Nanocor (Arlington Heights, USA)	MXD6/clay	$\rho = 1.22 \text{ g.cm}^{-3}$ $\eta_r = 2.5$ Clay content = 3.3 to 3.6 wt%
Linear Low Density Polyethylene	Sclair-FP120D	Nova Chemicals (Calgary, Alberta, CANADA)	LLDPE	MFI (190°C/2.16kg) = 1 g/10 min $\rho = 0.92 \text{ g.cm}^{-3}$
Linear Low Density Polyethylene grafted with Maleic Anhydride	Bynel-4125	DuPont (Wilmington, DE, USA)	LLDPE-g-MA	MFI (190°C/2.16kg) = 2.5 g/10 min $\rho = 0.93 \text{ g.cm}^{-3}$

M_n : Number average molecular weight

ρ : Density

η_r : Relative viscosity = (η/η_0) where η_0 is the viscosity of the solvent.

MFI: Melt flow index

8.2.2 Film preparation

Multilayer films prepared with a co-extrusion cast process had five layers:

- PA6, MXD6 and their nanocomposites as the oxygen barrier layer (core)
- LLDPE as the moisture resistant layers (skins)
- LLDPE-g-MA as the tie layers

The films were prepared using a Labtech Engineering Co-Extrusion Multilayer Line with four single-screw extruders (type LE20-30C) with 20 mm screw diameter and a 30 length/diameter (*L/D*) ratio. The feed-block with (A/B/C/D/A) design for five-layer and a flat die with 30 cm width were used to process the films. The aromatic (i.e. MXD6 and MXD6/clay) and aliphatic nylons (i.e. PA6 and PA6/clay) were dried prior to extrusion in a vacuum oven at 130 °C for 5 h and 80 °C for 24 h, respectively. The temperature profile from the hopper to the die was 275/280/280/285 °C for the aliphatic nylons, 280/285/285/290 °C for the aromatic ones, 215/220/225/225 °C for the LLDPE, and 210/215/220/225 °C for the LLDPE-g-MA. The co-extrusion line was equipped with a slit die followed by rapid cooling using an air knife with 13 psi pressure. Chill rolls set at the ambient temperature were used to stretch the films to obtain 100 µm thick films including 35 µm, 10 µm and 45 µm thicknesses in the core, tie and the skin layers respectively. The temperature for die, feed block and connections were set at 280 °C. The die gap was adjusted at 2 mm. The screw speeds were set at 80 rpm, 35 rpm and 30 rpm for the skin, core and tie layer extruders, respectively.

8.3 Characterizations

Rheological properties

Dynamic rheological measurements were conducted using an Advanced Rheometric Expansion System (ARES, TA Instruments) (Rheometric Scientific Inc., USA) strain-controlled rheometer equipped with a conventional oven for temperature control. Small amplitude oscillatory shear (SAOS) deformation was applied using a 25 mm diameter parallel plate geometry and a 1.2 mm gap under nitrogen atmosphere. The linear viscoelastic properties of the neat polymers and nanocomposites were measured between 0.06 to 100 rad/sec. Prior to frequency sweep tests, time sweep tests were performed at 6.28 rad/s for 20 min to check the sample thermal stability. The rheological tests were conducted at 270 °C for the MXD6 and MXD6/clay and at 240 °C for the PA6, PA6/clay and LLDPE. In order to avoid the effect of humidity on rheological measurements, the nylon pellets and disk samples were dried at 80 °C for 24 h in a vacuum oven and then they were kept in a desiccator. It should be pointed out that due to the nylon instability at high temperatures and long time (nearly 45 min)⁴¹, all the frequency sweep tests for the nylon and nylon/clay samples have been performed from high to low frequencies.

Thermal analysis

Differential Scanning Calorimetry (DSC) Q1000 (TA Instruments, New-Castle, DE, USA) was used for thermal analysis of the films. The scanning cycle was conducted under nitrogen atmosphere between 10 to 280 °C under heating and cooling rates of 10 °C/min. At the end of the first heating ramp, the samples were held at 280 °C for 3 min to erase their thermomechanical

history before cooling. The crystallinity (X_c (%)) of the core layer of the multilayer films was calculated according to the following equation:

$$X_c (\%) = \frac{\Delta H_m - \Delta H_{cc}}{\Delta H_o(1 - x)} \times 100 \quad (8.1)$$

where

x	=	the clay fraction
ΔH_m and ΔH_{cc}	=	the melting and cold crystallization enthalpy obtained from the heating scan
ΔH_o	=	heat of fusion for 100% crystalline PA6 and MXD6, which are taken as 190 and 175 J/g, respectively ^{42, 43} .

The skin layer crystallinity (X_c (%)) was estimated by dividing the heat of fusion of LLDPE resin by 294 J/g⁴⁴ (the theoretical value for 100% crystalline polyethylene homopolymer).

Heat fusion of each layer (ΔH_i) is obtained by heat fusion from the heating scan (ΔH_j) divided by weight fraction (wt) of that layer:

$$\Delta H_i = \frac{\Delta H_j}{wt} \quad \text{and} \quad wt = \frac{\frac{\mu_i}{\sum \mu_i} \times \rho_i}{\sum (\frac{\mu_i}{\sum \mu_i} \times \rho_i)} \quad (8.2)$$

where μ_i and ρ_i are the thickness and density of each layer, respectively.

Modulated DSC (MDSC) used for the purpose of deconvolution of the melting endotherm of the LLDPE and cold crystallization exothermic of the aromatic nylon that appear on the film heating ramp. In MDSC, a liner 3 °C/min heating rate, 60 s modulation period, and a ± 0.45 °C temperature amplitude were selected.

X-ray diffraction

Wide angle X-ray diffraction (WAXD) measurements were carried out using Philips X'Pert X-ray apparatus (Netherlands). The generator was set up at 50 kV and 40 mA and a copper $\text{CuK}\alpha$ radiation ($\lambda=1.54056 \text{ \AA}$) was selected. The samples were scanned at 0.04 °/s from 2 to

10°, mainly for clay exfoliation and from 10 to 50° to evaluate the presence of nylon crystalline structure.

Morphology

Transmission electron microscopy (TEM) (JEOL JEM-2100F, Japan, operating at 200 kV) was used to observe clay dispersion quality in the aromatic and aliphatic nylon matrices. To evaluate the orientation of silicate platelets, microtoming was performed along the machine direction. For cutting, the specimens were imbedded in epoxy resin and microtomed with an Ultracut FC microtome (Leica, Germany) with a diamond knife.

Scanning electron microscopy (SEM) (Hitachi S4700 with a cold field emission gun, FEG-SEM) was used to measure the layer thickness. The films were broken in liquid nitrogen and were coated with gold.

Spectrum 65 FT-IR polarized microscopic (Spotlight 400, PerkinElmer) (Waltham, MA) was used to investigate the multilayer films' cross section and measure the layer thickness. The films were gently stood between the rounded clips, while MD plane was vertical and perfectly in parallel with the mold sidewall to avoid possible movement, and then were molded in epoxy. The cross section surfaces were polished and scanned under the FTIR microscope.

Barrier property

Oxygen transmission rate (OTR) for the multilayer films in accordance with the D-3985-81 ASTM standard was measured using MOCON OXTRAN (Minneapolis, USA) oxygen permeability tester at 25 °C, 0% relative humidity, and 1 atm pressure. A 98% nitrogen (N_2) and 2% hydrogen (H_2) mixture was used as the carrier gas and 100% oxygen (O_2) was used as the test gas. The test ended when the oxygen flux changed by less than 1% during a 40 min test

cycle. The reported data have been normalized (multiplied) by the core layer thickness and are an average of four tests.

Water vapor transmission rate (WVTR) for the multilayer films in accordance with D-6701 ASTM standard was measured using MOCON AQUATRAN® Model 1 (Minneapolis, USA) water vapor permeability tester at 37.8 °C, 100% relative humidity and 1 atm pressure.

Mechanical properties

Tensile tests in both the machine and transverse directions (MD and TD, respectively) were carried out using INSTRON-3365 (USA). Young modulus, tensile toughness, elongation at break and yield strength were measured according to D 882-02 ASTM standard. Samples with 25 mm width, 250 mm length, and 30 µm thickness were stretched at 5 mm/min.

The Elmendorf tear resistance of the multilayer films was measured in both MD and TD according to ASTM standard D1922 using a ProTear (Thwing Albert Instrument Co. USA) testing machine. The specimens were cut to 76 mm in width by 63 mm in length (63-mm specimen dimension is the tear direction). The puncture resistance was evaluated according to ASTM standard D2582 using 250 N load cell of Instron E3000R6454 (USA). The film displacement was recorded against the force (N) and the maximum force was reported as the puncture strength. A needle with 0.5 mm radius was used to pierce the film at 25 mm/min.

The flex crack resistance of the multilayer films was investigated using a Gelbo Flex Tester (model GFT 392) (Vinatoru, NC, USA) according to the ASTM F392-93 standard. The reported data are an average of pinholes detected in 15 samples, with 280 × 200 mm dimensions, after 900 full flex cycles implemented for 20 min.

Optical property

Optical property of the films in the term of haze values were determined according to D-1003 ASTM standard using a LAMBDA 1050 spectrophotometers from PerkinElmer.

8.4 Results and Discussion

8.4.1 Rheological properties of the polymer melts

Coextruding polymers with different rheological properties can cause melt disturbance or interfacial layer instability⁴⁵ and encapsulation^{1, 46}. To avoid these phenomena and to maintain the final product quality, the rheological properties of skin, tie and core layers should be similar. The linear viscoelastic properties of the neat and in-situ polymerized nanocomposites of aromatic and aliphatic nylons (core layer) as well as the LLDPE (skin layer) are shown in Figure 8.1. The storage modulus (G') as a function of time are illustrated in Figure 8.1 (a).

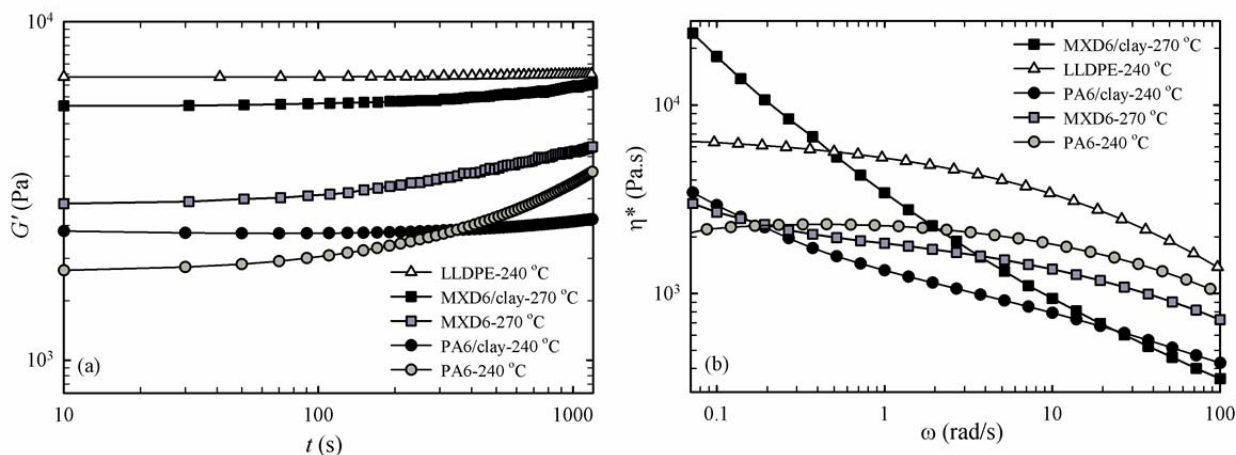


Figure 8-1 (a) Storage modulus (G') versus time for PA6, PA6/clay and LLDPE at 240 °C, and for MXD6 and MXD6/clay at 270 °C; $\omega = 6.28$ rad/s. (b) Complex viscosity (η^*) versus frequency for PA6, PA6/clay and LLDPE at 240 °C, and for MXD6 and MXD6/clay at 270 °C.

According to our previous study¹⁶, the increase in the storage modulus of the nylon resins at the end of the dynamic time sweep test could be attributed to the possible interchange or polycondensation reactions^{24, 25, 47}. The rate of G' increase for the nylon/clay nanocomposites

was lower than that of the neat nylons. As was discussed in our previous work¹⁶, the presence of clay platelets induces a spatial hindrance and inhibits the interchange reactions. As expected, the LLDPE showed a plateau (i.e. constant G'), suggesting no reaction or degradation occurred during the dynamic time sweep test. The complex shear viscosity (η^*) of the core (nylons) and skin (LLDPE) resins as a function of frequency are depicted in Figures 8.1 (b). A noticeable shear thinning behavior above $\omega = 1$ rad/s was observed for the LLDPE. A similar behavior was observed for the LLDPE-g-MA as the tie layer (data are not shown). A higher complex viscosity of the nylon/clay nanocomposite compared to the corresponding neat resin in the low frequency region suggests that, due to a strong particle-matrix or particle-particle interaction, a secondary network structure forms at low frequency, which breaks down at the higher frequencies^{16, 48-50}. As seen, the storage modulus (G') and viscosity of the LLDPE is relatively higher than for the nylon resins. Since, skin layers in a coextruded multilayer film undergo a higher shear rate than the polymer in core layer, it is better to select a resin with slightly higher viscosity for skin layers than for core layer.

Generally, to prevent the interfacial instability in coextrusion processes, selected materials in a multilayer film structure should have an elasticity ratio near one⁵¹. As seen in Figure 8.2, the interfacial instability between the layers significantly affects the clarity and quality of the coextruded PA6 and MXD6 multilayer films.

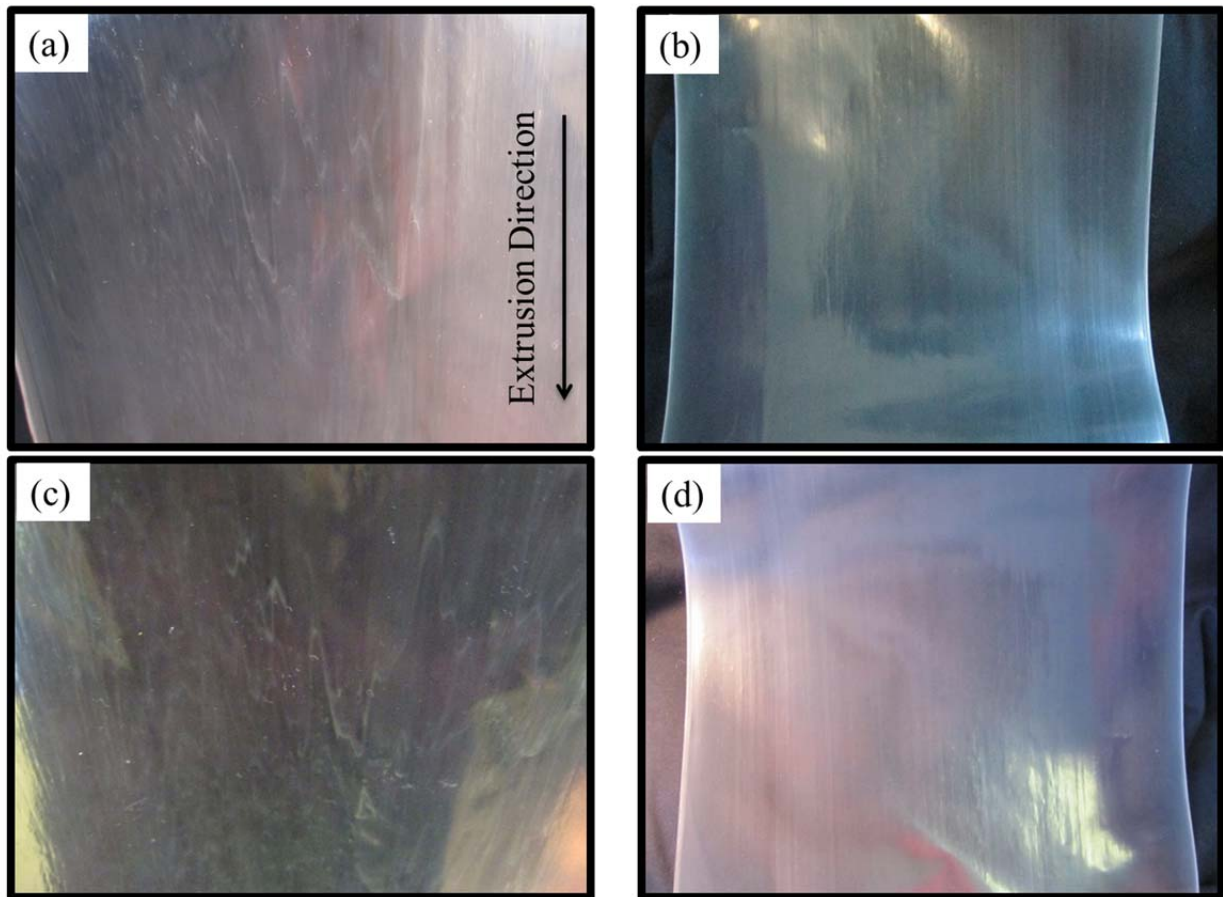


Figure 8-2 Photograph showing unstable (left-sides) and stable (right-sides) interfaces of five-layer coextruded multilayer (a) and (b) PA6/LLDPE films and (c) and (d) MXD6/LLDPE films.

As the instability increases, the interface can become wavier ². Encapsulation in the coextrusion process strongly depends on the viscosity ratio of molten polymers in the feed-block channel. Viscosity of the individual layer decreases from the center to the channel wall due to a higher shear rate near the wall. As a consequence, flow viscosity at the channel center is high due to minimum shear rate at this area. According to Dooley et al. ³ in a coextrusion process, melt flows attempt to rearrange themselves to place the lowest viscosity layer on the outside of flow, against the wall, for which the shear rate is the highest. Encapsulation is mainly caused when the viscosity ratio at neighbor layers is high or the arrangement of the layers is inverted. To minimize instability as a result of encapsulation, the polymers and processing conditions

should be chosen such that polymers have the same viscosities at the merging point. Additionally, the elasticity ratio plays a very important role in the interfacial instability problem⁵¹. The stabilizing or destabilizing effects of elasticity are a very strong function of geometric flow arrangement^{51, 52}. Wilson et al.⁵² has shown that the viscosity and elasticity ratios in the adjacent layers, near one should theoretically result in a stable interface. According to Lamnawar, Maazouz and coworkers^{36, 37}, interfacial defects such as encapsulation and flow instability could be generated from the interfacial phenomena involving an interdiffusion process, interfacial slippage and interfacial reaction which occur at the adjacent layer interface in the coextrusion process. It is difficult to theoretically and experimentally determine the role of the physicochemical affinity that occurs at the polymer/polymer interface of neighboring layers in controlling the interfacial defects and interfacial flow stability.

8.4.2 Morphology of cross-section

The Fourier transform infrared spectroscopy (FTIR) and scanning electron microscopy (SEM) of the multilayer film cross-section with neat nylons as the core layer are shown in Figures 8.3 and 8.4, respectively.

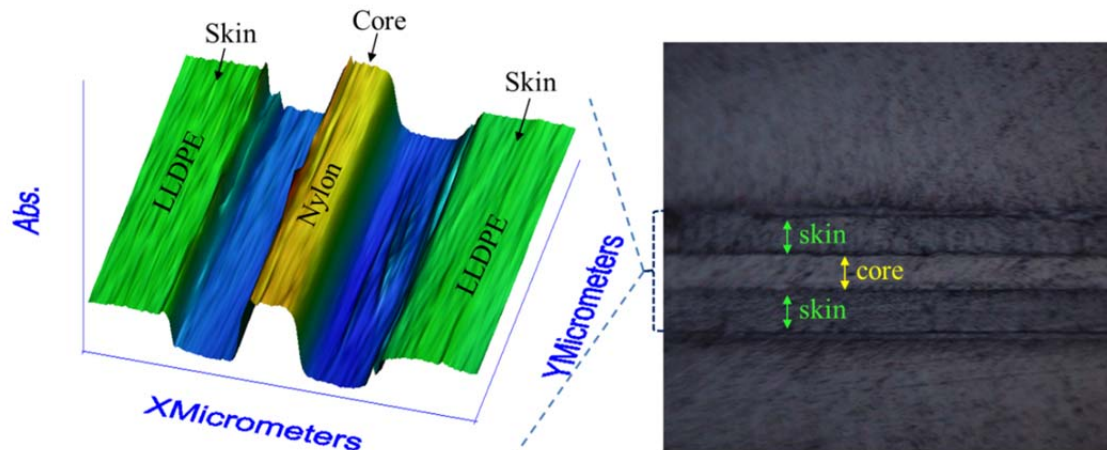


Figure 8-3 FTIR micrograph of cross-section for coextruded PA6/LLDPE multilayer film.

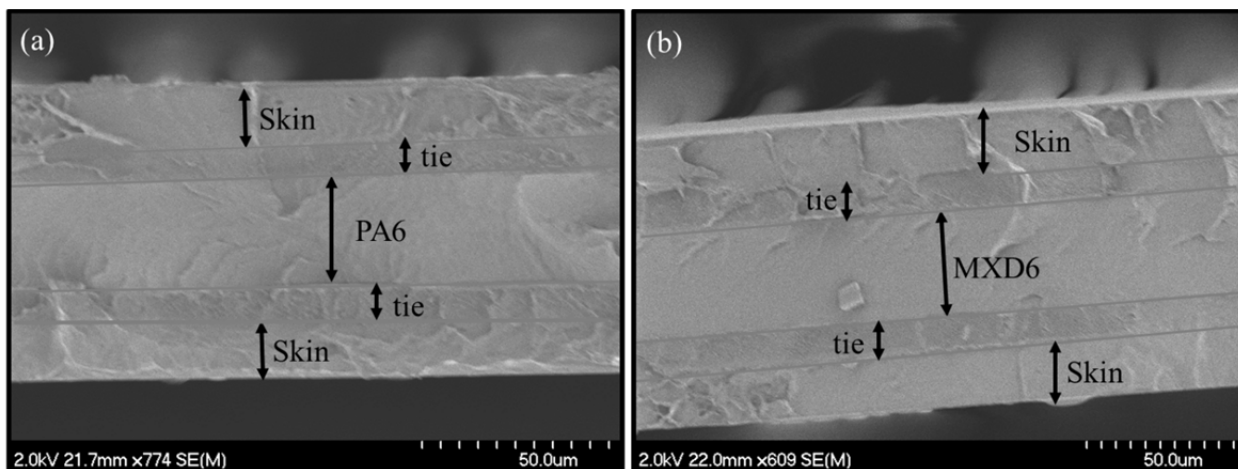


Figure 8-4 Scanning electron micrographs of cross-section for (a) PA6/LLDPE and (b) MXD6/LLDPE coextruded multilayer films.

FTIR imaging technique and SEM were used to determine the layer ratio of the multilayer films and also to detect interfacial instabilities that may arise in coextrusion film processing. However, due to peak overlapping in the FTIR microscopic image of the LLDPE and LLDPE-g-MA, layer distribution of the skin and tie layers could not be obtained directly from FTIR. To overcome this drawback, SEM analysis was able to successfully show the core, tie and skin

layers. Figure 8.4 illustrates the interfacial stability of the coextruded PA6/LLDPE and MXD6/LLDPE multilayer films. Similar stable configurations were also observed for the coextruded nylon nanocomposite films (images are not shown). The X-ray diffraction profiles for the nanoclay composite films at low diffraction angles are depicted in Figure 8.5.

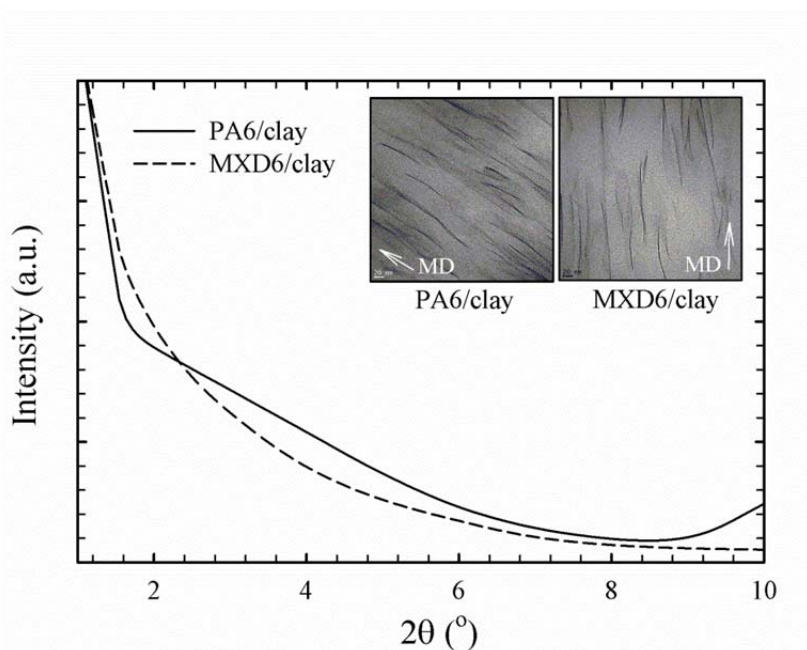


Figure 8-5 X-ray diffraction patterns for PA6/clay and MXD6/clay nanocomposites.

No peak in the cross-section diffraction intensity profiles of the coextruded PA6/clay and MXD6/clay films at low 2θ (below 10°) are observed. This indicates that the dispersed clay morphology in the nylon nanocomposites we used are close to the state of exfoliation^{53, 54}. This is attributed to a good affinity between nylon matrices and clay platelets⁵⁵. The TEM micrographs (see Figure 8.5) also display individual dispersed silicate layers in both aliphatic and aromatic nylon nanocomposite films, confirming the XRD results. It is clear that the individual layers are well aligned in machine direction. Clay platelets have high tendency to orient themselves in the flow direction during the cast film process^{56, 57}, due to their planar structure with high aspect ratio⁵⁸.

8.4.3 Thermal properties

The DSC heating curves of the coextruded PA6/LLDPE and MXD6/LLDPE as well as their nanocomposite multilayer films display two endotherms assigned to melting the LLDPE and nylon crystals (Figure 8.6 (a)). The endothermic peak at 220 °C in the first heating ramp of the PA6 is due to melting the α -form crystals. The PA6 α crystalline phase formed during thermal induced reorganization of the thermodynamically unstable γ crystalline phase¹⁶.

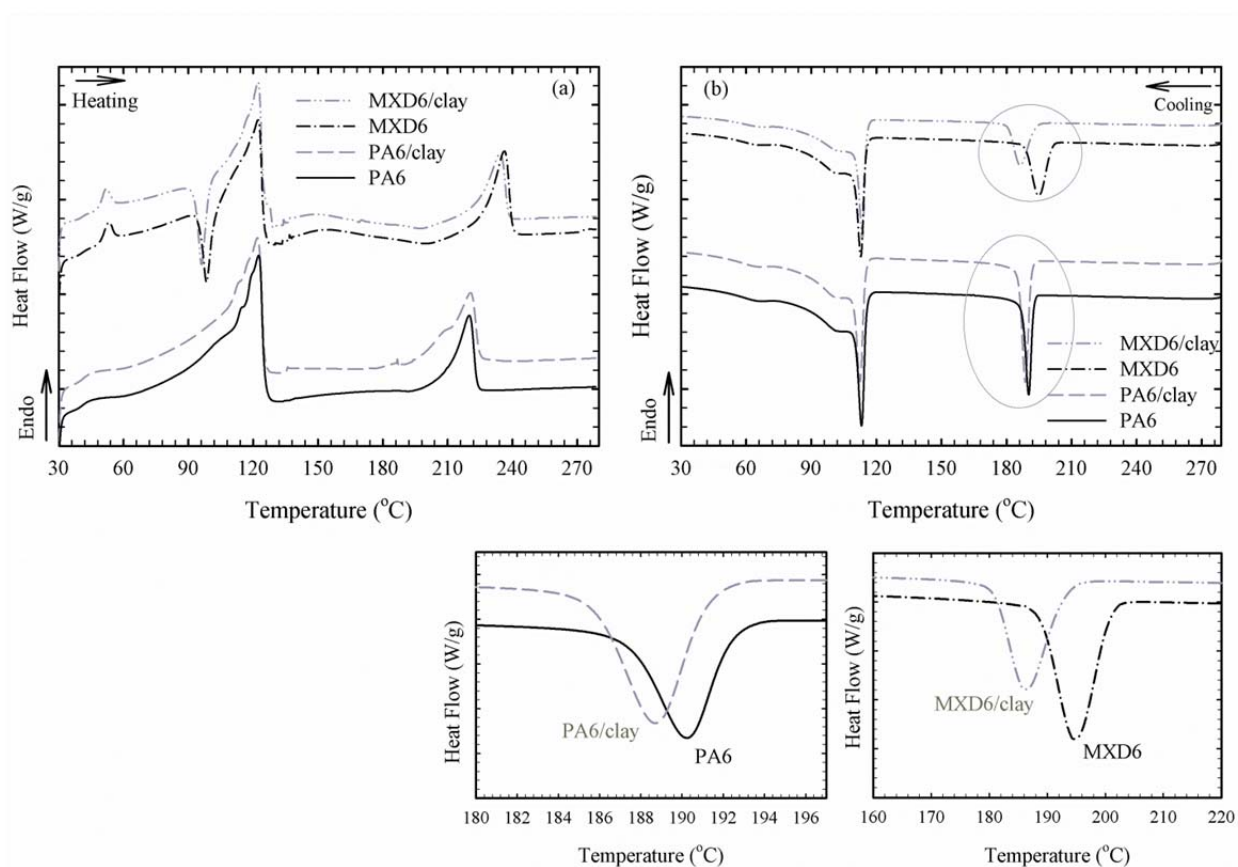


Figure 8-6 DSC thermograms for coextruded PA6/LLDPE, nano-clay filled PA6/LLDPE, MXD6/LLDPE and nano-clay filled MXD6/LLDPE multilayer films; (a) first heating ramp, (b) cooling (crystallization) ramp.

A small shoulder at about 207 °C on the main endotherm peak of coextruded nano-clay filled PA6/LLDPE indicates the melting of γ crystalline phases. The addition of clay into PA6 facilitates the production of aligned arrays of H-bonded sections that act as stable γ nuclei^{54, 59}.

The absence of a cold crystallization exotherm above the glass transition temperature of the coextruded PA6 films, i.e. about 50 °C (see Figure 8.6 (a)), suggests that no additional PA6 crystalline phase was generated from the PA6 amorphous phase during the DSC heating scan. It means that chain immobilization during the solidification process after the cast extrusion cannot occur in the PA6 layer. Cold crystallization exothermic peaks in the first heating scans of the coextruded MXD6/LLDPE and nano-clay filled MXD6/LLDPE multilayer films are observed between 85-135 °C which are in agreement with the results obtained by Seif et al ⁶⁰. During film processing, the orientation of chains in the coextruded MXD6/LLDPE can act as nucleating sites for further crystallization with increasing temperature. The small exothermic peak at about 200 °C, just below the endothermic peak, in the first heating cycle of the coextruded MXD6 multilayer films is attributed to the crystal reorganization of the polymer matrix ⁴². In other words, it could be ascribed to the melting and quick recrystallization of MXD6 films, as already shown by several authors ^{61, 62}. The melting endotherm of the LLDPE layer appears in the same temperature range for all multilayer films. The broad peak ranging from 50 °C to 130 °C with the maximum around 122°C results from the melting of LLDPE chains. Multiple melting endotherms for LLDPE were reported due to differences distribution of molecular weight and short-chain branching in copolymer chains ⁶³.

The DSC cooling cycle thermograms show that the incorporation of clay into the nylon matrix lowers the crystallization temperatures (T_c) (see Figure 8.6 (b)). A similar behavior was also reported by other researchers and could be associated to the effect of clay platelets inducing a delay on the crystal growth ^{11, 59}. However, some authors reported that the clay platelets act as heterogeneous nucleating agents that increase the crystallization temperature of nylon nanocomposites in comparison with pristine PA6 ^{54, 64, 65}. This contradiction can be explained by

the hindrance effect of clay platelets on the polymer chain diffusion and crystal growth⁶⁶. Wu et al.⁶⁷ claimed that the hydrogen bonding for crystalline formation of PA6 can become weak by the presence of clay. A highly important parameter for the crystallization behavior of PA6/clay nanocomposites is the exfoliation degree of clay layers in PA6 matrix. The shift in the crystallization temperature due to the presence of clay is higher for the MXD6/clay compared to the PA6/clay. It is speculated that due to the strong polymer-particle interaction in MXD6/clay, the diffusion of polymer chains to form crystals, and consequently their growth, is hindered⁶⁶. The exothermic crystallization peak of the LLDPE layer was observed between 125 to 85 °C with a sharp exothermic at 112 °C and a shoulder at about 102 °C due to non-homogeneous distribution of branches along the LLDPE copolymer chains⁶⁸. The crystallization temperature of LLDPE is strongly affected by molecular weight, molecular weight distribution, type of comonomer, concentration of side-chain branching, and their distribution along the polymer backbone⁶³. The presence of two exothermic peaks is often observed in LLDPE copolymers⁶⁸. According to Watanabe et al.⁶⁸, the sharp peak is known to be due to the crystallization of the polymer chains with high molecular weight and low branching content, while the small shoulder is because of the crystallization of the polymer chains with low molecular weight and high branching content.

In the DSC heating thermogram of the coextruded MXD6/LLDPE multilayer films (Figure 8.6 (a)), the broad endotherm melting of the LLDPE overlaps with the MXD6 exothermic cold crystallization peak. Deconvolution of the peaks in the range of 80 to 160 °C is applied using a linear heat flow rate superimposed with a small amplitude sinusoidal temperature profile in MDSC. Reversing and non-reversing signals, shown in Figure 8.7, are not related to the concept of thermodynamic reversibility.

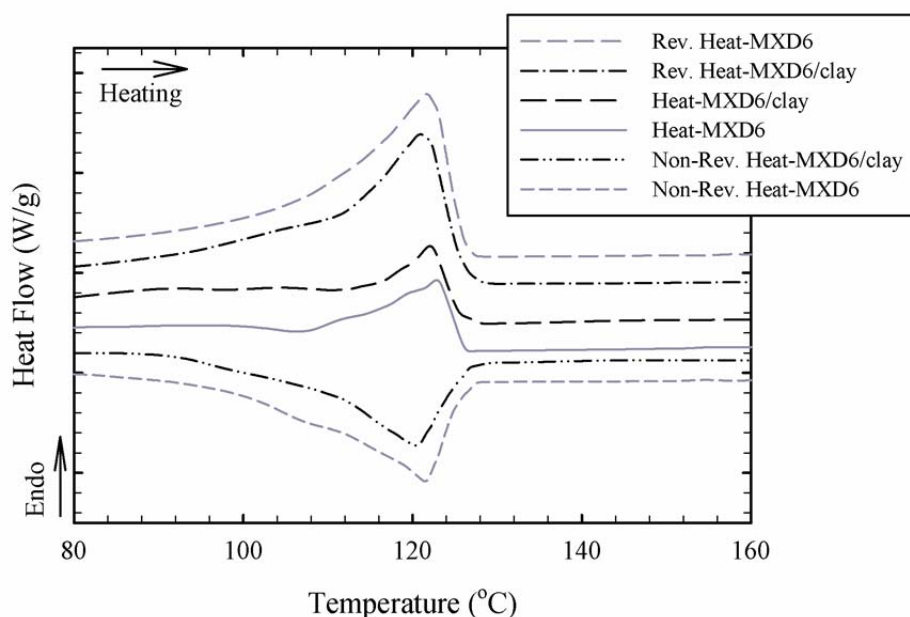


Figure 8-7 MDSC cold crystallization thermograms of coextruded MXD6/LLDPE and nano-clay filled MXD6/LLDPE multilayer films.

The thermal transitions related to the heat capacity changes of the coextruded MXD6/LLDPE multilayer films such as glass transition and melting temperatures can be measured with the reversing signal. The non-reversing signal represents the kinetic processes such as crystallization, decomposition and chemical reaction⁶⁹. The DSC cooling results presented in Figure 8.6 (b) were used to calculate the crystallinity of each resin after erasing their thermomechanical history, while the first DSC heating cycle results were used to obtain the film crystallinity after the coextrusion process. Table 8.2 summarizes the main thermal characteristics of the coextruded multilayer films (i.e. the crystallization temperature (T_c), melting point (T_m), cold crystallization temperature (T_{cc}), resin crystallinity ($X_{c, resin}$), and film crystallinity ($X_{c, film}$)).

Table 8.2 Thermal properties of coextruded PA6/LLDPE, nano-clay filled PA6/LLDPE, MXD6/LLDPE and nano-clay filled MXD6/LLDPE multilayer films.

LLDPE/tie/A/tie/LL	T_c	T_m	T_{cc}	$\Delta H_{Cooling}$	$\Delta H_{Heating}$	$X_{c, resin} (\%)$	$X_{c, film} (\%)$
DPE	(°C)	(°C)	(°C)	(J/g)	(J/g)		
A=PA6	191	220	-	62 ± 0.5	58 ± 0.7	33 ± 0.1	30 ± 1
A=PA6/clay	188	207, 220	-	73 ± 2	71 ± 0.8	40 ± 1	38 ± 1
A=MXD6	195	237	122	57 ± 0.2	24 ± 1	33 ± 0.3	14 ± 0.5
A=MXD6/clay	186	234	120	59 ± 0.3	29 ± 1.2	35 ± 0.1	17 ± 1
LLDPE skin layer	112	122	-	139 ± 0.2	135 ± 2	48 ± 0.5	44 ± 1

The numbers after ± sign are standard deviations.

Crystallinity of polyamide based nanocomposites is controlled by the polyamide matrix, molecular weight, clay concentration and the level of clay exfoliation^{55, 70}. As reported in Table 8.2, the crystallinity of the PA6/clay and MXD6/clay layers in the coextruded multilayer films are close to their neat polymer layers. In addition, the crystallinity of the neat and nanocomposite MXD6 layers in the coextruded multilayer films is relatively low, which is related to the high relaxation time of the MXD6 due to the chain stiffness¹⁶. Since in the cast extrusion process, the films are cooled rapidly, the processing time scale is much shorter than the crystallization characteristic time and, as a result, a less crystals are formed in the MXD6 and MXD6/clay layer of the coextruded multilayer films. However, the MXD6 crystallinity obtained from the second

heating cycle is drastically higher than the MXD6 layer in the multilayer films, indicating that the processing conditions, particularly cooling rate, have a significant effect on crystallinity.

8.4.4 Barrier properties

The oxygen transmission rates (OTR) for the coextruded PA6/LLDPE and MXD6/LLDPE as well as their nanocomposite based multilayer films normalized by the core layer thickness are shown in Figure 8.8. The oxygen barrier of the coextruded MXD6/LLDPE multilayer film was more than five times better than the PA6/LLDPE multilayer film processed under the same conditions. Substituting the neat PA6 core layer with the nanocomposite PA6 core layer of similar thickness decreased the oxygen permeability by about 58 %. A similar improvement was also observed in the oxygen barrier of the coextruded aromatic polyamide films.

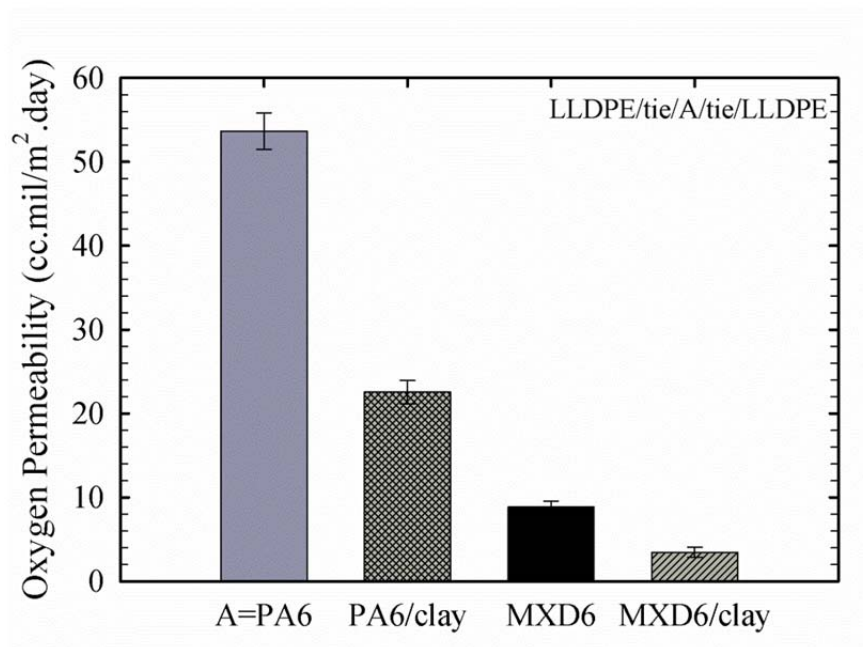


Figure 8-8 Oxygen permeability for coextruded PA6/LLDPE, nano-clay filled PA6/LLDPE, MXD6/LLDPE and nano-clay filled MXD6/LLDPE multilayer films.

The coextruded aromatic Nylon/LLDPE multilayer films show a better barrier in spite of their low crystallinity (see Table 8.2). It is known that gas diffusion coefficient in polymers is strongly

dependent on tortuosity and free volume. In literature ^{18, 71}, the free volume of MXD6 was reported to be 13.6 % less than that of PA6 ^{18, 71}. This indicates that, although the aliphatic layer has a higher crystallinity than the aromatic layer in the coextruded multilayer film (see Table 8.2), however, the aromatic chains are more packed than those of the aliphatic ones and as a consequence, the coextruded aromatic multilayer film has a much lower oxygen transmission rate.

Under steady state, the gas permeation through a coextruded multilayer film is inversely proportional to the layer thicknesses. The total gas permeation coefficient (P) through the coextruded multilayer films can be estimated by summing the permeation resistance of each layer using Eq (8.3) ¹:

$$\frac{1}{P} = \left(\frac{1}{\mu}\right) \sum_{i=1}^n \left(\frac{\mu_i}{P_i}\right) \quad (8.3)$$

where

μ_i	=	layer thickness
P_i	=	permeation coefficient
n	=	number of layers in the coextruded films.

In order to estimate the oxygen permeation coefficient of the coextruded multilayer films, the oxygen permeation of the single layers was determined and is presented in Figure 8.9. It should be pointed out that the data were normalized with respect to the film thickness. The oxygen permeation of the PA6/clay and MXD6/clay single layers has been reported in our previous study ¹⁶.

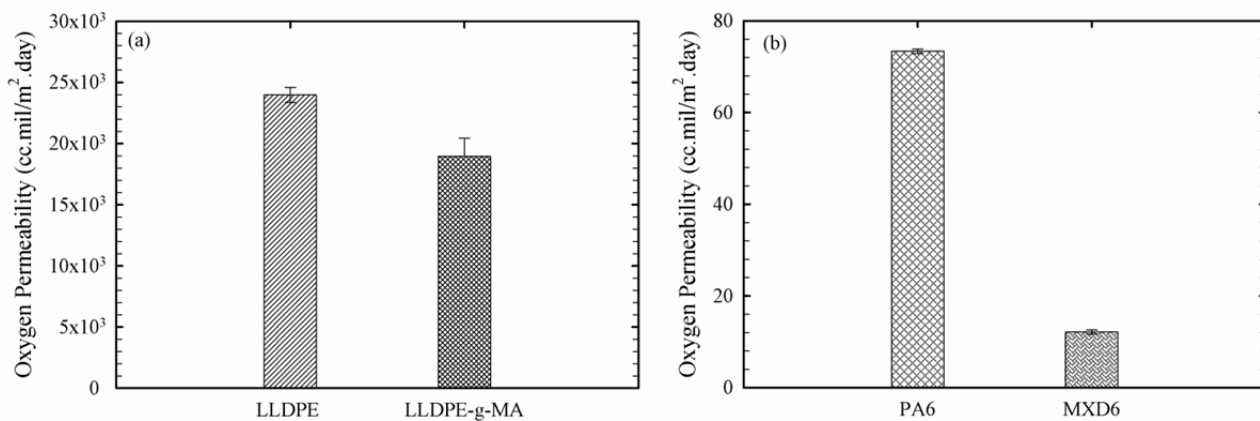


Figure 8-9 Oxygen permeability for monolayer film (a) LLDPE and LLDPE-g-MA. (b) PA6 and MXD6.

The oxygen permeation of the coextruded multilayer films were calculated using the model described by Eq. (8.3) and the results are reported in Table 8.3.

Table 8.3 Measured and calculated oxygen barrier properties of coextruded multilayer films.

	Experimental	Calculated
LLDPE/tie/A/tie/LLDPE	permeability (cc.mil/m ² .day)	permeability (cc.mil/m ² .day)
A=PA6	253 ± 2.7	255
PA6/clay	59 ± 2.3	100
MXD6	23 ± 0.4	26
MXD6/clay	12 ± 0.3	16

The numbers after ± sign are standard deviations.

It is clear that the calculated data are quite different from the experimental results for the coextruded nanocomposite multilayer films (30-50% difference). It should be mentioned that the series resistance model that was used (Eq. (8.3)) to estimate the overall oxygen barrier properties of the multilayer films may not be accurate. A single layer polymer film may not display exactly the same barrier properties compared to when that polymer is used as a layer in a coextruded multilayer structure. The difference can be explained by the changes in chains orientation and polymer crystallinity as well as the boundary effects (e.g. transcrystallization) of adjacent layers⁷². Moreover, the stiffness and viscosity of the polymer chains close to the interface could be enhanced due to crosslinking effect of the PE layer at the interface, or due to the covalent bonding of the PE-g-MA with the nylon chains³⁷. In other words, a good compatibility of the neighboring layers due to the reactivity between the maleic-anhydride reactive groups and the –COOH and –NH₂ end-groups of the nylon could provide a good adhesion at the polymer/polymer interface in the multilayer structure which significantly affect the final barrier

properties of the multilayer structure³⁷. The mechanism and kinetics of the reaction between the epoxide ring of PE-g-MA layer and –COOH and –NH₂ groups of PA6 layer in the melt state during coextrusion process have been investigated by others in literature³⁷. It was shown that the polymer chain configurations and the diffusion rate of the –COOH and –NH₂ groups in PA6 layer could control the reaction rate at the interface. A competition between polymer/polymer interdiffusion and the interfacial reaction in the multilayer coextruded cast films of PA6 / PE-g-MA was shown in their work³⁷. In a recent study done by Sallem-Idrissi et al.⁶¹, it was reported that the PA6 orientation in a multilayer structure does not follow the same pattern as the monolayer films; hence a lower PA6 crystalline phase orientation was observed in multilayer films. Additionally, PA6 crystallinity (X_c) was reported to increase by about 20 % in multilayer structure compared to monolayer film processed under the same conditions⁶¹.

The water vapor transmission rates (WVTR) of the coextruded aromatic and aliphatic nylons as well as their nanocomposite multilayer films are displayed in Figure 8.10.

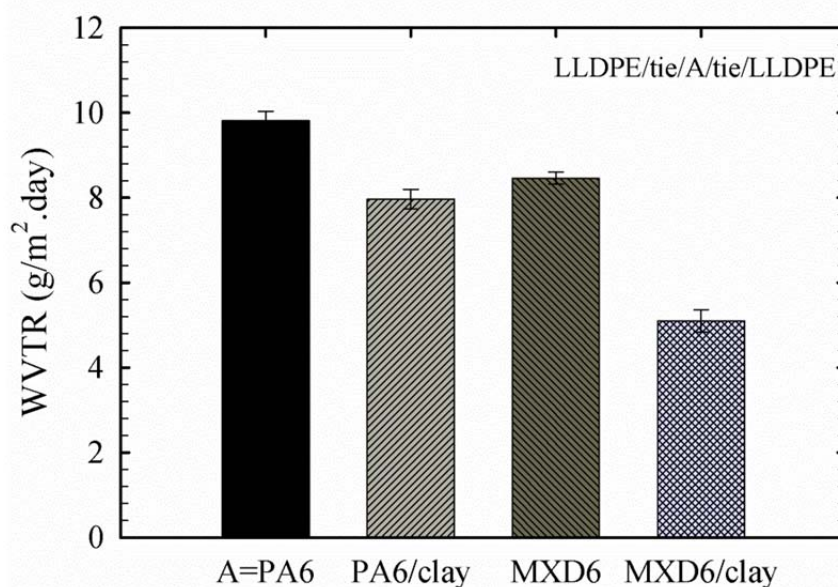


Figure 8-10 Water vapor transmission rate for coextruded PA6/LLDPE, nano-clay filled PA6/LLDPE, MXD6/LLDPE and nano-clay filled MXD6/LLDPE multilayer films.

The water vapor transmission rate of the coextruded MXD6 multilayer film is lower than the PA6 samples. Other investigations showed that the barrier properties of MXD6 films improved as the relative humidity increased from 0 to 60 %^{12, 17}. According to Gavara et al.¹³, forming hydrogen bonds between the amide groups caused by water molecules creates small changes in the MXD6 crystalline structure and consequently decreases the available moisture paths in the polymer matrix. It has been speculated by Hu et al.¹² that it is energetically more favorable for water molecules to form hydrogen bonds with MXD6 chains than to reside in free volume holes. Another theory by Krizan et al.⁷³ stated that water molecules in MXD6 matrix compete with permeant gas for excess free volume, therefore, the pathway available for gas diffusion is reduced. The permeation behavior of semicrystalline MXD6 in contact with water molecules was also characterized by Buquet et al.⁷⁴. They demonstrated that after moisture diffuses through the polymer matrix, a water-induced crystallization phase takes place at the interface of polymer chains and water molecules. It consequently improved the MXD6 moisture barrier properties. Adding 4 wt% clay into the coextruded PA6/LLDPE multilayer film improved its water vapor barrier by about 27%. In addition, incorporating clay in the coextruded MXD6/LLDPE improved their moisture barrier about 58%. These results are in a good agreement with Thellen et al.⁷⁵ who reported a 56% reduction in the MXD6 nanocomposite water vapor permeability. The most likely cause of the drastic change in the MXD6 water vapor barrier in the presence of clay could be related to an increase in the water-induced crystallization phase.

8.4.5 Mechanical properties

The tensile properties of the coextruded multilayer films in both machine (MD) and transverse (TD) directions are summarized in Table 8.4.

Table 8.4 Mechanical properties (stiffness, tensile strength, elongation at break and toughness) of coextruded PA6/LLDPE, nano-clay filled PA6/LLDPE, MXD6/LLDPE and nano-clay filled MXD6/LLDPE multilayer films in MD and TD.

LLDPE/tie/A/tie/LL DPE	Stiffness (MPa)	Tensile Strength (MPa)	Elongation at Break (%)	Toughness (J/m ³)
A=PA6-MD	330 ± 20	38.8 ± 2	365 ± 30	5172 ± 300
A=PA6-TD	358 ± 30	29.6 ± 4	400 ± 25	4758 ± 300
A=PA6/clay-MD	840 ± 30	41.4 ± 1.9	340 ± 24	4863 ± 148
A=PA6/clay-TD	670 ± 40	36.9 ± 3.6	368 ± 19	4547 ± 180
A=MXD6-MD	1127 ± 110	26.7 ± 4.2	309 ± 20	2886 ± 200
A=MXD6-TD	1177 ± 137	23.7 ± 2.6	160 ± 30	2200 ± 160
A=MXD6/clay-MD	1318 ± 105	32.7 ± 2.3	38 ± 5	576 ± 60
A=MXD6/clay-TD	1322 ± 63	29.8 ± 2.8	9.2 ± 3.8	80.3 ± 6

The numbers after ± sign are standard deviations.

The coextruded MXD6/LLDPE multilayer films show a higher stiffness compared to the PA6/LLDPE ones. Although the PA6 layer crystallinity was higher than the MXD6, both barrier properties and mechanical stiffness of the coextruded MXD6/LLDPE multilayer films were higher than the PA6/LLDPE. This can be explained by higher interaction and stiffness of the aromatic chains compared to the aliphatic ones as discussed in our previous study¹⁶. It should be pointed out that for both the aromatic and aliphatic nylon coextruded films, the tensile strength is slightly higher in MD than in TD, which is attributed to the chain orientation in the machine

direction due to stretching and fast cooling during the cast film processing ⁷⁶. The mechanical performances of the coextruded PA6/LLDPE multilayer films reveal more flexibility compared to the MXD6/LLDPE. As a result, PA6/LLDPE had higher elongation at break and toughness than the MDX6/LLDPE. The mechanical properties of the coextruded multilayer films are greatly influenced not only by the nylon but also by the LLDPE and tie layers. As seen, the elongation at break and toughness of the coextruded PA6 multilayer films are high and the substituting the neat PA6 with its nanocomposite does not affect significantly those properties. The elongation of coextruded multilayer films is strongly influenced by crystallinity, type, and crystal orientation in both core and skin layers.

The tear resistance of the coextruded nylons and their nanocomposite multilayer films along MD and TD are presented in Figure 8.11. The coextruded nanocomposite multilayer films show a lower tear resistance than the neat nylon films. The same behavior was reported for Polyethylene terephthalate, polypropylene, and low density polyethylene nanocomposites films compared to their neat films ⁷⁷⁻⁷⁹. The resistance to tear propagation for the coextruded multilayer films in TD was higher than in MD due to the higher polymer chain orientation in the flow direction.

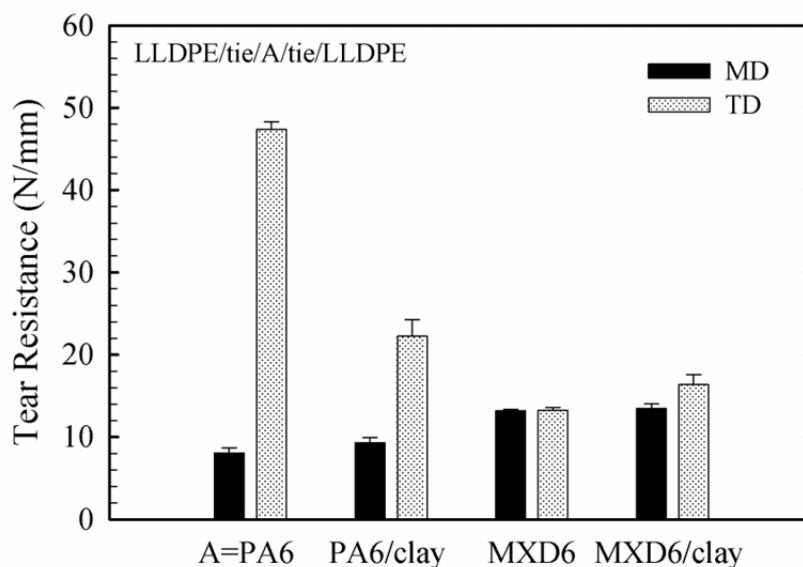


Figure 8-11 Tear resistance for coextruded PA6/LLDPE, nano-clay filled PA6/LLDPE, MXD6/LLDPE and nano-clay filled MXD6/LLDPE multilayer films.

In Figure 8.11, it is obvious that the differences to tear propagation resistance in TD and MD are very significant in the coextruded PA6/LLDPE multilayer film. This can be explained by the amorphous and crystal phase orientation in the pristine and nanocomposite films. In our previous study performed on the single layers of aromatic and aliphatic nylons⁸⁰, it was shown that the amorphous and crystalline phases had a lower orientation in the flow direction in the nanocomposite films compared to the neat polymer films. These were interpreted by the spatial hindrance caused by the clay platelets. Figure 8.11 also shows that the tear resistance of the coextruded PA6/LLDPE was much higher than that of the MXD6/LLDPE due to the higher stiffness and lower relaxation rate of the aromatic chains, which induced little crystallinity in the MXD6. In addition, the coextruded MXD6/LLDPE multilayer film shows almost the same tear resistance in TD and MD, which is related to its low and random crystalline phase orientation⁸⁰. This is also supported by the mechanical properties of the coextruded MXD6/LLDPE films as

small differences were observed in the mechanical stiffness and tensile strength of the coextruded MXD6/LLDPE multilayer film in MD and TD (see Table 8.4).

The puncture resistance of the coextruded multilayer neat nylons and their nanocomposite films is shown in Figure 8.12.

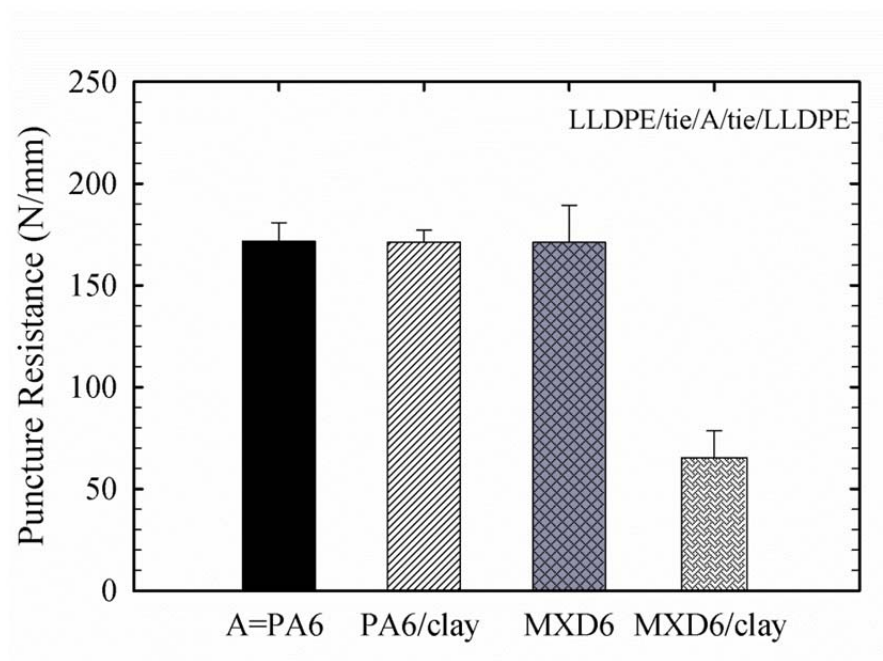


Figure 8-12 Puncture resistance for coextruded PA6/LLDPE, nano-clay filled PA6/LLDPE, MXD6/LLDPE and nano-clay filled MXD6/LLDPE multilayer films.

As illustrated, after replacing PA6 with PA6/clay in the core layer of coextruded multilayer films, the puncture resistance was maintained, probably due to the flexible LLDPE layers. In other words, the overall response to puncture propagation is greatly influenced not only by the PA6 layer but also by the two LLDPE and tie layers. The puncture resistance of the coextruded nano-clay filled MXD6/LLDPE multilayer film is about 62% lower than the coextruded MXD6/LLDPE. It has also been reported that the puncture resistance of PET/clay nanocomposite single layer film was 60% lower in comparison with neat PET⁷⁷. This could be related to the strong interfacial adhesion between the exfoliated clay surface and nylon matrix¹⁶.

Moreover, the MXD6/clay is more brittle because of the higher crystallinity compared to the neat aromatic nylon. This brittleness induced by adding nanoparticles to the polymer matrix led to reducing the elongation at break, and hence to reducing the puncture resistance.

Another important property of multilayer films, which makes them suitable for many food packaging applications, is their flex crack resistance. In fact, during the manufacturing process of packaged food, such as the vertical form fill and sealing process, the package made of multilayer films is subjected to many deformations among which the ones in the flexural mode are the most important. The ability to resist crack development is related to the chemical and molecular structure, nature of polymer chains; dispersion, shape and nanoparticle size, and particle-particle and polymer-particle interactions. The flex crack resistance of the coextruded multilayer nylons and their nanocomposite films are displayed in Figure 8.13.

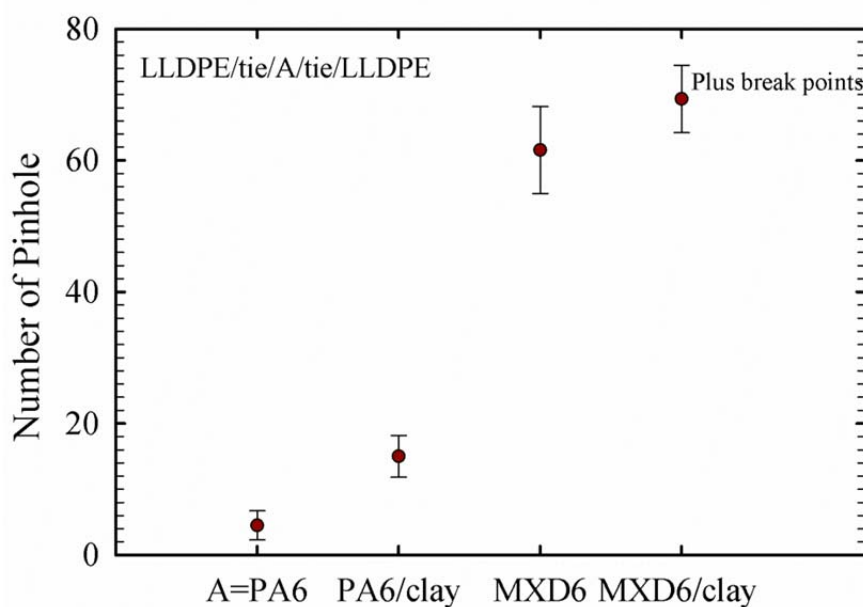


Figure 8-13 Flex crack resistance for coextruded PA6/LLDPE, nano-clay filled PA6/LLDPE, MXD6/LLDPE and nano-clay filled MXD6/LLDPE multilayer films.

The PA6/LLDPE multilayer films show the highest flex crack resistance. The ability of the coextruded films to resist against crack propagation decreased by about 3.5 times, when the neat

PA6 core layer of the multilayer films was substituted with the nanocomposites core layer. Nanoclay induced reduction effect on PA6 resistance to cracking can be attributed to the participation of the polymer chains in crystalline structure. In other words, it can be anticipated that crystals and nanoclay act synergistically and contribute sufficient anisotropy and rigidity to cause more cracking. The coextruded aromatic nylon/LLDPE multilayer films showed a lower flex crack resistance compared to those made from the aliphatic ones. This could be due to the fact that the aromatic polymer has more rigidity and is more brittle because of its very strong intermolecular chain interactions. The coextruded nano-clay filled PA6/LLDPE multilayer films did not tear in the crack propagation, while PA6/clay in the core layer was replaced with MXD6/clay, longitudinal cracking and breaking points were observed during the test. As reported by Cotterell et al.⁸¹, any toughening action of nanoclay composites strongly depends on the delamination ability of exfoliated nanoclay from the host polymer matrix and also depends on particle size, shape, aspect ratio, exfoliation state and inter bonding energy. On the other hand, due to the strong bonding between nanoclay particles and MXD6 chains, delaminating or splitting particles would be more difficult to achieve and the polymer becomes more brittle. In this case, it appears that the polyamide/nanoparticle bonding is strong and therefore the MXD6 nanocomposite films exhibited the least degree of flex crack resistance.

8.4.6 Optical properties

Figure 8.14 shows that the MXD6/LLDPE multilayer film has the lowest haze due to its lower crystallinity (see Table 8.2). The presence of silicate layers reduces the clarity and increases the haze of the nanocomposite films. In our previous study¹⁶, it was shown that crystallinity of the PA6/clay and MXD6/clay are higher than their neat resins. The effect of clay on the haze is higher for the aromatic nanocomposite compared to the aliphatic one.

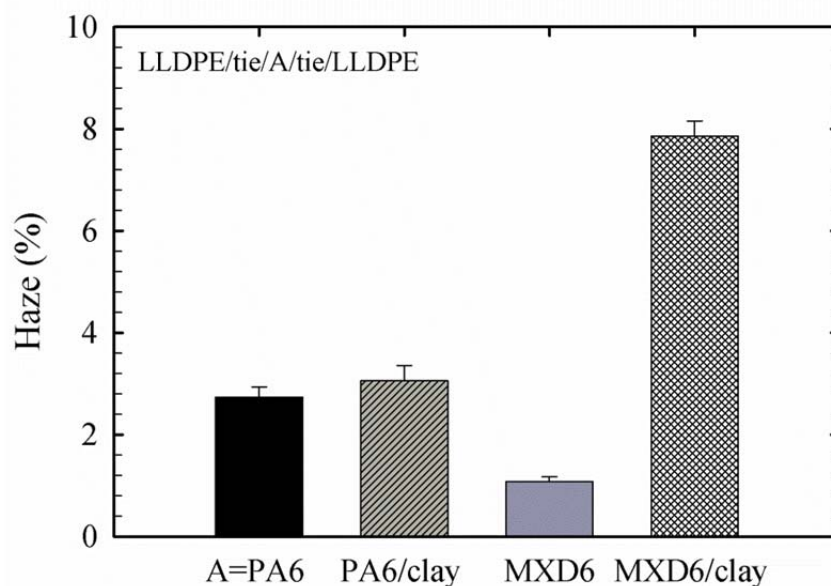


Figure 8-14 Haze of coextruded PA6/LLDPE, nano-clay filled PA6/LLDPE, MXD6/LLDPE and nano-clay filled MXD6/LLDPE multilayer films.

It is obvious that the good MXD6 transparency was significantly lowered after incorporating clay. A similar result was also reported for PET/clay nanocomposites as the PET film haze increased by 9 times after adding nanoclay⁷⁷. It can be explained that adding clay in MXD6 increases the polymer matrix crystallinity that can effectively scatter light. Another possibility for the lower transparency in the MXD6/clay might be due to the very strong MXD6 hydrogen bonding with the clay surface, which significantly affects the refractive index⁸².

8.5 Conclusions

Five-layer coextruded multilayer films were produced through the casting process. The processing parameters were optimized to minimize interfacial melt flow instability and improve film uniformity. The MXD6 layer in the multilayer films showed a lower crystallinity compared to the PA6 layer. However, oxygen permeation rate of the neat MXD6/LLDPE coextruded multilayer film was 5 times better than for the neat PA6/LLDPE multilayer film. An

improvement of about 58% was observed in the oxygen barrier, when the neat nylons in the core layer were substituted with the nanocomposites. The series resistance model was not able to predict the multilayer film barrier properties based on the nanocomposites. A single layer polymer film did not display the same barrier properties compared to when that polymer was used as a layer in a coextruded multilayer structure. It was due to the changes in chains orientation and crystallinity of the polymer as well as the boundary effects of the adjacent layers. The MXD6/LLDPE coextruded multilayer film showed better moisture resistance compared to the PA6/LLDPE multilayer film. The nano-clay filled MXD6/LLDPE multilayer film showed the lowest water vapor transmission rate due to an increase in the water-induced crystallization phase by incorporating the nanoclay in the MXD6. The coextruded PA6/LLDPE multilayer films showed higher toughness, tear and flex crack resistance compared to those with MXD6 as the core layer. The haze increased with substituting the neat MXD6 with the nanocomposite MXD6 or with the aliphatic polyamide as the core layer.

8.6 Acknowledgment

Financial support from NSERC (Natural Science and Engineering Research Council of Canada) and of the industrial partners of 3SPack Chair Saputo and Prolamina is gratefully acknowledged.

8.7 References

1. Wagner JR. Hand Book of Multilayer flexible packaging technology and applications for food, personal care and over-the counter pharmaceutical industries. Burlington, USA: Elsevier Inc., 2010.
2. Ganpule HK and Khomami B. An investigation of interfacial instabilities in the superposed channel flow of viscoelastic fluids. *Journal of Non-Newtonian Fluid Mechanics*. 1999; 81: 27-69.
3. Dooley J, Hyun KS and Hughes K. An experimental study on the effect of polymer viscoelasticity on layer rearrangement in coextruded structures. *Polym Eng Sci*. 1998; 38: 1060-71.
4. Kojima Y, Usuki A, Kawasumi M, et al. Mechanical properties of nylon 6-clay hybrid. *J Mater Res*. 1993; 8: 1185-9.
5. Usuki A, Kojima Y, Kawasumi M, et al. Synthesis of nylon 6-clay hybrid. *J Mater Res*. 1993; 8: 1179-84.
6. Oshinski AJ, Keskkula H and Paul DR. Rubber toughening of polyamides with functionalized block copolymers: 1. Nylon-6. *Polymer*. 1992; 33: 268-83.
7. Kojima Y, Usuki A, Kawasumi M, Okada A, Kurauchi T and Kamigaito O. Synthesis of nylon 6-clay hybrid by montmorillonite intercalated with ϵ -caprolactam. *Journal of Polymer Science, Part A: Polymer Chemistry*. 1993; 31: 983-6.
8. Gupta B, Lacrampe M-F and Krawczak P. Polyamide-6/clay nanocomposites. *Polym Polym Compos*. 2006; 14: 13-38.
9. Cho JW and Paul DR. Nylon 6 nanocomposites by melt compounding. *Polymer*. 2001; 42: 1083-94.

10. Dennis HR, Hunter DL, Chang D, et al. Effect of melt processing conditions on the extent of exfoliation in organoclay-based nanocomposites. *Polymer*. 2001; 42: 9513-22.
11. Poisson C, Guerengomba J, Lacrampe M-F, et al. Mechanical, optical and barrier properties of PA6/nanoclay-based single- And multilayer blown films. *Polym Polym Compos*. 2008; 16: 349-58.
12. Hu YS, Mehta S, Schiraldi DA, Hiltner A and Baer E. Effect of water sorption on oxygen-barrier properties of aromatic polyamides. *J Polym Sci Pol Phys*. 2005; 43: 1365-81.
13. Gavara R and Hernandez RJ. The effect of water on the transport of oxygen through nylon6-films *Journal of Polymer Science Part B-Polymer Physics*. 1994; 32: 2375-82.
14. Huang CH, Wu JS and Huang CC. Predicting the permeability and tensile behavior of high density polyethylene/tie/polyamide 6 three-layer films. *Polym Int*. 2004; 53: 2099-106.
15. Sadeghi F and Ajji A. Structure, Mechanical and Barrier Properties of Uniaxially Stretched Multilayer Nylon/Clay Nanocomposite Films. *Int Polym Proc*. 2012; 27: 565-73.
16. Fereydoon M, Tabatabaei SH and Ajji A. Rheological, crystal structure, barrier, and mechanical properties of PA6 and MXD6 nanocomposite films. *Polymer Engineering & Science*. 2013; published online: n/a-n/a.
17. Lagaron JM, Gimenez E, Gavara R and Saura JJ. Study of the influence of water sorption in pure components and binary blends of high barrier ethylene-vinyl alcohol copolymer and amorphous polyamide and nylon-containing ionomer. *Polymer*. 2001; 42: 9531-40.
18. Ammala A, Pas SJ, Lawrence KA, Stark R, Webb RI and Hill AJ. Poly(m-xylene adipamide)-montmorillonite nanocomposites: effect of organo-modifier structure on free volume and oxygen barrier properties. *J Mater Chem*. 2008; 18: 911-6.

19. Ammala A, Hill AJ, Lawrence KA and Tran T. Poly(m-xylene adipamide)-kaolinite and poly(m-xylene adipamide)-montmorillonite nanocomposites. *J Appl Polym Sci.* 2007; 104: 1377-81.
20. Tomomichi Kanda and Mori A. Gas-Barrier Multi-Layer Structure *Kanagawa*. Japan: Mitsubishi Gas Chemical Company Inc., Tokyo (JP), 2007.
21. Mueller C, Roger Kaas, Bertrand Fillon, Sandrine Tournier and Lerda J-J. *Thermoplastics film structures having improved barrier and mechanical properties US20020150729 A1*. USA2002.
22. Shibayama M, Uenoyama K, Oura JI and Nomura S. Miscibility and crystallinity control of nylon-6 and poly(m-Xylene adipamide) blends. *Polymer.* 1995; 36: 4811-6.
23. Takeda Y, Keskkula H and Paul DR. Toughening of phase-homogenized mixtures of nylon-6 and poly(m-xylene adipamide) with a functionalized block copolymer. *Polymer.* 1992; 33: 3394-407.
24. Takeda Y and Paul DR. Phase homogenization of mixtures of poly(m-xylene adipamide) and nylon 6 by interchange reactions. *Polymer.* 1991; 32: 2771-8.
25. Takeda Y and Paul DR. The effect of physical interactions on melt-phase homogenized of mixtures of poly(M-Xylene Adipamide) with aliphatic polamides induced by interchange reactions. *Polymer.* 1992; 33: 3899-907.
26. Takeda Y, Keskkula H and Paul DR. TOUGHENING OF PHASE-HOMOGENIZED MIXTURES OF NYLON-6 AND POLY (META-XYLENE ADIPAMIDE) WITH A FUNCTIONALIZED BLOCK COPOLYMER. *Polymer.* 1992; 33: 3394-407.
27. Takashige M, Kanai T and Yamada T. Easy tear film of biaxially oriented PA 6/MXD 6 blend by double bubble tubular film process. *Int Polym Proc.* 2004; 19: 147-54.

28. Takashige M and Kanai T. Easy tear multilayer film of biaxially oriented PA6/MXD6 by double bubble tubular film process. *Int Polym Proc.* 2005; 20: 100-4.
29. Dooley J and Tung H. Coextrusion. *Encyclopedia of Polymer Science and Technology.* John Wiley & Sons, Inc., 2002.
30. Dooley J. Viscoelastic Flow Effects in Multilayer Polymer Coextrusion. Eindhoven, the Netherlands: Technische Universiteit Eindhoven, 2002.
31. Mitsoulis E. Multilayer sheet coextrusion: Analysis and design. *Adv Polym Tech.* 1988; 8: 225-42.
32. Han CD. *Multiphase Flow in Polymer Processing.* New York: Academic Press, 1981.
33. Yu TC and Han CD. Stratified two-phase flow of molten polymers. *J Appl Polym Sci.* 1973; 17: 1203-25.
34. Han CD. A study of bicomponent coextrusion of molten polymers. *J Appl Polym Sci.* 1973; 17: 1289-303.
35. Han CD and Shetty R. Studies on multilayer film coextrusion II. Interfacial instability in flat film coextrusion. *Polymer Engineering & Science.* 1978; 18: 180-6.
36. Lamnawar K, Zhang H and Maazouz A. Coextrusion of Multilayer Structures, Interfacial Phenomena. *Encyclopedia of Polymer Science and Technology.* John Wiley & Sons, Inc., 2002.
37. Lamnawar K and Maazouz A. Role of the interphase in the flow stability of reactive coextruded multilayer polymers. *Polymer Engineering & Science.* 2009; 49: 727-39.
38. Schrenk WJ, Bradley NL, Alfrey T and Maack H. Interfacial flow instability in multilayer coextrusion. *Polymer Engineering & Science.* 1978; 18: 620-3.

39. Dooley J, Hyun KS and Hughes K. An experimental study on the effect of polymer viscoelasticity on layer rearrangement in coextruded structures. *Polymer Engineering & Science*. 1998; 38: 1060-71.
40. Heng F and Mitsoulis E. Numerical simulation of wire-coating coextrusion. *Int Polym Process*. 1989; 4: 44-56.
41. Ayer RK and Leonov AI. Comparative rheological studies of polyamide-6 and its low loaded nanocomposite based on layered silicates. *Rheol Acta*. 2004; 43: 283-92.
42. Doudou B, Dargent E and Grenet J. Crystallization and melting behaviour of poly(m-xylene adipamide). *J Therm Anal Calorim*. 2006; 85: 409-15.
43. Picard E, Vermogen A, Gérard JF and Espuche E. Barrier properties of nylon 6-montmorillonite nanocomposite membranes prepared by melt blending: Influence of the clay content and dispersion state: Consequences on modelling. *Journal of Membrane Science*. 2007; 292: 133-44.
44. Hong H, Zhang Z, Chung TCM and Lee RW. Synthesis of new 1-decene-based LLDPE resins and comparison with the corresponding 1-octene- and 1-hexene-based LLDPE resins. *J Polym Sci, Part A: Polym Chem*. 2007; 45: 639-49.
45. Dooley J and Rudolph L. Viscous and Elastic Effects in Polymer Coextrusion. *Journal of Plastic Film and Sheeting*. 2003; 19: 111-22.
46. Lamnawar K, Bousmina M and Maazouz A. 2D Encapsulation in Multiphase Polymers: Role of Viscoelastic, Geometrical and Interfacial Properties. *Macromolecules*. 2011; 45: 441-54.
47. Walia PS, Gupta RK and Kiang CT. Influence of interchange reactions on the crystallization and melting behavior of nylon 6,6 blended with other nylons. *Polym Eng Sci*. 1999; 39: 2431-44.

48. Ren J, Casanueva BF, Mitchell CA and Krishnamoorti R. Disorientation Kinetics of Aligned Polymer Layered Silicate Nanocomposites. *Macromolecules*. 2003; 36: 4188-94.
49. Lee KM and Han CD. Rheology of Organoclay Nanocomposites: Effects of Polymer Matrix/Organoclay Compatibility and the Gallery Distance of Organoclay. *Macromolecules*. 2003; 36: 7165-78.
50. Lertwimolnun W and Vergnes B. Influence of compatibilizer and processing conditions on the dispersion of nanoclay in a polypropylene matrix. *Polymer*. 2005; 46: 3462-71.
51. Khomami B and Ranjbaran MM. Experimental studies of interfacial instabilities in multilayer pressure-driven flow of polymeric melts. *Rheol Acta*. 1997; 36: 345-66.
52. Wilson GM and Khomami B. An experimental investigation of interfacial instabilities in multilayer flow of viscoelastic fluids. Part II. Elastic and nonlinear effects in incompatible polymer systems. *Journal of Rheology (1978-present)*. 1993; 37: 315-39.
53. Maiti P and Okamoto M. Crystallization Controlled by Silicate Surfaces in Nylon 6-Clay Nanocomposites. *Macromol Mater Eng*. 2003; 288: 440-5.
54. Miri V, Elkoun S, Peurton F, et al. Crystallization Kinetics and Crystal Structure of Nylon6-Clay Nanocomposites: Combined Effects of Thermomechanical History, Clay Content, and Cooling Conditions. *Macromolecules*. 2008; 41: 9234-44.
55. Fornes TD, Yoon PJ, Keskkula H and Paul DR. Nylon 6 nanocomposites: the effect of matrix molecular weight. *Polymer*. 2001; 42: 09929-40.
56. Bafna A, Beaucage G, Mirabella F and Mehta S. 3D Hierarchical orientation in polymer-clay nanocomposite films. *Polymer*. 2003; 44: 1103-15.
57. Usuki A, Hasegawa N, Kadoura H and Okamoto T. Three-Dimensional Observation of Structure and Morphology in Nylon-6/Clay Nanocomposite. *Nano Lett*. 2001; 1: 271-2.

58. Yalcin B, Ergungor Z, Konishi Y, Cakmak M and Batur C. Molecular origins of toughening mechanism in uniaxially stretched nylon 6 films with clay nanoparticles. *Polymer*. 2008; 49: 1635-50.
59. Fornes TD and Paul DR. Crystallization behavior of nylon 6 nanocomposites. *Polymer*. 2003; 44: 3945-61.
60. Seif S and Cakmak M. Stress - Optical behavior of Poly(m-xylylenediamine adipamide) (Nylon MXD6): Influence of molecular weight. *Polymer*. 2010; 51: 3762-73.
61. Sallem-Idrissi N, Miri V, Elkoun S, et al. Trichroic infrared analysis of the strain-induced structural changes in the PA6 layer of PA6/PE multilayer films under biaxial drawing. *Polymer*. 2009; 50: 5812-23.
62. Yalcin B and Cakmak M. Superstructural hierarchy developed in coupled high shear/high thermal gradient conditions of injection molding in nylon 6 nanocomposites. *Polymer*. 2004; 45: 2691-710.
63. Wilfong DL and Knight GW. Crystallization mechanisms for LLDPE and its fractions. *J Polym Sci Pol Phys*. 1990; 28: 861-70.
64. Devaux E, Bourbigot S and El Achari A. Crystallization behavior of PA-6 clay nanocomposite hybrid. *J Appl Polym Sci*. 2002; 86: 2416-23.
65. Ma CCM, Kuo CT, Kuan HC and Chiang CL. Effects of swelling agents on the crystallization behavior and mechanical properties of polyamide 6/clay nanocomposites. *J Appl Polym Sci*. 2003; 88: 1686-93.
66. Homminga DS, Goderis B, Mathot VBF and Groeninckx G. Crystallization behavior of polymer/montmorillonite nanocomposites. Part III. Polyamide-6/montmorillonite

nanocomposites, influence of matrix molecular weight, and of montmorillonite type and concentration. *Polymer*. 2006; 47: 1630-9.

67. Liu X and Wu Q. Phase transition in nylon 6/clay nanocomposites on annealing. *Polymer*. 2002; 43: 1933-6.

68. Watanabe S, Sano N, Noda I and Ozaki Y. Surface Melting and Lamella Rearrangement Process in Linear Low Density Polyethylene. *The Journal of Physical Chemistry B*. 2009; 113: 3385-94.

69. Jones KJ, Kinshott I, Reading M, Lacey AA, Nikolopoulos C and Pollock HM. The origin and interpretation of the signals of MTDSC. *Thermochim Acta*. 1997; 304–305: 187-99.

70. Shishan W, Dingjun J, Xiaodong O, Fen W and Jian S. The structure and properties of PA6/MMT nanocomposites prepared by melt compounding. *Polym Eng Sci*. 2004; 44: 2070-4.

71. Winberg P, Eldrup M, Pedersen NJ, van Es MA and Maurer FHJ. Free volume sizes in intercalated polyamide 6/clay nanocomposites. *Polymer*. 2005; 46: 8239-49.

72. Tabatabaei SH, Carreau PJ and Aji A. Microporous membranes obtained from PP/HDPE multilayer films by stretching. *Journal of Membrane Science*. 2009; 345: 148-59.

73. T.D. Krizan JCC, P.S. Blatz, W.J. Koros (Ed.). *Barrier Polymers and Structures*, American Chemical Society, Washington, DC. 1990, p.111–25 (Chapter 5).

74. Buquet CL, Doudou BB, Chappey C, Dargent E and Marais S. Permeation properties of poly(m-xylene adipamide) membranes. *Journal of Physical Chemistry B*. 2009; 113: 3445-52.

75. Thellen C, Schirmer S, Ratto JA, Finnigan B and Schmidt D. Co-extrusion of multilayer poly(m-xylylene adipimide) nanocomposite films for high oxygen barrier packaging applications. *Journal of Membrane Science*. 2009; 340: 45-51.

76. Tabatabaei SH, Carreau PJ and Aiji A. Effect of processing on the crystalline orientation, morphology, and mechanical properties of polypropylene cast films and microporous membrane formation. *Polymer*. 2009; 50: 4228-40.
77. Ghasemi H, Carreau PJ, Kamal MR and Tabatabaei SH. Properties of PET/clay nanocomposite films. *Polym Eng Sci*. 2012; 52: 420-30.
78. Lin Y, Hiltner A and Baer E. Nanolayer enhancement of biaxially oriented polypropylene film for increased gas barrier. *Polymer*. 2010; 51: 5807-14.
79. Shah RK, Krishnaswamy RK, Takahashi S and Paul DR. Blown films of nanocomposites prepared from low density polyethylene and a sodium ionomer of poly(ethylene-co-methacrylic acid). *Polymer*. 2006; 47: 6187-201.
80. Fereydoon M, Tabatabaei SH and Aiji A. X-ray and Trichroic Infrared Orientation Analyses of Uniaxially Stretched PA6 and MXD6 Nanoclay Composite Films. *has been submitted to Macromolecules*. 2013: n/a-n/a.
81. Cotterell B, Chia JYH and Hbaieb K. Fracture mechanisms and fracture toughness in semicrystalline polymer nanocomposites. *Engineering Fracture Mechanics*. 2007; 74: 1054-78.
82. Hu YS, Prattipati V, Hiltner A, Baer E and Mehta S. Improving transparency of stretched PET/MXD6 blends by modifying PET with isophthalate. *Polymer*. 2005; 46: 5202-10.

CHAPTER 9

GENERAL DISCUSSION

In food packaging, especially for the dairy products such as cheese, the packaging material should provide excellent oxygen, moisture, odor and gas barrier protection to prevent spoilage and to extend the shelf life. The packaging films also require having good mechanical properties to protect food, and also to prevent the controlled atmosphere inside the package from being lost. Finally, a good package needs to have an acceptable optical property to preserve the general appearance expected by consumers. Most of the food packages are composed of a multilayer film structure to achieve the desired requirements depending on the application. The multilayer films consisting of a core layer having good barrier and mechanical properties sandwiched between two polyolefin layers is commonly used in the food packaging industry. Among all the high oxygen barrier polymers used in the flexible packaging, nylon has gained a lot of attention due to its high stiffness, toughness, tensile strength, flex crack and puncture resistance as well as low oxygen transmission rate.

The first part of this work is aimed at understanding the differences between the microstructure and the macro-scale properties of aliphatic and aromatic nylons and their in-situ polymerized nanocomposites. The rheological and thermal properties, morphology, molecular orientation, ability to crystallize (i.e. fast or slow crystallization rate), type of crystalline structure as the key factors for the production of the precursor films which in turn control the final film properties have been investigated. Either direct (XRD and TEM) or indirect (rheology) morphological studies suggested that clay platelets were close to the state of exfoliation in both the aliphatic and aromatic nylon nanocomposites. In the dynamic rheological study, the high storage modulus in the low frequencies for the nanocomposites indicated the high clay dispersion

in the polymer matrices. The weighted relaxation spectra evaluated from dynamic moduli showed a longer relaxation time for the MXD6 compared to the PA6. This could be attributed to the higher intermolecular interactions and rigidity of the MXD6 chains caused by benzoic rings.

Our findings also showed that the crystallinity of the PA6/clay and the MXD6/clay was higher than their neat polymers. In addition, the crystallinity of the neat and nanocomposite MXD6 films was quite low due to the low crystallization characteristic time. In addition, a longer relaxation time of the MXD6 compared to the PA6 resulted in the slower rate of crystallization and lower crystallinity in the former. Although, the crystallinity of the MXD6 films was lower compared to the PA6 films, the permeability to oxygen was more than 5 times better for the former. The free volume of the MXD6 was reported to be 13.6 % less than that of the PA6 and could be the main reason for the better barrier properties in the former. It was also found that annealing improved the oxygen barrier and the crystallinity of the PA6 and the MXD6 as well as their nanocomposite films. It suggests that annealing caused less chain mobility, which led to an increase in tortuosity and permeation reduction. The MXD6 monolayer film showed larger Young's modulus and tensile strength compared to the PA6. The elongation at break and the toughness was higher for the PA6 monolayer film than for the MXD6 due to the higher flexibility of the PA6. The mechanical study suggested that adding clay to nylon, either aliphatic or aromatic, improved the mechanical performance without sacrificing tear strength and puncture resistance.

Subsequently, the effect of uniaxial stretching on the orientation of clay, crystal phase and amorphous region of precursor films was studied using the WAXD and the FTIR. Afterward, the effect of stretching on the thermal, barrier and mechanical properties of the aliphatic and aromatic nylon films and their nanocomposites was investigated.

The WAXD analysis showed a significant orientation of the *c*-axis of the clay along ND, indicating that the clay platelets were aligned in the MD-TD plane. The 3D cone curvature of the clay orientation became narrower, sharper and more concentrated in the center for the drawn films, implying more orientation. The clay platelets alignment in the MD for the PA6/clay film was greater than that for the MXD6/clay film. A higher MXD6/clay interaction combined with a low crystallinity of the MXD6 could explain a lower clay orientation, after stretching, in comparison with the aliphatic nylons. It was found that the clay orientation in MD was not affected significantly by stretching.

X-ray analysis revealed that the γ_1 crystal population of both nylons was mainly formed during rapid cooling of the cast films. However, only the PA6/clay films showed an extra γ_2 crystal population. In other words, two populations of γ crystals having different orientations with regards to the oriented clay platelets were observed in the PA6/clay films. The orientation of γ_1 and γ_2 crystal populations increased after uniaxial deformation. The orientation of the γ_2 calculated from the WAXD pole figures implied that the *b*-axis of the γ_2 crystal population was preferentially oriented along MD. This orientation increased drastically after the uniaxial stretching. The *b*-axis orientation of the γ_2 crystal population along TD decreased significantly upon uniaxial drawing. It can be concluded that the γ_2 crystal population is oriented in the TD-ND plane of the precursor or stretched PA6/clay films. In other words, the γ_2 crystal population in the PA6/clay films had a *b*-axis parallel to MD and a *c*-axis parallel to the normal vector of the clay plane due to the epitaxial arrangement of the γ_2 unit cells in the nylon nanocomposites. This is a different orientation from the γ_1 crystal population.

The FTIR analysis also suggested the lower amorphous orientation in the PA6/clay films compared to the pristine PA6, which was related to the spatial hindrance in the vicinity of the

clay platelets. The orientation of the amorphous phase was much lower than the crystalline phase after uniaxial deformation.

A systematic quantitative analysis was conducted to investigate the correlation between the microstructure (i.e. the orientation of amorphous and crystalline phases and the clay alignment) and the macro-scale properties (i.e. mechanical and barrier properties) of the precursor and uniaxially stretched aromatic and aliphatic nylons and their nanocomposite films. Various characteristics such as the thermal cold crystallization temperature, crystallinity, oxygen permeability and mechanical properties were considered to shed light on the controlling factors in the gas permeation through the films.

The precursor MXD6/clay had significantly better barrier property, attributed to its lower free volume and more packed chains compared to the PA6/clay film. The oxygen permeability of the stretched films increased with increasing draw ratio up to a critical value for each sample, while further stretching resulted in a reduction in the oxygen permeation. In fact, during hot stretching of either the aliphatic or aromatic nylon films at low draw ratios, the polymer chains relaxed and the chain entanglements decreased and as a result, the chain mobility increased and, accordingly, the free volume and gas permeation increased. After a critical draw ratio, the amorphous and crystalline chains alignment along the drawing direction increased. Therefore, a more packed structure of the polymer chains at the higher draw ratio lowered the free volume and resulted in a reduction in the gas permeation. The results from the mechanical test also revealed the same chain morphology transformation during uniaxial deformation.

At the last step of this project, multilayer films were prepared with cast co-extrusion and consisted of five layers: aliphatic and aromatic nylons and their nanocomposite as the high oxygen barrier layer (core), Linear Low Density Polyethylene (LLDPE) as the high moisture

barrier layers (skins) with the tie layers. The simultaneous processing of polymers with different rheological properties during coextrusion can cause melt disturbance or interfacial layer instability and encapsulation. To avoid these phenomena and to maintain the quality of final products, the rheological properties of the skin, tie and core layers should be similar. Since, the skin layer in a coextruded multilayer film undergoes higher shear rate than the polymer in core layer, it was expected to select a resin with slightly higher rheological properties than core. The viscoelastic properties of the neat and in-situ polymerized nanocomposites of aromatic and aliphatic nylons as well as the LLDPE showed that the storage modulus (G') and the viscosity of LLDPE was relatively higher than for the nylon resins. The selected materials were successfully coextruded with a minimum interfacial instability between the melt flows in the feed block.

The DSC analysis of the coextruded MXD6/LLDPE and nano-clay filled MXD6/LLDPE multilayer films displayed the higher thermal cold crystallization temperature of the MXD6 compared to the single layer MXD6 film. The difference can be explained by the changes in chains orientation of the MXD6 when used in monolayer and multilayer films. It suggested that the polymer chain orientation in a multilayer structure does not follow the same pattern as the monolayer films. Additionally, crystallinity (X_c) of the pristine and nanocomposite nylon films was higher in multilayer structure compared to the monolayer films. In addition, the series resistance model was not able to predict the multilayer film barrier properties based on the nanocomposites. Our findings indicated that a single layer of the pristine and nanocomposite aromatic and aliphatic nylon films did not display exactly the same barrier properties compared to when that polymer was used as a layer in a coextruded multilayer structure. The difference can be explained by the changes in chains orientation and polymer crystallinity as well as the boundary effects (e.g. transcrystallization) of adjacent layers. The oxygen permeation rate of the

neat MXD6/LLDPE coextruded multilayer film was 5 times better than for the neat PA6/LLDPE multilayer film. An improvement of about 58% was observed in the oxygen barrier, when the neat nylons in the core layer were substituted with the nanocomposites.

The MXD6/LLDPE coextruded multilayer film showed better moisture resistance compared to the PA6/LLDPE multilayer film. The nano-clay filled MXD6/LLDPE multilayer film showed the lowest water vapor transmission rate due to an increase in the water-induced crystallization phase by incorporating the nanoclay in the MXD6. The formation of hydrogen bonds between the amide groups caused by water molecules created small changes in the crystalline structure of the MXD6 and consequently, decreased the available moisture paths in the polymer matrix. After diffusion of moisture through the polymer matrix, a water-induced crystallization phase takes place at the interface of polymer chains and water molecules. It consequently improved the barrier properties of the MXD6 by moisture. In addition, incorporating clay in the coextruded MXD6 improved moisture barrier by about 58%. The strain-induced crystalline phase was also observed above a critical draw ratio during the uniaxial deformation of the MXD6/clay monolayer films.

The mechanical study suggested that for both aromatic and aliphatic nylon coextruded films, tensile strength was slightly higher in the MD than in the TD. Also the resistance to tear propagation for coextruded multilayer films in the TD was higher than in the MD, attributed to the chain orientation in the machine direction due to the stretching and the fast cooling during the cast film processing. The differences were more significant in the coextruded PA6/LLDPE multilayer film. This could be explained by the level of amorphous and crystal phase orientation in the pure and nanocomposite films. The same behavior was observed for the monolayer films. The coextruded PA6/LLDPE multilayer films showed higher toughness, tear and flex crack

resistance compared to those with the MXD6. The puncture resistance of the nano-clay filled MXD6/LLDPE multilayer film was about 62% lower than coextruded MXD6/LLDPE. This could be related to the strong interfacial adhesion between the exfoliated clay surface and the nylon matrix. The PA6/LLDPE multilayer films showed the highest flex crack resistance. The ability of the coextruded films to resist against crack propagation decreased by about 3.5 times, when the neat PA6 core layer of the multilayer films was substituted with the nanocomposites core layer. The coextruded aromatic nylon/LLDPE multilayer films showed a lower flex crack resistance compared to those made from the aliphatic ones. This could be due to the fact that the aromatic polymer has more rigidity and is more brittle because of its very strong intermolecular chain interactions. On the other hand, due to the strong bonding between nanoclay particles and the MXD6 chains, delaminating or splitting particles would be more difficult to achieve and the polymer becomes more brittle. The haze increased with substituting the neat MXD6 with the nanocomposite MXD6 or with the aliphatic polyamide as the core layer.

CHAPTER 10

CONCLUSIONS AND RECOMMENDATIONS

10.1 Conclusions

In this dissertation, first, monolayer films of aliphatic (PA6) and aromatic (MXD6) nylons and their in-situ polymerized nanocomposites with 4 wt% clay were prepared using a cast film extrusion process. Chill roll stretching and rapid cooling using an air knife were applied. The extent of nanoclay intercalation and exfoliation, thermal, rheological, crystal structure, crystallinity and non-isothermal crystallization, barrier and mechanical properties of films were studied.

The rheological results showed that the storage modulus increased with time, which was attributed to the amide interchange reactions and polycondensation between the nylon chains. The shear thinning behavior of the MXD6/clay nanocomposite was more prominent and occurred at lower frequencies compared to the PA6/clay, because of the stronger interactions in the former. A longer relaxation time for the MXD6 was related to its higher intermolecular interactions compared to the PA6 and resulted in the slower rate of crystallization and the lower crystallinity in the former. Adding clay drastically increased the rate of crystallization, particularly for the MXD6. Annealing improved the oxygen barrier and crystallinity of the PA6 and the MXD6 as well as their nanocomposite films and this was more pronounced for the latter. The γ crystalline phase was dominant for the annealed PA6/clay films whereas this crystalline form significantly transformed to the more stable α phase for the annealed PA6 films. In addition, annealing caused the formation of γ and α crystals in the MXD6 and its nanocomposite films. The MXD6 showed five times better oxygen barrier compared to the PA6. Due to a

stronger polymer chain interaction of the MXD6, there is a lower amount of free volume and gas diffusion path for the MXD6 than for the PA6. Incorporating clay in the PA6 and the MXD6 enhanced the oxygen barrier by 40 % and 46 %, respectively. The MXD6 showed much larger Young's modulus and tensile strength compared to the PA6. The elongation at break and toughness was higher for the PA6 than for the MXD6 due to the higher flexibility of the PA6. For both the aromatic and aliphatic nylons, the modulus and yield strength were slightly higher in MD than in TD, which was attributed to the chain orientation in the machine direction in the cast film processing. Adding clay to the nylon improved the mechanical performance without sacrificing the tear strength and puncture resistance.

In the next step, first, the effect of stretching on orientation of clay, crystalline phase and amorphous region of aliphatic and aromatic nylons and their nanocomposites were studied. Then, the effect of stretching on the thermal, barrier and mechanical properties of the nylon films in correlation with the orientation of crystals and amorphous phases and the clay alignment were fundamentally investigated. The precursor films were uniaxially stretched at 110 °C with draw ratios varying from 1.5 to 5 with the optimized rate of 400 mm/min. The changes in the orientation of clay and crystal axes of all the crystalline phases and amorphous region were examined using X-ray diffraction and Trichroic Infrared analyses. It was found that the clay platelets were mainly oriented in the machine direction (MD) and their orientation was slightly improved upon uniaxial stretching. X-ray analysis showed that the γ crystals (designated as γ_1) of both nylons were mainly formed during rapid cooling of cast films. However, only the PA6/clay films showed an extra γ crystal population (designated as γ_2). WAXD and FTIR analyses revealed that the c -axis of γ_1 crystal population was oriented in the normal and transverse directions (ND and TD), while the c -axis of γ_2 was aligned in the normal direction (ND),

indicating that this later crystal population formed perpendicular to the (001) plane of the clay platelets. The orientation of γ_1 and γ_2 crystal populations increased after uniaxial deformation. A small amount of the α phase crystals in the aliphatic nylons was found by FTIR and their orientation improved after uniaxial deformation. Also, the aromatic nanoclay composite films showed a small amount of crystalline phase induced by the presence of the clay. Finally, the amorphous phase showed a lower orientation in the nanocomposite films, which was explained by the spatial hindrance caused by the presence of the clay platelets.

Orientation of the crystalline and amorphous phases as well as clay alignment plays an important role in determining the permeability coefficient to diffusing gases through the polymer films. Higher orientation results in a lower diffusion coefficient and hence lower permeability. Our results showed that upon uniaxial stretching, the chain alignment and clay orientation improved significantly; therefore, a significant improvement in the mechanical and gas barrier properties of the stretched films is expected to be obtained.

The effect of uniaxial drawing on the crystal structure, thermal, mechanical and oxygen barrier properties of aliphatic and aromatic nylons as well as their in-situ polymerized nanocomposites was investigated and compared. The cold crystallization temperature (T_{cc}) of the uniaxially stretched MXD6 films drastically shifted to the lower temperatures with draw ratio. For the MXD/clay films, T_{cc} first decreased with draw ratio up to 3, and then increased upon further stretching. This behavior was attributed to the existence of water molecules during stretching which caused a reduction in enthalpy of the extra-cold crystallization. Nevertheless, the level of crystallinity of the oriented films increased. The oxygen permeability of the stretched films increased with draw ratio up to a critical value for each sample, while further stretching resulted in a reduction in oxygen permeation. At low draw ratios, the chain mobility increased,

resulting in less chain entanglements and accordingly more free volume. At higher draw ratios (beyond the critical value), the more packed structure of polymer chains lowered the free volume and resulted in a reduction in the oxygen permeation. The oxygen relative permeability of the precursor and uniaxially oriented nanocomposite films were determined with different geometrical models. With considering the Herman orientation function of the clay obtained from the previous step of this study as the real orientation parameter (κ) in the theoretical model, the calculated relative permeability from the model was more consistent with the experimental values. The relative oxygen permeability of the oriented films revealed that the experimental data and the predicted values obtaining from the theoretical models were closer for the aromatic nanocomposite films compared to the aliphatic ones. This is due to the lower level of crystallinity and orientation in the former. The effective aspect ratio of the clay (ϕ) as the effective tortuous path of the diffusant through the nanocomposite films, in the precursor and the stretched PA6/clay and MXD6/clay films were calculated using Bharadwaj's model and the experimental Herman orientation function of the clay (κ) obtained from the previous step of this study. The Young's modulus of the PA6 and the PA6/clay films significantly increased upon the uniaxial stretching. The Young's modulus enhancement after the uniaxial deformation was less significant for the aromatic nylons. The elongation at break of the PA6 and PA6/clay films reduced with draw ratio. In contrast, upon a small uniaxial deformation, the flexibility of the stretched MXD6 improved remarkably (ca. 25 times) compared to the precursor film. This behavior was related to the changes in the chain mobility and the orientation of the aromatic nylon upon the uniaxial drawing.

The last part of this work is aimed at understanding the role of the microstructure and the phase orientation of exfoliated nano-clay filled aromatic and aliphatic nylons, which were used

as the core layer in the coextruded multilayer films, on the barrier and mechanical properties. For this purpose, the coextruded multilayer films with PA6 and MXD6 nylons as well as their in-situ polymerized nanocomposites, as an oxygen barrier layer (core), and a linear low-density polyethylene (LLDPE) as the moisture barrier layers (skin) with the tie layers were produced and characterized. Five-layer films were prepared by cast coextrusion and rapidly cooled using an air knife. The dynamic rheological measurements conducted in the first step of this work allowed us to process the multilayer films with the minimum interfacial melt flow instability. The oxygen permeation analysis revealed that the substitution of the neat MXD6 in the core layer of the multilayer films with the neat PA6 decreased the oxygen transmission rate more than five times. An improvement of about 58% was observed in the oxygen barrier, when the neat nylons in the core layer were substituted with the nanocomposites. The monolayer nylon films did not display the same barrier properties compared to when that they were used as a layer in a coextruded multilayer structure. Therefore, the series resistance model was not able to predict the multilayer film barrier properties based on the nanocomposites. It was due to the changes in the chains orientation and the crystallinity of the polymer as well as the boundary effects of the adjacent layers. The MXD6/LLDPE multilayer film showed better moisture resistance compared to the PA6/LLDPE multilayer film. The coextruded PA6/LLDPE multilayer films showed higher toughness, tear and flex crack resistance compared to MXD6/LLDPE. The pristine MXD6 based multilayer film showed a lower haze compared to the PA6 films due to very little crystallinity in the former.

10.2 Recommendations

In the previous section, we summarized what has been accomplished in this thesis concerning the fabrication of high barrier monolayer and multilayer aromatic and aliphatic nylon films and their nanocomposites through cast extrusion followed by stretching and uniaxial drawing. For the continuation of this work and future research, the following unexplored topics are recommended:

- 1) The role of diffusion and reaction of tie layers between PE skin layers and nylon core layer is very important to be discussed in correlation with the barrier and mechanical properties. A fundamental study on the reaction rate and reaction kinetic as well as a fundamental investigation on the diffusion modeling at the polymer/polymer interface for the coextruded PA6/LLDPE, nano-clay filled PA6/LLDPE, MXD6/LLDPE and nano-clay filled MXD6/LLDPE multilayer films can be conducted.
- 2) In this dissertation, the main focus was on the core layer (high oxygen barrier) of a multilayer film. It is suggested that the effect of material used in the tie and skin layers (high moisture barrier) on the final properties of a multilayer films to be studied. It is suggested the nanocomposites of low density polyethylene (LDPE), high density polyethylene (HDPE) and polypropylene (PP) be used in the skin layer. Moreover, the effect of incorporating nanoclay in the tie layer on the seal, mechanical, optical, oxygen and water vapor barrier properties of multilayer films could be investigated. The level of maleic anhydride grafting on the adhesion between both tie/core and tie/skin and accordingly thermal, barrier, seal and mechanical properties of multilayer film could also be studied.
- 3) The effect of uniaxial deformation on thermal, oxygen barrier and mechanical properties of PA6 and MXD6 nanocomposite films was investigated. The effect of biaxial stretching on

the orientation, barrier properties and mechanical performance of the films could be compared with those obtained upon the uniaxial deformation.

4) Coextruded multilayer films with PA6/MXD6 blends as the oxygen barrier layer, a linear low-density polyethylene (LLDPE) as the moisture barrier layers and a linear low density polyethylene grafted with maleic anhydride (LLDPE-g-MA) as the tie layers have the combined advantages of superior flex crack resistance of PA6 and high barrier properties of MXD6. The influence of MXD6/PA6 blend ratio in the core layer on crystallinity, optical, tensile, oxygen and water vapor barrier properties as well as puncture and tear resistances of coextruded multilayer films can be investigated.

REFERENCES

1. Ebnesajjad, S., *Plastic Films in Food Packaging: Materials, Technology and Applications*. 2012: Elsevier Science.
2. Fereydoon, M., S.H. Tabatabaei, and A. Aji, *Rheological, crystal structure, barrier, and mechanical properties of PA6 and MXD6 nanocomposite films*. *Polymer Engineering & Science*, 2013. **published online**: p. n/a-n/a.
3. Lagaron, J.M., et al., *Study of the influence of water sorption in pure components and binary blends of high barrier ethylene-vinyl alcohol copolymer and amorphous polyamide and nylon-containing ionomer*. *Polymer*, 2001. **42**(Compendex): p. 9531-9540.
4. Hu, Y.S., et al., *Effect of water sorption on oxygen-barrier properties of aromatic polyamides*. *Journal of Polymer Science Part B: Polymer Physics*, 2005. **43**(11): p. 1365-1381.
5. *Gas Barrier Properties*, in <http://www.mgc.co.jp/eng/products/nop/nmxd6/barrier.html>. 2013, Mitsubishi Gas Chemical Company Technical Information Brochure.
6. Ammala, A., et al., *Poly(m-xylene adipamide)-montmorillonite nanocomposites: effect of organo-modifier structure on free volume and oxygen barrier properties*. *Journal of Materials Chemistry*, 2008. **18**(8): p. 911-916.
7. Ammala, A., et al., *Poly(m-xylene adipamide)-kaolinite and poly(m-xylene adipamide)-montmorillonite nanocomposites*. *Journal of Applied Polymer Science*, 2007. **104**(3): p. 1377-1381.
8. Wagner, J.R., *Hand Book of Multilayer flexible packaging technology and applications for food, personal care and over-the counter pharmaceutical industries*. 2010, Elsevier Inc.: Burlington, USA.
9. Zhang, Z., I.J. Britt, and M.A. Tung, *Permeation of oxygen and water vapor through EVOH films as influenced by relative humidity*. *Journal of Applied Polymer Science*, 2001. **82**(8): p. 1866-1872.
10. Lagarón, J.M., et al., *Characterization of extruded ethylene-vinyl alcohol copolymer based barrier blends with interest in food packaging applications*. *Macromolecular Symposium*, 2003. **198**(1): p. 473-482.
11. Tamber, H.S., *PVDC as a barrier material in packaging applications*. 1998, SME: Dearborn, MI, United States.
12. Hsieh, T.-H. and K.-S. Ho, *Effects of thermal stability on the crystallization behavior of poly(vinylidene chloride)*. *Journal of Polymer Science Part A: Polymer Chemistry*, 1999. **37**(16): p. 3269-3276.

13. Ghasemi, H., et al., *Preparation and characterization of PET/clay nanocomposites by melt compounding*. Polymer Engineering and Science, 2011. **51**(6): p. 1178-1187.
14. Yin, M., et al., *In-situ synthesis of poly(ethylene terephthalate)/clay nanocomposites using TiO₂/SiO₂ sol-intercalated montmorillonite as polycondensation catalyst*. Polymer Engineering and Science, 2009. **49**(8): p. 1562-1572.
15. Davis, C.H., et al., *Effects of melt-processing conditions on the quality of poly(ethylene terephthalate) montmorillonite clay nanocomposites*. Journal of Polymer Science Part B: Polymer Physics, 2002. **40**(23): p. 2661-2666.
16. Jabarin, S.A. and E.A. Lofgren, *Thermal stability of polyethylene terephthalate*. Polymer Engineering and Science, 1984. **24**(13): p. 1056-1063.
17. Tabatabaei, S.H. and A. Ajji, *Crystal structure and orientation of uniaxially and biaxially oriented PLA and PP nanoclay composite films*. Journal of Applied Polymer Science, 2012. **124**(6): p. 4854-4863.
18. Kato, M., et al., *Preparation and properties of polyethylene-clay hybrids*. Polymer Engineering and Science, 2003. **43**(6): p. 1312-1316.
19. Weinkauff, D.H. and D.R. Paul, *Gas transport properties of thermotropic liquid-crystalline copolyesters. I. The effects of orientation and annealing*. Journal of Polymer Science Part B: Polymer Physics, 1992. **30**(Compendex): p. 817-835.
20. Weinkauff, D.H. and D.R. Paul, *Gas transport properties of thermotropic liquid-crystalline copolyesters. II. The effects of copolymer composition*. Journal of Polymer Science Part B: Polymer Physics, 1992. **30**(Compendex): p. 837-849.
21. Ramathal, H. and A. Lawal, *Barrier properties of a thermotropic liquid-crystalline polymer*. Journal of Applied Polymer Science, 2003. **89**(Compendex): p. 2457-2463.
22. Lange, J. and Y. Wyser, *Recent innovations in barrier technologies for plastic packaging*. Packaging Technology and Science, 2003. **16**(4): p. 149-158.
23. Gavara, R. and R.J. Hernandez, *The effect of water on the transport of oxygen through nylon6-films*. Journal of Polymer Science Part B-Polymer Physics, 1994. **32**(14): p. 2375-2382.
24. Fornes, T.D. and D.R. Paul, *Crystallization behavior of nylon 6 nanocomposites*. Polymer, 2003. **44**(14): p. 3945-3961.
25. Li, Y. and W.A. Goddard, *Nylon 6 Crystal Structures, Folds, and Lamellae from Theory*. Macromolecules, 2002. **35**(22): p. 8440-8455.
26. Zhang, Y., et al., *Phase stability and melting behavior of the α and γ phases of nylon 6*. Journal of Applied Polymer Science, 2011. **120**(4): p. 1885-1891.

27. Liu, X. and C. Breen, *High-Temperature Crystalline Phases in Nylon 6/Clay Nanocomposites*. Macromolecular Rapid Communications, 2005. **26**(13): p. 1081-1086.
28. Miri, V., et al., *Crystallization Kinetics and Crystal Structure of Nylon6-Clay Nanocomposites: Combined Effects of Thermomechanical History, Clay Content, and Cooling Conditions*. Macromolecules, 2008. **41**(23): p. 9234-9244.
29. Magniez, K., B.L. Fox, and M.G. Looney, *Nonisothermal crystallization behavior of poly(m-xylene adipamide)/montmorillonite nanocomposites* Journal of Polymer Science Part B: Polymer Physics, 2009. **47**(13): p. 1300-1312
30. Ota, T., et al., *Crystal structure of poly(m-xylylene adipamide)*. Journal of Polymer Science Part B: Polymer Physics, 1966. **4**(6): p. 959-974.
31. Lagarón, J.M., et al., *Study of the influence of water sorption in pure components and binary blends of high barrier ethylene-vinyl alcohol copolymer and amorphous polyamide and nylon-containing ionomer*. Polymer, 2001. **42**(23): p. 9531-9540.
32. T.D. Krizan, J.C.C., P.S. Blatz, W.J. Koros (Ed.), *Barrier Polymers and Structures*, American Chemical Society, Washington, DC. 1990. 111–125 (Chapter 5).
33. Buquet, C.L., et al., *Permeation Properties of Poly(m-xylene adipamide) Membranes*. Journal of Physical Chemistry B, 2009. **113**(11): p. 3445-3452.
34. Shibayama, M., et al., *Miscibility and crystallinity control of nylon-6 and poly(m-Xylene adipamide) blends*. Polymer, 1995. **36**(25): p. 4811-4816.
35. Takeda, Y. and D.R. Paul, *The effect of physical interactions on melt-phase homogenized of mixtures of poly(M-Xylene Adipamide) with aliphatic polamides induced by interchange reactions*. Polymer, 1992. **33**(18): p. 3899-3907.
36. Takeda, Y. and D.R. Paul, *Phase homogenization of mixtures of poly(m-xylene adipamide) and nylon 6 by interchange reactions*. Polymer, 1991. **32**(15): p. 2771-2778.
37. Takeda, Y., H. Keskkula, and D.R. Paul, *TOUGHENING OF PHASE-HOMOGENIZED MIXTURES OF NYLON-6 AND POLY (META-XYLENE ADIPAMIDE) WITH A FUNCTIONALIZED BLOCK COPOLYMER*. Polymer, 1992. **33**(16): p. 3394-3407.
38. Brandon, K., et al., *The performance of several oxygen scavengers in varying oxygen environments at refrigerated temperatures: implications for low-oxygen modified atmosphere packaging of meat*. International Journal of Food Science & Technology, 2009. **44**(1): p. 188-196.
39. Braga, L.R., et al., *Evaluation of absorption kinetics of oxygen scavenger sachets using response surface methodology*. Packaging Technology and Science, 2010. **23**(6): p. 351-361.

40. Giles, G.A. and D.R. Bain, *Materials and development of plastics packaging for the consumer market*. 2000: Sheffield.
41. Hasebe, T., et al., *Recent advances in diamond-like carbon films in the medical and food packing fields*. New Diamond and Frontier Carbon Technology, 2007. **17**(Compendex): p. 263-279.
42. Shirakura, A., et al. *Diamond-like carbon films for PET bottles and medical applications*. in *ICMCTF 2005*. 2006. Elsevier.
43. Abbas, G.A., et al., *Structural investigation and gas barrier performance of diamond-like carbon based films on polymer substrates*. Carbon, 2005. **43**(Compendex): p. 303-309.
44. Faisant, J.B., et al., *Morphology, thermomechanical and barrier properties of polypropylene-ethylene vinyl alcohol blends*. Polymer, 1998. **39**(3): p. 533-545.
45. De Petris, S., et al., *Study of blends of nylon 6 with EVOH and carboxyl-modified EVOH and a preliminary approach to films for packaging applications*. Journal of Applied Polymer Science, 1998. **68**(4): p. 637-648.
46. Citterio, C., et al., *Physico-chemical characterization of compatibilized poly(propylene)/aromatic polyamide blends*. 1999. **270**(1): p. 22-27.
47. Hu, Y., et al. *Oxygen barrier enhancement of pet by blending with an aromatic polyamide*. in *ANTEC 2004 - Annual Technical Conference Proceedings, May 16, 2004 - May 20, 2004*. 2004. Chicago, IL., United states: Society of Plastics Engineers.
48. Wu, W., et al., *Morphology and barrier mechanism of biaxially oriented poly(ethylene terephthalate)/poly(ethylene 2,6-naphthalate) blends*. Journal of Applied Polymer Science, 2006. **101**(Compendex): p. 1309-1316.
49. Liang Y, O.S., Logsdon J, Cho JW and Lan T, *Nanoeffect in in-situ Nylon-6 Nanocomposites*. Nanocor Technical Paper, Nanocor Inc., Arlington Heights, USA, 2001.
50. Choudalakis, G. and A.D. Gotsis, *Permeability of polymer/clay nanocomposites: A review*. European Polymer Journal, 2009. **45**: p. 967-984.
51. Alexandre, M. and P. Dubois, *Polymer-layered silicate nanocomposites: preparation, properties and uses of a new class of materials*. Materials Science and Engineering Reports, 2000. **28**(1-2): p. 1-63.
52. Okada, A. and A. Usuki, *Twenty Years of Polymer-Clay Nanocomposites*. Macromolecular Materials and Engineering, 2006. **291**(12): p. 1449-1476.
53. Sadeghi, F. and A. Ajji, *Structure, Mechanical and Barrier Properties of Uniaxially Stretched Multilayer Nylon/Clay Nanocomposite Films*. International Polymer Processing, 2012. **27**(5): p. 565-573.

54. Yalcin, B., et al., *Molecular origins of toughening mechanism in uniaxially stretched nylon 6 films with clay nanoparticles*. Polymer, 2008. **49**(6): p. 1635-1650.
55. Kojima, Y., et al., *Mechanical properties of nylon 6-clay hybrid*. Journal of Materials Research, 1993. **8**(Compendex): p. 1185-1189.
56. Usuki, A., et al., *Synthesis of nylon 6-clay hybrid*. Journal of Materials Research, 1993. **8**(Compendex): p. 1179-1184.
57. Cho, J.W. and D.R. Paul, *Nylon 6 nanocomposites by melt compounding*. Polymer, 2001. **42**(3): p. 1083-1094.
58. Fornes, T.D., et al., *Nylon 6 nanocomposites: the effect of matrix molecular weight*. Polymer, 2001. **42**(25): p. 09929-09940.
59. Mohanty, S. and S.K. Nayak, *Mechanical, thermal and viscoelastic behavior of nylon 6/clay nanocomposites with cotreated montmorillonites*. Polymer-Plastics Technology and Engineering, 2007. **46**(4): p. 367-376.
60. Yeh, J.-T., et al., *Oxygen barrier and blending properties of blown films of blends of modified polyamide and polyamide-6 clay mineral nanocomposites*. Applied Clay Science, 2009. **45**(Compendex): p. 1-7.
61. Usuki, A., et al., *Characterization and properties of nylon 6. Clay hybrid*. 1990, ACS: Washington, DC, USA. p. 651-652.
62. Picard, E., et al., *Barrier properties of nylon 6-montmorillonite nanocomposite membranes prepared by melt blending: Influence of the clay content and dispersion state: Consequences on modelling*. Journal of Membrane Science, 2007. **292**(1-2): p. 133-144.
63. Kojima, Y., et al., *Synthesis of nylon 6-clay hybrid by montmorillonite intercalated with -caprolactam*. Journal of Polymer Science, Part A: Polymer Chemistry, 1993. **31**(Compendex): p. 983-986.
64. Gupta, B., M.-F. Lacrampe, and P. Krawczak, *Polyamide-6/clay nanocomposites*. Polymers and Polymer Composites, 2006. **14**(1): p. 13-38.
65. Dennis, H.R., et al., *Effect of melt processing conditions on the extent of exfoliation in organoclay-based nanocomposites*. Polymer, 2001. **42**(Compendex): p. 9513-9522.
66. Poisson, C., et al., *Mechanical, optical and barrier properties of PA6/nanoclay-based single- And multilayer blown films*. Polymers and Polymer Composites, 2008. **16**(6): p. 349-358.
67. Thellen, C., et al. *Nylon Nanocomposites Films for Food Packaging*. in *Society of Plastics Engineers Annual Technical Conference ANTEC*. 2006. USA.

68. Kojima, Y., et al., *Sorption of water in nylon 6-clay hybrid*. Journal of Applied Polymer Science, 1993. **49**: p. 1259-1264.
69. Pramoda, K.P., et al., *Thermal degradation behavior of polyamide 6/clay nanocomposites*. Polymer Degradation and Stability, 2003. **81**(1): p. 47-56.
70. Tung, J., et al., *Rheological and mechanical comparative study of in situ polymerized and melt-blended nylon 6 nanocomposites*. Polymer, 2005. **46**(23): p. 10405-10418.
71. Russo, G.M., G.P. Simon, and L. Incarnato, *Correlation between Rheological, Mechanical, and Barrier Properties in New Copolyamide-Based Nanocomposite Films*. Macromolecules, 2006. **39**(11): p. 3855-3864.
72. Yano, K., et al., *Synthesis and properties of polyimide clay hybrid*. Journal of Polymer Science Part a-Polymer Chemistry, 1993. **31**(10): p. 2493-2498.
73. Shelley, J.S., P.T. Mather, and K.L. DeVries, *Reinforcement and environmental degradation of nylon-6/clay nanocomposites*. Polymer, 2001. **42**(13): p. 5849-5858.
74. Brody, A.L., *"Nano, nano" food packaging technology*. Food Technology, 2003. **57**(12): p. 52-54.
75. Usuki, A., et al., *INTERACTION OF NYLON-6 CLAY SURFACE AND MECHANICAL-PROPERTIES OF NYLON-6 CLAY HYBRID*. Journal of Applied Polymer Science, 1995. **55**(1): p. 119-123.
76. Tie Lan, J.C., Ying Liang, Jerry Qian, and Peter Maul, *Application of nanomer in nanocomposites from concept to reality* Nanocor Technical Paper, Nanocor Inc., Arlington Heights, USA, 2001., 2001.
77. Tabatabaei, S.H., P.J. Carreau, and A. Ajji, *Structure and properties of MDO stretched polypropylene*. Polymer, 2009. **50**(16): p. 3981-3989.
78. Lin, Y.J., et al., *Oxygen permeability of biaxially oriented polypropylene films*. Polymer Engineering & Science, 2008. **48**(4): p. 642-648.
79. Chu, F. and Y. Kimura, *Structure and gas permeability of microporous films prepared by biaxial drawing of β -form polypropylene*. Polymer, 1996. **37**(4): p. 573-579.
80. Tabatabaei, S.H., P.J. Carreau, and A. Ajji, *Microporous membranes obtained from polypropylene blend films by stretching*. Journal of Membrane Science, 2008. **325**(2): p. 772-782.
81. Soon, K., et al., *Morphology, barrier, and mechanical properties of biaxially deformed poly(ethylene terephthalate)-mica nanocomposites*. Polymer Engineering & Science, 2012. **52**(3): p. 532-548.

82. Abu-Zurayk, R. and E. Harkin-Jones, *The influence of processing route on the structuring and properties of high-density polyethylene (HDPE)/clay nanocomposites*. Polymer Engineering & Science, 2012. **52**(11): p. 2360-2368.
83. Tabatabaei, S.H., P.J. Carreau, and A. Ajji, *Microporous membranes obtained from PP/HDPE multilayer films by stretching*. Journal of Membrane Science, 2009. **345**(1-2): p. 148-159.
84. Lin, Y., A. Hiltner, and E. Baer, *Nanolayer enhancement of biaxially oriented polypropylene film for increased gas barrier*. Polymer, 2010. **51**(24): p. 5807-5814.
85. Liu, R.Y.F., et al., *Oxygen-barrier properties of cold-drawn polyesters*. Journal of Polymer Science Part B-Polymer Physics, 2002. **40**(9): p. 862-877.
86. Qureshi, N., et al., *Oxygen-barrier properties of oriented and heat-set poly(ethylene terephthalate)*. Journal of Polymer Science Part B: Polymer Physics, 2000. **38**(13): p. 1679-1686.
87. Wu, W., et al., *Morphology and barrier mechanism of biaxially oriented poly(ethylene terephthalate)/poly(ethylene 2,6-naphthalate) blends*. Journal of Applied Polymer Science, 2006. **101**(3): p. 1309-1316.
88. Armstrong, S., et al., *Gas permeability of melt-processed poly(ether block amide) copolymers and the effects of orientation*. Polymer, 2012. **53**(6): p. 1383-1392.
89. Ben Doudou, B., E. Dargent, and J. Grenet, *Relationship between draw ratio and strain-induced crystallinity in uniaxially hot-drawn PET-MXD6 films*. Journal of Plastic Film & Sheeting, 2005. **21**(3): p. 233-251.
90. Hu, Y.S., et al., *Improving transparency of stretched PET/MXD6 blends by modifying PET with isophthalate*. Polymer, 2005. **46**(14): p. 5202-5210.
91. Cole, K.C., et al., *Biaxial deformation of polyamide-6: Assessment of orientation by means of infrared trichroism*. Polymer Engineering and Science, 2004. **44**(2): p. 231-240.
92. Cole, K.C., J. Denault, and M.N. Bureau, *Infrared spectroscopy studies of structure and orientation in clay-reinforced polyamide-6 nanocomposites*. Macromolecular Symposium, 2004. **205**(1): p. 47-60.
93. Penel-Pierron, L., et al., *Structural and mechanical behavior of nylon-6 films. II. Uniaxial and biaxial drawing*. Journal of Polymer Science Part B: Polymer Physics, 2001. **39**(11): p. 1224-1236.
94. Miri, V., et al., *Strain-induced disorder-order crystalline phase transition in nylon 6 and its miscible blends*. Polymer, 2007. **48**(17): p. 5080-5087.

95. Seguela, R., *On the Strain-Induced Crystalline Phase Changes in Semi-Crystalline Polymers: Mechanisms and Incidence on the Mechanical Properties*. Journal of Macromolecular Science, Part C, 2005. **45**(3): p. 263-287.
96. Sallem-Idrissi, N., et al., *Trichroic infrared analysis of the strain-induced structural changes in the PA6 layer of PA6/PE multilayer films under biaxial drawing*. Polymer, 2009. **50**(24): p. 5812-5823.
97. Penel-Pierron, L., et al., *Structural and mechanical behavior of nylon 6 films part I. Identification and stability of the crystalline phases*. Journal of Polymer Science Part B: Polymer Physics, 2001. **39**(5): p. 484-495.
98. Sadeghi, F. and A. Ajji, *Structure, Mechanical and Barrier Properties of Uniaxially Stretched Multilayer Nylon/Clay Nanocomposite Films*. International Polymer Processing, 2012. **5**: p. 565-573.
99. Ganpule, H.K. and B. Khomami, *An investigation of interfacial instabilities in the superposed channel flow of viscoelastic fluids*. Journal of Non-Newtonian Fluid Mechanics, 1999. **81**(1-2): p. 27-69.
100. Dooley, J., K.S. Hyun, and K. Hughes, *An experimental study on the effect of polymer viscoelasticity on layer rearrangement in coextruded structures*. Polymer Engineering and Science, 1998. **38**(7): p. 1060-1071.
101. Huang, C.H., J.S. Wu, and C.C. Huang, *Predicting the permeability and tensile behavior of high density polyethylene/tie/polyamide 6 three-layer films*. Polymer International, 2004. **53**(12): p. 2099-2106.
102. Tomomichi Kanda and A. Mori, *Gas-Barrier Multi-Layer Structure in Kanagawa*. 2007, Mitsubishi Gas Chemical Company Inc., Tokyo (JP): Japan.
103. Mueller, C., et al., *Thermoplastics film structures having improved barrier and mechanical properties in US20020150729 A1*. 2002: USA.
104. Takashige, M., T. Kanai, and T. Yamada, *Easy tear film of biaxially oriented PA 6/MXD 6 blend by double bubble tubular film process*. International Polymer Processing, 2004. **19**(2): p. 147-154.
105. Takashige, M. and T. Kanai, *Easy tear multilayer film of biaxially oriented PA6/MXD6 by double bubble tubular film process*. International Polymer Processing, 2005. **20**(1): p. 100-104.
106. Takeda, Y., H. Keskkula, and D.R. Paul, *Toughening of phase-homogenized mixtures of nylon-6 and poly(m-xylene adipamide) with a functionalized block copolymer*. Polymer, 1992. **33**(16): p. 3394-3407.
107. Selke, S.E.M., *Understanding Plastic packaging Technology*. 1997: New York, Hanser.

108. Hernandez, R.J. and C.A.H. (Ed.), *Handbook of Plastics, Elastomers and Composites*, ed. 3. 1996, New York McGraw-Hill.
109. Takahashi, S., et al., *Gas barrier properties of butyl rubber/vermiculite nanocomposite coatings*. *Polymer*, 2006. **47**(9): p. 3083-3093.
110. Bharadwaj, R.K., *Modeling the Barrier Properties of Polymer-Layered Silicate Nanocomposites*. *Macromolecules*, 2001. **34**(26): p. 9189-9192.
111. Choudalakis, G. and A.D. Gotsis, *Permeability of polymer/clay nanocomposites: A review*. *European Polymer Journal*, 2009. **45**(4): p. 967-984.
112. Del Nobile, M.A., et al., *Modeling the oxygen barrier properties of nylon film intended for food packaging applications*. *Journal of Food Science*, 2003. **68**(6): p. 2017-2021.
113. Koike, Y. and M. Cakmak, *Real time development of structure in partially molten state stretching of PP as detected by spectral birefringence technique*. *Polymer*, 2003. **44**(15): p. 4249-4260.
114. Ayer, R.K. and A.I. Leonov, *Comparative rheological studies of polyamide-6 and its low loaded nanocomposite based on layered silicates*. *Rheologica Acta*, 2004. **43**(3): p. 283-292.
115. Doudou, B., E. Dargent, and J. Grenet, *Crystallization and melting behaviour of poly(m-xylene adipamide)*. *Journal of Thermal Analysis and Calorimetry*, 2006. **85**(2): p. 409-415.
116. Hong, H., et al., *Synthesis of new 1-decene-based LLDPE resins and comparison with the corresponding 1-octene- and 1-hexene-based LLDPE resins*. *Journal of Polymer Science Part A: Polymer Chemistry*, 2007. **45**(4): p. 639-649.
117. Griffiths, P.R. and J.A. de Haseth, in *Fourier Transform Infrared Spectrometry*. 2006, John Wiley & Sons, Inc.
118. Sibilía, J.P., *Orientation in nylon 6 films as determined by the three-dimensional polarized infrared technique*. *Journal of Polymer Science Part A-2: Polymer Physics*, 1971. **9**(1): p. 27-42.
119. Garton, A., D.J. Carlsson, and D.M. Wiles, *Molecular Orientation Measurements in Polymers by Infrared Spectral Subtraction*. *Appl. Spectrosc.*, 1981. **35**(4): p. 432-435.
120. Holmgren, A. and X. Yang, *A Polarized Fourier Transform Infrared Spectrometry Attenuated Total Reflection Study of Bentonite Settled onto Magnetite*. *The Journal of Physical Chemistry C*, 2008. **112**(42): p. 16609-16615.
121. Loo, L.S. and K.K. Gleason, *Fourier Transform Infrared Investigation of the Deformation Behavior of Montmorillonite in Nylon-6/Nanoclay Nanocomposite*. *Macromolecules*, 2003. **36**(8): p. 2587-2590.

122. Arimoto, H., et al., *Crystal structure of the γ -form of nylon 6*. Journal of Polymer Science Part A: General Papers, 1965. **3**(1): p. 317-326.
123. Cullity, B.D. and S.R. Stock, *Elements of X-Ray Diffraction*. 2 ed. 2001, New Jersey: Prentice Hall.